

# Advanced algorithms for the analysis of PIV images

**Alessandro Masullo**

Department of Aerospace Engineering

University of Bristol



A dissertation submitted to the University of Bristol in  
accordance with the requirements of the degree of  
Doctor of Philosophy in the Faculty of Engineering.

JANUARY 2017



## **Abstract**

Particle Image Velocimetry (PIV) is non-intrusive measurement technique that estimates velocity fields by analysing the displacement of seeding particles injected in the flow. A typical PIV arrangement involves a fluid experiment, neutrally buoyant seeding particles, a source of light, lenses and a camera to record images. The physics of PIV and the optimal experimental settings were deeply investigated in the last twenty years, qualifying it as one of the most mature and adopted optical techniques for flow measurements. In spite of its capabilities, the integrity of PIV measurements is strongly affected by the quality of particle images, which can be compromised in certain experimental conditions.

An typical situation which is considered critical in PIV is the measurement of displacements near interfaces. In fact, due to factors like light reflections, reduced amount of seeding particles and corrupted images, the analysis of velocities near objects is still considered nowadays one of the most challenging aspects of PIV. Moreover, in order to guarantee a reliable measurement, several restrictions are imposed in terms of flow gradients, which must be confined within a certain range. Complex flow fields like shock-waves, shear layers and boundary layers constitute prohibitive cases that hinder reliable velocity extraction.

While some of these impediments can be partially overcome from an experimental point of view, the aim of this thesis is focussed on the improvement of PIV measurements from an algorithmic side, investigating novel solutions to analyse PIV images. In particular, five novel techniques are suggested and scrutinised throughout this thesis to enhance the measurement near interfaces and to allow the detection of flow fields dominated by strong velocity gradients.

The results of this thesis show that while important improvements can be obtained by the adoption of the proposed techniques, both in terms of measurement accuracy and computation time for the analysis, the limitations of PIV still constitute a challenging problem that remains nowadays open.



## **Acknowledgements**

This work would have never been possible without the indispensable help of my supervisor Raf. From the first time we met, he always considered me as a colleague, rather than a PhD student, giving me all the freedom I needed to explore the craziest ideas, while guiding me and teaching me with his great experience. Countless are the hours that we spent brainstorming in his office until late, investigating new ideas, creating new algorithms, finding explanations to phenomenons, or even just debugging a software. Raf has been the best guide that I could wish for, teaching me how to do research and always advising me for the best path for my career.

I also want to thank my family, Franco, Rossana and Cristina for supporting me through this long journey. They always believed in me and they have been there whenever I needed it, in spite of the distance that separated us.

Finally I want to thank my girlfriend Ana and all my colleagues from the office 1.67, Imanol, Alex, Will, Matt and everyone else. Thank you for everything!



## Publications

The research of this thesis has resulted to the journal and conference papers listed below.

Journal publications:

- *Automated mask generation for PIV image analysis based on pixel intensity statistics* Masullo, A. & Theunissen, R. May 2017, Experiments in Fluids
- *On the applicability of numerical image mapping for PIV image analysis near curved interfaces* Masullo, A. & Theunissen, R. 10 Apr 2017, Measurement Science and Technology
- *Adaptive vector validation in image velocimetry to minimise the influence of outlier clusters* Masullo, A. & Theunissen, R. Mar 2016, Experiments in Fluids
- *POD-based Background Removal for Particle Image Velocimetry* Mendez, M. A., Raiola, M., Masullo, A., Discetti, S., Ianiro, A., Theunissen, R. & Buchlin, J-M. Jan 2017, Experimental Thermal and Fluid Science

An additional paper entitled “On dealing with multiple correlation peaks in PIV” was submitted to the journal Experiments in Fluids in November 2017 and is currently under review.

Conference papers:

- *Improvement of PIV dynamic range in the presence of velocity gradients using multiple correlation peak analysis and self-adaptive windows* Masullo, A. & Theunissen, R. 4 Jul 2016, The International Symposia on Applications of Laser Techniques to Fluid Mechanics
- *Improvement in universal PIV outlier detection by means of coherence adaptivity* Masullo, A. & Theunissen, R. 14 Sep 2015, 11th International Symposium on Particle Image Velocimetry, At Santa Barbara
- *The feasibility of using CFD meshing in PIV image processing near curvy interfaces* Masullo, A. & Theunissen, R. 14 Sep 2015, 11th International Symposium on Particle Image Velocimetry, At Santa Barbara
- *Improved and robust universal PIV/PTV outlier detection in the presence of clusters* Masullo, A. & Theunissen, R. 15 Jun 2015, 10th Pacific Symposium on Flow Visualization and Image Processing
- *Near-wake analysis of perforated disks with varying hole topology* Theunissen, R., Worboys, R. & Masullo, A. 7 Jul 2016, The International Symposia on Applications of Laser Techniques to Fluid Mechanics



## List of symbols and abbreviations

### Acronyms used throughout the thesis

<i>CMOS</i>	Complementary Metal–Oxide–Semiconductor (image sensor)
<i>CW</i>	Correlation Window (same as IW)
<i>DNS</i>	Direct Numerical Simulation
<i>IW</i>	Interrogation Window
<i>LDA</i>	Laser Doppler Anemometry
<i>PIV</i>	Particle Image Velocimetry
<i>POD</i>	Proper Orthogonal Decomposition
<i>ppp</i>	Particles Per Pixel (seeding density)
<i>PTV</i>	Particle Tracking Velocimetry
<i>Re</i>	Reynolds number
<i>RMS</i>	Root mean square
<i>SNR</i>	Signal to Noise Ratio
<i>WOR</i>	Windows Overlap Ratio
<i>WS</i>	Window Size

## Chapter 1

### Acronyms

<i>LKT</i>	Lucas-Kanade Tracker
------------	----------------------

### Symbols

$x,y$	Space coordinates within an image
-------	-----------------------------------

## Chapter 2

### Acronyms

<i>JB</i>	Jarque-Bera test
<i>PDF</i>	Probability Density Function

## Symbols

$(x, y)$	Space coordinates within an image
$N$	Number of PIV images recorded in sequence
$JB$	Jarque-Bera statistic
$x$	Set of observations (i.e. sequence of intensity values for a pixel in time)
$E\{\cdot\}$	Expectation or Expected value
$s$	Skewness
$s$	Seeding density
$k$	Kurtosis
$\mu$	Mean
$\sigma$	Standard deviation
$t$	Time
$p$	P-value (probability)
$\nu$	Number of degrees of freedom of a distribution
$\chi$	Chi-squared distribution
$Pr\{\cdot\}$	Probability of $\{\cdot\}$
$n$	Number of particle images
$\varepsilon$	Error (difference between real and estimated masks)
$W, H$	Image width and height
$M_{i,j}$	Element in pixel position $(i, j)$ of the mask $M$

## Chapter 3

### Acronyms

$PDF$	Probability Density Function
$PDE$	Partial Derivative Equation
$IM$	Image mapping
$IMVR$	Image Mapping with Vector Relocation
$ASVR$	Adaptive Sampling with Vector Relocation
$ASIM$	Adaptive Sampling with Image Mapping
$ASIMVR$	Adaptive Sampling with Image Mapping and Vector Relocation
$CSVR$	Cartesian Sampling with Vector Relocation
$CSIM$	Cartesian Sampling with Image Mapping

## Symbols

$(x, y)$	Space coordinates on the physical plane (the image)
$(\xi, \eta)$	Space coordinates on the logical plane (mapped coordinates)
$\Delta A$	Local cell area for the mesh solution
$N_{\xi, \eta}$	Number of optimal pixels for image resampling
$u_{x, y}$	Velocity components on the physical plane
$u_{\xi, \eta}$	Velocity components on the logical plane
$(dx, dy)$	Increment on the physical plane
$(d\xi, d\eta)$	Increment on the logical plane
$J$	Jacobian matrix
$WS_{\xi, \eta}$	Window size on the logical plane (in logical units)
$WS_{\xi, \eta}^*$	Window size on the logical plane (in logical pixels)
$WS_{x, y}$	Window size on the physical plane (width and height)
$\gamma$	Curvilinear length of the mapped window size on the physical plane
$\epsilon_{transf}$	Error of the mesh
$\epsilon_{phy}$	Error on the physical plane
$\epsilon_{log}$	Error on the logical plane
$\epsilon_{ASIM, ASVR, etc.}$	Error for each of the techniques tested
$\rho$	Radius of curvature
$\theta$	Angle (angular coordinate for the polar transformation)
$U_{inf}$	Free stream velocity
$\beta$	Bias error
$\sigma$	Random error

## Chapter 4

### Acronyms

<i>LKT</i>	Lucas-Kanade Tracker
<i>FFT</i>	Fast Fourier Transform
$WS_{init}$	Initial window size
$WS_{final}$	Final window size

## Symbols

$(x,y)$	Pixel position
$T$	Template image (i.e. correlation window A)
$I$	Input image (i.e. correlation window B)
$W$	Warping function
$p$	Parameters of the warping function
$\Delta p$	Correction of parameter $p$
$N_p$	Total number of pixels in an image
$H$	Hessian matrix
$(\cdot)^T$	Transpose symbol
$(u,v)$	Velocity components
$N$	Number of pyramid levels for LKT
$N_{it}$	Number of iterations
$I_d$	Image disparity
$\lambda$	Eigenvalues

## Chapter 5

### Acronyms

$MPPIV$	Multiple Peak PIV
$MGRID$	Multi-Grid PIV
$MGRIDF$	Multi-Grid PIV with SNR filter
$LFC$	Local Field Correction PIV
$DSIW$	Different Size Interrogation Window
$RD$	Residual Displacement

## Symbols

$P$	Correlation peak value
$N$	Number of peaks
$\sigma_{thr}$	User defined threshold
$W_i$	$i$ -th correlation window
$\Phi$	Cross-correlation
$ds$	Sub-pixel displacement
$\mu$	Mean
$\sigma$	Standard deviation
$(u, v)$	Velocity components
$(\hat{u}, \hat{v})$	Estimated velocity components
$(u_{id}, v_{id})$	Ideal velocity components (ground truth)
$\delta$	Boundary layer thickness
$\varepsilon$	Normalized error
$S$	Rate of strain
$\lambda$	Sinusoid wavelength
$\phi$	Sinusoid phase
$A$	Sinusoid amplitude
$D_{disc}$	Disc diameter

## Chapter 6

### Acronyms

$AGW$	Adaptive Gaussian Windowing
$awmed$	Average-weighted median
$med$	Median

**Symbols**

$\varepsilon$	Allowed velocity variation (background noise)
$\varepsilon_\alpha$	Allowed velocity variation for the vector angle
$\Phi$	Generic surface (i.e. coherency)
$W$	Matrix of weights
$\sigma$	Deviation of velocity components from the median
$(u, v)$	Velocity components
$C$	Coherence function
$C_{u,v}$	Components of the coherence function
$T$	Validation threshold (usually set to 2)
$L$	Level of neighbourhood
$N_o$	Number of neighbours
$\Delta_w$	Averaging interval for awmed
$r^*$	Normalised residual
$r_{\alpha, V }$	Angular and intensity component of normalised residual
$\alpha$	Angle between vectors
$\delta_I$	Image disparity
$M$	Random vector magnitude
$C_f$	Clustering factor
$V_s$	Spurious vector (randomly imposed)
$(u_s, v_s)$	Components of spurious vector (randomly imposed)
$D_{disc}$	Disc diameter
$N_c$	Number of correct vectors in the field
$N_i$	Number of imposed outliers
$N_t$	Number of total vectors in the field
$N_w$	Number of correct vectors classified as outliers
$N_m$	Number of missed outliers
$R_o$	Ratio of over-detection
$R_u$	Ratio of under-detection
$R_o^*$	Ratio of over-detection rescaled with $N_t$

*“Any sufficiently advanced technology is indistinguishable from magic”*



### **Author's Declaration**

I declare that the work in this dissertation was carried out in accordance with the regulations of the University of Bristol. The work is original except where indicated by special reference in the text and no part of the dissertation has been submitted for any other degree.

Any views expressed in the dissertation are those of the author and in no way represent those of the University of Bristol.

The dissertation has not been presented to any other University for examination either in the United Kingdom or overseas.

Signed:

Dated:



# Contents

<b>1</b>	<b>Introduction</b>	<b>1</b>
1.1	Background and problem statement . . . . .	1
1.2	Motivation and outline of the thesis . . . . .	4
1.2.1	Measurement close to interfaces . . . . .	4
1.2.2	Measurement of velocity gradients . . . . .	6
1.2.3	Vector validation . . . . .	8
<b>2</b>	<b>Mask detection</b>	<b>11</b>
2.1	Abstract . . . . .	11
2.2	Introduction . . . . .	11
2.3	Methodology . . . . .	13
2.3.1	Normality test . . . . .	13
2.3.2	Pre-processing . . . . .	16
2.3.3	Minimum number of images required . . . . .	17
2.4	Post-processing . . . . .	17
2.5	Numerical assessment . . . . .	20
2.6	Experimental case . . . . .	22
2.7	Limitations . . . . .	25
2.8	Conclusions . . . . .	25
<b>3</b>	<b>Image mapping</b>	<b>29</b>
3.1	Abstract . . . . .	29
3.2	Introduction . . . . .	29
3.3	Problem definition and general image mapping methodology . . . . .	32
3.4	Mathematical background of body-conforming image mapping . . . . .	34
3.4.1	Hyperbolic vs. Elliptic mesh . . . . .	35
3.4.2	Hyperbolic mesh generation . . . . .	37
3.4.3	Numerical solution of the hyperbolic mesh equations . . . . .	38
3.4.4	Displacement conversion . . . . .	39

3.5	Practical implementation of cross-correlation using body conforming numerical grids . . . . .	40
3.5.1	Interface boundary definition . . . . .	40
3.5.2	Interpolation of mesh coordinates . . . . .	41
3.5.3	Correlation in the logical plane and enhanced re-sampling . . . . .	42
3.5.4	Interrogation window sizing on the logical plane . . . . .	45
3.5.5	Computational expense . . . . .	49
3.6	Numerical Assessment . . . . .	49
3.6.1	Inherent Error source 1: Mesh interpolation and displacement transformation . . . . .	50
3.6.2	Inherent Error Source 2: Mesh curvature influence on the particles distortion . . . . .	53
3.6.3	Limits of image mapping in a complete PIV analysis . . . . .	55
3.6.4	Summary: feasibility of image mapping . . . . .	62
3.7	Conclusions . . . . .	63
<b>4</b>	<b>Optical flow</b>	<b>65</b>
4.1	Abstract . . . . .	65
4.2	Introduction . . . . .	65
4.3	Methodology . . . . .	67
4.3.1	Choice of warping function . . . . .	68
4.3.2	Pyramidal implementation . . . . .	70
4.4	Reliability . . . . .	73
4.4.1	Measure of quality . . . . .	73
4.4.2	Image background . . . . .	74
4.4.3	Image disparity . . . . .	74
4.4.4	User defined parameters . . . . .	77
4.5	Computational cost . . . . .	78
4.6	Conclusions . . . . .	79
<b>5</b>	<b>Multiple-peak PIV</b>	<b>81</b>
5.1	Abstract . . . . .	81
5.2	Introduction . . . . .	81
5.3	Methodology . . . . .	85
5.3.1	Multiple peak detection . . . . .	86
5.3.2	Vector allocation . . . . .	89
5.4	Numerical assessment . . . . .	91
5.4.1	Boundary layer . . . . .	92
5.4.2	Sinusoid test . . . . .	95

---

5.4.3	Computational effort . . . . .	97
5.5	Experimental application . . . . .	98
5.6	Conclusions . . . . .	105
<b>6</b>	<b>Vector validation</b>	<b>107</b>
6.1	Abstract . . . . .	107
6.2	Introduction . . . . .	108
6.3	Problem Statement: coherency . . . . .	110
6.4	Methodology . . . . .	113
6.4.1	Coherence adaptive neighbourhood level . . . . .	113
6.4.2	Adaptive angle and magnitude median normalised residual . . . . .	115
6.5	Numerical assessment . . . . .	119
6.5.1	Evaluated test cases . . . . .	119
6.5.2	Validation algorithm performance . . . . .	123
6.6	Experimental application . . . . .	127
6.6.1	Porous disc . . . . .	132
6.6.2	Over-expanded supersonic jet . . . . .	136
6.7	Conclusions . . . . .	140
<b>7</b>	<b>Conclusions</b>	<b>145</b>
7.1	Summary of results . . . . .	145
7.2	Future work . . . . .	147



# List of Figures

1.1	Example of PIV images describing a typical configuration for the acquisition of the images (left) and a standard procedure for the image analysis (right). . . . .	1
1.2	Example of PIV images: (a) ideal image with bright spots on a dark background and (b) experimental image of a turbine blade with strong light reflections and interfaces (taken from the 1st PIV challenge, case C). . . . .	2
1.3	(a) Interrogation areas for PIV images recorded a two time steps (represented in different colours) and (b) their cross-correlation map. . . . .	3
1.4	Example of PIV analysis for challenging experimental conditions: (a) expected velocity field (time averaged), streamlines and contour map for the horizontal velocity; (b) instantaneous snapshot of velocity field obtained with PIV. The figure shows severe clusters of outliers in regions of strong gradients and corrupted measurements near the interface. Details on this experiment can be found at Section 5.5 . . . . .	5
1.5	(a) Interrogation window for PIV image next to an interface (dark area). (b) Cross-correlation map of the previous region, with broadened peak due to the interface. . . . .	6
1.6	Effect of displacement gradients on the correlation map. Figure shows the correlation map between interrogation windows subjected to a shear flow of varying intensity. In-plane gradients are respectively: (a) 0.01, (b) 0.05, (c) 0.1 and (d) 0.5 pixels/pixel. Predominant peaks are marked with red dots. . . . .	7
1.7	Example of PIV velocity field affected by outliers. Wrong vectors are marked with a red cross. . . . .	9
2.1	Illustration of the principle used for the mask detection: the probability distributions of pixel intensities have very distinguishable shapes depending on whether pixels belong to flow regions or objects . . . . .	14

2.2	Histogram of the p-values for a set of experimental images (micro-channel flow, see Section 2.6). The distribution of p-values presents the typical bi-modal distribution due to the presence of flow (low p-values) and object (high p-values). The automatic threshold discerns flow regions from the object by maximising the separability of the histogram. . . . .	15
2.3	Example of signal pre-processing, applicable in case of decaying laser intensity. (a) Synthetic Gaussian noise combined with decreasing average light intensity and (b) histogram; (c) high pass filtered signal with (d) restored Gaussian histogram. . . . .	16
2.4	Number of independent PIV images necessary to allow the correct functioning of the proposed masking algorithm against seeding density. The plots are shown for different probabilities as expressed by equation 2.8. . . . .	18
2.5	Example of application of the proposed sequence of morphological operations to (a) an artificially perturbed mask. (b) The application of closure removes single-pixel sized holes from the mask; (c) the filling operation closes any major size hole in the mask and (d) the majority operation allows a final clean from any smaller scale perturbation. . . . .	19
2.6	Three samples of cylinder images used for the synthetic analysis. Cylinders of 100 (left), 200 (centre) and 400 pixels (right) in diameter were generated using Gaussian noise. . . . .	20
2.7	Results of the Monte Carlo simulation for the mask detection of the three synthetic cylinders. The plots present the error of the mask detected versus the number of PIV images used for that detection error. . . . .	21
2.8	Result of the mask detection algorithm for the cylinder of 100 pixels of diameter using 200 images, showing a detail of the edges of the detected mask, together with the imposed mask and the respective overlap. . . . .	21
2.9	(a) Automatically detected mask for the micro-channel overlapped with a sample of the set of images (contrast enhanced for clarity), (b) histogram of the grey levels for a pixel belonging to the mask and (c) seeded flow portion. . . . .	23
2.10	Automatically detected mask for the transparent aerofoil (a); histogram of the grey levels for a pixel belonging to the aerofoil (b) and a pixel belonging to the shadow (c), both detected as part of the mask because of similar histograms. . . . .	24
2.11	Results of the automated mask detection for the lung test case, overlapped with a sample of the set of images (a); histogram of the grey levels for a pixel belonging to the object (b) and to a noisy area within the channel (c), both detected as mask. . . . .	26
3.1	Three tier structure of the chapter. . . . .	32
3.2	Description of the iterative algorithm. . . . .	34

3.3	Illustration of the concept of image mapping: (left) curvilinear coordinates $(\xi, \eta)$ are fitted in the physical plane to the object with boundary condition $f(x, y)$ ; (right) the curved interface becomes a straight line after transformation into the logical plane. . . . .	35
3.4	Solution of a hyperbolic mesh near the leading edge of an airfoil in case of (a) constant cell area, yielding an increasingly high cell-aspect ratio near the nose with radial distance (b) adjusting the cell area proportional to the Jacobian. This reduces the numerical cell-aspect ratio and minimises artificial displacement gradients when mapping images according to the generated mesh. . . . .	38
3.5	(a) Illustration of a self-intersecting mesh in case of concave boundary geometries without the application of artificial smoothing yielding non-unique image mapping and (b) the result of incorporating a smoothing factor. . . . .	39
3.6	(a) A logical mask provided as an image, clearly illustrating the discrete nature of the boundary edge. (b) Processing of boundary points extracted from the edges of the mask as per the Douglas-Pecker line simplification algorithm. . . . .	40
3.7	Plot of the coordinates mapping for the example mesh proposed in Figure 3.5. (a-b) Physical coordinates plotted against structured logical coordinates. (c-d) Logical coordinates plotted against scattered physical coordinates. . . . .	42
3.8	Description of the interpolation process of image intensities for correlation windows. (a) Logical pixels (filled rectangles bounded by red circles) are distributed on the logical plane. The grey grid represents the logical units. (b) The locations are mapped from the logical to the physical plane and image intensities on the physical plane are interpolated to yield the logical pixel intensities. . . . .	44
3.9	(a) Effect of the enhanced resampling for the case of the leading edge of a Joukowski airfoil shape. (b) The same correlation window is shown on the logical plane. (c) Logical correlation window adopting constant sampling and (d) the enhanced resampling showing the effectiveness of the method. Exemplary cross-correlation maps in case of (e) constant sampling and (f) enhanced resampling. Enhanced resampling improves the circularity of the particle images and correlation peak symmetry. . . . .	46
3.10	Iterative window repositioning and sizing in the logical plane: (a) correlation windows are located in the physical plane and (b) their centroids are mapped into the logical plane. (c) Window sizes are based on the Jacobian of the coordinate transformation at the corresponding window centres, potentially causing overlap with the interface boundary. (d) Logical windows are relocated and re-evaluated in size until no residual overlap with $\eta = 0$ . (e) Logical window areas extending below $\eta = 0$ are ignored and vectors are relocated to the centre of the reduced window. . . . .	48

3.11	Sample of PIV image for the Joukowsky aerofoil depicted with the numerical mesh (down-sampled for illustration purposes) used for the image mapping. . . . .	50
3.12	(a) Numerical error in mesh transformation, in $\log_{10}$ scale, after sequential coordinate transformation (physical plane $\rightarrow$ logical plane $\rightarrow$ physical plane). (b) Magnitude of the gradient of the coordinate transformation's Jacobian. (c) Amplification of random displacement error in the logical plane originating from coordinate transformation. . . . .	52
3.13	Description of the assessment of mesh-curvature influence. The correlation window size is chosen according to the circumference of the circle of smallest radius. . . . .	54
3.14	(a) Bias error $\beta$ and (b) random error $\sigma$ in measured particle image displacement versus cylinder radius with varying particle image diameter. Dashed line represent errors for cylinders of infinite radius. . . . .	54
3.15	Comparison of displacement error between ASIM and ASVR. Number of iterations: 3. Correlation window size: 90 $\rightarrow$ 25. No image noise. . . . .	57
3.16	Comparison of displacement error between ASIMVR and ASVR. Number of iterations: 3. Correlation window size: 90 $\rightarrow$ 25. No image noise. . . . .	58
3.17	Comparison of displacement error between (a) ASIM and ASVR, (b) ASMIVR and ASVR. Number of iterations: 3. Correlation window size: 90 $\rightarrow$ 25. With image noise. . . . .	59
3.18	Comparison of displacement error between (a) ASIM and ASVR, (b) ASMIVR and ASVR. Number of iterations: 1. Correlation window size: 25. With image noise. . . . .	60
3.19	Comparison of displacement error between CSIM and ASVR. Number of iterations: 3. Correlation window size: 90 $\rightarrow$ 25. (a) No image noise, (b) with image noise. . . . .	61
3.20	Distribution of correlation windows' centres the first iteration for (a) ASVR and ASIM and (b) CSVR and CSIM. Only by vector relocation can data be collected even closer to the airfoil than with image mapping. . . . .	61
4.1	Application of LKT with parabolic warping function to experimental images in (a) case of strong image gradients (red arrows depict the estimated vectors) and (b) complex velocity field (the two interrogation windows are overlapped in blue and yellow in a single colour image). . . . .	69
4.2	Illustration of the pyramidal approach for the Lucas-Kanade algorithm. . . . .	71
4.3	Velocity displacement predictor ( $u$ component) for interrogation windows analysed with LKT and linear warping function. . . . .	72
4.4	Two sequential PIV images of a vortex (a-b). Images convoluted with a Gaussian before being sub-sampled for the pyramidal approach (c-d) . . . . .	75

4.5	Magnitude of gradients pertaining the images in Figure 4.4. . . . .	76
4.6	Displacement field for the highest level of the pyramidal LKT in case of (a) original non-filtered images and (b) high-pass filtered images. . . . .	76
4.7	Detail of interrogation windows containing steady particles with varying image intensity. Red arrows show the wrong optical flow estimated by LKT, scaled for displaying purpose. . . . .	77
4.8	Comparison of computational time for Lucas-Kanade and cross-correlation (direct and FFT), for an interrogation window of variable size and a synthetic image describing a displacement of 1 pixel. . . . .	79
5.1	Effect of displacement gradients on the correlation map. The figure illustrates the correlation map between interrogation windows subjected to a shear flow of varying intensity. In-plane gradients are respectively: (a) 0.01, (b) 0.05, (c) 0.1 and (d) 0.5 pixels/pixel. As the gradient increases, the correlation map contains multiple detectable peaks, marked with red dots. . . . .	83
5.2	Flow chart of the MP-PIV algorithm. Notice the collocation of two different sets of correlation points: correlation windows to detect displacements and sub-correlation windows to anchor vectors. . . . .	86
5.3	Examples of correlation maps with multiple peaks due to (a) bad correlation and (b) multiple displacements. . . . .	87
5.4	The principle of triangle thresholding as an automated method to discern strong peaks from correlation noise. The blue plots represents the histogram (PDF) of the correlation map, with the black line connecting the maximum of the correlation (on the x-axis) with the maximum value of the PDF (on the y-axis). The red plots represents the distance between the max-max line and the values of the histogram. The maximum value of this distance, shifted by an offset of typically 0.1, yields the automatic threshold. . . . .	88
5.5	Illustration of the correlation peak refining process using Signal-to-Noise Ratio ( <i>SNR</i> ). The example shows an application containing 50 randomly generated peaks, extracted from a normal distribution, sorted from the highest to the smallest. The first peak selection is based on peak amplitude through the triangle-threshold method. The secondary selection is based on the consecutive <i>SNR</i> with a user-defined lower limit. . . . .	89
5.6	Layout of correlation and sub-correlation windows adopted in the MP-PIV algorithm. Correlation windows (green) are used to detect multiple displacements peaks. No vector is allocated in these areas. Instead, sub-correlation windows (red) are used to assess each of the selected potential particle displacements. Displacements yielding the highest correlation peak within a sub-window are anchored to the geometrical centre of the sub-correlation window. . . . .	90

5.7	Boundary layer profiles across the initial interrogation window ( $WS_{init} = 65\text{pixels}$ ), for different freestream pixel displacements ( $U_\infty$ ), imposed in the numerical assessments. . . . .	93
5.8	Results for the boundary layer simulation. Normalised error plots are presented for three different levels of seeding density: (a) 0.03, (b) 0.1 and (c) 0.3 ppp. . .	94
5.9	Plots of the normalised amplitude $\hat{A}/A$ for the numerical assessment involving a sinusoidal displacement field considering three different amplitudes: (a) $A=3$ , (b) $A=5$ and (c) $A=7$ pixels. . . . .	96
5.10	Computational time for different techniques analysed in Table 5.1. The computational time for MP-PIV is strongly dependent on the complexity of the flow field. . . . .	98
5.11	(a) Sketch of the porous disc tested. The green line indicates the location of the PIV measurement plane. (b) Exemplary PIV image recording illustrating the reflections off the disc surface (left) and mirror images/reflections (middle). Flow is from left to right. . . . .	99
5.12	Average displacement field (sub-sampled for displaying purpose) and average displacement magnitude for the disc images. Red dashed lines are the locations where profiles are extracted (Figures 5.13 and 5.14). . . . .	100
5.13	Profiles of mean horizontal velocity component extracted along respectively $y/D_{disc} \approx \pm \frac{1}{6}$ in Figure 5.12. See Table 5.1 for a description of the considered methods. . . . .	101
5.14	Vertical profiles of the $u$ component of the mean velocity extracted along the vertical red dashed lines of Figure 5.12 at respectively $x/D_{disc} \approx 0.1$ and $x/D_{disc} \approx 0.45$ . Description of the methods in the legend can be found in Table 5.1. . . . .	102
5.15	Average residual displacements for (a) MP-PIV, (b) LFC, (c) MGRID, (d) MGRIDE, (e) DSIW. Values of the residual for (e) DSIW were cut because the same scale as other methods was used for consistency. MP-PIV attains the lowest levels of residual near the jets area, where gradients are the strongest. . .	103
5.16	Horizontal profiles of the residual displacement extracted along the red dashed lines ( $y/D_{disc} \approx \pm \frac{1}{6}$ respectively) of Figure 5.12. . . . .	104
5.17	Vertical profiles of the residual extracted at respectively $x/D_{disc} \approx 0.1$ and $x/D_{disc} \approx 0.45$ (red dashed lines of Figure 5.12). . . . .	105

6.1	Illustration of the need for adaptive neighbourhood selection in vector validation. (a) Detail of a scrutinised vector and its closest neighbours. Only by expanding the local neighbourhood does it become clear these vectors belong to (b) outlier cluster or (c) a valid flow structure or. Symbols in (c) indicate which vectors are considered incoherent based on [67] ( <i>blue circle</i> ) and the median test of [96] ( <i>orange triangle</i> ). . . . .	111
6.2	Acceptable vector variations for a fluctuation level $\varepsilon$ in (a) both horizontal and vertical velocity components $u$ and $v$ respectively for larger and (b) small vector magnitudes. Limits in variations with adaptive angle variations $\varepsilon_\alpha$ for (c) large and (d) small vector magnitudes. . . . .	112
6.3	Three steps in adaptive vector validation; based on a metric for vector coherency the number of vectors in the local vicinity is increased to provide a reliable basis for subsequent outlier detection. . . . .	113
6.4	(a) Incremental neighbourhood level with $L_{\min} = 0$ in case of a vector placement on the nodes of a structured grid (b) Illustration of the automatic evaluation of the required neighbourhood level $L$ indicated by the greyscale. The central area of the flow field has been artificially contaminated with outliers. Towards the centre of the cluster the level increases, indicative of strongly incoherent vectors necessitating an enlarged number of vectors for validation. . . . .	115
6.5	(a) Vector validation involves the comparison of the central (black) vector with the predicted vector (grey) on the basis of the neighbouring vectors. The prediction follows from an average-weighted median. (b) Weights in the $\text{awmed}(\cdot)$ operator depend on the distance between the investigated vector and its neighbours following equation 6.9 and are reflected in the bar widths. An interval $\Delta w$ is centred on the weighted median (solid black line) and the weighted average is taken of the data overlapping the defined interval. . . . .	118
6.6	Flow test cases used to assess vector validation algorithms (a) turbulent channel flow [99] (b) isolated vortex [100] (c) DNS simulation of isotropic turbulence [53]. . . . .	120
6.7	Sample vector field with imposed outliers located at red circles, with $M = 1$ (a) $C_f = 1$ , (b) $C_f = 8$ and (c) $C_f = 32$ . . . . .	122
6.8	Evolution in normalised (a) under-detection and (b) over-detection ratios (normalisation by maximum value) with varying $\Delta w$ for flow fields representing an isolated vortex [99], turbulent channel flow [100] and DNS simulation of isotropic turbulence [53]. . . . .	124

6.9	Influence of cluster-size and outlier magnitude on neighbourhood level $L$ in the case of the vortex flow (a) $C_f = 1$ (isolated outliers), $M = 0.1$ (b) $C_f = 10$ , $M = 0.1$ (c) $C_f = 10$ , $M = 10$ . With increasing size of outlier clusters and outlier magnitude, the number of neighbours $N_o$ considered in the average-weighted median operation increases adaptively. Increased neighbourhood levels emanate from the outliers to surrounding vectors, indicative of their non-localised detrimental influence towards over-detection. . . . .	126
6.10	Comparison between universal outlier detection (NMT), distance-weighted outlier detection (DW-NMT), NMT and DW-NMT extended with a variable neighbourhood (ANMT and ADW-NMT) and the proposed adaptive weighted angle and magnitude thresholding (AWAMT) in terms of the evolution in under-detection $R_u$ and $R_u^*$ (left column) and over-detection $R_o$ (right column) with increasing cluster size of outliers for the case of unstructured velocity data of a cellular vortex (top row), turbulent channel flow (middle row) and structured DNS simulation data of isotropic turbulence (bottom row). The maximum magnitude of the outlier was set at 10% of the local velocity ( $M = 0.1$ ). . . . .	128
6.11	Comparison between vector validation methodologies applied to velocity fields contaminated with imposed outlier clusters of varying size and fixed magnitude. The maximum magnitude of the outlier was set at 100% of the local velocity ( $M = 1$ ). See Figure 6.10 for further details and legend entries. . . . .	129
6.12	Comparison between vector validation methodologies applied to velocity fields contaminated with imposed outlier clusters of varying size and fixed magnitude. The maximum magnitude of the outlier was set at 10 times the local velocity ( $M = 10$ ). See Figure 6.10 for further details and legend entries. . . . .	130
6.13	Comparison between vector validation methodologies applied to velocity fields contaminated with imposed outlier clusters of fixed size ( $C_f = 8$ ) and varying magnitude. See Figure 6.10 for further details and legend entries. . . . .	131
6.14	Ensemble-averaged flow field (under-sampled by a factor 3 in both directions for clarity) of 500 snapshots of the near-wake behind the porous disc. Dashed red lines indicate the locations of the extracted velocity profiles. . . . .	133
6.15	Comparison of the number of replaced vectors across the PIV data series (500 images) as per the outcome using (left) NMT vector validation (right) AWAMT vector validation. Dashed lines indicate the locations of profile extraction. . . . .	133
6.16	(a) Profiles in horizontal velocity component extracted along the vertical directions indicated in Figure 6.14. (b) Comparison of streamwise velocity along the lower jet centreline obtained from LDA and PIV data incorporating NMT, ANMT and AWAMT validation. . . . .	135

---

6.17	(a) Profiles in longitudinal turbulence intensity extracted along the vertical directions indicated in Figure 6.14. (b) Comparison in longitudinal turbulence intensity along the lower jet centreline obtained from LDA and PIV data incorporating AWAMT and NMT validation. . . . .	137
6.18	(a) Experimental PIV recording of an over-expanded jet at Mach 3.33 (contrast enhanced for clarity) and (b) Ensemble averaged velocity field (undersampled by a factor 2 for readability). Red lines indicate the locations of the extracted profiles. . . . .	138
6.19	Comparison of the number of replaced vectors across the PIV data series (280 images) for the case of the over-expanded supersonic jet as per the outcome using (left) NMT vector validation (right) AWAMT vector validation. . . . .	139
6.20	(a) Profiles in average horizontal velocity extracted along the vertical directions indicated in Figure 6.18b. (b) Mean streamwise velocity along the jet centreline.	141
6.21	(a) Profiles in longitudinal turbulence intensity extracted along the vertical directions indicated in Figure 6.18b. (b) Comparison in probability distribution of horizontal velocity at $x/D_{noz} = 0.28$ incorporating NMT and AWAMT vector validation in PIV. . . . .	142



# Chapter 1

## Introduction

### 1.1 Background and problem statement

Particle Image Velocimetry (PIV) is a widely known technique used to visualise and measure flow displacements [5]. A typical PIV experiment is represented in Figure 1.1: seeding particles are injected in the flow and illuminated with a strong source of light (typically a laser) such that they scatter sufficient light to make them appear in image recordings. Images of the particles are recorded at regular time intervals and subsequently processed to analyse displacements. The seeding particles must be properly chosen to have the same density as the fluid (quasi), in order to be neutrally buoyant. In these conditions, particles will follow the fluid motion thanks to the drag force (Stokes' drag law [79]), therefore the analysis of their displacement can be related to the measurement of instantaneous velocities.

Typical images of PIV tracer particles appear like blurred white spots on a black background [4]. To achieve this type of image, ideal experimental settings [51] require seeding particles to be homogeneously distributed, uniformly sized and evenly illuminated on a completely dark background (Figure 1.2a). Unfortunately, ideal experimental conditions are only

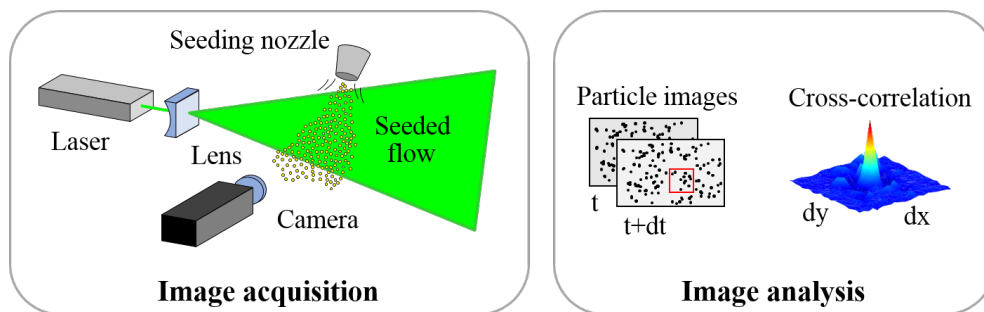


Figure 1.1: Example of PIV images describing a typical configuration for the acquisition of the images (left) and a standard procedure for the image analysis (right).

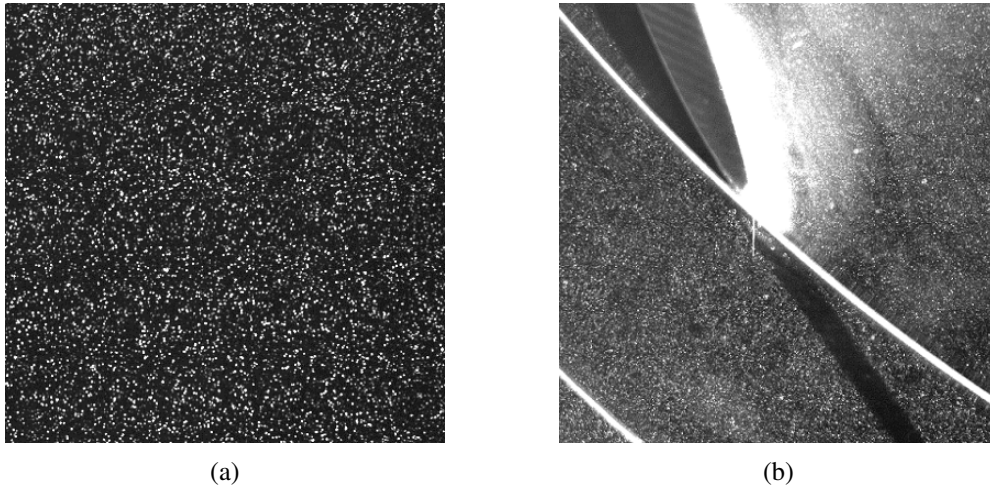


Figure 1.2: Example of PIV images: (a) ideal image with bright spots on a dark background and (b) experimental image of a turbine blade with strong light reflections and interfaces (taken from the 1st PIV challenge, case C).

possible under strictly controlled circumstances and industrial applications often require measurements in unevenly illuminated environments with flows contaminated by obstacles, background images and light reflections (Figure 1.2b). Furthermore, the area in vicinity of objects often constitutes the main region of interest of the experiment due to the appearance of boundary layers. Near-wall regions require the implementation of special strategies to obtain reliable measurements, in fact, they are usually populated by fewer seeding particles than the main flow and they often present strong light reflections which degrade the signal quality [42]. Experimental precautions can be taken to minimise light reflections, although these procedures often involve the use of toxic paint and expensive seeding particles and still do not produce ideal images [72]. These issues pose severe limitations to the application of PIV in cases like boundary layers, turbo-machinery, bubbles, free-surfaces, turbulence and water waves ([30],[40], [112], [109]).

In addition to this constraint, several restrictions also apply to the flow gradients that can be measured with PIV. The analysis of images is typically performed by dividing the region of interest into small interrogation areas<sup>1</sup> and processing them with cross-correlation. If the regions are sufficiently small to neglect in-plane displacement gradients [3], the correlation map will produce a strong peak located at the particles displacement (Figure 1.3). Previous works in the literature suggest an upper limit to displacement gradients on the order of 0.05 pixels/pixel for standard cross-correlation [51] or 0.5 pixels/pixel for more advanced iterative multigrid algorithms [89]. However, when in-plane gradients exceed those values, the correlation map broadens increasing the uncertainty of the measurement. Incrementing the gradients

<sup>1</sup>Throughout this work, the following expressions will be used as synonyms: correlation window, interrogation window, interrogation region, interrogation area.

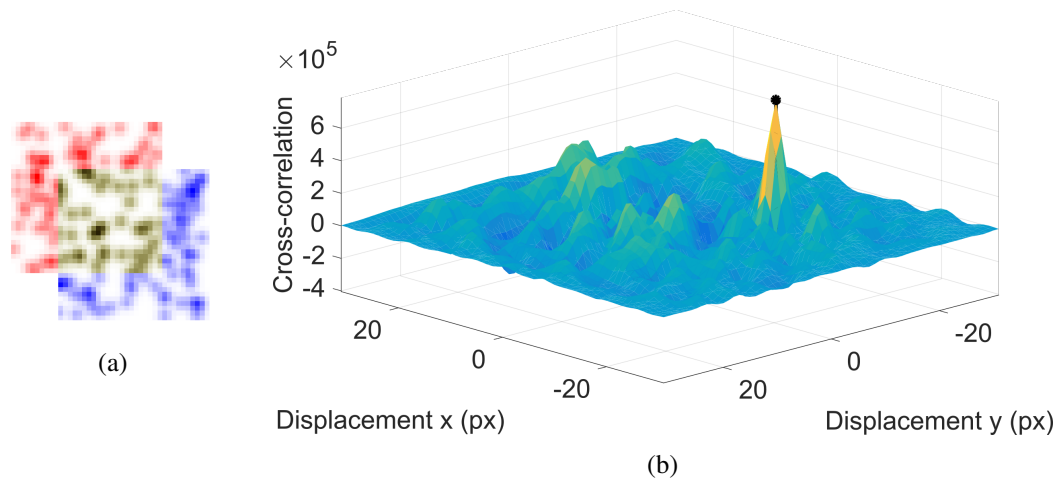


Figure 1.3: (a) Interrogation areas for PIV images recorded a two time steps (represented in different colours) and (b) their cross-correlation map.

even further will cause the correlation peak to splinter into multiple spikes [124], rendering the measurement completely unreliable (see Figure 1.6). Existing PIV algorithms are unable to cope with these conditions, although they are really common in flow fields dominated by strong gradients like jets [7], boundary layers [109], shock waves [126] and shear flows.

When obstacles appear in the interrogation areas, or particle motion is affected by strong in-plane gradients, the aforementioned distortion of the correlation peak can produce wrong vectors [119]. Outliers are typically isolated vectors, but if not detected properly, they can cause the formation of outlier clusters. When wrong vectors form clusters they are very difficult to detect and can strongly deteriorate the quality of the measurement.

An illustration of the PIV limitations above described can be observed in Figure 1.4, presenting a challenging test case for standard PIV algorithms. The experimental settings consist of a section of a perforated plastic disc, simulating a porous material (see Section 5.5 for more details on the experiment), whose expected velocity field is depicted in Figure 1.4a. The air is flowing from left to right and the velocity field is characterised by two strong horizontal jets originating from the centre of the disc that are very difficult to capture. Figure 1.4b shows the instantaneous displacement field produced by a standard PIV algorithm. Because of the intense gradients near the jets, correlation maps are strongly deformed and produce several outliers that corrupt the entire measurement. Velocities near the disc surface also show a bias towards zero due to the non-masked pixel intensities of the light reflection from the disc. Complex displacement fields like the one in Figure 1.4 highlight the requirement of special PIV algorithms to provide reliable velocity measurements.

## 1.2 Motivation and outline of the thesis

The aforementioned limitations of PIV set the basis for the aim of this work, which is the development of advanced algorithms to overcome these constrictions. In particular, the methodologies proposed in Chapter 2 and 3 are dedicated to the problem of measurement close to stationary interfaces, while Chapter 4 and 5 discuss the problem of displacement gradients. In Chapter 6, the problem of outliers in velocity fields is investigated, while Chapter 7 summarises the results of this thesis.

Some chapters of this thesis were peer reviewed and published on scientific journals. In particular, Chapter 2 was published in [58], Chapter 3 in [59] and Chapter 6 in [57]. Finally, Chapter 5 is currently under review for a publication in *Experiments in Fluids*.

### 1.2.1 Measurement close to interfaces

The problem of PIV measurements close to interfaces is of great interest within the community of PIV users and has been deeply analysed in the past, although a final solution is still far from found. From an experimental point of view, the most common solutions adopted require special treatments of the interfaces, like black coating, use of electro-polished materials or transparent media [72]. The use of fluorescent particles as seeding tracer, combined with special filters, was successfully adopted to eliminate the disturbing light reflected from the objects [98]. Although experimental solutions can help to enhance the measurement of velocities close to surfaces, not only can they be expensive, but they are not suitable for all the experimental settings. Moreover, even in case of ideal conditions, the overlap between the interrogation window and the interface still causes an increased error in vicinity of walls and objects [65]. Figure 1.5 elucidates this problem with an example of interrogation window overlapping with an object: due to the presence of this interface, the peak becomes broader and its position harder to detect.

Let aside the experimental aspects of the PIV analysis, the most common strategy to analyse images corrupted by objects and interfaces is the implementation of logical masks [36]. Masking techniques allow the analysis of different areas of the image by simply excluding part of it from the calculations [83]. By using masks, conditions like multi-phase flows can be analysed adopting different techniques for each phase of the flow [35]. In the last two decades, different approaches have been proposed to deal with interfaces. Methods like particle image mirroring [110], adaptive window position and orientation [105] and image deformation using coordinate transformation [85] have been studied to improve the accuracy of the measurements, and will be further discussed in Chapter 3. In spite of the numerous works published to overcome this limitation of PIV, the problem of measurements close to objects still remains a very difficult task and, as it will be showed in this work, constitutes a challenging field of research.

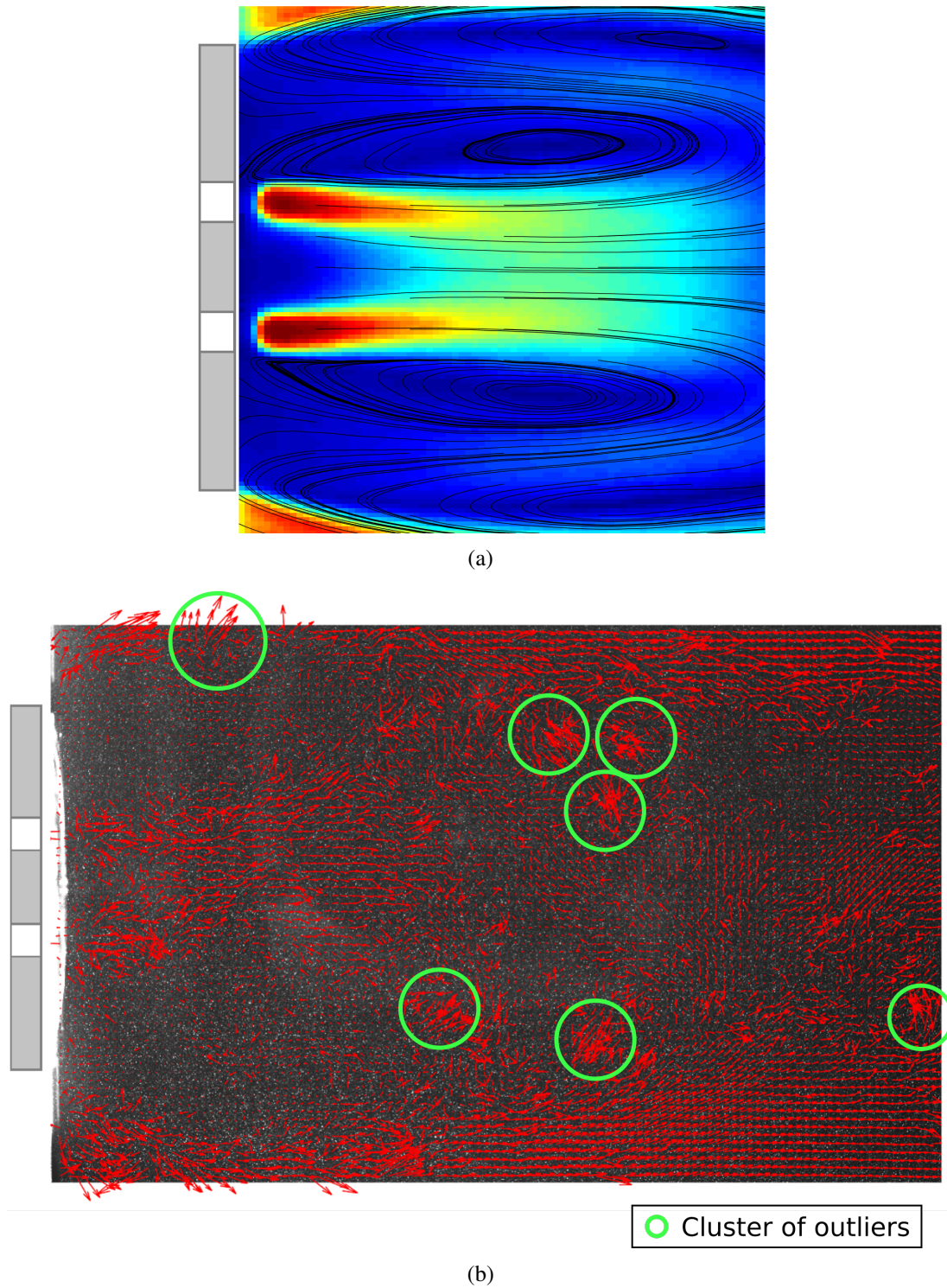


Figure 1.4: Example of PIV analysis for challenging experimental conditions: (a) expected velocity field (time averaged), streamlines and contour map for the horizontal velocity; (b) instantaneous snapshot of velocity field obtained with PIV. The figure shows severe clusters of outliers in regions of strong gradients and corrupted measurements near the interface. Details on this experiment can be found at Section 5.5

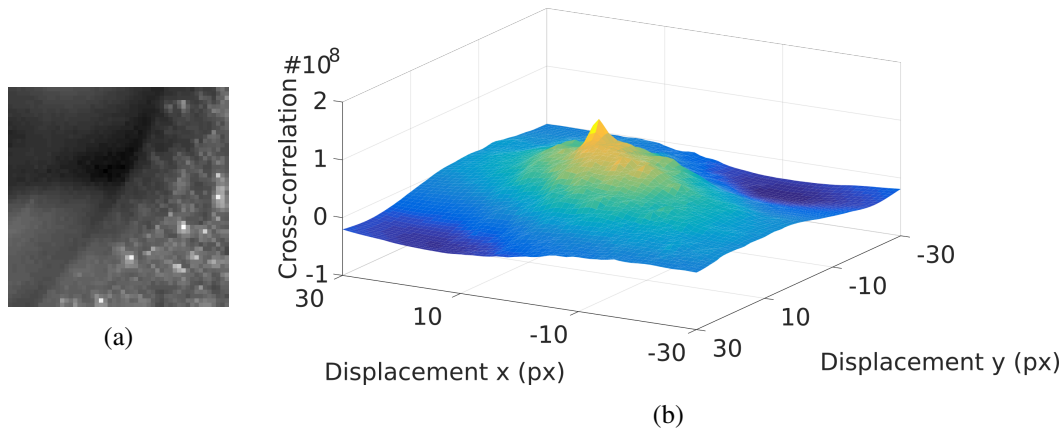


Figure 1.5: (a) Interrogation window for PIV image next to an interface (dark area). (b) Cross-correlation map of the previous region, with broadened peak due to the interface.

Logical masks are typically produced manually. The work presented in Chapter 2 concerns a technique that is able to generate PIV masks in a completely automatic way. Based on a sequence of several images, the methodology suggested takes advantage of image statistics to automatically discern flow pixels from boundary pixels. The assumption is that pixels belonging to objects only vary in time because of noise, therefore a normality test on the time history of pixels is used to evaluate their probability to be part of the mask. An automatic threshold is then adopted to generate a mask from this probability distribution, with minimal user input.

The analysis of images near objects is pushed beyond the adoption of masks in Chapter 3, where the effect of overlap between correlation windows and masked objects is studied into details. A solution to minimise this overlap is suggested based on image transformation. The methodology adopted utilizes a numerical mesh to transform pixel intensities of particle images to a logical plane, where the object boundaries become straight lines. Cross-correlation is performed with rectangular windows on the logical plane, so that the overlap with the interface can be easily avoided. The study involves the analysis of numerical meshes and their suitability for PIV image deformation, together with the introduction of a novel method of pixel sampling to minimise the effect of distortion on the correlation map.

### 1.2.2 Measurement of velocity gradients

In standard PIV algorithms, the integrity of measurements strongly depends on the detectability of peaks in the cross-correlation map. If the interrogation window is sufficiently small to neglect in-plane gradients, seeding particles between two images overlap for a certain displacement producing a single strong peak in the correlation map. The quality of the peak is typically measured in terms of signal to noise ratio (SNR), which is defined as the ratio between the maximum of the correlation map and the second highest peak [123]. If this ratio is close to 1, the

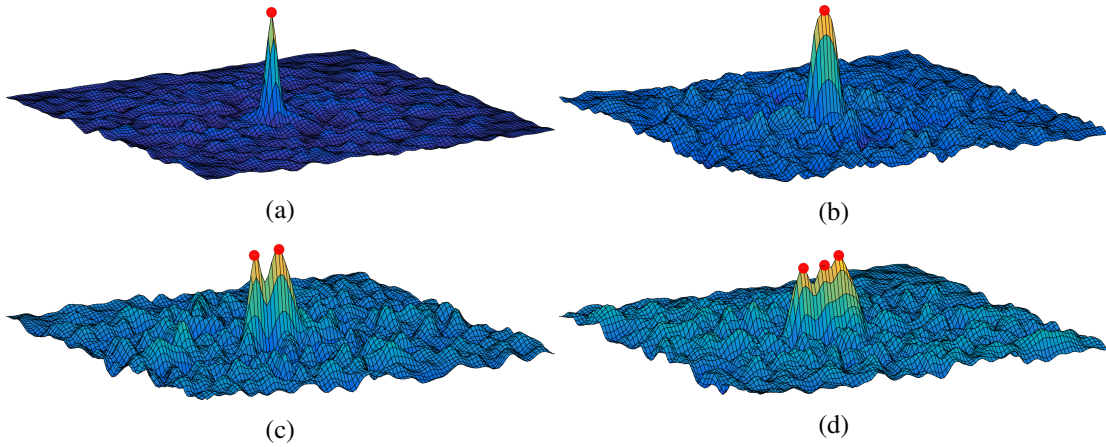


Figure 1.6: Effect of displacement gradients on the correlation map. Figure shows the correlation map between interrogation windows subjected to a shear flow of varying intensity. In-plane gradients are respectively: (a) 0.01, (b) 0.05, (c) 0.1 and (d) 0.5 pixels/pixel. Predominant peaks are marked with red dots.

measurement is considered unreliable and it is rejected. Figure 1.6 shows the cross-correlation map between two interrogation windows subjected to a shear flow of varying intensity. When displacement gradients are less than 0.05 pixels/pixel [51], the SNR is higher than 1 and the peak is suitable for the measurement of displacements (Figure 1.6a). If gradients reach the limit of 0.05 pixels/pixel, the shape of the peak stretches in the direction of the flow (Figure 1.6b), increasing the uncertainty of the measurement. Further increases in the gradients' intensity cause peak splintering (Figure 1.6c-d), which produces values of SNR close to 1 and renders the measurement through standard PIV algorithms completely impossible, since each peak is considered unreliable based on the SNR criterion.

It should be clear to the reader that the limitation of PIV in case of strong in-plane gradients comes from the adoption of cross-correlation. A different approach to analyse the particle motion, which is gaining more attention in the PIV community only in the last few years, is what in the computer science is well-known as optical flow [11]. Implementations of optical flow techniques in PIV analysis are not very common, although some examples can be found in [62] and [63]. The great advantage of using optical flow over cross-correlation, is that the resulting displacements are not simply discrete averages across each interrogation window, but dense pixel-wise displacement fields, and can thus describe more complex velocity fields in term of gradients. The work presented in Chapter 4 investigates the implications of adopting a particular optical flow technique, the Lucas-Kanade Tracker (LKT), for the analysis of PIV images. It will be shown that the adoption of linear or quadratic models to describe the optical flow make this technique an enticing alternative to cross-correlation. However, implementation of optical flow techniques requires particular attention to several parameters and phenomenon that will be discussed in detail in Chapter 4.

A different approach to deal with strong gradients in the interrogation window is adopted in Chapter 5, where an advanced solution based on cross-correlation is proposed. As already mentioned, standard PIV algorithms adopt the SNR as an indicator of quality of the highest peak, however, the SNR does not take into account the absolute height of peaks: if the SNR is close to one, but two or more strong peaks are present in the correlation map, information about multiple displacements is present and can be extracted. This condition can be appreciated in Figure 1.6c and d, where the correlation peak is splintered into 2 and 3 distinct peaks, marked with red dots. Standard PIV algorithms would completely disregard the analysis of such windows, but displacements contained in those peaks can be essential for the analysis of complex velocity fields. The solution proposed in Chapter 5 adopts a sophisticated peak detection system which automatically discerns strong peaks from the correlation noise and produces multiple displacements per correlation window. It will be shown that the proposed methodology is able to reduce the error in case of strong in-plane displacement gradients and increase the spatial resolution in case of high amplitude oscillations.

### 1.2.3 Vector validation

The last chapter of the thesis, Chapter 6, investigates an important aspect of PIV algorithms which is the vector validation. Experimental PIV images are often affected by noise, artefacts, defect of cameras, background and so forth. As already observed, these anomalies can affect the image analysis producing wrong vectors (see Figure 1.7). Outliers constitute a severe limitation in the implementation of iterative PIV algorithms, where images are repeatedly analysed using past information [89]. In fact, if outliers are not properly detected and replaced, the iterative procedure might fail, producing clustered outliers in the displacement field. More importantly, outliers can bias the statistics of the velocity fields, that are important to understand the flow behaviour [92]. On the other hand, the excessive use of validation routines brings to the opposite problem of over-detection, that produces an artificial smoothing of the measurements. The aim of Chapter 6 is to develop a new outlier detection method which is robust in case of clustered outliers and reduces the amount of over-detected vectors.

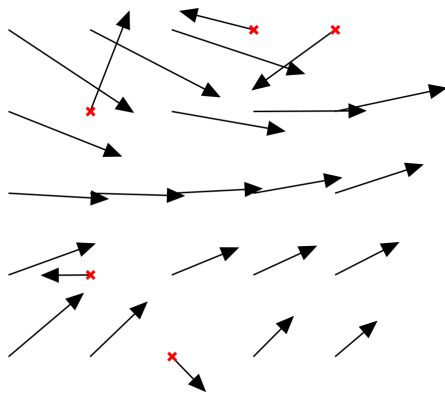


Figure 1.7: Example of PIV velocity field affected by outliers. Wrong vectors are marked with a red cross.



## Chapter 2

### Mask detection

The content of this chapter was published in the journal *Experiments in Fluids* with the title “Automated mask generation for PIV image analysis based on pixel intensity statistics” [58].

#### 2.1 Abstract

The measurement of displacements near the vicinity of surfaces involves advanced PIV algorithms requiring accurate knowledge of object boundaries. These data typically comes in the form of a logical mask, generated manually or through automatic algorithms. The automatic detection of masks usually necessitates special features or reference points such as bright lines, high contrast objects and sufficiently observable coherence between pixels. These are however not always present in experimental images necessitating a more robust and general approach. This chapter proposes a novel method for the automatic detection of static image regions which do not contain relevant information for the estimation of particle image displacements and can consequently be excluded or masked out. The method does not require any a-priori knowledge of the static objects (i.e. contrast, brightness or strong features) as it exploits statistical information from multiple PIV images. Based on the observation that the temporal variation in light intensity follows a completely different distribution for flow and object regions, the method utilizes a normality test and an automatic thresholding method on the retrieved probability to identify regions to be masked. The method is assessed through a Monte Carlo simulation with synthetic images and its performance under realistic imaging conditions is proven based on three experimental test cases.

#### 2.2 Introduction

The most suitable image for PIV analyses constitutes homogeneously distributed bright particle images on a completely dark background. As already mentioned in the previous chapter,

this ideal scenario is not always possible as the flow region of interest can be occupied by objects producing artefacts (light reflections, shadow areas, local variations in seeding density, etc.) hindering the measurement quality [119]. If the required particle image displacement measurement is in the near vicinity of a surface, special care must be taken in adequate surface preparation during the experimental phase [72], images must be properly pre-processed by means of e.g. background subtraction [60] or advanced image interrogation processes are to be adopted ([83], [35], [111]). Such advanced PIV analysis routines typically involve the exclusion of object regions within cross-correlation windows as to minimise distortions in the cross-correlation map, consequently limiting associated displacement bias errors [106]. This in turn requires knowledge of the imaged object boundaries to enable seeded flow regions to be discerned from non-seeded object regions. The generation of such logical masks thus constitutes a critical step, independent from the PIV algorithm used.

Logical masks are typically generated manually when the geometry of the object is very simple and clearly detectable in the PIV images. However, the manual approach becomes unreliable and too time-consuming when complex aerodynamic shapes are involved or several image sets need to be analysed with many different masks. Some examples of automated mask generation have been reported in literature: in [25], strong light reflections of the object were manually detected to generate the initial mask, which was dynamically moved using the a-priori knowledge of the object motion. In [86], the air-water interface was successfully detected exploiting the image intensity gradients through the Radon transform. [26] dealt with the motion of a moving body by implementing a tracking method and moving to an object-fixed coordinate system, allowing the use of a manual mask to the moving object. [21] applied a combination of contrast enhancement and intensity thresholding to identify bubbles in two-phase flows. However, shadows caused by the obstruction of the laser light also constitute unwanted image regions, yet these are not defined by high intensity boundaries. Moreover, experimental settings often produce complex images where objects contours are dark, vague and blurred. Objects thus become hardly detectable even for a human observer, limiting the application of typical masking algorithms. Alternatively, the spatial coherence between image pixels is involved to filter and identify object regions by means of low-pass filtering [121], median filtering [91], etc. Due to the finite extent of the filter kernels, such operations tend to introduce inaccuracies in the localisation of the object boundaries and are influenced by noise in the grey-scale distributions. [22] discriminated objects on the basis of inherent differences in their motion. This however demands objects to be identified a-priori. Similarly, [41] utilised the variation in flow velocities to completely remove stagnant objects. In case of temporally well-resolved PIV recordings, frequency analyses of the time-evolution in pixel intensities allows the identification of objects [93]. This methodology is however only conducive for time-resolved PIV recordings involving dynamic objects.

This chapter proposes a general, robust methodology for the automatic detection of static

image regions containing no information relevant in the cross-correlation operation. Without any special requirement for the image regions to be excluded (shape, luminosity or contrast), the method takes advantage of the statistical information contained within each individual pixel across several independent PIV images. A statistical test distinguishes unseeded image regions from image sections of interest with pixel accuracy. The underlying principle is the understanding that the temporal intensity variation of pixels constituting the unseeded partitions is mainly due to camera noise, producing a normal-distributed intensity histogram [116]. Pixels of seeded image regions on the other hand are characterized by the strong alternation of bright and dark values, producing highly skewed histograms [116]. A normality test is therefore performed on the time history of each pixel of the image to distinguish objects from particle images. Unlike filtering operations, the categorisation is performed pixel-wise and therefore does not incorporate neighbouring pixels. As a result of an automatic thresholding on the p-value of the normality test, the proposed method is fully autonomous and independent of user input. The technique is fully assessed on synthetic images and the application to several experimental cases is proposed to show its suitability for a variety of real conditions.

## 2.3 Methodology

### 2.3.1 Normality test

Considering a sequence of  $N$  PIV images, for each pixel the evolution in intensity across the image sequence can be extracted. Pixel intensities pertaining the imaged flow region will be characterised by strong alternations of high and low values due to the passage of tracer particles. Corresponding intensity probability density functions consequently exhibit a strong skewness Figure 2.1. Conversely, pixels associated with the imaged object display intensity variations principally due to camera noise, which is typically normally distributed [116]. This observation leads to a method to automatically categorise pixels within PIV images, by means of a pixel-wise normality tests. Given that the proposed methodology is based on probability density functions, validity is independent of the temporal resolution in the acquired images.

Normality tests are a tool to compute the likelihood of a set of data to be modelled by a Gaussian probability density function (PDF). Existing literature offers several tests for normality such as D’Agostino’s K-squared test [20], the Kolmogorov-Smirnov test [28], the Pearson’s chi-squared test [74] etc. Lead by simplicity of implementation, the method of choice in this work is the Jarque-Bera test, for which the heuristic can be easily evaluated on the basis of data skewness and kurtosis [44]. For a set of observations  $x$  (i.e. the set of intensity values of same pixel) with mean  $\mu$  and standard deviation  $\sigma$ , the skewness  $s$  and kurtosis  $k$  are defined as:

$$s = \frac{E(x - \mu)^3}{\sigma^3} \quad (2.1)$$

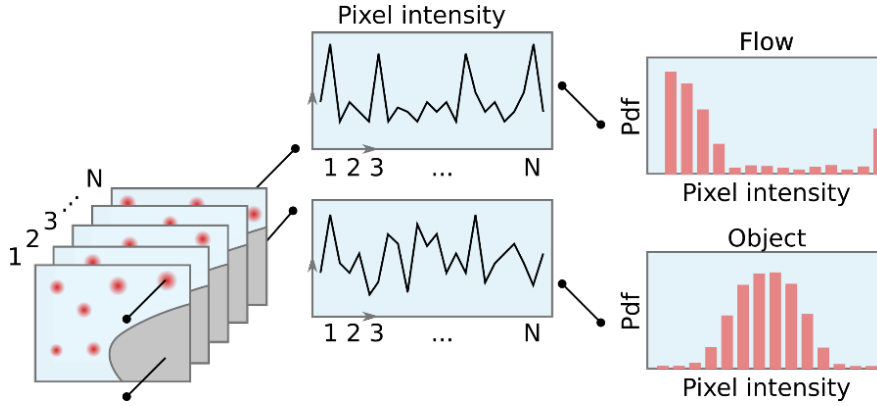


Figure 2.1: Illustration of the principle used for the mask detection: the probability distributions of pixel intensities have very distinguishable shapes depending on whether pixels belong to flow regions or objects

$$k = \frac{E(x - \mu)^4}{\sigma^4} \quad (2.2)$$

where  $E(t)$  represents the expected value of  $t$ . For a normally distributed dataset, the expected value of the kurtosis will equal 3 with a skewness of 0. The Jarque-Bera statistic quantifies the dataset discrepancies from these expected ideal values:

$$JB = \frac{N}{6} \left( s^2 + \frac{(k-3)^2}{4} \right) \quad (2.3)$$

where  $N$  is the size of the sample  $x$  (i.e. number of PIV images). The statistic expressed by 2.3, under the null hypothesis of  $x$  being normally distributed, is asymptotically distributed as a chi-squared with two degrees of freedom [44]. Thanks to this assumption, the p-value for the Jarque-Bera test can be evaluated as:

$$p = 1 - \chi_{(2)}^2(JB) \quad (2.4)$$

where the general chi-squared with  $\nu$  degrees of freedom is defined as:

$$\chi_{(\nu)}^2(x) = \int_0^x \frac{t^{\frac{\nu-2}{2}} e^{-\frac{t}{2}}}{2^{\frac{\nu}{2}} \Gamma(\frac{\nu}{2})} dt \quad (2.5)$$

with  $\Gamma$  being the gamma function:

$$\Gamma(x) = \int_0^{\infty} t^{x-1} e^{-t} dt \quad (2.6)$$

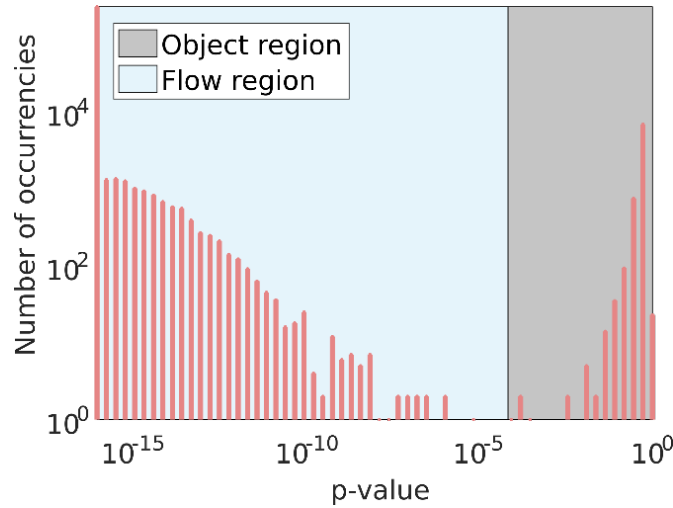


Figure 2.2: Histogram of the p-values for a set of experimental images (micro-channel flow, see Section 2.6). The distribution of p-values presents the typical bimodal distribution due to the presence of flow (low p-values) and object (high p-values). The automatic threshold discerns flow regions from the object by maximising the separability of the histogram.

Given a p-value for each pixel of the image, the null hypothesis of normality can be accepted (noise-dominated region) or rejected (flow region) based on the comparison with a cut-off level. This level is typically set to 0.05 [44].

The aim of the presented technique is not to test the normality of boundary pixels in an absolute sense, but rather to discern them from regions of strong non-normality due to the presence of particle images. Empirical studies lead to the conclusion that flow regions are typically characterized by extremely low p-values whereas regions void of any signal usable for cross-correlation usually present p-values which can be several orders of magnitude higher (Figure 2.2). Once the p-value is evaluated for each image pixel, an automatic threshold exploiting the peculiar bimodality of the probability in p-values across the image can be adopted to discern low p-values (image regions of interest) from high p-values (statistically irrelevant regions) to generate a binary mask. In this work, the Matlab function *otsuthresh* was used as implementation of Otsu's method [70], together with a median filter of a fixed 3 by 3 kernel to enhance the bimodality of the histogram [33]. The reader should note that this automatic implementation of the threshold ensures a robust distinction of flow from object areas even when related pixels are not perfectly normally distributed, as flow regions will continue to have a much lower distribution of p-values due to their more skewed pdf as corroborated by the theoretical intensity pdf suggested by [116].

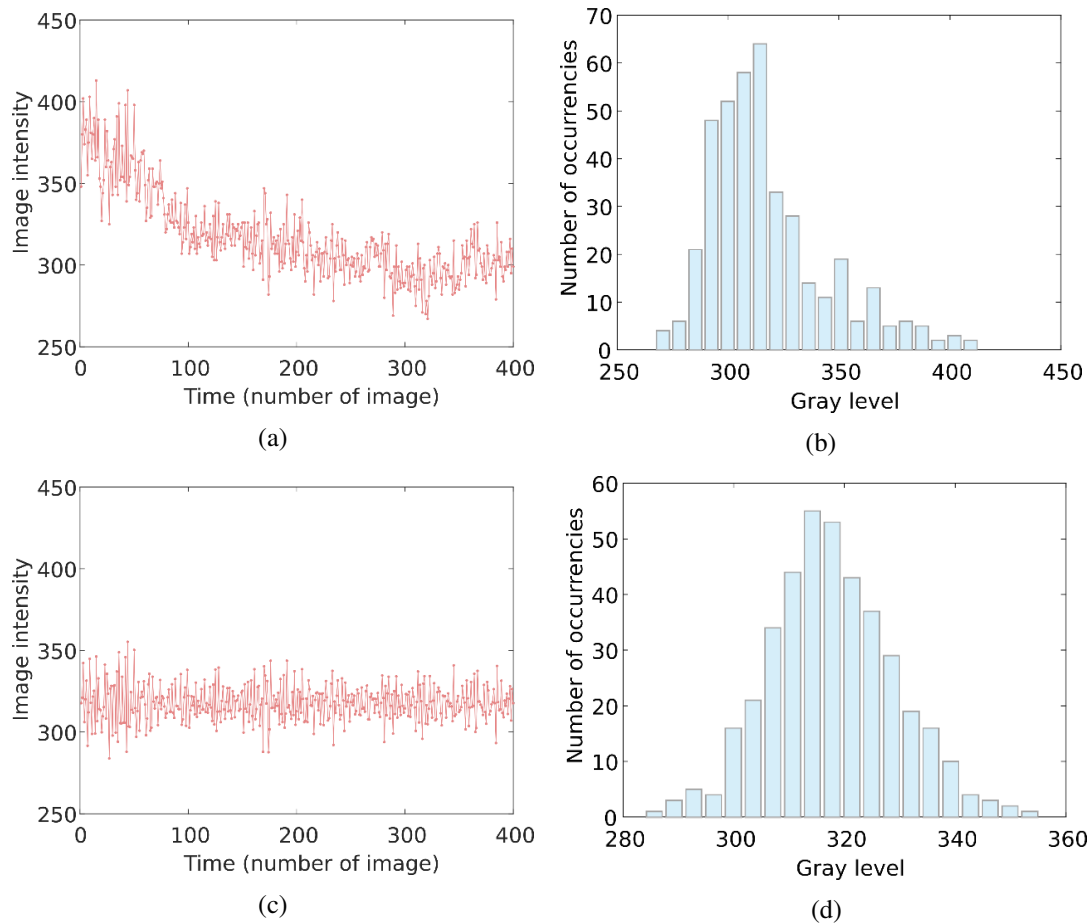


Figure 2.3: Example of signal pre-processing, applicable in case of decaying laser intensity. (a) Synthetic Gaussian noise combined with decreasing average light intensity and (b) histogram; (c) high pass filtered signal with (d) restored Gaussian histogram.

### 2.3.2 Pre-processing

The assumption of normally distributed noise can be violated when the laser light intensity varies across the image sequence, producing artificially skewed histograms of pixel intensity. An example of this behaviour is shown in Figure 2.3a-b, where a normally distributed pixel intensity was combined with a decreasing average light intensity. The histogram produced by this light distribution could easily be mistaken for a particle image, as it is not normally distributed. However, even exceptional cases like this do not prevent the application of the proposed mask detection algorithm since a simple additional pre-processing step can be implemented to equalize the light intensity. For example, a high pass filter can be applied to the time history of the intensities of the individual pixels to reduce the effect of the light variation and restore the Gaussian shape of the histogram. The high pass filtered signal is presented in Figure 2.3c, together with its normally distributed histogram in Figure 2.3d.

Another common scenario where the hypothesis of normally distributed noise could be violated, is in case of a double pulsed laser. Due to the possible discrepancies in manufacturing of the laser cavities, the light intensity of the two consecutive PIV images might be different, producing two sets of images that have a skewed or bimodal intensity distribution. In such a case, the mask detection algorithm should be applied independently on the two image sets, producing two different masks of which the logical union can be used as final mask.

### 2.3.3 Minimum number of images required

Besides a sufficient number of images to ensure validity of the normality statistics, a secondary condition for the proposed methodology to work is that each pixel of the flow region should be occupied by a particle image at least once in the entire PIV sequence. The number of images based on the first condition depends on the image quality and consequently cannot be estimated a-priori. The second condition, on the other hand, can be exploited to estimate an absolute minimum number of images necessary to allow the correct functioning of the mask detection. The probability of having  $n$  particles in a control volume  $V$  follows a Poisson distribution [2]:

$$\Pr\{n \text{ particles in } V\} = \frac{s^n}{n!} e^{-s} \quad (2.7)$$

where  $s$  is the concentration of seeding particles. The probability of a pixel being occupied by a particle image at least once in a sequence of  $N$  images is described by a binomial distribution. From equation 2.7, for  $n = 1$ , follows:

$$\Pr\{1 \text{ particle per pixel}\} = 1 - (1 - s \cdot e^{-s})^N \quad (2.8)$$

Equation 2.8 can be used to estimate a necessary number of images  $N$ , for a given probability  $Pr$ . Equation 2.8 is graphically presented in Figure 2.4 and is indicative of the applicability of the method. Based on the author's experience, a probability between 90% and 99% is often enough to reliably generate a mask, which means that for seeding densities of 0.1, 0.01 and 0.001, the minimum number of images needed is about 40, 300 and 2000.

## 2.4 Post-processing

The application of the normality test explained in the previous section leads to the generation of a mask based solely on the time history of each pixel and as such independent of the spatial coherence between image pixels. The spatial information can be used in a post-detection phase to enhance the quality of the mask, especially when insufficient images are available. In such

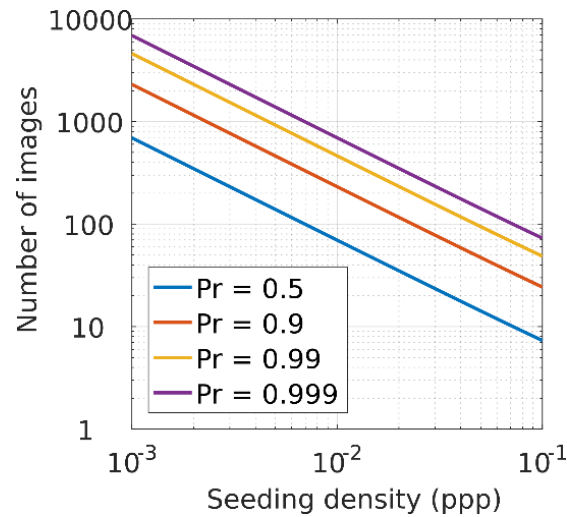


Figure 2.4: Number of independent PIV images necessary to allow the correct functioning of the proposed masking algorithm against seeding density. The plots are shown for different probabilities as expressed by equation 2.8.

cases spurious random pixels might be excluded by the algorithm producing pixel-sized holes in the binary mask generated. To increase the robustness of the mask, morphological operations can be included to simplify the binary image preserving the characteristics of the shape and eliminating irrelevancies [38]. While the reader may require alternative operations when dealing with special geometries, the morphological operations of closing and filling proposed in this work are fundamental. All morphological operations can be performed using the Matlab routines *bwmorph* and *imfill*. The closing process allows to smoothen contours and to eliminate small holes whereas the process of filling allows to close every area of the binary mask that cannot be reached by filling in the background from the edge of the image. The majority process allows a final cleansing of the mask by recursively setting a pixel to 1 when more than half of the pixels in the immediate neighbourhood are 1. Figure 2.5 illustrates the achievable improvements by means of the morphological operations where an example mask is artificially perturbed with noise and holes (Figure 2.5a). After the closing process pixel-sized holes have disappeared (Figure 2.5b). The bigger hole inside the mask is removed as a result of the filling process (Figure 2.5c) and the recursive application of majority (Figure 2.5d) filters out smaller pixel-sized structures without altering the main shape of the mask.

The reader should note that the adoption of morphological operations, despite being beneficial from a general point of view, may cause unwanted effects on the smallest scale of the geometry (8 by 8 pixels). Operations like majority would reduce the size of every sharp corner of the mask by one pixel. Although the advantages of using morphological operations may well outweigh smaller issues on this scale, its use should therefore be considered as a facultative addition to the main methodology.

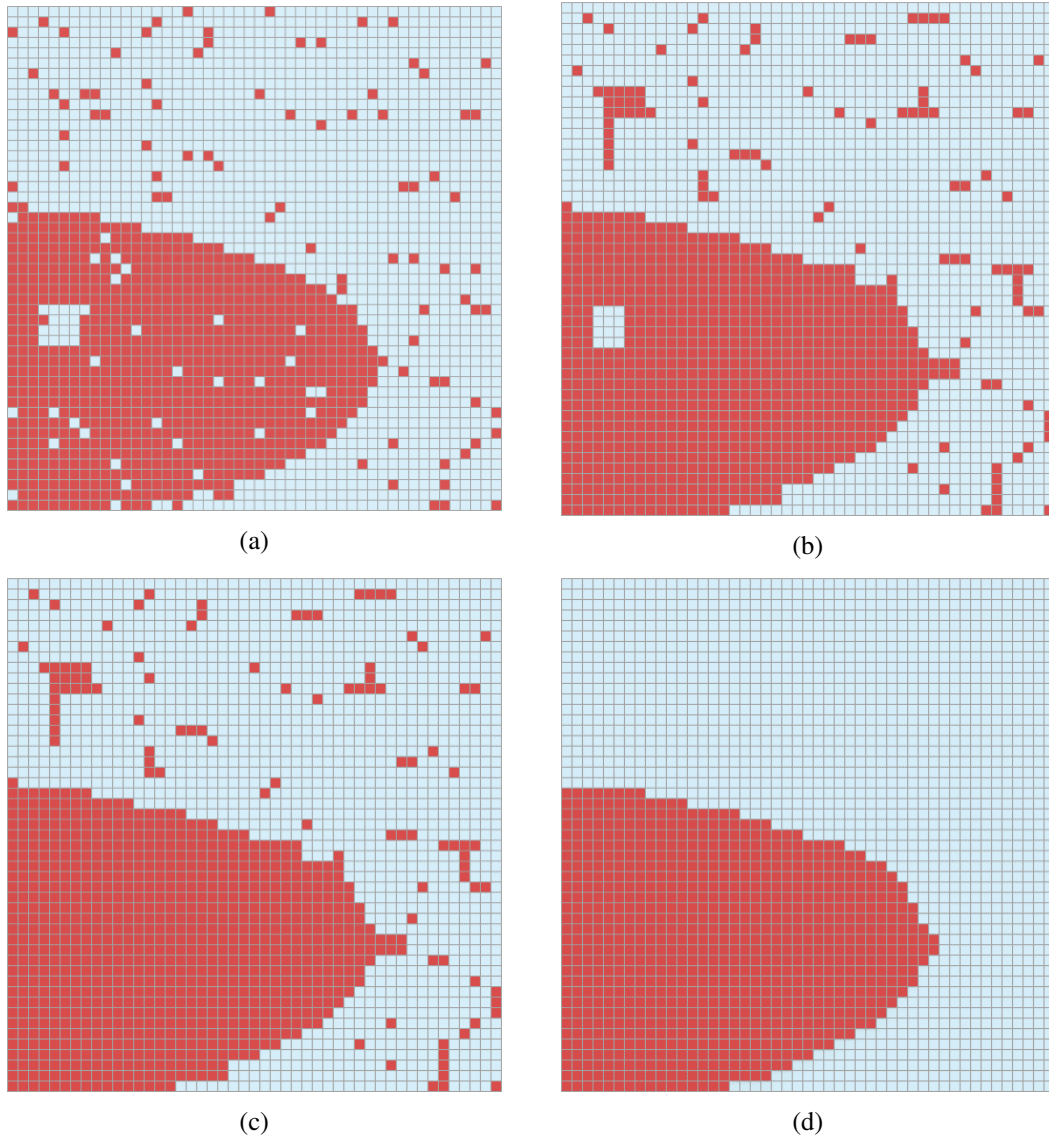


Figure 2.5: Example of application of the proposed sequence of morphological operations to (a) an artificially perturbed mask. (b) The application of closure removes single-pixel sized holes from the mask; (c) the filling operation closes any major size hole in the mask and (d) the majority operation allows a final clean from any smaller scale perturbation.

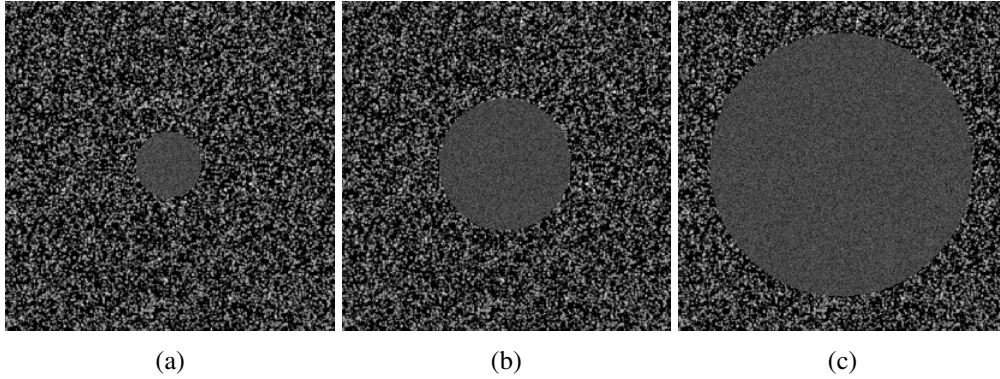


Figure 2.6: Three samples of cylinder images used for the synthetic analysis. Cylinders of 100 (left), 200 (centre) and 400 pixels (right) in diameter were generated using Gaussian noise.

## 2.5 Numerical assessment

To assess the validity of the proposed masking methodology and investigate the minimum number of images required for the approach to be reliable, Monte Carlo simulations involving synthetic PIV images were performed. Cylinders of three different diameters of 100, 200 and 400 pixels, occupying 3%, 13% and 50% of the entire image area respectively served as object. Pixel intensities within the cylinders were randomly drawn from a Gaussian distribution with a mean normalized intensity of 0.12 and standard deviation of 0.03. Images were 500 by 500 pixels in size, discretized in 16 bits, with randomly distributed particles in the flow regions having a diameter of 3 pixels and a seeding density of 0.1 ppp (Figure 2.6).

For each cylinder, 200 independent images were generated a total of 100 times to obtain statistically meaningful average results. For each size of the set, the error  $\varepsilon$  in the estimation of the mask area was evaluated as:

$$\varepsilon = \frac{100}{WH} \sum_{i=1}^W \sum_{j=1}^H |M_{i,j} - \hat{M}_{i,j}| \quad (2.9)$$

where  $W$  and  $H$  are the width and height of the image in pixels,  $M$  is the ideal mask and  $\hat{M}$  is the estimated mask. Results for the error  $\varepsilon$  are presented in Figure 2.7 and show a similar behaviour for all cylinders.

When fewer than 20 images are used for the mask detection, the outcome of the algorithm is erroneous due to an insufficient number of independent occurrences to distinguish normally distributed pixels from highly skewed pixels in flow regions. However, increasing the number of images analysed, the mask error quickly drop to  $10^{-1}$  or less for a set of 40 images. After this value, the error reaches a constant level as increasing the number of images does not affect

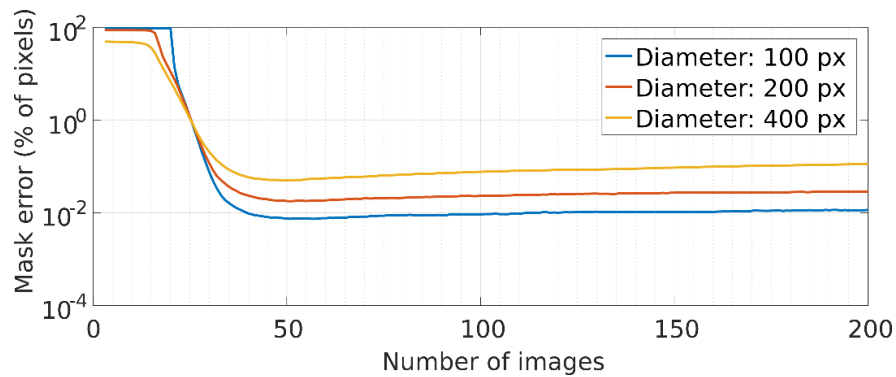


Figure 2.7: Results of the Monte Carlo simulation for the mask detection of the three synthetic cylinders. The plots present the error of the mask detected versus the number of PIV images used for that detection error.

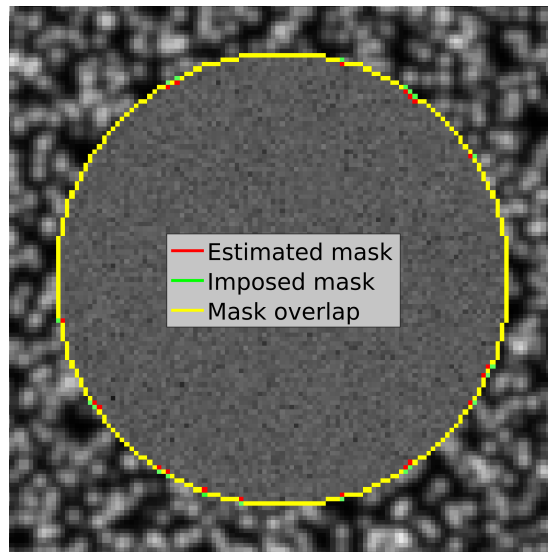


Figure 2.8: Result of the mask detection algorithm for the cylinder of 100 pixels of diameter using 200 images, showing a detail of the edges of the detected mask, together with the imposed mask and the respective overlap.

the normality test anymore. This number of images is further confirmed by the theoretical estimation of equation 2.8, where 40 images with a seeding density of 0.1 ppp yields a probability of 98% of pixels being occupied at least by a particle image throughout the PIV sequence.

A detail of the resulting mask detected for a cylinder of 100 pixels in diameter using 200 PIV images is shown in Figure 2.8, demonstrating a near perfect agreement with the imposed mask.

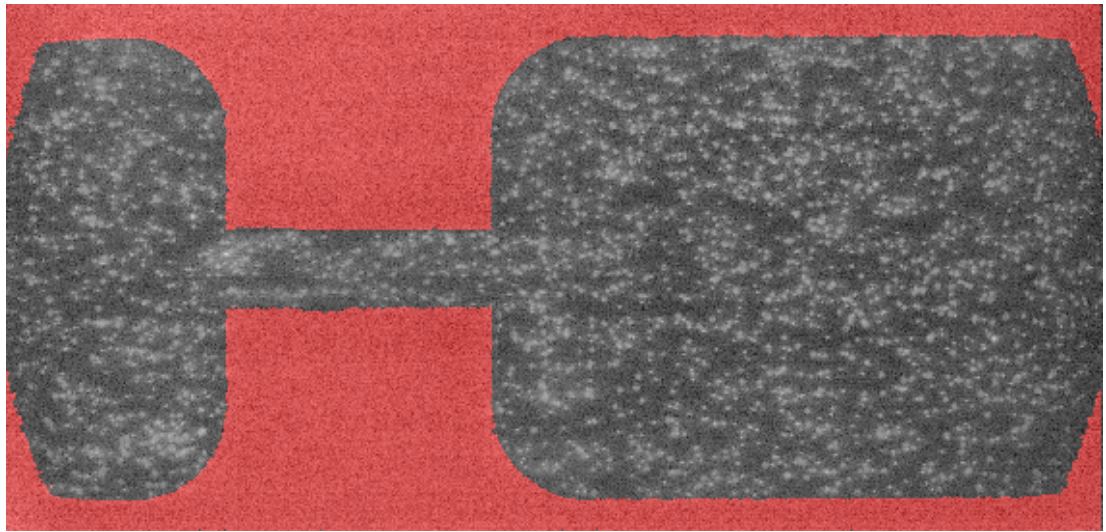
## 2.6 Experimental case

In order to validate the performances of the automatic mask detection in experimental conditions, three experimental test cases are proposed: (a) a micro-channel flow; (b) a transparent acrylic aerofoil and (c) a pipe junction simulating a lung. The first test case comprises 600 PIV images of a micro-channel flow driven by 200 bar of pressure, constituting Case A of the 4th International PIV Challenge [47]. The resulting mask is presented in Figure 2.9a, where a sample of the original PIV images is superimposed with the estimated mask shown in red. In addition to the mask, Figure 2.9b and Figure 2.9c respectively show a histogram of the grey levels in time for pixels belonging to the masked area and flow region. The plots are in agreement with the observation that masked regions are characterized by normally distributed histograms, whereas seeded image regions present a strongly skewed distribution in grey levels. For the histograms presented in Figure 2.9b-c, values of skewness are respectively  $5.1 \cdot 10^{-3}$  and 2.0.

The second test case comes from an experiment performed in the Low turbulence wind tunnel of the University of Bristol. PIV experiments were performed using a 200mJ Nd:Yag laser and 4 MP FlowSense EO camera on a NACA0024 airfoil at a chord-based Reynolds number of  $1.4 \cdot 10^5$ . The airfoil was manufactured out of acrylic to reduce light reflections in vicinity of the surface. A total of 400 images were acquired in 16 bits image depth. The final mask is presented in Figure 2.10a and illustrates how both aerofoil and light shadow area are detected by the masking algorithm. Both regions are characterized by the lack of information due to the absence of particles and present normally distributed grey levels. Figure 2.10b and Figure 2.10c show two histograms for a pixel belonging to the aerofoil and a pixel belonging to the shadow respectively; as already mentioned, both the histograms are normally distributed and contribute to the masked region, however, the histogram for the aerofoil region (Figure 2.10b) has a mean value which is higher than the shadow area (Figure 2.10c), confirming that the suitability of the method is independent from the brightness and the contrast of the masked region.

The reader should notice that the shadow areas produced by the aerofoil are not entirely detected as mask. Due to the transparent material used to manufacture the object, the casted shadows are not as dark as those produced by an opaque object but they gradually fade from dark to bright (see detail of Figure 2.10a). This implies that particle images also disappear progressively as they cross the shadow: those areas where the particle image intensity is on par with the random noise are detected as mask, while the regions that may contain valuable information about the displacements are maintained as flow regions, producing the pattern observed in Figure 2.10a.

The final test case involves 534 images of a flow bifurcation simulating a lung at  $Re = 2.24$  [104]. The 8 bits discretization renders the test case challenging as sporadic noisy areas within the seeded flow region do not produce significant skew in the PDFs. Figure 2.11b



(a)

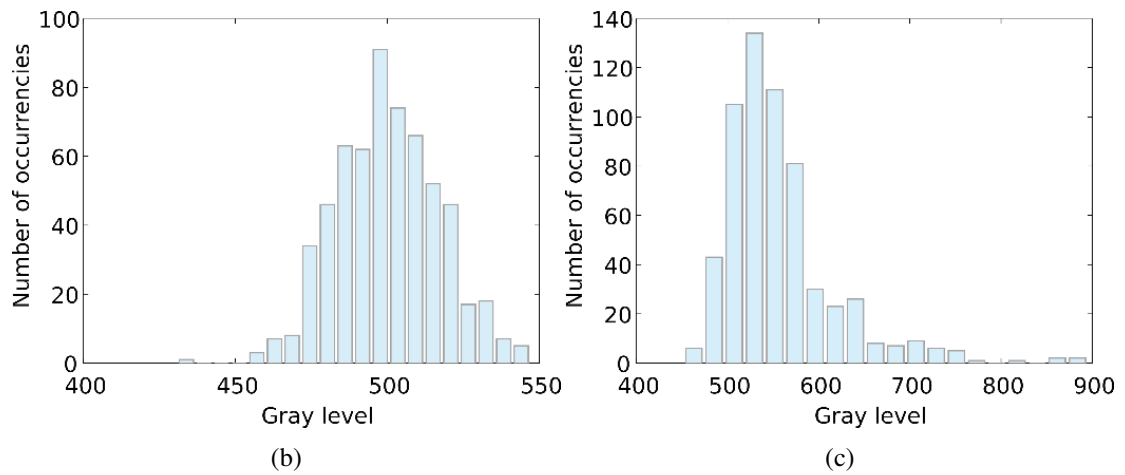
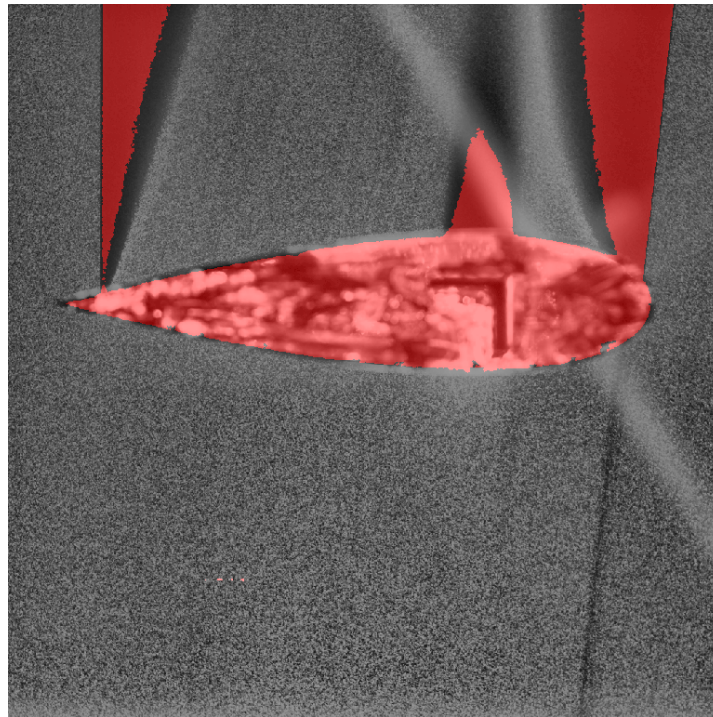
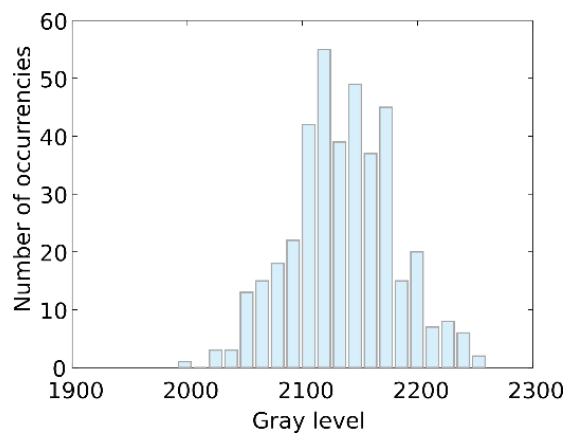


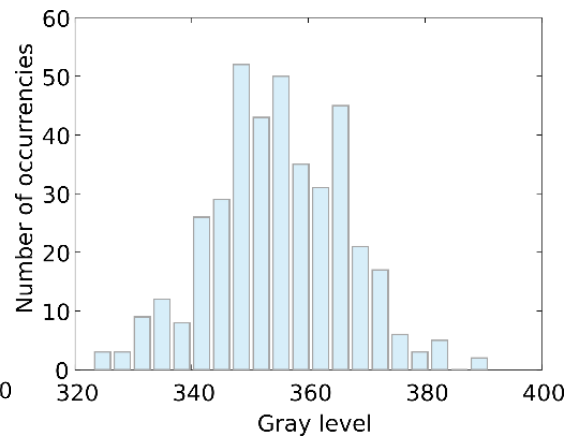
Figure 2.9: (a) Automatically detected mask for the micro-channel overlapped with a sample of the set of images (contrast enhanced for clarity), (b) histogram of the grey levels for a pixel belonging to the mask and (c) seeded flow portion.



(a)



(b)



(c)

Figure 2.10: Automatically detected mask for the transparent aerofoil (a); histogram of the gray levels for a pixel belonging to the aerofoil (b) and a pixel belonging to the shadow (c), both detected as part of the mask because of similar histograms.

and  $c$  respectively show the histograms of pixels belonging to the boundary region and noisy flow area. Both present a normal distribution. This strong image noise in the flow region, coupled with the bright intensity of the particles and the low bit discretization produces small regions within the flow area to be masked out. Overall, the geometry of the object is correctly retrieved and the occurrence of these additional masked regions is restricted to very small domains. As mentioned in the previous section, these regions can be easily cleaned through the application of additional morphological operations. It is however important to note that the mask is based on statistical information of the PIV images and the exclusion of those masked regions from a PIV analysis does not affect the cross-correlation results as those pixels do not contain information from a statistical point of view.

## 2.7 Limitations

The automatic mask detection proposed in this chapter requires objects in PIV images to be stationary. With the analysis based on the time history of each pixel, vibrations or deformations of the regions to be masked would combine time history of objects with time history of flow regions, hampering the correct classification of the pixels. Conditions like rigid motion and vibrations can be easily tackled by implementing a tracking method and moving the analysis to an object-fixed coordinate system [26]. The presence of ghost particles on reflective surfaces constitute a more complex case. If the experimental settings were such that particle images were reflected within the objects to be masked, the mask detection will not be able to discern real particles from reflected ones. These regions will subsequently be characterized on the basis of pixels containing (reflected) particle images and will consequently be excluded from the masked region.

## 2.8 Conclusions

A novel method for the automatic detection of static masks for PIV is proposed. The method does not require any specific feature in terms of brightness or contrast of the images as it exploits pixel-wise statistical information regarding image intensity extracted across several PIV images. Statistically irrelevant image regions are discerned from seeded regions of interest based on the assumption that variations of light intensity in the former are normally distributed in time, while the latter are skewed by the alternation of background and bright particles. The Jarque-Bera test is used to test the normality of the pixel intensity in time and an automatic threshold based on Otsu's method is adopted to categorise image pixels based on p-values. Numerical assessments by means of Monte Carlo simulations on synthetic images were performed to investigate the minimum number of images needed for the normality test to be effective and

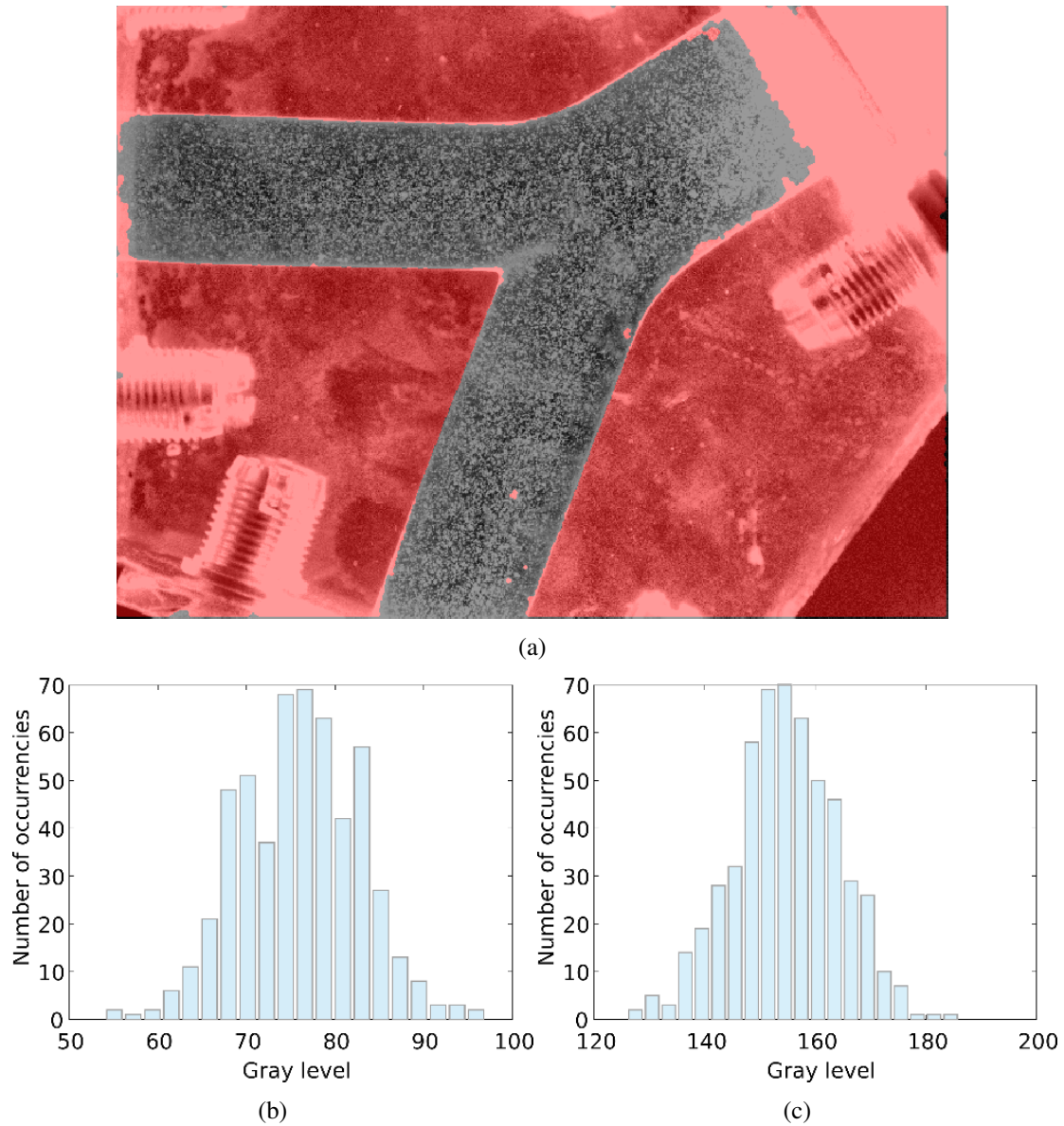


Figure 2.11: Results of the automated mask detection for the lung test case, overlapped with a sample of the set of images (a); histogram of the grey levels for a pixel belonging to the object (b) and to a noisy area within the channel (c), both detected as mask.

results showed that at least 40 images are necessary for the method to reliably identify the masked regions. The experimental application on three different sets of PIV images additionally confirmed the applicability of the method for different conditions of background, particle dimensions, seeding densities and levels of quantization, showing visual agreement of the detected masks with the objects in the images.



# Chapter 3

## Image mapping

The content of this chapter was published in the journal *Measurement Science and Technology* with the title “On the applicability of numerical image mapping for PIV image analysis near curved interfaces” [59].

### 3.1 Abstract

This chapter scrutinises the general suitability of image mapping for particle image velocimetry (PIV) applications. Image mapping can improve PIV measurement accuracy by eliminating overlap between the PIV interrogation windows and an interface, as illustrated by some examples in the literature. Image mapping transforms the PIV images using a curvilinear interface-fitted mesh prior to performing the PIV cross correlation. However, degrading effects due to particle image deformation and the Jacobian transformation inherent in the mapping along curvilinear grid lines have never been deeply investigated. Here, the implementation of image mapping from mesh generation to image resampling is presented in detail, and related error sources are analysed. Systematic comparison with standard PIV approaches shows that image mapping is effective only in a very limited set of flow conditions and geometries, and depends strongly on a-priori knowledge of the boundary shape and streamlines. In particular, with strongly curved geometries or streamlines that are not parallel to the interface, the image-mapping approach is easily outperformed by more traditional image analysis methodologies invoking suitable spatial relocation of the obtained displacement vector.

### 3.2 Introduction

As already mentioned in the Chapter 1, the most common analysis process for PIV images involves the subdivision of pairs of consecutive images into sub-areas, and subsequently estimating the displacement of the particle images captured within these areas by means of statistical

operators such as cross-correlation [4]. To increase the accuracy of the obtained displacements beyond pixel level, sub-pixel resolution is achieved by Gaussian fitting of the correlation peak [114]. Detrimental effects of displacement gradients on accuracy are then counteracted through iterative multi-grid approaches [89] incorporating image deformation.

Although very versatile and widely used, it is well recognised that cross-correlation based techniques only provide robust and reliable measurements in interrogation areas free of interfaces or boundaries. Both the decrease in number of particle images contributing to the correlation and the presence of strong light reflections close to interface degrade cross-correlation performances [51]. This problem has been extensively addressed in literature with a variety of proposed attempts to minimise reflections in the image recording stage. Among such solutions are the use of fluorescent paint, electropolished materials or transparent media [72]. Nevertheless, ideal experimental settings are not always possible and reliable data must still be extracted from images acquired in such non-perfect conditions. For this reason in the last decade effort has been spent on the algorithmic side of PIV analyses. Some of the most common methods to reduce the effect of boundaries present is to adopt masking techniques to exclude identified image regions ([83]; [35]). Masking techniques, described in Chapter 2, are often enhanced by an automatic vector relocation based on the centroid of the truncated correlation window [111], such that the new vector location offers a more representable attribution of local seeding displacement. A different approach followed by [110] consists in mirroring particle images located within the flow region across interfaces, reducing the detrimental effects on the correlation map. However, the inherent displacement errors will strongly be related to the velocity field curvature and degree of overlap between the correlation windows and mirrored interface. To circumvent such a dependency on mutual overlap between the interface and correlation window [105] introduced the concept of adapting both the location and aspect ratio of the correlation windows to the presence of interfaces. Overlap between correlation windows and interfaces was minimized by adjusting the position, orientation and size of the windows leading to drastic improvements in spatial resolution.

A completely alternative approach, which is the case study of this chapter, involves the distortion of correlation windows by means of image mapping to follow the interface geometry, thus completely avoiding the capture of interfaces within correlation windows. Image mapping techniques usually perform a transformation of the images in a logical space in which the problem of matching particle images patterns is solved. [85] adopted this methodology to directly evaluate vorticity. In their study, particle images were deformed through a Cartesian to polar transformation and processed through cross-correlation, allowing the explicit deduction of vorticity. A similar image mapping was used to deform images in the near vicinity of a wavy wall through curvilinear coordinate transformations [64], followed by a one-dimensional method of estimation of the wall friction velocities by means of ensemble correlation of interrogation windows one pixel in height. Similarly, [45] and [71] used textons to track a free

surface, from which regularized coordinates were generated to map the particle images into a straight interface.

Despite the apparently successful use of image mapping in previous works, both an in-depth analysis of the inherent parameters defining the image mapping and a comparison with traditional cross-correlation has never been presented. Moreover, all studies mentioned consider only imaged sections of interfaces whereas common aeronautical applications may involve more strongly curved geometries captured in their entirety such as e.g. aerofoils. The aim of this chapter is therefore to fill this lack by documenting and investigating the individual stages in the image mapping process and study the generality of image mapping for PIV applications from the generation of the body-conforming mesh for a generic surface of interest, to the effects of the deformation on the cross-correlation map and related displacement measurements. Possible error sources involved in each stage of the process are scrutinized and assessed with synthetic images in order to provide the reader with a complete understanding of the image mapping method.

This chapter has an underlying three-tiered structure. To aid the reader an overview of the objectives of each tier is provided in Figure 3.1. The general concept underlying image mapping and its location within typical image analysis processes are discussed in section 3.3. Section 3.4 provides further background information regarding image mapping by addressing the mathematical aspects behind numerical mesh generation and the necessary re-scaling of obtained particle image displacement estimates. The second tier of the chapter focusses on the practical aspects of image mapping, starting with the generation a general continuous body-fitted mesh from a typical, pixelised, user-defined mask. After presenting the adopted interpolation method for the involved coordinate transformations, the appropriate correlation window sizing and cross-correlation operation are discussed. In the process of finding the limits of applicability of image mapping, optimal solutions are found to minimise the errors involved in each stage of method. Accordingly, this chapter presents a novel technique to minimise distortions in the cross-correlation maps due to deformed particle images caused by the inherent image transformations. This however comes at the expense of computational cost, which is discussed in paragraph 3.5.5. In the final section this chapter presents a thorough and detailed error analysis based on computer generated PIV images for each of the key stages in image mapping. Error sources caused by the coordinate transformation and curvature in the generated numerical mesh are highlighted. Since the benefits of image mapping were already shown in the existing literature, the aim of the current chapter is more focused on the analysis of the limits of the image mapping method, which are encountered in the study of strongly curved surfaces. For this reason simulated PIV images of the flow over a Joukowsky airfoil are utilised when juxtaposing the performances of image mapping with standard PIV and advanced adaptive approaches. Here understanding the real advantages of such a mapping technique for PIV is pursued. Even when combining image mapping with adaptive approaches in attempts

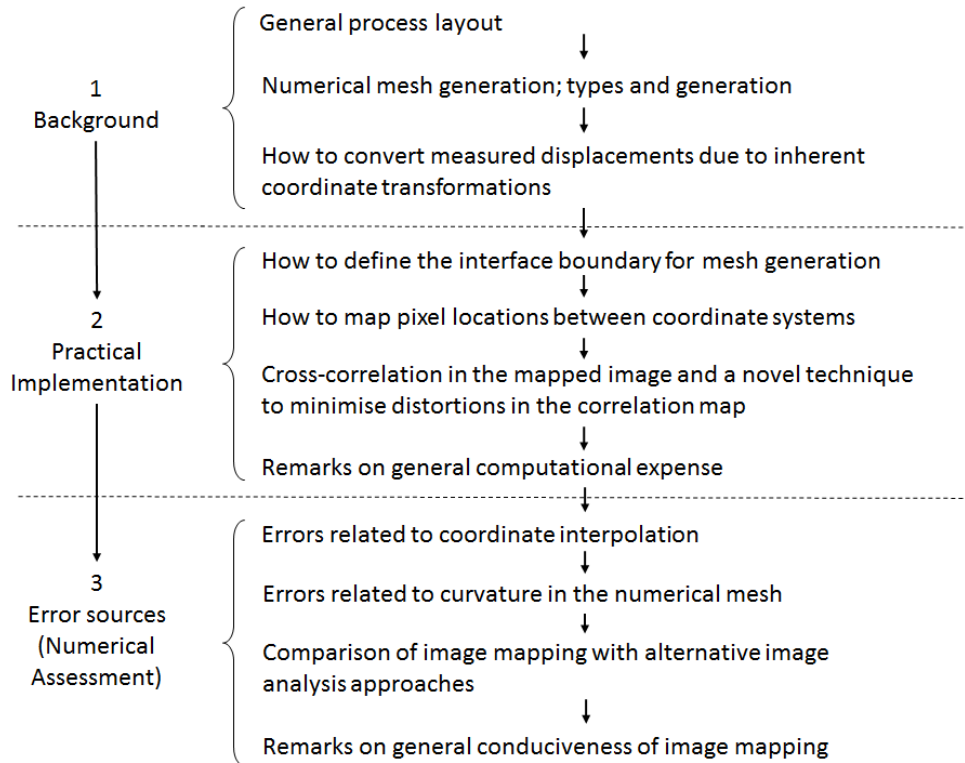


Figure 3.1: Three tier structure of the chapter.

to maximise the performances of image mapping, no distinct ameliorations were achieved. It will be shown instead that the problem of affected image quality due to the deformation of image mapping constitutes one of the strongest sources of error. Paragraph 3.6.4 presents general remarks on the applicability of image mapping, in which the reader will be discouraged from the use of such a technique. Instead it is argued that more conventional image analysis methodologies are more reliable and robust.

### 3.3 Problem definition and general image mapping methodology

Robustness of cross-correlation of interrogation areas in proximity of curvy surfaces is hampered not only due to flow-induced effects, such as stronger gradients in velocities, but also stronger dissemblance of the image recording from the ideal condition due to optical degradations. The latter mainly constitutes light reflections and a truncation in PIV signal related to the reduction in particle seeding density across the interface [103]. Dedicated image routines are therefore needed to ensure cross-correlation operations will retain sufficiently high signal-to-noise ratios and safeguard accuracy.

One possible means is to avoid any overlap between cross-correlation windows and inter-

faces entirely. To this extent a numerical boundary-fitted mesh originated from a mask of the curvy surface can be generated. The user-defined binary mask indicates the location of the objects within the image recording and is used as a boundary condition for a system of partial derivative equations (PDE) defining the body-conforming coordinate system. The solution to these equations generates a discrete set of points representing the transformation from the physical plane, i.e. the original images, to a computational plane. Original images are subsequently transformed such that the curvilinear mesh in the logical plane is represented as a rectilinear one. Here the surface becomes a straight line and correlation windows aligned with this straight boundary can be imposed such that any interface overlap is avoided.

In ideal conditions (e.g. when the interface geometry exhibits a high curvature radius), the transformed images can be suitably analysed by standard PIV image analyses routines as suggested by [64]. Interfaces characterized by strong curvatures on the other hand may introduce additional deformations of the correlation map. As will be shown in Section 3.6.2, these degrading effects may even outweigh image mapping's potential benefit of avoiding the overlap with the interface. In order to push image mapping to its limits and achieve optimal measurements, the method may be further extended through combinations with an adaptive spatial sampling [106] as assessed in Section 3.6.3. Previous works in literature show that the spatial resolution near interfaces can be improved by means of adapting the spatial distribution of correlation windows and their size on the basis of identified flow features [105] or to the presence of interfaces [106]. It should be noted that such adaptive image interrogation processes adopting image mapping are already quite advanced with added degrees of complexity. However, such state-of-the-art approaches have been considered in this manuscript to allow an objective assessment of potential advantages of image mapping in PIV analyses. The adaptive approach adopted in the current work allows an automatic selection of the window properties such that correlation windows are automatically reduced in size towards the interface. After this stage correlation windows are divided into two categories depending on their distance from the identified surface. Those far away from the surface will be straightforwardly processed with cross-correlation, whereas those in vicinity of the curvy surface will be deformed one by one using the numerical mapping and converted back into physical displacements. The basic idea behind this approach can be summarized by what in CFD analysis is known as the Chimera approach [101].

A flowchart of the general image interrogation methodology is presented in Figure 3.2. The overall layout remains analogous to the classical iterative predictor-corrector scheme with refinement of window sizes presented by [89]. Once interrogation windows are distributed adaptively across the image, cross-correlation is performed utilising either pixel intensities of the original image or re-interpolated grey levels according the numerical mesh transformation. The latter requires additional operations which will be elucidated in section 3.5.3. Sub-pixel accuracy is achieved with a nine-points two-dimensional Gaussian regression expressed in an

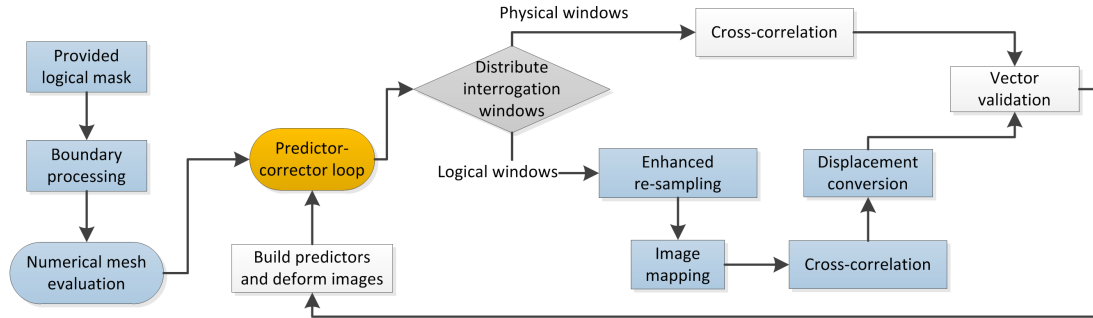


Figure 3.2: Description of the iterative algorithm.

explicit formulation [66] capable of dealing with potentially deformed correlation peaks as a result of non-linear image mapping. Displacements evaluated on mapped images are subsequently converted back on to the physical plane by means of the Jacobian (obtained from the PDEs), merged with physical displacement vectors obtained through traditional methodologies and validated using a non-structured vector validation routine [57]. The scattered displacements are interpolated on a pixel-wise grid by means of natural neighbours interpolation [14] to provide a predictor for iterative image deformation [87] and further reduce the effects of velocity gradients.

The incorporation of the numerical mesh-based image mapping and adaptive correlation window localisation thus constitutes additional processing steps within a standard PIV analysis. In the remainder of this chapter it is the concept of image mapping near strongly curved geometries and the analysis of the associated measurement errors that will be the subject of investigation.

### 3.4 Mathematical background of body-conforming image mapping

Prior to presenting the mathematical background underpinning the coordinate transformations constituting image mapping, some pivotal definitions used throughout this chapter are outlined to improve clarity. The plane defined by spatial coordinates  $(x, y)$  will represent the physical plane which is equivalent to the captured PIV images expressed in terms of recorded pixel coordinates. The  $(\xi, \eta)$  plane is defined as the mapped or logical plane, where  $\xi$  and  $\eta$  are the curvilinear coordinates attributed to the angular and radial directions respectively. It is on this plane that the original image recordings will be transformed as per Figure 3.3. The Chimera area then refers to the finite extent of the numeric mesh on the physical plane, which is the only part of the image transformed and analysed on the logical plane (see also Figure 3.20 for an illustration).

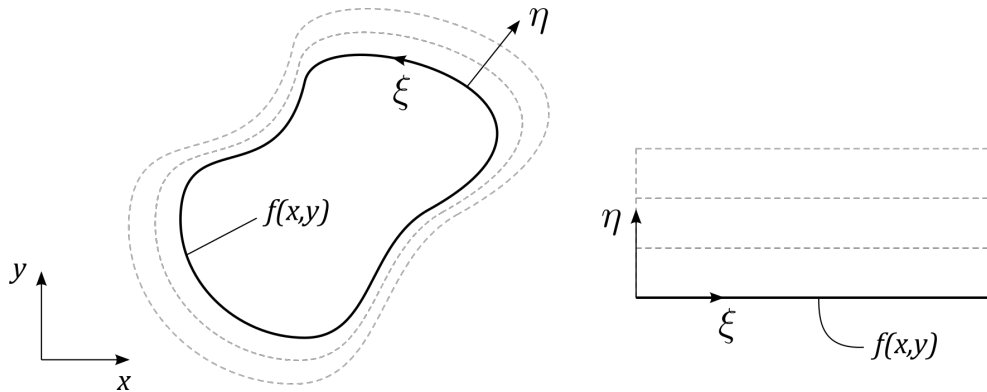


Figure 3.3: Illustration of the concept of image mapping: (left) curvilinear coordinates  $(\xi, \eta)$  are fitted in the physical plane to the object with boundary condition  $f(x, y)$ ; (right) the curved interface becomes a straight line after transformation into the logical plane.

### 3.4.1 Hyperbolic vs. Elliptic mesh

Numerical meshes in computational fluid dynamics (CFD) are used to discretize the non-linear partial differential equations (PDEs) modelling the flow in order to allow the computation of an approximate solution. These meshes can be categorised as either structured or unstructured. While the former is defined by the intersection of curvilinear coordinate surfaces, the latter lacks any relation between coordinate directions. The current intention is for the mapping to describe the spatial rearrangement of image intensities when altering reference coordinate systems. As digital images are composed of intensities defined in pixel elements which are already arranged in an array format, structured meshes are consequently the most suitable grid type.

The generation of a structured mesh can be performed through several approaches of which the most common constitute analytical transformations, algebraic schemes and other based on partial derivative equations (PDE). Details regarding numerical grid generation can be found in [108] but it presently suffices to note that while analytical transformations are the fastest and most accurate, their use is limited to more simplistic analytical geometries such as cylinders, sinusoidal walls, etc. In view of the intended general applicability of image mapping these will be left out of consideration. Grid generation based on partial differential equations is typically slower than its algebraic counterpart but is the preferred choice in the present work as they offer a higher degree of mesh smoothness and can concomitantly be expected to minimise image artefacts caused by image mapping. In fact, algebraic meshes are based on transfinite interpolation and are more likely to result in overlapping of the boundaries [108].

The numerical mesh is a discrete set of curvilinear coordinates  $(\xi, \eta)$  satisfying either an elliptic or hyperbolic system of PDE equations. Independent of their classifications, these equations describe the coordinate transformations when alternating between the physical  $(x, y)$  and

logical  $(\xi, \eta)$  plane. Elliptic meshes are obtained by solving the system of elliptic equations presented in equation 3.1 through iterative schemes based on finite differences. The equation of this mesh comes from an analogy to a stretching membrane attached to the boundary of the object. These meshes are perfectly suitable for closed domains, where all the boundary geometries are specified and are considered best in terms of smoothness [107].

$$\begin{cases} \frac{\partial^2 \xi}{\partial x^2} + \frac{\partial^2 \xi}{\partial y^2} = 0 \\ \frac{\partial^2 \eta}{\partial x^2} + \frac{\partial^2 \eta}{\partial y^2} = 0 \end{cases} \quad (3.1)$$

Starting from the object geometry identified in the image recordings, boundary conditions are provided in terms of  $x$  and  $y$ . However, the solution to equation 3.1 expresses the unknown angular  $\xi$ , and radial coordinates  $\eta$ , as functions of the physical coordinates,  $x$  and  $y$ . System 3.1 is therefore usually rearranged such that the physical coordinates become the unknowns and the boundary condition can be defined with respect to the body geometry when  $\eta = 0$ , as illustrated in Figure 3.3. An additional user-defined non-homogenous term can be added to the equations to promote special grid properties such as line spacing, orthogonality, etc.

Alternatively a hyperbolic system of partial differential equations forms the basis for the intended mesh generation. Here the equations are analogous to the description of waves transporting disturbances on water surfaces;

$$\begin{cases} \frac{\partial x}{\partial \xi} \frac{\partial x}{\partial \eta} + \frac{\partial y}{\partial \xi} \frac{\partial y}{\partial \eta} = 0 \\ \frac{\partial x}{\partial \xi} \frac{\partial y}{\partial \eta} - \frac{\partial y}{\partial \xi} \frac{\partial x}{\partial \eta} = \Delta A \end{cases} \quad (3.2)$$

The first equality in equation 3.2 imposes orthogonality while the second controls the local cell area through  $\Delta A$ . Parameter  $\Delta A$  is user-defined and can subsequently take on any form;  $\Delta A = \text{constant}$ ,  $\Delta A = \Delta A(x, y)$  or  $\Delta A = \Delta A(\xi, \eta)$ . The solution starts from the geometry of the boundary conditions and propagates outwards until a user-defined extent. For this reason, this type of mesh is more suitable for open domains.

It is important to note that when attempting to generate a body-conforming mesh to map PIV images, the purpose of the grid, and therefore its inherent characteristics, will be slightly different from those used in CFD. Computational fluid dynamics utilises the mesh to obtain a discrete solution of the underlying flow equations at every grid node, therefore, an accrual of mesh points in vicinity of the surface is beneficial to the estimate of velocity near the object. In the current work, instead, the mesh is used to deform images that are thereafter analysed in

sub-areas to evaluate the displacement of particle images. The choice of optimal mesh characteristics should thus introduce the least amount of artificial displacement gradients in the logical plane as these are well-known to hinder reliable cross-correlation [115]. For this reason, the optimal mesh should maintain a constant node density independent of the distance from the boundary or its curvature radius. When comparing elliptic and hyperbolic meshes, the former tends to automatically densify the number of points where surfaces have a lower radius of curvature and has the opposite behaviour where surfaces are smoother. This effect is to be avoided for image mapping purposes because of the aforementioned artificial gradients. Moreover, the iterative approach required to solve an elliptic system of partial differential equations renders the associated mesh generation slower compared to the hyperbolic type, where a faster marching technique can be adopted [108]. These motivations lead the grid choice to a hyperbolic mesh.

### 3.4.2 Hyperbolic mesh generation

Having identified hyperbolic meshes as most suitable for PIV image analyses, this section highlights aspects in the mesh generation which require careful consideration. Utilising the hyperbolic partial differential equations expressed in 3.2 and a complementary boundary condition describing the pixel locations  $(x, y)$  of the interface geometry in terms of logical coordinates  $(\xi, \eta)$ , the solution of the well-posed system of equations provides for each combination of curvilinear coordinates  $(\xi, \eta)$  the corresponding physical coordinates  $(x, y)$ . This constitutes the image mapping. In this work, a simple first-order explicit solver was chosen because of its low computational effort. Although the problem expressed in 3.2 is closed, three more parameters must be specified to generate the desired mesh; the local cell area  $\Delta A$ , the wall-normal extent of the mesh and a smoothening factor. Maintaining a uniform cell area may be the most simplistic approach, yet it leads to severe stretching of the cell aspect ratio when increasing the radial extent of the mesh in regions of stronger boundary curvature as illustrated in Figure 3.4a. In Section 3.6.2 it will be shown that such stretching introduces detrimental artificial displacement gradients in the mapping and should be categorically avoided. The area of the cells must therefore increase according to the spreading of the radial coordinate  $\eta$ . Here, an automatic adjustment of  $\Delta A$  to the transformation's tangential derivatives is proposed;

$$\Delta A = \Delta A(\xi, \eta) = \Delta A_0 \sqrt{\left(\frac{\partial x}{\partial \xi}\right)^2 + \left(\frac{\partial y}{\partial \xi}\right)^2} \quad (3.3)$$

with  $(\cdot)_0$  designating the initial condition, a small constant usually set by trial and error to obtain a stable solution. The effect of altering the cell-area according to the local Jacobian is exemplified in Figure 3.4b. The reader should bear in mind that the illustrated mesh in

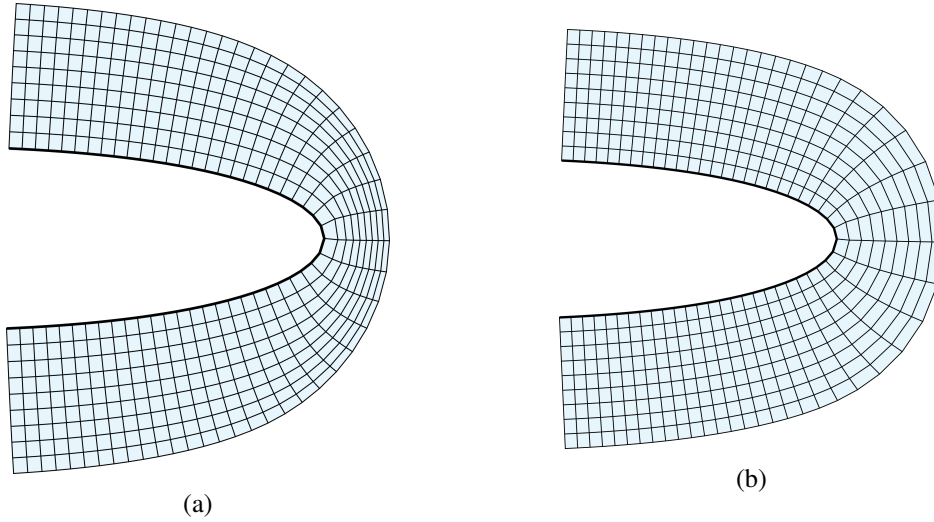


Figure 3.4: Solution of a hyperbolic mesh near the leading edge of an airfoil in case of (a) constant cell area, yielding an increasingly high cell-aspect ratio near the nose with radial distance (b) adjusting the cell area proportional to the Jacobian. This reduces the numerical cell-aspect ratio and minimises artificial displacement gradients when mapping images according to the generated mesh.

Figure 3.4 is representative of the subsequent image deformation and is not related to the sizing or positioning of interrogation windows.

The extent of the numerical mesh is defined by the user and should equal at least one initial correlation window size. The degree of grid smoothening must be selected considering the shape of the interface and is of pivotal importance both for numerical stability and mesh coherence. As an example, in absence of artificial smoothening, concave shaped interfaces are attributed meshes which intersect themselves as they propagate outwards. This creates a non-unique surjective transformation of the mesh as illustrated in Figure 3.5a. Incorporation of artificial smoothening by means of adding an explicit second-order dissipation term to the right hand side of equation (2) as proposed by [16] renders a more conducive mapping (Figure 3.5b).

### 3.4.3 Numerical solution of the hyperbolic mesh equations

The relationship between physical coordinates  $(x, y)$  and logical coordinates  $(\xi, \eta)$  is expressed in 3.2 from which follows:

$$x_\eta = -\frac{\Delta A}{\lambda} y_\xi, y_\eta = \frac{\Delta A}{\lambda} x_\xi, \text{ with } \lambda = x_\xi^2 + y_\xi^2 \quad (3.4)$$

By introducing a four-point stencil, the discrete values of  $x$  and  $y$  can be expressed as  $x_{i,j}$  and  $y_{i,j}$ , where the indices  $i$  and  $j$  depict the discrete location along the logical axis  $\xi$  and  $\eta$ .

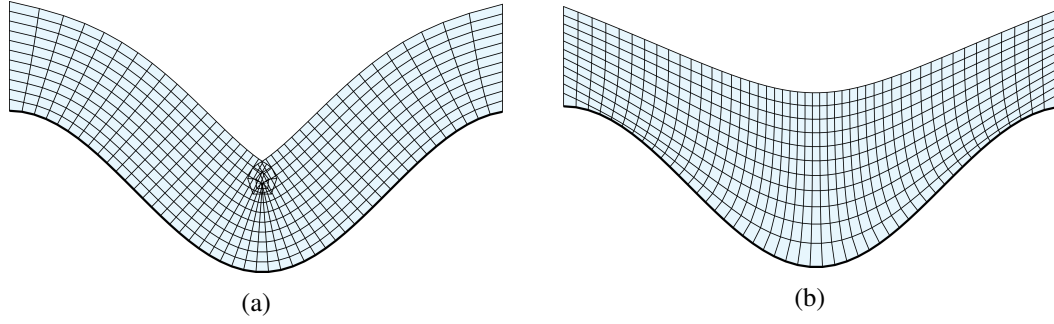


Figure 3.5: (a) Illustration of a self-intersecting mesh in case of concave boundary geometries without the application of artificial smoothing yielding non-unique image mapping and (b) the result of incorporating a smoothing factor.

Following this approach, partial derivatives in 3.4 can be discretised using second order central differences;

$$\frac{x_{i,j+1} - x_{i,j-1}}{2\Delta\eta} = -\left(\frac{\Delta A}{\lambda}\right)_{i,j} \frac{y_{i+1,j} - y_{i-1,j}}{2\Delta\xi}, \quad \frac{y_{i,j+1} - y_{i,j-1}}{2\Delta\eta} = \left(\frac{\Delta A}{\lambda}\right)_{i,j} \frac{x_{i+1,j} - x_{i-1,j}}{2\Delta\xi} \quad (3.5)$$

with:

$$\lambda_{i,j} = \left(\frac{x_{i+1,j} - x_{i-1,j}}{2\Delta\xi}\right)^2 + \left(\frac{y_{i+1,j} - y_{i-1,j}}{2\Delta\xi}\right)^2 \quad (3.6)$$

The term  $\Delta A_{i,j}$  is defined as per 3.3. These equations can be rearranged to yield an expression for the unknowns  $x$  and  $y$  at the next value of the stencil in the marching direction  $\eta$ , i.e.  $(x_{i,j+1}, y_{i,j+1})$ , in terms of  $x_{i,j}$ ,  $y_{i,j}$ ,  $x_{i-1,j}$ ,  $y_{i-1,j}$ ,  $x_{i+1,j}$  and  $y_{i+1,j}$ . Starting from the solution on the boundary condition ( $\eta = 0$ ), the solution will thus propagate in the direction of increasing  $\eta$ .

### 3.4.4 Displacement conversion

When images will be transformed into the logical  $(\xi, \eta)$  plane and evaluated, corresponding particle image displacements  $d\xi$  and  $d\eta$  must be converted into physical displacements  $dx$  and  $dy$  in order to be meaningful. The transformation of logical displacements is achieved using the Jacobian  $[J]$  of the transformation, expressed by equation 3.7.

$$\begin{bmatrix} dx \\ dy \end{bmatrix} = \begin{bmatrix} \frac{\partial x}{\partial \xi} & \frac{\partial x}{\partial \eta} \\ \frac{\partial y}{\partial \xi} & \frac{\partial y}{\partial \eta} \end{bmatrix} \begin{bmatrix} d\xi \\ d\eta \end{bmatrix} = [J] \begin{bmatrix} d\xi \\ d\eta \end{bmatrix} \quad (3.7)$$

Derivatives appearing in 3.7 are evaluated through an interpolation of the second-order finite differences of the physical coordinates  $(x, y)$  with respect to  $\xi$  and  $\eta$ .

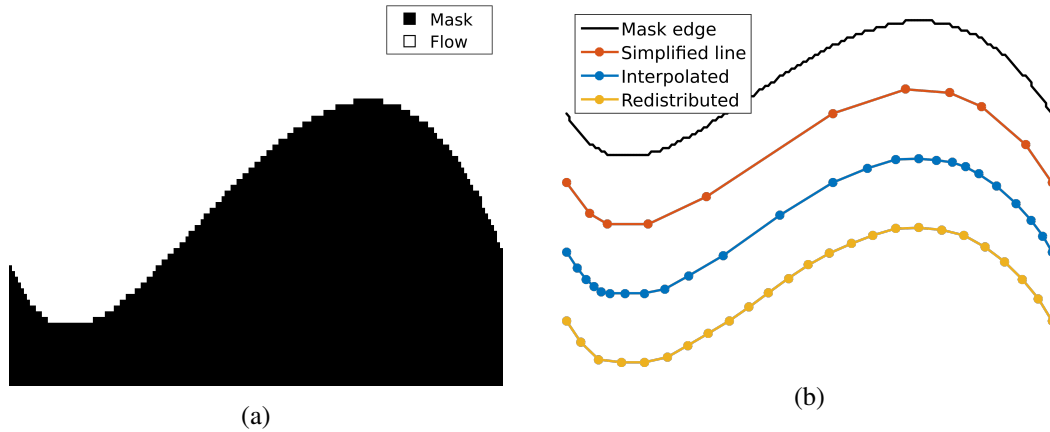


Figure 3.6: (a) A logical mask provided as an image, clearly illustrating the discrete nature of the boundary edge. (b) Processing of boundary points extracted from the edges of the mask as per the Douglas-Peucker line simplification algorithm.

### 3.5 Practical implementation of cross-correlation using body conforming numerical grids

#### 3.5.1 Interface boundary definition

The generation of the numerical mesh starts from the boundary condition provided in the form of a logical binary image identifying the object (see Chapter 2). As a direct consequence of pixelisation, edges cannot be straightforwardly used as mesh boundary conditions but need to be properly smoothed and rearranged (Figure 3.6). The process of boundary smoothing can be performed in different ways and several techniques have been tested among which Gaussian convolution, discrete cosine transform [32] and Fourier descriptors [29]. In spite of the number of the techniques tested, all smoothing functions applied to the mask edges produce artificial oscillations due to the non-random nature of the quantization error of the discrete pixel positions making up the interface boundary. In order to overcome this problem, a line simplification algorithm is chosen, for which the Douglas-Peucker algorithm [23] has been efficiently adopted.

The process of generating a boundary condition from the provided masking image for subsequent mesh generation is depicted in Figure 3.6b and consists of four main steps. Edges are first extracted from the logical mask by means of classical edge detection routines. Since the edge of the mask is made of discrete pixels the suggested algorithm simplifies the step-shaped curve by iteratively reducing the number of points and selecting subsets with the aim of attaining a difference between the original and sub-sampled edge below a defined threshold<sup>1</sup>. Following a spline interpolation of the simplified edges to reconstitute the number of

<sup>1</sup>This step was automatically performed using the matlab function “reducem”

edge pixels, edge points are redistributed along the spline curve to be equidistant. The latter is of importance since a non-equally distributed mesh introduces artificial deformation into the mapped image, affecting the quality of the cross-correlation and therefore the displacement measurement accuracy. The number of points used to re-interpolate the simplified edge will affect the number of points of the mesh in the angular direction and consequently the accuracy of the transformation. For this reason the mesh density should be selected to ensure each image pixel is covered by at least one mesh node.

Another important aspect concerning the generation of the boundary conditions for a numeric mesh appertains the overall topology. The main obstacle is that the logical plane is always rectangular shaped. Although the transformation from a general shape to a rectangle can be quite straightforward (e.g. L- or C-shaped boundaries need only straightening) closed shapes need further attention. An annulus, for instance, cannot be transformed into a rectangular shape unless a branch cut is introduced on the physical plane. No general solution exists to overcome the inherent problem and the user is obliged to recursively adjust the mesh on a case-by-case basis to ensure continuity across the branch cut when interrogation windows overlap with it. Particular topological conditions could be needed also in case of shape singularities or strong curvature (e.g. the trailing edge of an aerofoil).

### 3.5.2 Interpolation of mesh coordinates

The hyperbolic numerical mesh is generated through the system of equations 3.2, which can be solved adopting e.g. the approach recorded in Section 3.4.3. Independent of the adopted solver, the obtained numerical solution consists of a discrete set of data points in the physical plane  $(x_{ij}, y_{ij})$ , which are located on the nodes of the numerical mesh and for which the corresponding equivalent in the logical plane  $(\xi_{ij}, \eta_{ij})$  is known. Figure 3.7a-b show an example of those discrete points in the form of a 3D surface for a simple sinusoidal mesh. It should be noted that the locations  $(\xi_{ij}, \eta_{ij})$  constitute the nodes of an equispaced rectangular grid and that the samples  $(x_{ij}, y_{ij})$  do not need to coincide with original pixel locations. As will be shown in section 4.3, cross-correlation in the logical plane however requires image intensities defined at a higher resolution, i.e. at locations between the available  $(\xi_{ij}, \eta_{ij})$  samples. The transformation between a general point on the logical  $(\xi, \eta)$  plane and the physical  $(x, y)$  plane thus requires an interpolation of the discrete point locations. In the current work, a quintic spline scheme [10] was adopted.

The inverse transformation from the physical plane to the logical plane, which is depicted in Figure 3.7c-d, is also performed through interpolation, although additional attention is required since the coordinates  $(\xi, \eta)$  are distributed on the nodes of the mesh on the physical plane and, as such, do not constitute a structured grid as required for spline interpolation. For this reason,

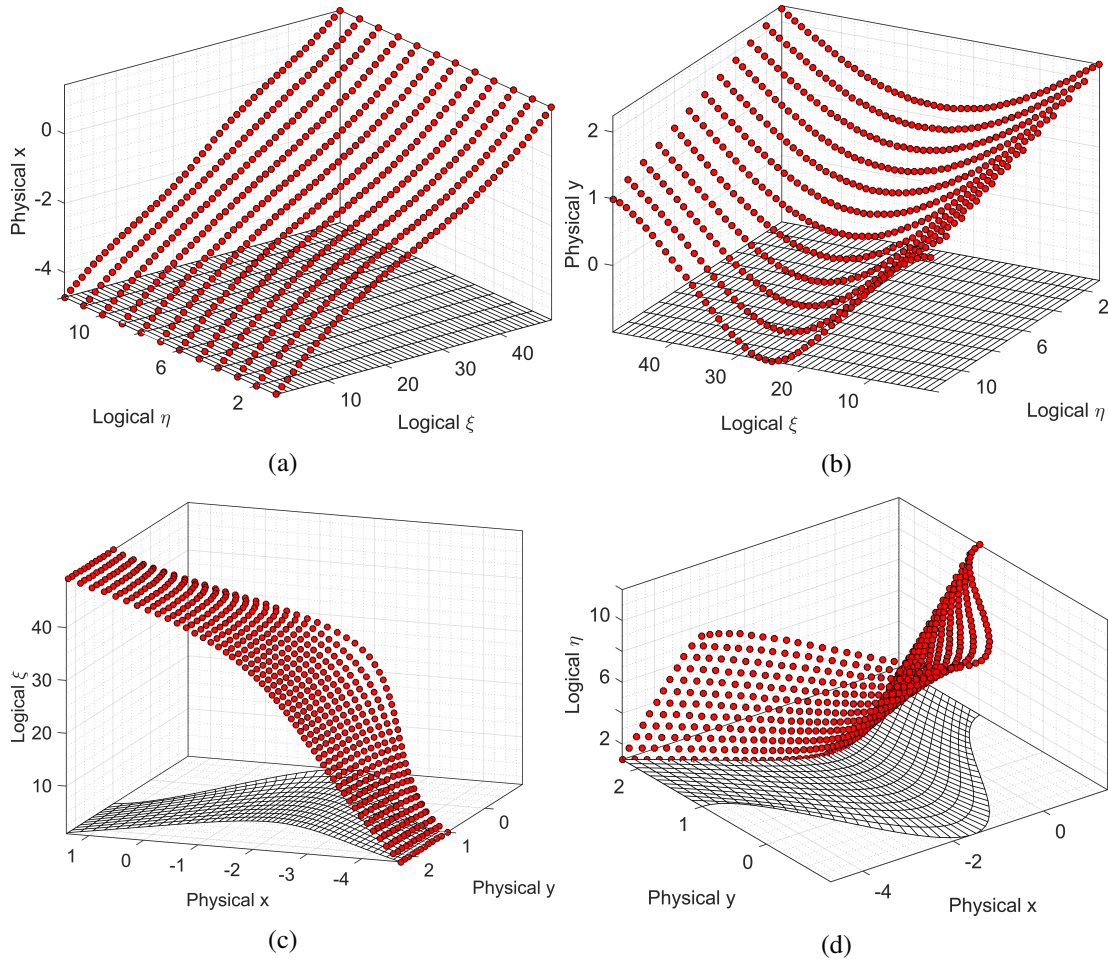


Figure 3.7: Plot of the coordinates mapping for the example mesh proposed in Figure 3.5. (a-b) Physical coordinates plotted against structured logical coordinates. (c-d) Logical coordinates plotted against scattered physical coordinates.

a non-structured interpolant is needed and in this work, a natural neighbours interpolation [14] has been selected accordingly.

### 3.5.3 Correlation in the logical plane and enhanced re-sampling

Following the generation of the numerical mesh, interrogation window centres are distributed on the physical plane and, in line with the Chimera approach, analysed differently according to their distance from the interface boundary (see Section 3.3). Interrogation areas of which the centroid is located outside the numerical mesh are analysed directly by means of cross-correlation on the physical plane as per standard PIV. Correlation windows whose centroid falls within the boundary fitted mesh will utilise the logical plane, where rectangular correlation windows are constructed and analysed by means of standard cross-correlation.

Physical pixel	the standard picture element, i.e. pixel, of the (original) image in the physical plane
Logical / mapped pixel	the picture element of the image mapped onto the logical plane
Logical unit	radial and angular units in the logical plane defined by the numerical mapping

Table 3.1: Definition of main units used in the description of correlation in the logical plane.

The relations established in paragraph 3.5.2 describing image mapping between the different coordinate systems allow a complete reconstruction of the image recordings onto the logical plane. This is the common approach adopted in previous studies ([64], [45], [71]), followed by cross-correlating intensities in the logical plane. However, digital images are not continuous but composed of discrete, square elements, i.e. physical pixels. Image mapping will consequently distort these pixel units. Due to the potentially strong non-linearity of the mesh shape and the consequent divergence (or convergence) of the radial lines in proximity of a curved surface, the use of a uniquely predefined correlation window size in the logical plane expressed in terms of physical pixels produces under-sampled (or over-sampled) particles at further distances from the boundary. The mapped particle intensity distributions consequently become strongly elliptical in the vertical (or horizontal) direction, biasing the outcome of the correlation operator as illustrated in Figure 3.9b, c and e.

This effect in itself is detrimental to the accuracy attainable with image mapping and any subsequent error analysis would as a result disfavour image mapping. Instead, to enable an objective evaluation of the overall applicability of image mapping, a fix to reduce this unfavourable effect is presented. The solution is a more robust approach involving image re-sampling of logical pixels prior to cross-correlating whereby the image mapping is performed on the basis of individual interrogation windows using an independent number of sampling points. As the process involves a transformation of the various units between the physical and logical plane, Table 3.1 summarizes main related definitions to assist the reader, which are graphically clarified in Figure 3.8.

Strongly curved meshes distort the shape of the particle images as illustrated in Figure 3.9a-b. The stretched particle images (Figure 3.9c) create a distorted correlation map (Figure 3.9e) and negatively affect the mapping-related bias error as argued by [83]. To this extent, a re-sampling process is introduced. Starting from a logical rectangular interrogation window, whose sizing will be covered in section 3.5.4, the radial and angular dimensions of its mapped equivalent in the physical plane are evaluated in terms of physical pixel units. This yields a length  $\gamma_k$  (in physical pixels) for each curvilinear side  $k$  of the physical window. To maintain the circular shape of the particle images in the logical plane, the number of mapped pixels  $N_\xi$  and  $N_\eta$  along the tangential and radial directions respectively within each logical correlation

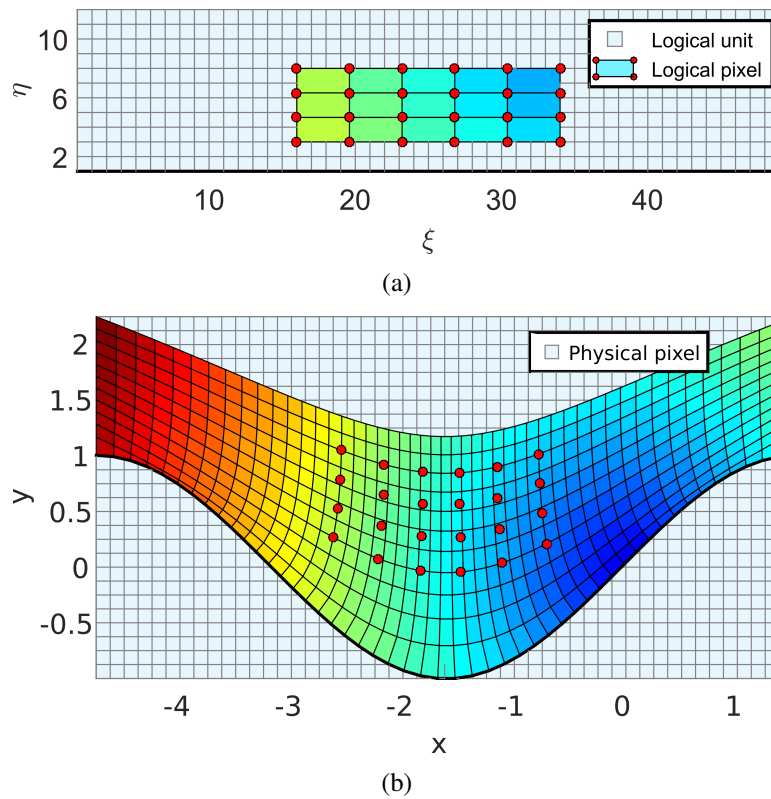


Figure 3.8: Description of the interpolation process of image intensities for correlation windows. (a) Logical pixels (filled rectangles bounded by red circles) are distributed on the logical plane. The grey grid represents the logical units. (b) The locations are mapped from the logical to the physical plane and image intensities on the physical plane are interpolated to yield the logical pixel intensities.

window is then selected automatically considering these extents;

$$\begin{cases} N_{\xi} = \frac{1}{2}(\gamma_{\text{top}} + \gamma_{\text{bottom}}) \\ N_{\eta} = \frac{1}{2}(\gamma_{\text{left}} + \gamma_{\text{right}}) \end{cases} \quad (3.8)$$

The enhanced resampling thus re-evaluates the number of logical pixels dividing the logical, rectangular shaped correlation window ensuring a sufficient number of pixels to produce equally stretched particles in the horizontal and vertical direction (Figure 3.9d). The shape of the particles in the mapped windows is consequently preserved yielding symmetric correlation peaks (Figure 3.9f). The improvement can also be shown by evaluating a Gaussian fit of the correlation peaks, shown in Figure 3.9e-f, and evaluating the ratio between the horizontal and vertical widths. This ratio equals 5.2 for a constant sampling and 1.2 for the re-sampled correlation window, illustrating the improved correlation symmetry. Image intensities within the logical pixels are retrieved by quintic spline interpolation [9] of the original intensity distribution in the corresponding physical locations obtained by forward mapping [122]. The reader should note that these logical pixels, which are arranged in a Cartesian manner in the logical plane (red circles in Figure 3.8a) can consist of several logical units (Figure 3.8a).

The outcome of the subsequent cross-correlation operation on the logical interrogation areas yields a displacement quantified in terms of logical pixels. These in turn depend on the number of imposed (re-) sampling points expressed in 3.8, necessitating a rescaling prior to the Jacobian-based conversion of displacements from the logical plane to the physical plane (cf. equation 3.7). The conversion from logical pixels into logical units, for each displacement, is given by:

$$u_{\xi,\eta} = u_{\xi,\eta}^* \frac{WS_{\xi,\eta}}{N_{\xi,\eta}} \quad (3.9)$$

Subscripts denote consideration of either the tangential  $\xi$  or radial direction  $\eta$ ,  $U_{\xi,\eta}$  represents the displacement converted into logical units,  $u_{\xi,\eta}^*$  symbolises the displacement in logical pixels resulting from the correlation in the logical plane and  $WS_{\xi,\eta}$  indicates the extent of the window in the logical plane in terms of logical units. The determination of  $WS_{\xi,\eta}$  will be discussed in section 3.5.4.

### 3.5.4 Interrogation window sizing on the logical plane

Contrary to standard PIV algorithms, interrogation window sizing during the process of image mapping is more complicated due to the non-linear correspondence between physical and logical interrogation window sizes;

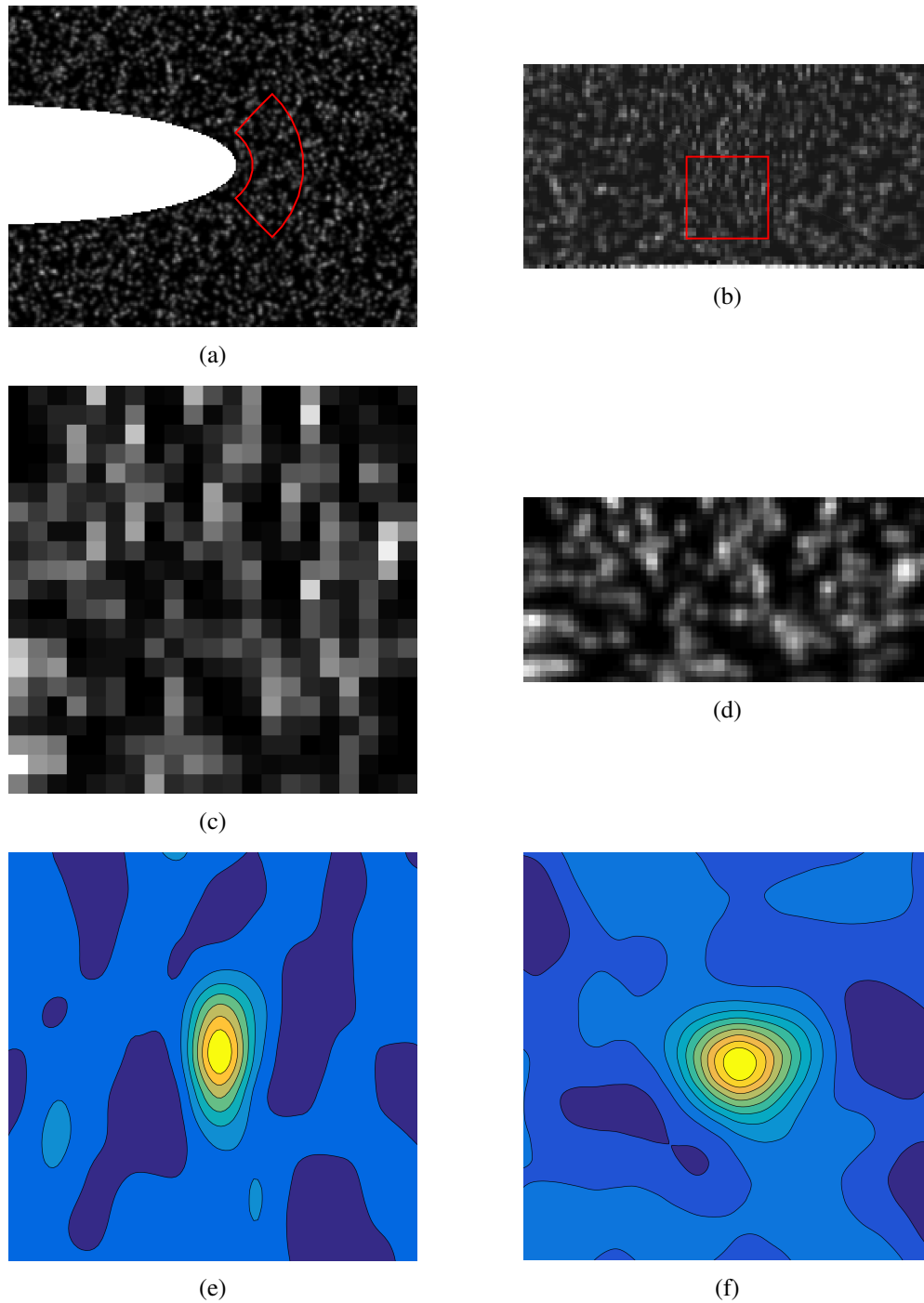


Figure 3.9: (a) Effect of the enhanced resampling for the case of the leading edge of a Joukowski airfoil shape. (b) The same correlation window is shown on the logical plane. (c) Logical correlation window adopting constant sampling and (d) the enhanced resampling showing the effectiveness of the method. Exemplary cross-correlation maps in case of (e) constant sampling and (f) enhanced resampling. Enhanced resampling improves the circularity of the particle images and correlation peak symmetry.

$$\begin{bmatrix} WS_{\xi} \\ WS_{\eta} \end{bmatrix} = [J(x,y)]^{-1} \begin{bmatrix} WS_x \\ WS_y \end{bmatrix} \quad (3.10)$$

where  $WS_x$  and  $WS_y$  are the horizontal and vertical window sizes on the physical plane. Variables  $WS_{\xi}$  and  $WS_{\eta}$  depict the angular and radial sizes respectively on the logical plane. This dependency was already highlighted in paragraph 3.5.3 in the context of particle image distortions. As per equation 3.10, due to the spatial dependency of the Jacobian, equally sized correlation windows in the physical plane will yield non-uniform window sizes in the logical plane and vice-versa. This problem has never been clearly stated in existing literature and this chapter accordingly proposes two different solutions to automatically adjust the size and the position of the correlation windows on the logical plane.

The first implementation, referred to as (straightforward) Image Mapping (IM), involves a recursive re-evaluation of interrogation area size and position on the logical plane in order to maintain the significance of the imposed window size. Once interrogation windows are distributed on the physical plane as per standard PIV (Figure 3.10a) and selected spatial locations are transformed from physical to logical coordinates using the inverse mapping functions  $\xi(x,y)$  and  $\eta(x,y)$  (section 3.5.2, Figure 3.10b), window sizes are converted from physical pixels into logical units using equation 3.10. This yields the logical window sizes  $WS_{\xi}$  and  $WS_{\eta}$  which appear in equation 3.9 (Figure 3.10c). As per the original aim of applying image mapping to avoid any overlap between correlation windows and identified interfaces, logical interrogation windows are then shifted to avoid overlap with the horizontal line at  $\eta = 0$  referencing the interface boundary (Figure 3.10d). The shifted logical positions correspond with new values of the Jacobian and therefore new window sizes on the physical plane. Window dimensions on the logical plane are then re-calculated and the process is repeated until none of the correlation windows extends below  $\eta = 0$ . This is typically satisfied in only 2 iterations.

The second implementation of the window sizing algorithm, known as Image Mapping with Vector Relocation (IMVR), is a modification of IM, taking advantage of the vector relocation technique [111]. Correlation windows in the logical plane are now allowed to exhibit a certain degree of overlap with  $\eta = 0$  and, contrary to shifting the window in its entirety, are cut-off followed by a repositioning of the resulting velocity vector. The first steps of the second approach thus remain identical to those of the IM method (Figure 3.10a-c). In IMVR, the portion of those correlation windows extending below  $\eta = 0$  is now masked from the process of cross-correlation and the resulting vector is consequentially relocated in the centre of the remaining area (Figure 3.10d).

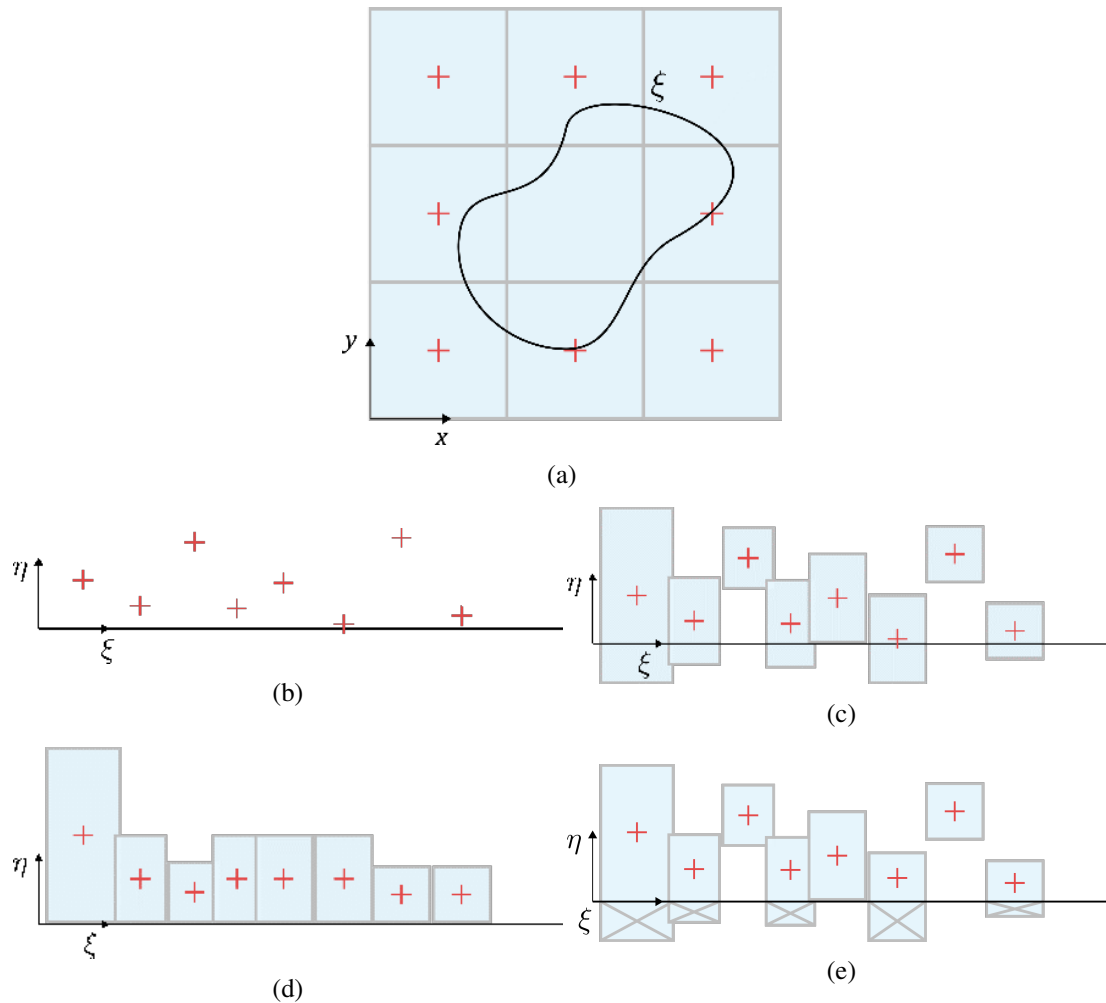


Figure 3.10: Iterative window repositioning and sizing in the logical plane: (a) correlation windows are located in the physical plane and (b) their centroids are mapped into the logical plane. (c) Window sizes are based on the Jacobian of the coordinate transformation at the corresponding window centres, potentially causing overlap with the interface boundary. (d) Logical windows are relocated and re-evaluated in size until no residual overlap with  $\eta = 0$ . (e) Logical window areas extending below  $\eta = 0$  are ignored and vectors are relocated to the centre of the reduced window.

### 3.5.5 Computational expense

It is clear that the combination of the additional operations underpinning image mapping must come at some elevated computational cost. A distinction can be made between one-off additional effort for the generation of the numerical mesh throughout the multi-grid interrogation process and a persistent one due to the mapping of particle images (Figure 3.10). The mesh is generated once and remains invariant in case of stationary interfaces whereas the repeated effort related to the mapping, instead, cannot be prevented. The PIV image could be deformed in its entirety only once before the analysis. The reader is strongly discouraged to take this approach, especially when highly curved surfaces are considered due to the resulting strongly deformed particle images (Figure 3.9c-e). The suggested solution of enhanced re-sampling (Figure 3.9d-f), on the other hand, requires the interpolation of both numerical mesh data and image grey levels for every interrogation area. Although this process can be quickly accomplished by means of quintic splines, it nevertheless typically augments the overall processing time by 3 to 6 times the time spent on the cross-correlation operator, depending on the density of the numerical mesh and its wall-normal extent. This additional load, however, only applies to the Chimera region where image mapping is involved and does not affect all the correlation windows.

## 3.6 Numerical Assessment

To discern advantages and disadvantages of the image mapping process and associated inherent errors, methodic analyses have been performed on the basis of numeric simulations. Three different error analyses are presented to investigate every aspect involved in the application of image mapping to PIV. The first analysis, presented in Section 3.6.1, investigates the errors originated by the use of a numeric mesh in the conversion of points and vectors and does not involve any use of images or cross-correlation. The mesh adopted for this study was generated around a strongly curved Joukowski aerofoil and is depicted in red in Figure 3.11. In Section 3.6.2, attention is focussed on the effect of the deformation of particle images on bias and random error. Therefore a single correlation window for a flow around a cylinder is analysed with cross-correlation and a simple analytical transformation is adopted for the image mapping. Finally, Section 3.6.3 investigates the error involved in the application of image mapping to a full PIV algorithm, juxtaposing the obtained particle image displacement estimates with alternative advanced techniques for measurements close to surfaces. For this analysis, the Joukowski aerofoil from Section 3.6.1 is re-used to generate a set of synthetic images (Figure 3.11) together with the numerical mesh used for the image mapping process.

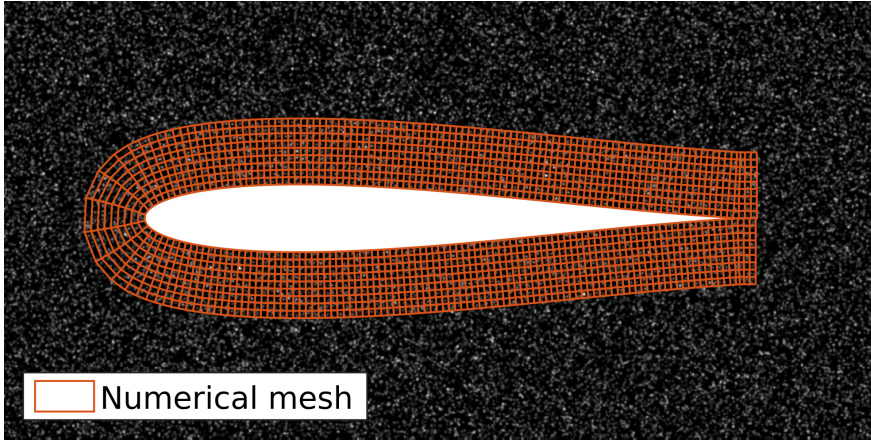


Figure 3.11: Sample of PIV image for the Joukowski aerofoil depicted with the numerical mesh (down-sampled for illustration purposes) used for the image mapping.

### 3.6.1 Inherent Error source 1: Mesh interpolation and displacement transformation

Independent of the adopted numerical mesh, the transformation from physical to logical plane must be carried out through an interpolation (cf. paragraph 3.5.2). Independent of the PIV algorithm in which image mapping is implemented, this inherently produces a numerical error for both vector components and locations when converted and is non-negligible although often overlooked in existing literature. Quantification of this error is not straightforward though because of the lack of explicit analytical expressions specifying the transformations. A simplistic analysis is proposed by consecutive mapping of spatially distributed points from the physical plane to the logical plane (inverse transformation) and back (direct transformation) as shown in Figure 3.7. The error heuristic,  $\epsilon_{\text{transf}}$ , is then defined as the difference between the initial point locations and their doubly-converted position, as expressed by:

$$\epsilon_{\text{transf}} = \left\| \begin{array}{l} x^*(\xi^*(x_k, y_k), \eta^*(x_k, y_k)) - x_k \\ y^*(\xi^*(x_k, y_k), \eta^*(x_k, y_k)) - y_k \end{array} \right\| \quad (3.11)$$

where  $x^*(\cdot)$ ,  $y^*(\cdot)$  and  $\xi^*(\cdot)$ ,  $\eta^*(\cdot)$  are respectively the interpolation of the numerical solutions for the physical and logical coordinates of the mesh, as described in Section 3.5.2, and  $x_k$  and  $y_k$  are sampling points distributed over the physical plane. The contour of  $\epsilon_{\text{transf}}$  is depicted for a hyperbolic mesh generated over a Joukowski aerofoil in Figure 3.12a, in logarithmic scale.

The observed error with regard to distribution and magnitude is conservative as it considers both errors originating from the direct and inverse transformations, with the latter being less

accurate due to the scattered nature of the required interpolation (cf. paragraph 3.5.2). In reality, the two transformations are never used consecutively, for which reason this result must be considered as an upper error limit. Figure 3.12a illustrates the maximum expected error in the vector position to be less than  $10^{-3}$  pixels, i.e. one order of magnitude below the commonly accepted limit in displacement accuracy ( $\approx 0.01$  pixels) obtainable with standard PIV [42]. Nevertheless, Figure 3.12a shows that highest errors in transformation are encountered in proximity of the leading edge. The reader is reminded that this error analysis is independent from the PIV analysis as it only originates from the mapping of points using the mesh transformation. However, this general tendency is independent of the mesh density (cf. paragraph 3.5.1) and is related to the divergence of the characteristic mesh lines in presence of surface curvature. The digression of the lines is evidenced by the strong derivatives of the Jacobian shown in Figure 3.12b, which increase in magnitude as the distance from the aerofoil increases. The same effect can be observed on the trailing edge too, where mesh lines are instead converging. Unfortunately, this additional error will occur exactly where velocity gradients and image deformation are stronger, contributing overall to a deterioration of the measurement accuracy in these regions.

Mapping of velocity components, in theory, should be less prone to error than mapping of points, as it involves a simple rearrangement of equation 3.7. The Jacobian in this equation is evaluated using derivatives of the structured mesh data on the logical plane and this step is therefore more accurate than the inverse transformation of the points, with negligible error throughout the entire PIV algorithm. However, the conversion of velocity components is affected by a different source of error which is not related to the interpolation but rather to an amplification of the standard PIV error connected to the use of the Jacobian itself. This amplification can be easily illustrated by considering a simple polar to Cartesian transformation;  $x = \rho \cdot \cos(\theta)$  and  $y = \rho \cdot \sin(\theta)$ . When the displacement field on the logical plane is subjected to an error  $\epsilon_{\log}$ , the transformed error on the physical  $\epsilon_{\text{phy}}$  scales with radial distance.

$$\begin{aligned} \begin{bmatrix} dx \\ dy \end{bmatrix} + \epsilon_{\text{phy}} &= \begin{bmatrix} \cos(\theta) & -\rho \sin(\theta) \\ \sin(\theta) & \rho \cos(\theta) \end{bmatrix} \left( \begin{bmatrix} d\rho \\ d\theta \end{bmatrix} + \epsilon_{\log} \right) = \\ &= [J] \begin{bmatrix} d\rho \\ d\theta \end{bmatrix} + [J]\epsilon_{\log} \rightarrow \|\epsilon_{\text{phy}}\| = \|\epsilon_{\log}\| \sqrt{1 + \rho^2} \end{aligned} \quad (3.12)$$

In case of the Joukowski aerofoil, the norm of the Jacobian is depicted in Figure 3.12b and a similar amplification of the error is observed in Figure 3.12c. Here, an artificially imposed probability density function of the magnitude of normally distributed random noise,  $\sigma$ , with a standard deviation of 0.1 pixels was superimposed on the ideal velocity field near the Joukowski aerofoil's leading edge on the physical plane. When the same noise is superim-

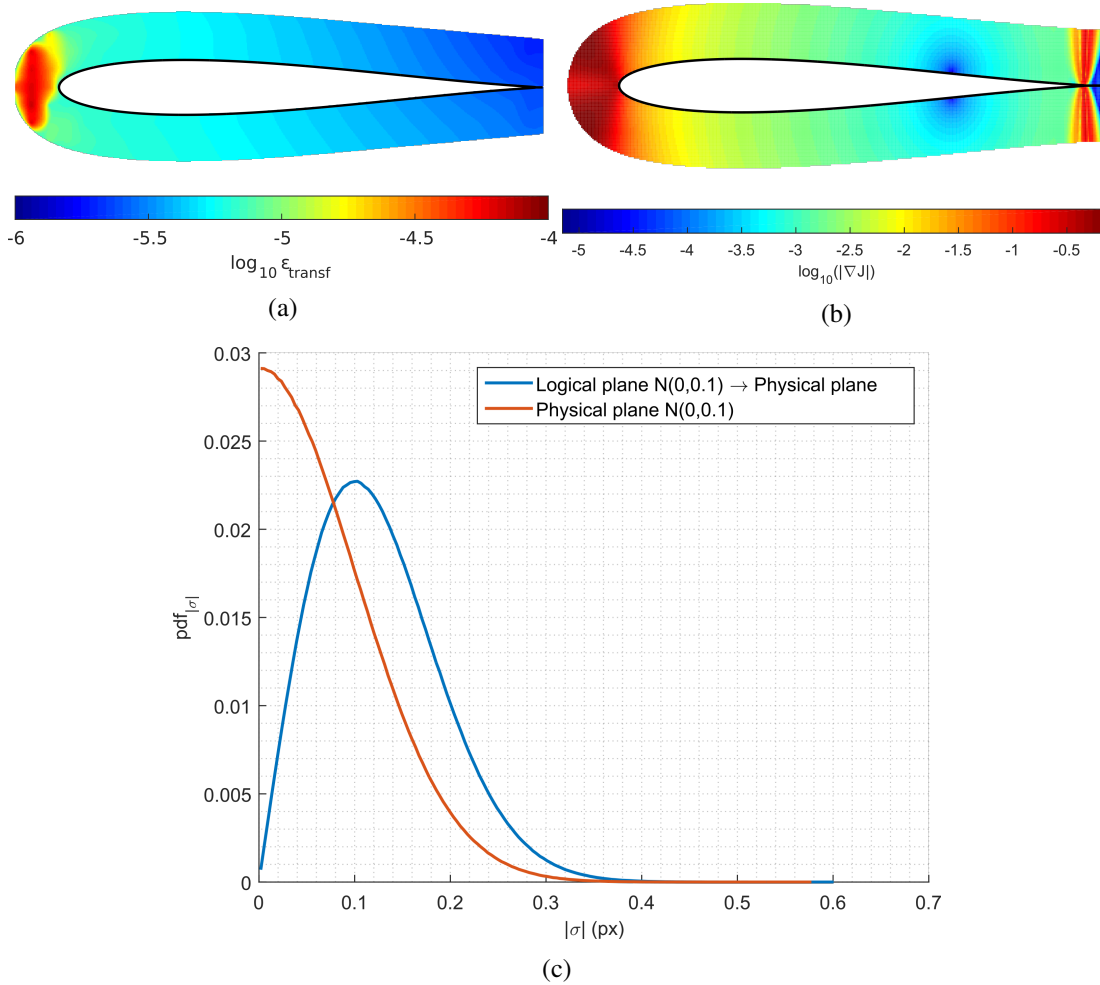


Figure 3.12: (a) Numerical error in mesh transformation, in  $\log_{10}$  scale, after sequential coordinate transformation (physical plane $\rightarrow$ logical plane $\rightarrow$ physical plane). (b) Magnitude of the gradient of the coordinate transformation's Jacobian. (c) Amplification of random displacement error in the logical plane originating from coordinate transformation.

posed to ideal displacements on the logical plane and converted back into the physical plane, noise is amplified by a factor 1.6 (Figure 3.12c). The reader is reminded that this error amplification is independent of the PIV algorithm used, but is related to the geometry of the mesh adopted for image mapping. This error source may affect the quality of the measurements, especially in regions of stronger mesh curvature, thus limiting the general application of image mapping to PIV. Even if no other cause of mesh-related error was present, a random noise of a measurement will be amplified according to the mesh curvature simply because of the use of image mapping.

### 3.6.2 Inherent Error Source 2: Mesh curvature influence on the particles distortion

When implementing image mapping within a PIV image interrogation process, special attention must be paid to the distortion of particle images as these establish the signal for cross-correlation. In line with findings reported in the previous paragraph, this error source will be strongly dependent on the mesh arching. To isolate and quantify the source of measurement inaccuracy pertinent to the mesh curvature, a special test case was designed using synthetic images. A single correlation window was deformed using a Cartesian  $(x, y)$  to polar  $(\rho, \theta)$  transformation around a cylinder of variable radius  $\rho$ , ranging from 10 ( $\rho_{\min}$ ) to 700 pixels ( $\rho_{\max}$ ). To nullify the influence of velocity gradients, a constant shift of 1.25 logical pixels was imposed along the  $\theta$ -axis in the logical plane. Using the Jacobian in equation 3.7 with conventional polar coordinate transformations corresponding displacements in the physical  $(\delta x, \delta y)$  and logical plane  $(\delta \rho, \delta \theta)$  were expressed as:

$$\begin{cases} \delta x = -U_{\text{inf}}\rho \sin(\theta) \\ \delta y = U_{\text{inf}}\rho \cos(\theta) \end{cases} \text{ and } \begin{cases} \delta \rho = 0 \\ \delta \theta = U_{\text{inf}} = 1.25 \end{cases} \quad (3.13)$$

To decouple the error due to particle deformation from other effects connected to image mapping, the size of the interrogation window on the logical plane was kept constant while testing multiple cylinder radii (cf. Figure 3.13). The logical height of the window  $WS_{\rho}$  was arbitrarily set to 35 logical pixels, while the logical width  $WS_{\theta}$  was based on the largest angular extent (i.e. the circumference) of the minimum radius tested;  $WS_{\theta} = 2\pi\rho_{\min} \approx 63$ . Physical particle images were thus sampled using a constant number of logical pixels.

However, as the physical extent of logical pixels depended on their radial location within the correlation window, particle images were resampled following a 1:1 ratio nearest to the cylinder radius (i.e. one logical pixel per physical pixel) and under-sampled by a factor  $1 + 35/\rho$  furthest. Accordingly, this test allowed assessing solely the effect of elliptical warping due to mesh curvature. Bias and random errors in measured displacement, noted as  $\beta$  and  $\sigma$

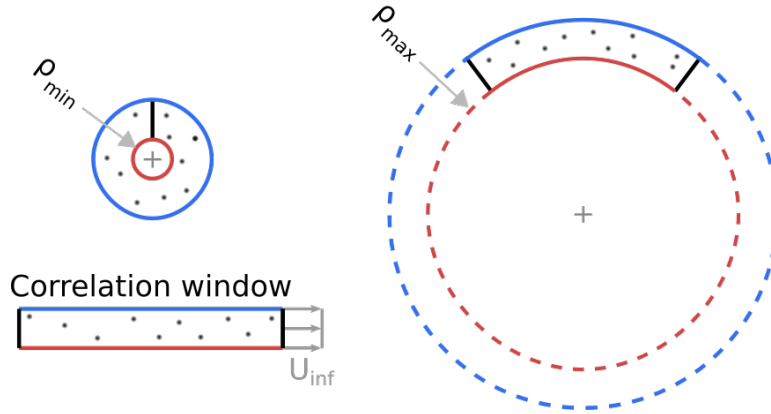


Figure 3.13: Description of the assessment of mesh-curvature influence. The correlation window size is chosen according to the circumference of the circle of smallest radius.

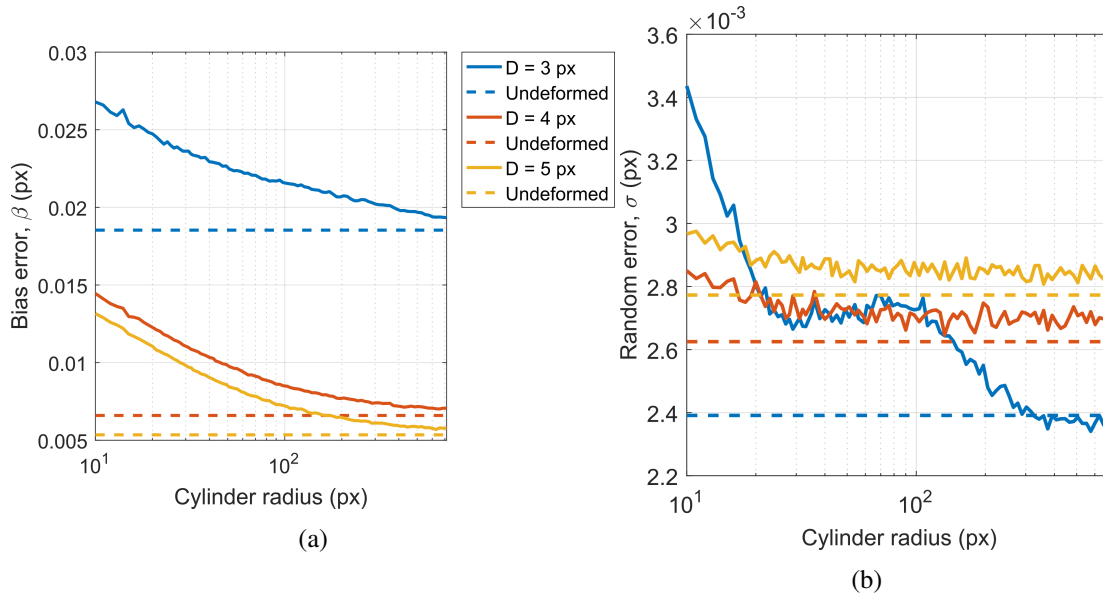


Figure 3.14: (a) Bias error  $\beta$  and (b) random error  $\sigma$  in measured particle image displacement versus cylinder radius with varying particle image diameter. Dashed line represent errors for cylinders of infinite radius.

respectively, for different particle diameters following Monte-Carlo simulations involving  $10^4$  synthetic images are plotted against the cylinder radii in Figure 3.14. The error for a correlation window of the same size, non-deformed (i.e. infinite cylinder radius), shifted by the same rigid displacement, is also depicted for comparison as a dashed line.

A strong dependency between error and cylinder radius can be observed in both Figure 3.14a and b. Comparing the undeformed (dashed lines) with the deformed bias error (solid lines), Figure 3.14a indicates the implementation of image mapping to augment the displacement bias error. Independent of the particle image diameters, this additional bias error can be

up to  $8 \cdot 10^{-3}$  pixels in case of the strongest deformation tested (i.e. minimum cylinder radius) and decreases monotonically as the cylinder radius increases, reaching a minimum of  $8 \cdot 10^{-4}$  pixels for the maximum radius tested. This behaviour is to be expected as the size of the cylinder affects the deformation of the particle images, increasing their elliptical shape. For all the particle diameters analysed, results are in accordance with the existing literature, with smaller particle diameters presenting a higher bias error, as they tend to degrade the accuracy of correlation peak sub-pixel fitting [116]. Inspection of Figure 3.14b reveals a similar behaviour for the random error, with image mapping introducing an additional error in the measurements inversely proportional to the cylinder radius. For cylinder radii exceeding 100 pixels random errors increase with particle image diameter. In case of strong deformations a rapid increase in random error can be observed for the smaller particle image diameter, yielding error levels exceeding those for larger diameters. The discrepancy between the asymptotic behaviour of the curves shown in Figure 3.14 and the corresponding reference cases is due to numerical errors originating from the different interpolation processes intrinsic to image mapping.

It is important to stress the fact that the mapping was here defined analytically. Presented errors in this subsection therefore reflect the influence of mesh curvature only and not mesh type. When using image mapping, a decrease in the measurement accuracy can thus be expected where mesh curvature is stronger merely due to the particle image deformation. Notwithstanding, actual advantages of image mapping will be case dependent (geometry shape, mesh type, flow gradients, correlation window distribution, etc.) and may outweigh the above error.

### 3.6.3 Limits of image mapping in a complete PIV analysis

In this section, image mapping has been embedded within PIV image analysis processes and compared with alternative advanced PIV interrogation routines. Numerical simulations presented afore have indicated measurement errors in particle image displacement, inherent to image mapping, to be strongly affected by the mesh curvature. To assess the limits of applicability of image mapping and investigate the maximum extent of these errors, a Joukowski aerofoil characterized by a strongly curved surface was therefore selected as a test case representative of aeronautical applications. Synthetic images were generated with seeding consisting of randomly distributed Gaussian shaped particle images with diameters selected from a normal probability (3 pixels mean, 1 pixel variance) and a concentration of 0.1 particles per pixel. Images had a bit depth of 8 with mean particle intensities of 120 and standard deviation of 40 grey levels. The analytical inviscid flow around a Joukowski airfoil enabled the direct evaluation of resulting measurement errors in case of realistic aerodynamic shapes containing regions of high surface curvature.

Five combinations of image interrogation procedures (summarised in Table 3.2) have been tested for different settings such as interrogation window size, number of predictor-corrector

	<b>Corr. win. distribution</b>	<b>Image Mapping</b>	<b>Vector Relocation</b>
<b>ASVR</b>	Adaptive (AS)	No	Yes (VR)
<b>ASIM</b>	Adaptive (AS)	Yes (IM)	No
<b>ASIMVR</b>	Adaptive (AS)	Yes (IM)	Yes (VR)
<b>CSVR</b>	Cartesian (CS)	No	Yes (VR)
<b>CSIM</b>	Cartesian (CS)	Yes (IM)	No

Table 3.2: Interrogation procedures considered in image interrogation performance assessment.

iterations and image noise. The algorithms combined different implementations of correlation window distributions, vector relocation and image mapping. Being the measurement in the near vicinity of the object the main interest of this chapter, the attention was focussed on the implementation of image mapping combined with an adaptive sampling distribution as proposed by [106]. For this implementation, formally referred to as Adaptive Sampling (AS), correlation windows are adaptively located to allow an automatic selection of the window properties. The density of correlation windows increases automatically towards the interface, with a consequent increase in windows overlap too, as depicted in Figure 3.20a. The combination of adaptive sampling and vector relocation [111], whereby no use is made of image mapping, will be referred to as ASVR (Adaptive Sampling Vector Relocation). This approach will serve as a basis for the comparison of the performances with more advanced techniques. The image mapping algorithm, as described in Section 3.5.4, can be implemented with or without vector relocation, yielding the ASIM (Adaptive Sampling Image Mapping, cf. Figure 3.10d) and ASIMVR (Adaptive Sampling Image Mapping with Vector Relocation, cf. Figure 3.10e) approaches. An adaptation of the algorithms on a standard Cartesian grid is also proposed for the sake of comparison, referred to as CSVR (Cartesian Sampling Vector Relocation) and CSIM (Cartesian Sampling Image Mapping). An overview of the conceptually different methodologies is provided in Table 3.2.

In the following, plots depict the total measurement error  $\varepsilon$  averaged over 1000 synthetic images. For each velocity field the reconstruction error is quantified by interpolating the measured displacements (natural neighbor interpolation was adopted),  $dx_m$  and  $dy_m$ , on a pixel-wise grid and evaluating the difference with the theoretical, analytical, displacements,  $dx_a$  and  $dy_a$ , in the corresponding location;  $\varepsilon = \sqrt{(dx_m - dx_a)^2 + (dy_m - dy_a)^2}$ . To ease comparison between the different interrogation approaches, the ratio between errors is presented on a logarithmic scale;  $\log_{10}(\varepsilon_{ASIM}/\varepsilon_{ASVR})$ ,  $\log_{10}(\varepsilon_{ASIMVR}/\varepsilon_{ASVR})$ , and  $\log_{10}(\varepsilon_{CSIM}/\varepsilon_{CSVR})$ . Values close to zero indicate the two methods to have the same performances (error near unity ratio). This can be expected outside the Chimera area where no image mapping is invoked and differences between methodologies are marginal.

In the absence of image noise, Figure 3.15 shows the comparison of the error between ASIM and ASVR performed in 3 predictor-corrector iterations with window sizes reduced from

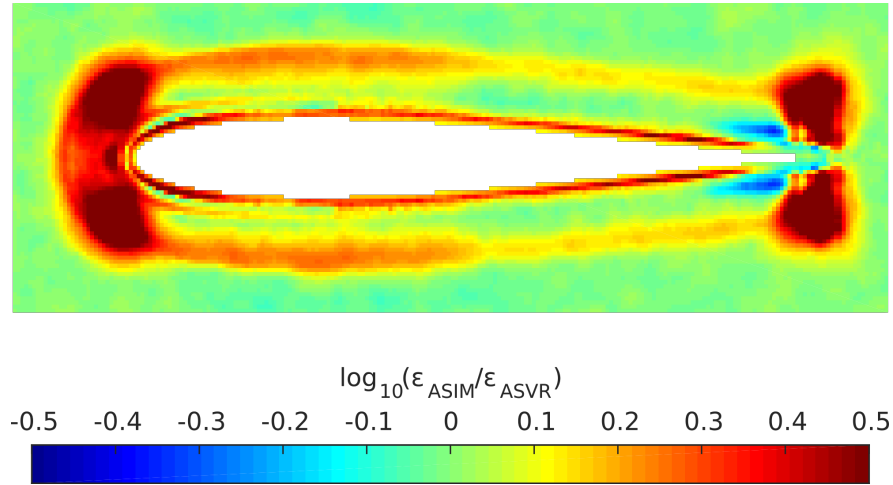


Figure 3.15: Comparison of displacement error between ASIM and ASVR. Number of iterations: 3. Correlation window size:  $90 \rightarrow 25$ . No image noise.

90 to 25 pixels. The spatial distribution in error presents patterns which can be attributed to the process of image mapping and to the characteristics of the numerical mesh. Starting from the leading edge, the highest error is concentrated in two agglomerations above and below the aerofoil. In these areas the Jacobian of the mesh reaches its maximum (Figure 3.12a), amplifying random fluctuations of the velocity field and increasing the error as described in Section 3.6.2. Moreover, due to the low radius of curvature of the aerofoil (10 pixels), this image area is affected by the strongest particle deformation and an additional error in terms of bias and random is expected, as already shown in Figure 3.14.

On the edge of the airfoil ASIM persistently attains a higher error. This consistent behaviour highlights an obstacle to the application of image mapping which has never been addressed in literature before. In fact, ASIM maintains a constant interrogation window size in proximity of a boundary and, as a consequence, the minimum distance between a displacement vector and the aerofoil boundary is at least half the minimum window size. Conversely, with ASVR vectors are repositioned to the centre of gravity of the correlation window portion occupied by the seeded flow. This yields a minimum distance of one-quarter of the minimum window size. Moreover, due to the lack of noise in the synthetic images, smaller interrogation windows are always associated to a smaller error. ASVR, whereby parts of the correlation windows overlapping with the aerofoil are masked automatically, results in analysing correlation windows which are smaller than the minimum set by the user. Therefore, in this particular case, ASVR produces better vectors which are closer to the aerofoil. It will be shown that in the presence of image noise this reasoning no longer holds.

Moving to the aft of the aerofoil, a behaviour in error similar to the leading edge is noticeable on the trailing edge. In proximity of the edge, a strong reduction in error is achieved with ASIM, yet accuracy rapidly reduces. The observed behaviour can be explained considering

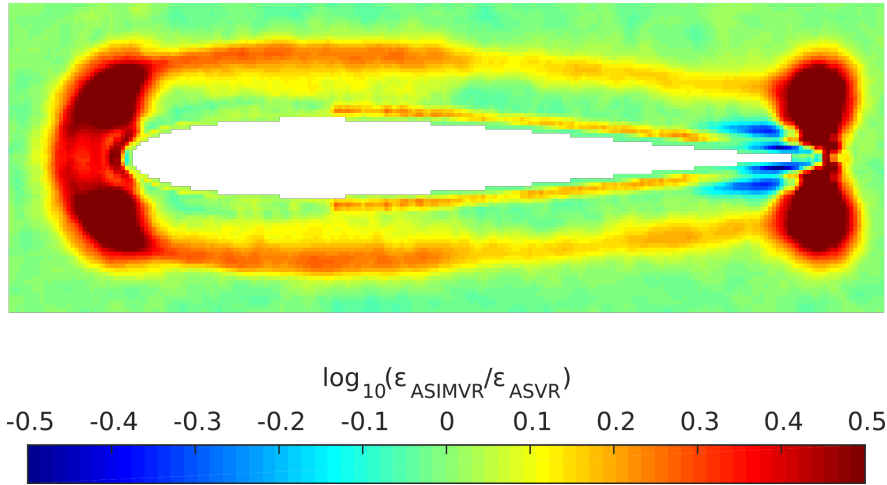


Figure 3.16: Comparison of displacement error between ASIMVR and ASVR. Number of iterations: 3. Correlation window size:  $90 \rightarrow 25$ . No image noise.

three different phenomena; the process of window repositioning on the logical plane described in Section 3.5.4; the adaptive point distribution and the interpolation effect of the predictor-corrector implemented in the algorithm. As already described in Section 3.5.4, correlation windows on the logical plane are automatically repositioned in order to keep the seeding density constant and to ensure they all have exactly the same area. This process inevitably produces a clustering of sampling points on the edges of the Chimera region, as shown in Figure 3.20. During the predictor-corrector process, the interpolation of velocity data in those areas of higher data density will produce a lower error of the velocity predictor and consequently a final error of ASIM which is lower than ASVR. The reader is reminded that this lower error is not related to the enhancement of the images produced by image mapping itself but rather to a mere effect of the interpolation due to the inherited clustering of data points.

The only difference between the implementation of image mapping in ASIM and ASIMVR is encountered near the airfoil edge (Figure 3.16). ASIMVR does not shift the window position to keep the area constant, but in an analogous way to ASVR, masks the correlation window area overlapping with the aerofoil on the logical plane and relocates the vector in the centre of gravity of the captured flow region. The effect shows an error of ASIMVR on the edge of the aerofoil which is on par with ASVR. In this case the application of image mapping results in no improvement of the measurement accuracy. However, it is important to stress that this result is only valid for the ideal case of images without artificial noise. The ASIMVR algorithm does not produce any clustering of points since no repositioning of logical windows is performed. Nevertheless, comparison of Figure 3.16 with Figure 3.15 indicates a noticeable reduction of displacement error near the trailing edge. Despite the minimum interrogation window size imposed by the user, the actual area adopted by ASIMVR for the cross-correlation depends of many different conditions. On the trailing edge, the numerical mesh is logically cut along the

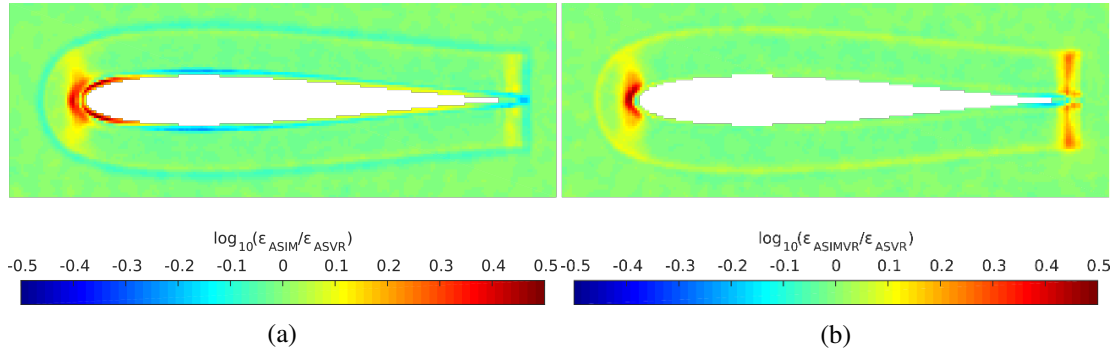


Figure 3.17: Comparison of displacement error between (a) ASIM and ASVR, (b) ASIMVR and ASVR. Number of iterations: 3. Correlation window size:  $90 \rightarrow 25$ . With image noise.

aerofoil chord as shown in Figure 3.11. Because of this discontinuity, interrogation windows close to the trailing edge analysed with ASIMVR will be smaller than windows positioned in the same area but analysed with ASVR. In absence of noise, this produces a smaller error for ASIMVR. With the purpose of understanding all the possible advantages and applications of image mapping, and proposing a more realistic case of images, the previous analysis has been repeated in the presence of artificial noise, in the form of a normal distribution with mean of 2.8% and standard deviation of 3.6% of the maximum intensity, added to the ideal images. The spatial distribution in displacement error produced by image mapping or standard adaptive PIV algorithms presents many similarities with the two previous cases. Now the relative importance of the error produced by the mesh transformation is dominated by the uncertainty brought by the artificial noise. Differences inherent to the image mapping technique are amplified accordingly.

Figure 3.17a presents the error ratios between ASIM and ASVR and shows features of high error similar to those in Figure 3.15. These are again due to the strong deformations in the numerical mesh. However, a remarkable reduction in error with ASIM can be noticed in proximity of the aerofoil boundary. Because of the presence of artificial noise, a smaller window size, such is the case in ASVR, does not necessarily produce a better quality vector. Consequently, ASIM is able to yield measurements with higher accuracy by ensuring that all correlation windows respect the minimum window imposed by the user. This result is in accordance with the improvements already shown in literature [45] where a reduction of the error is expected in case of low curvature radius and images affected by artificial noise. Another area of smaller error in Figure 3.17a is on the outer edge of Chimera which is ascribed to the higher density of sampling points.

Figure 3.17b shows the error ratio for ASIMVR and presents similar features to ASIM. Because of artificial noise, the inherent characteristic of using smaller windows, which was beneficial in absence of noise, now becomes harmful. For this reason, the error of ASIMVR on the edge of the aerofoil reaches levels on par with ASVR. The same reduction in window size

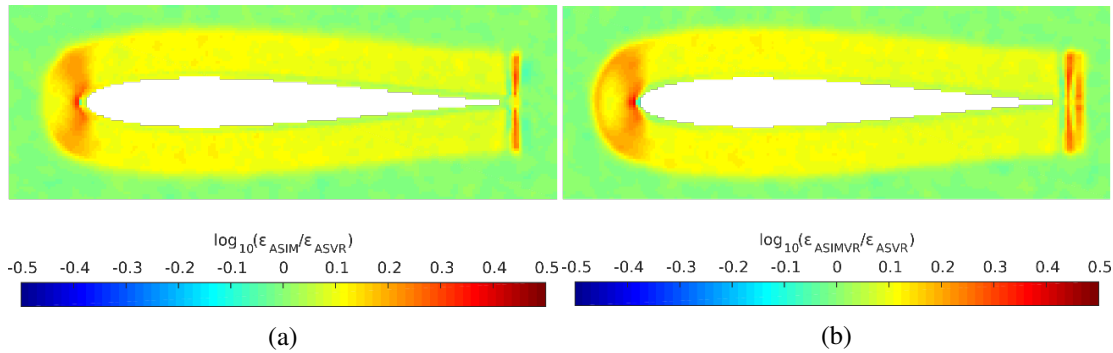


Figure 3.18: Comparison of displacement error between (a) ASIM and ASVR, (b) ASIMVR and ASVR. Number of iterations: 1. Correlation window size: 25. With image noise.

on the trailing edge due to the logical cut of the mask worsens the measurement precision. For the same reason, the error present on the outer area of the Chimera region is now negatively affected by the reduced window size and shows an increased level in Figure 3.17b compared to Figure 3.17a.

With the objective of deepening the understanding in the conduciveness of image mapping in PIV algorithms, the analysis of the Joukowski images has also been performed considering a single iteration thereby negating the predictor-corrector process. To allow the use of small correlation window sizes while maintaining a sufficient number of particle images per window, the maximum flow velocity magnitude was reduced to 1 pixel. Results are shown in Figure 3.18 for both ASIM and ASIMVR and present once again the typical patterns of the numerical mesh error. However, given the very strong reduction of the velocity gradient magnitudes due to the very small displacement, there seem to be no actual advantages in using image mapping anymore. In fact, in spite of the artificial noise, quasi-static correlation windows are rotated, stretched and deformed by the image mapping without bringing any reduction in the gradients of the velocity field. This finding is in accordance with the results shown in Figure 3.12c; the mere application of the image mapping process to a static displacement field amplifies the random fluctuation increasing the displacement error.

For the sake of completeness, a comparison with a structured Cartesian grid is also presented in Figure 3.19. The figure shows similar patterns to the previous adaptive sampling, with the only differences being patchy artefacts due to the non-uniform distribution of the sampling points. The reader should note that the previous analysis, based on the adaptive point distribution, does not depend on the type of sampling distribution adopted, but rather on the peculiar aspects of image mapping and its algorithmic implementations.

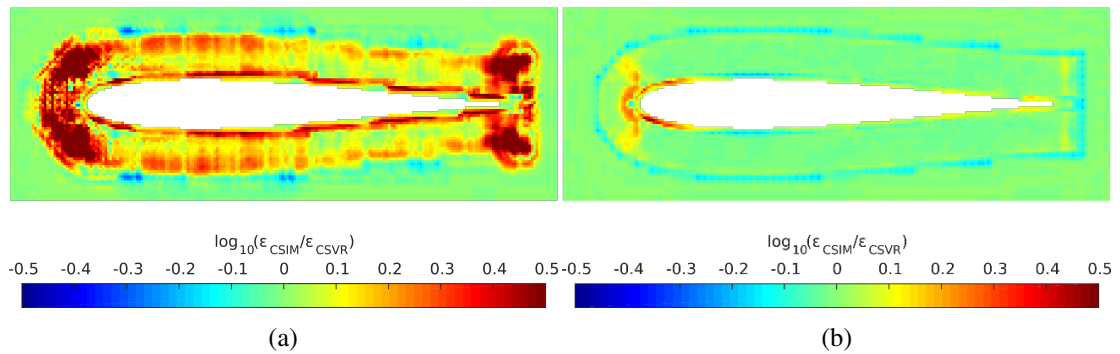


Figure 3.19: Comparison of displacement error between CSIM and ASVR. Number of iterations: 3. Correlation window size:  $90 \rightarrow 25$ . (a) No image noise, (b) with image noise.

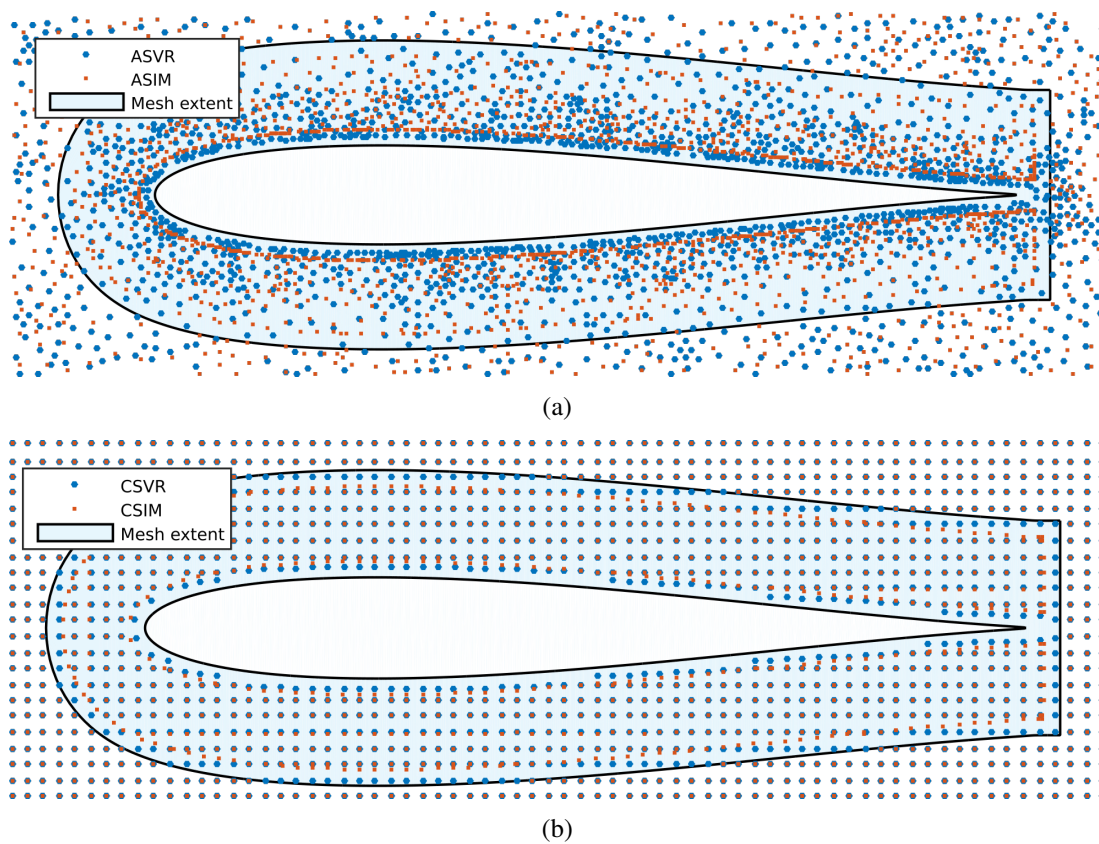


Figure 3.20: Distribution of correlation windows' centres the first iteration for (a) ASVR and ASIM and (b) CSVR and CSIM. Only by vector relocation can data be collected even closer to the airfoil than with image mapping.

### 3.6.4 Summary: feasibility of image mapping

The numerical assessment has indicated the applicability of image mapping not to be as simple and straightforward as suggested in previous works ([64],[71]). Instead, the final outcome of the measurement strongly depends on a case-by-case basis, including the geometric shape of the interface and details of the algorithmic implementation. Essentially, two dominant effects determine the degree to which image mapping can be beneficial; image deformation as a result of the imposed numerical mesh and the ability to maintain the image density in the vicinity of the object boundary.

Although the numerical mesh introduces a distortion of the particle images which is detrimental to the correlation accuracy as illustrated in Figure 3.14, depending on the alignment of the numerical mesh with the flow streamlines, the resulting artificial displacement gradients can be either constructive or unfavourable. In case of the cylinder flow presented in Figure 3.13 the mesh transformation straightens the curved streamlines in the logical plane, thereby minimising gradients. Contrarily, in the case of the Joukowski airfoil near the leading and trailing edge, the misalignment between the governing flow and imposed numerical mesh combined with the strong gradients in the Jacobian (Figure 3.12) led to a consistent deterioration of the PIV accuracy. Unfortunately, these effects cannot be quantified a-priori as the underlying flow field is exactly the subject of the analysis.

The results presented in paragraph 5.3 attest that image mapping does not generally yield an increase in accuracy, even when incorporated in advanced algorithms. Instead, the results suggest more simplistic interrogation methodologies to outperform those including image mapping. Only for very specific imaging and flow conditions marginal improvements could be attained by implementing image mapping. In the near vicinity of the Joukowski airfoil the ability of image mapping to avoid any overlap between the interrogation areas and the object meant that a more reliable cross-correlation could be achieved in the presence of image noise (Figure 3.17, Figure 3.19). However, this improvement was irrelevant in the absence of image noise (Figure 3.15, Figure 3.16). The potential gain in resolution consequently depends on two factors. First, the quality of the PIV images in proximity of the edges (i.e. severity of reflections, intensity of image noise, concentration of seeding, etc.). This can be partly influenced by adequate pre-processing methodologies (e.g. [60]). Second, the final correlation window size, which will typically involve trial and error. If the user selects a too large size to ensure a reliable correlation, no gain will be noticeable due to a too coarse resolution. Should the user opt for a too small correlation window size, independent of the analysis approach, cross-correlation will yield sporadic vectors.

## 3.7 Conclusions

The analysis of PIV images in vicinity of surfaces is typically hampered by a reduction in seeding density and the presence of light reflections, rendering the cross-correlation process unreliable. By constructing a body-conforming numerical mesh using the identified interface as boundary condition, overlap between interfaces and correlation windows can be completely eliminated. With image mapping intensity distributions are subsequently transformed into the curvilinear coordinate system converting the interface boundary into a straight line such that it can be excluded from the interrogation process, in theory circumventing the associated error.

Previous works have already shown the application of this method on relatively easy test cases, proving the feasibility of image mapping on sinusoidal-like surfaces and cylinders. However, the general applicability of image mapping for curved geometries has never been scrutinised, nor has the performance of image mapping ever been compared with alternative PIV interrogation methodologies. For these reasons, this chapter provides an in-depth analysis of the feasibility of image mapping in PIV, from the generation of boundary conditions from logical masking images to the construction of numerical meshes through to the problematic of image re-interpolation. For each stage, all potential error sources have been investigated and substantiated by assessments on synthetic test cases. In addition, improvements are proposed to negate some of the errors inherent to image mapping in an attempt to truly assess the general applicability of image mapping for PIV image analyses.

The generation of a proper numerical mesh for image mapping has been proven to be one of the most influential parts of the process. Divergence and convergence in characteristic mesh lines, quantified by the transformation Jacobian, not only introduces artificial displacement gradients in the mapped images, but also causes a distortion of the mapped particle images negatively impacting cross-correlation accuracy. To reduce adverse effects an enhanced resampling procedure has been suggested to restore the circular shape of mapped particle images. Nevertheless, besides errors originating from the coordinate interpolation inherent to image mapping, highly curved surfaces have been shown to introduce an additional bias error that, depending on the particle image diameter, can be strongly amplified times when the radius of curvature is as low as 10 pixels.

Numerical assessments involving the analytical flow around a Joukowski aerofoil have shown that image mapping can provide improvements in measurement accuracy only under very specific conditions. The ability to maintain a constant window size and seeding density in a correlation window in vicinity of the aerofoil allowed a reduction of the error in the areas of the boundary characterized by a lower curvature. However, surfaces of high curvature are always affected by strong image deformation and image mapping should therefore be avoided in these cases. Moreover, error improvements were only found in the presence of artificial

noise. This is to be expected since the increased error near surfaces is often due to a loss of seeding density and increase in background reflections. In absence of these circumstances, the advantages of using image mapping are strongly limited and a vector relocation technique, implemented in more standard and less computationally intense routines, could be sufficient for the analysis.

The benefit of image mapping was thus shown to be dependent on two specific conditions; the necessary alignment of the mesh lines with flow streamlines to avoid the generation of additional velocity gradients and adequate interrogation parameters near the object (correlation window size). These requirements have nearly always been fulfilled in existing literature adopting image mapping, which explains the relative success of the method. Both require a-priori knowledge of the underlying flow field and optimal processing parameters, which are exactly the unknowns in the performed image analysis. Considering the increased computational cost and added sources of error, the potential gain from implementing image mapping in conventional PIV interrogation schemes must therefore be evaluated on a case-by-case basis. When dealing with strongly curved geometries or when streamlines are not parallel to the interface, image mapping is without doubt ineffective and methodologies invoking adaptive image processing or particle tracking will warrant more favourable results.

# Chapter 4

## Optical flow

### 4.1 Abstract

This chapter investigates the use of an optical flow technique, the Lucas-Kanade tracker (LKT), to analyse particle displacements in PIV images. The choice of LKT is dictated by its ability to model displacement fields with any kind of polynomial function, with the potential to alleviate the limitations of cross-correlation in case strong in-plane gradients. Previous results found in the literature have already shown that optical flow techniques are able to accurately reconstruct the velocity field even in case of large gradients [63]. However, images adopted were often synthetic or produced in ideal experimental conditions, preventing any assessment of the optical flow reliability in more realistic lighting conditions. The attention of this chapter is focussed on the effect that different implementations of LKT can have on the outcome of the PIV analysis: different alternatives are scrutinised based on their complexity and behaviour, number of parameters involved and computational effort. In spite of the attracting premises, observations and analyses proposed in this chapter will show that the added computational time and the additional complexity in implementing LKT, constitute a strong impediment for its practical application to PIV.

### 4.2 Introduction

The choice of cross-correlation for the analysis of PIV images is driven by its speed, robustness and well-known mathematical properties [117]. However, one of its limitations is that it only provides a single translation per interrogation area, whose value can be assimilated to the average shift within the window. Because of this behaviour, cross-correlation is affected by a modulation effect similar to a moving average [8] limiting the spatial resolution of the measurement and causing inaccurate results in case of strong in-plane gradients. The intensity

of the smoothing depends on the size of the interrogation region: the wider the area, the more intensive will be the smoothing and the worse will be spatial resolution. Smaller interrogation regions allow a higher spatial resolution but they suffer from the problem of loss of particle image pairs [4]. A common suggestion is to impose a window size of at least four times the displacement magnitude [120].

The problem of correlation window sizes and their effect on velocity gradients was examined in [89], where an iterative multi-grid approach was proposed to mitigate the modulation effect. The solution suggested is to analyse the same pair of images multiple times with different window sizes: starting with a wide window, displacements are used to deform the images and predict velocities for smaller interrogation windows. This approach allows a trade off between the use of small and big interrogation regions, improving the behaviour of cross-correlation in case of strong velocity gradients.

Another peculiarity of cross-correlation is that it only provides integer values of the displacement, and additional peak-fitting solutions must be involved to estimate the sub-pixel displacement. This compartment brings to an unwanted bias of the measurement towards integers, known as peak-locking [114], which is particularly severe in case of small sized particle images. Several solutions were proposed in the last decades to alleviate this problem and enhance the measurement resolution. The most common is a three-points Gaussian fit of the correlation peak to extract its exact position with a sub-pixel accuracy [120]. This solution, however, still introduces a peak locking error in the measurement [18]. A more advanced solution is proposed in [66], where a nine-points Gaussian fit is adopted. This procedure accounts for possible deformations of the correlation peak and involves an explicit solution to the peak fitting problem.

An interesting alternative to analyse PIV images, which has never been fully investigated, is the use of optical flow techniques [12]. As it will be shown later in this chapter, these techniques estimate the optical flow between two interrogation areas producing a pixel-dense displacement field, unrestricted to integer values. For this reason, they constitute an attractive alternative to cross-correlation. The idea of using optical flow to analyse PIV images is not new, and previous works in literature have already shown its successful application ([76],[17]). The contribution of this chapter is not meant to be a complete analysis of optical flow techniques applied to PIV, but rather an investigation of a specific technique, the Lucas-Kanade tracker (LKT) [49]. The attention will be focused on the implications of using LKT as an alternative to cross-correlation, to improve the resolution of PIV in case of strong in-plane displacement gradients.

### 4.3 Methodology

Given a sequence of consecutive PIV images, two interrogation areas are extracted: a template image  $T(\underline{x})$  and an input image  $I(\underline{x})$ . These areas are the equivalent of the correlation windows used in standard PIV algorithms. The LKT estimates the warping  $\underline{W}$  that is necessary to match the template image with the input image. The warping  $\underline{W}$  is a parametrized function that depends on a set of  $n$  parameters  $\underline{p} = (p_1, \dots, p_n)$  and the pixel position  $\underline{x} = (x, y)$ . The choice of the warping function can vary according to the user's necessity, but for simplicity we can assume a linear warping function:

$$\underline{W}(\underline{x}, \underline{p}) = \begin{pmatrix} (1 + p_1)x + p_3y + p_5 \\ p_2x + (1 + p_4)y + p_6 \end{pmatrix} \quad (4.1)$$

The parameters  $\underline{p} = (p_1, \dots, p_6)$  describe the unknown displacement between  $T$  and  $I$ . Those parameters are estimated by minimizing the sum of the squared differences between the image  $T$  and the warped image  $I(\underline{W})$ :

$$\sum_{i=1}^{N_p} [I(\underline{W}(x_i, \underline{p})) - T(x_i)]^2 \quad (4.2)$$

where  $N_p$  is the total number of pixels of  $I$ . Image intensities  $I$  need to be calculated at the positions  $\underline{W}$ , which do not necessarily coincide with the discrete locations of the pixels. For this reason, interpolation is required to produce image values at non-discrete pixel positions. The minimization of equation 4.2 constitutes a non-linear problem: in fact, there is no linear relation between image intensities  $I$  and the pixel locations  $\underline{x}$ . To simplify the problem, the LKT algorithm starts from a known value of  $\underline{p}$  (which is usually set to zero) and tries to solve for small increments  $\Delta\underline{p}$  the equation:

$$\sum_{i=1}^{N_p} [I(\underline{W}(x_i, \underline{p} + \Delta\underline{p})) - T(x_i)]^2 \quad (4.3)$$

Knowing  $\Delta\underline{p}$  from equation 4.3, the solution  $\underline{p}$  is corrected as  $\underline{p}_{new} = \underline{p}_{old} + \Delta\underline{p}$ . The process is repeated iteratively until the correction  $\Delta\underline{p}$  becomes smaller than a threshold (or the number of iterations  $N_{it}$  exceeds the maximum set).

In order to iteratively solve for the parameter  $\underline{p}$ , equation 4.3 needs to be linearised and a first order Taylor expansion is adopted. Given the Jacobian of the transformation  $\partial\underline{W}/\partial\underline{p}$  and the gradient of the image  $\nabla I$ , an algebraic equation for  $\Delta\underline{p}$  can be written and a numerical solution for  $\underline{p}$  can be found:

$$\Delta \underline{p} = H^{-1} \sum_{i=1}^{N_p} \left[ \nabla I \frac{\partial W}{\partial p} \right]^T [T(x_i) - I(W(x_i, \underline{p}))] \quad (4.4)$$

where  $H$  is the Hessian matrix:

$$H = \sum_{i=1}^{N_p} \left[ \nabla I \frac{\partial W}{\partial p} \right]^T \left[ \nabla I \frac{\partial W}{\partial p} \right] \quad (4.5)$$

The LKT algorithm consists of iteratively solving equation 4.5 and updating the parameter  $\underline{p}_{new} = \underline{p}_{old} + \Delta \underline{p}$  through the following steps:

1. Image  $I$  is warped using the warping function  $\underline{W}(x_i, \underline{p})$
2. Evaluate the difference  $T(x) - I(\underline{W}(x_i, \underline{p}))$
3. Apply the warping to  $\nabla I$
4. Calculate the Jacobian  $\frac{\partial W}{\partial p}$
5. Calculate  $\nabla I \frac{\partial W}{\partial p}$
6. Evaluate the Hessian from equation 4.5
7. Evaluate the correction  $\Delta p$
8. Update  $p$  with the correction  $\Delta p$

The content of this chapter will focus on the implication of adopting LKT to PIV.

### 4.3.1 Choice of warping function

The choice of the warping function  $\underline{W}$ , typically assumed linear as per equation 4.1, can be adjusted to higher order functions to better describe high gradient flows and complex velocity fields. The use of higher order warping functions is not new to the computer vision ([94], [19]), but it has never been fully investigated for the application to PIV images. An example of higher order warping function is a quadratic transformation:

$$\underline{W}(x, \underline{p}) = \begin{pmatrix} p_1 x^2 + p_2 y^2 + p_3 xy + p_4 x + p_5 y + p_6 \\ p_7 x^2 + p_8 y^2 + p_9 xy + p_{10} x + p_{11} y + p_{12} \end{pmatrix} \quad (4.6)$$

The use of a higher order warping function should, in theory, allow a better description of the flow in case of high intensity gradients [63], however, the presence of quadratic terms

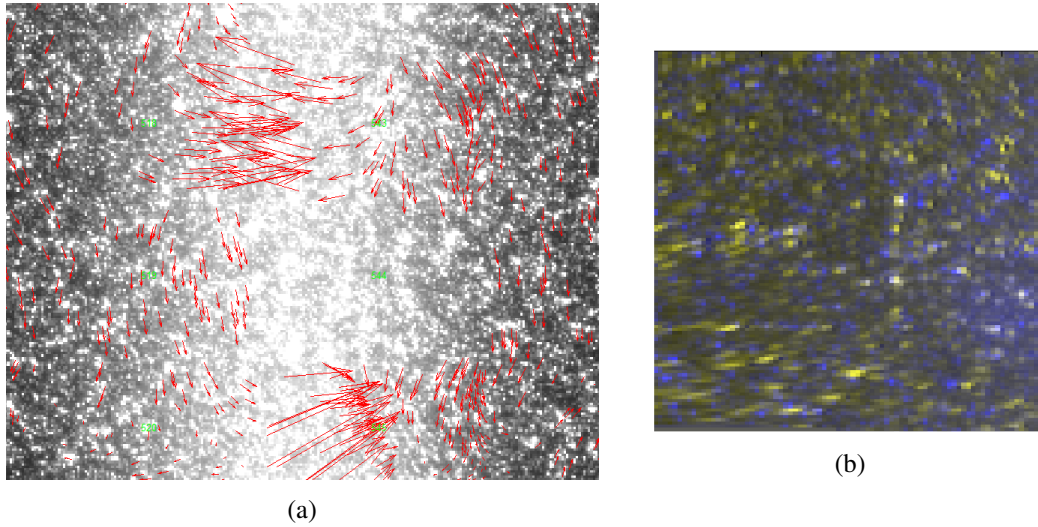


Figure 4.1: Application of LKT with parabolic warping function to experimental images in (a) case of strong image gradients (red arrows depict the estimated vectors) and (b) complex velocity field (the two interrogation windows are overlapped in blue and yellow in a single colour image).

in equation 4.6 was found to heavily affect the stability of the iterative process described in Section 4.3. This stability problem depends on the quality of the particle images, the velocity field, the interrogation window size, the noise and the presence of background. An example of application of quadratic warping function to experimental images is presented in Figure 4.1a. The image shows a few interrogation areas (centres ID numbered in green) of experimental images subjected to strong light gradients. Images were analysed with the parabolic warping function of equation 4.6 and sparse vectors were extracted from the dense displacement field for displaying purpose. The image shows that the parabolic displacement is correctly extracted on the left and right areas of the image, but wrong displacements are estimated in the central part, where the LKT is deceived by the strong light gradient.

An example of warping instability due to the complexity of the flow is shown in Figure 4.1b, where two interrogation windows are overlapped at the final stage of LKT. The blue image is fixed, the yellow image is being deformed to find the displacement and the white colour shows overlap. The figure shows that the central/right area of the image is properly matched, while the bottom left corner is deformed in a completely wrong way (notice the strong elliptical shape of the warped particles). This behaviour is due to the higher order of the warping function, that allows a complex description of the displacement field also when it fails, producing mixed good/bad velocity measurements. Unfortunately, discerning good and bad areas of the displacement field from interrogation areas like Figure 4.1b is a very difficult task.

Due to its highly unpredictable behaviour, the application of parabolic warping functions to experimental images is very challenging and must be implemented with strong attention to

configuration parameters (the discussion of LKT parameters is proposed in Section 4.4.4). A strategy adopted to improve the stability of LKT with parabolic warping functions relies on its displacement initialization. A non-zero displacement guess, used as initial value for  $\underline{p}$ , can be estimated using lower order warping functions or cross-correlation.

A simpler alternative to equations 4.6 and 4.1 is a constant warping function:

$$\underline{W}(\underline{x}, \underline{p}) = \begin{pmatrix} x + p_1 \\ y + p_2 \end{pmatrix} \quad (4.7)$$

In spite of its simplicity and low computational effort, equation 4.7 suffers from the same problem as cross-correlation, as it produces a single vector per interrogation window and it is not suitable to describe complex displacement fields. Moreover, the lower order of this model does not necessarily improve the stability; in fact, in case of high gradients (i.e. shear flow), the solution of a constant warping function may oscillate around two correct solutions, while a linear or parabolic warping functions would converge on the correct solution. The choice of the right warping function depends on the complexity of the flow, the size of the interrogation area, the amount of noise and other parameters which are left to the user's expertise. On top of this, combinations of different warping functions can also be adopted for different iterations of the displacement evaluation. However, the use of constant, linear and parabolic warping functions, combined together, introduces an even further level of complexity in the algorithm that renders its stability and reliability almost impossible to predict.

### 4.3.2 Pyramidal implementation

The linearisation applied to equation 4.3 to iteratively solve the parameter  $\underline{p}$  necessitates the hypothesis of small displacements ( $< 1$  pixel). Typical values of particles motion in PIV are in the range of 8-12 pixels or more, which would be unsuitable for this application. However, the problem of larger displacements can be dealt with through a pyramidal implementation of the LKT, which is described in [11]. The solution proposed is to sub-sample the images, so that a displacement of  $u$  pixels becomes  $u/2$  if the image is sub-sampled once, and  $u/2^N$  for  $N$  consecutive sub-samplings. In this way, a typical displacement of 10 pixels will be reduced to less than one pixel with  $N = 4$  sequential sub-samplings. The pyramidal LKT begins the motion analysis from the highest level of the pyramid (the most sub-sampled image): once (small) displacements are evaluated at this level, the solution is propagated as initial guess to the previous level of the pyramid, until the final image is analysed and the displacement is found. In order to correctly propagate information between the pyramid levels, images must be convoluted with a Gaussian function before each sub-sampling.

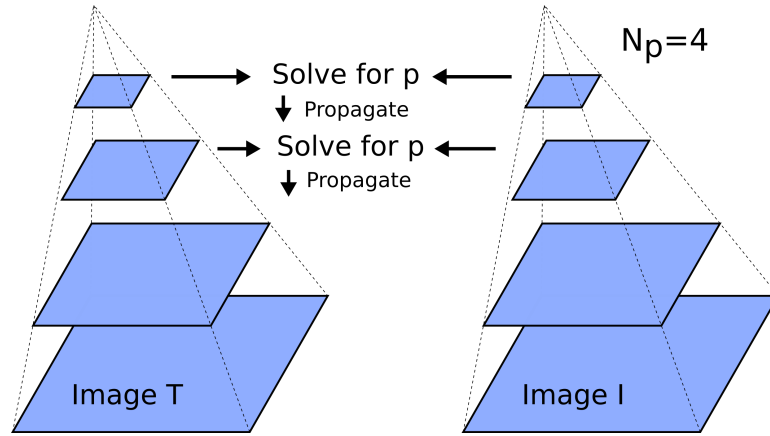


Figure 4.2: Illustration of the pyramidal approach for the Lucas-Kanade algorithm.

The application of the pyramidal approach to PIV poses some restrictions on the choice of adopted interrogation window size. In fact, if a displacement of  $u = 20$  pixels is analysed, a minimum of 5 pyramid levels are necessary to reduce the displacement to less than one pixel. However, if a window size of  $WS = 80$  pixels is selected, the sub-sampled window will be reduced to  $WS_{\text{sub}} = 80/2^5 \approx 3$  pixels, which is completely unsuitable for any application. In fact, image gradients necessary for LKT need to be estimated in the sub-sampled windows and a minimum window size of 7-11 pixels is necessary to avoid errors and instabilities. A possible solution to this limitation is the implementation of a multi-grid algorithm for LKT, as described later in this chapter.

### Cross-correlation as first guess

A different approach from the pyramidal LKT was also considered to deal with high intensity displacements ( $> 20$  pixels). Cross-correlation can be used to obtain a velocity guess for LKT to initialise  $\underline{p}$ . Although this solution proved to be effective in some cases (i.e. high intensity displacement with no gradients), it showed similar difficulties as standard PIV, when strong gradients are associated to high intensity displacements [115]. As it will be shown in Chapter 5, the best solution in this case is to use cross-correlation and resolve multiple displacements per correlation window by analysing multiple correlation peaks.

### Multi-grid implementation

The implementation of optical flows for PIV analysis in case of strong gradients and high intensity displacements was investigated even further with a multi-grid implementation [89] of LKT. In this case, LKT was adopted instead of cross-correlation to estimate the velocity field in each interrogation area with a predictor-corrector approach. The first problem faced for this

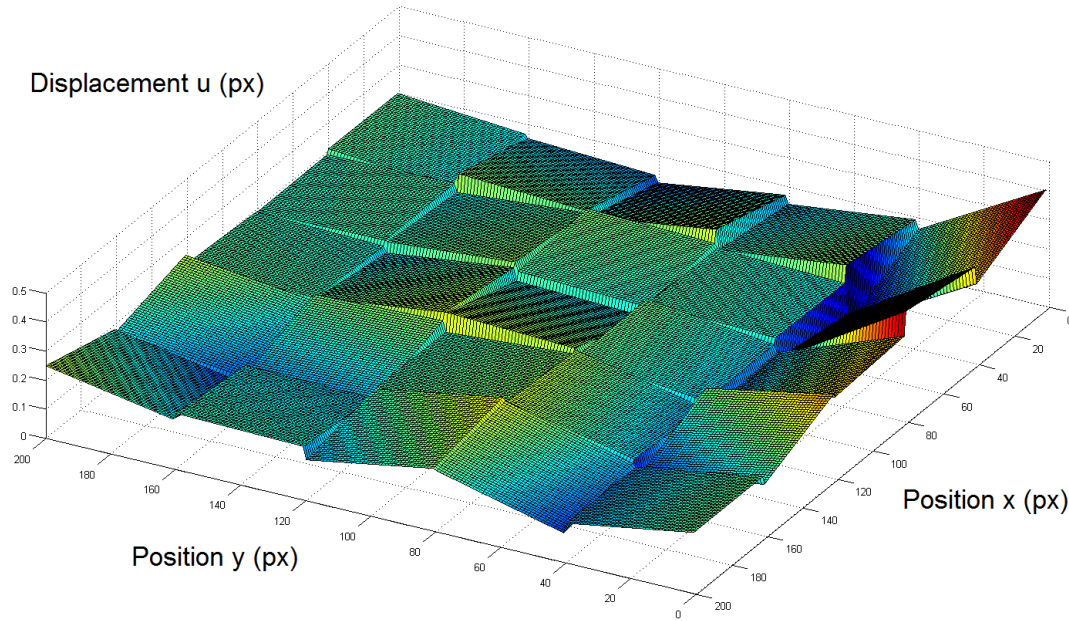


Figure 4.3: Velocity displacement predictor ( $u$  component) for interrogation windows analysed with LKT and linear warping function.

implementation was the interpolation of displacements. In fact, cross-correlation produces a single displacement vector per correlation window and the entire displacement field is interpolated on a pixel grid. With optical flow methods, each correlation window is resolved for each pixel. If the interrogation windows are not overlapping, the final displacement predictor will be discontinuous on the edges of the windows, as shown in Figure 4.3 for a linear warping function. This discontinuity can be very strong in case of parabolic warping functions and it must be resolved before interpolating the images. In this work, the solution adopted was a cubic smoothing spline [13]; although more efficient solutions are probably available, the implementation of LKT in a multi-grid approach will be shown to be not suitable for practical applications of PIV altogether.

Results obtained with this implementation of LKT were comparable with standard PIV. Although the use of a parabolic warping function can produce a higher spatial resolution in some specific cases tested (i.e. sinusoidal displacement field), LKT requires an excessive fine tuning of parameters when applied to PIV images (see Section 4.4.4). Moreover, the application to experimental images proved to be extremely challenging due to the presence of noise, background images, loss of pairs and similar problems that were not tested with synthetic images. Finally, in spite of the comparable results obtained [63], the computational time required to analyse a single pair of images results as one or more orders of magnitude higher than a standard FFT-based cross-correlation multi-grid algorithm, and its application is therefore strongly limited.

## 4.4 Reliability

### 4.4.1 Measure of quality

One of the main disadvantages of using an optical flow technique to measure the particle displacements for PIV is the lack of a reliable measurement of quality. When cross-correlation is used, the quality of the correlation peak is defined by the signal-to-noise ratio (SNR), which is the ratio between the maximum and the second highest peaks of the correlation map. Values of SNR close to the unity are indicative of uncertainty in the displacement estimation that should be discarded [50], while high values of SNR can be used to estimate the quality of the measurement [123]. The aim of optical flow techniques is to minimise the disparities between two images by iteratively adjusting the displacement field with a correction  $\Delta \underline{p}$ . When this correction is lower than a threshold, the algorithm stops and the displacement field is outputted. Three possible measurements of quality can be extracted from this process: the number of iterations necessary to converge  $N_{it}$ , the image disparity  $I_d$  and the norm of the correction  $dp = |\Delta \underline{p}|$ . The three parameters are connected with each other (i.e. a lower value of  $N_{it}$  may produce higher disparities  $I_d$ ) and none of them can be used as a single measure of quality. In fact, the behaviour of LKT is strongly unpredictable and the solution  $\underline{p}$  might oscillate around the correct solution: in such a case, the correction  $dp$  will never converge to zero but will oscillate between strongly positive and negative values, terminating with a high number of iterations  $N_{it}$ . If  $N_{it}$  or  $dp$  were to be used as measures of quality, the oscillating solution would be discarded even though the measurement is correct. The use of image disparities  $I_d$  was also considered as a measure of quality, although absolute levels of  $I_d$  are difficult to compare. In fact, if images were perfect and had the same intensity levels, a value of  $I_d$  close to zero would be an indication of good displacement. Unfortunately, the intensity of particle images can differ from two consecutive images, due to physical differences in the light source (non-perfect PIV laser cavities) and due to the cross-plane motion of the seeding particles. Therefore, similar values of  $I_d$  could indicate a good or bad displacement for different windows. A similar behaviour can be observed in Figure 4.4a and b, where a pair of PIV images presents a non homogeneous light intensity between the two frames. If the particles in the two frames were perfectly overlapping, the image disparity should ideally be zero everywhere. However, the upper region of Figure 4.4a presents a spurious background which is absent in Figure 4.4b, producing a higher image disparity in that region.

The problem of quantifying the reliability of displacements is very common in computer vision, where this topic is known as quality of features to track. One of the most adopted solutions [95] relies on the numerical definition of the parameter  $\Delta \underline{p}$  expressed in equation 4.4. Solving for displacements requires inverting the Hessian matrix  $H$ , described in equation 4.5. A condition for matrix  $H$  to be invertible, is that it has to be well-conditioned: the solution

proposed in [95] is to discern good from bad solutions by looking at the eigenvalues of  $H$ . If the minimum of the eigenvalues  $\lambda$  is higher than a threshold, the interrogation window is accepted. While this expedient can be implemented to discern windows containing particle images from low image-gradient areas, it is still insufficient to quantify the quality of the displacement for PIV, as the values of  $\Delta p$  could converge on a wrong solution (see Figure 4.1b).

#### 4.4.2 Image background

When PIV images are recorded in non-ideal conditions (i.e. non-constant laser intensity, non-dark background, presence of light reflective interfaces), background intensities and image artefacts may appear with the seeding particles. Figure 4.4a and b show an example of this case: two sequential images of a vortex are presented, where a white background only appears in the first image (white shade on the top edge). The gradients for these images, which drive the solution of LKT displacement, are presented in Figure 4.5a and b, and show that the variation of image intensity due to the seeding particles is stronger than the variation due to the background. If LKT is applied without pyramidal approach, the algorithm would fail because the displacement is about 8 pixels. However, when pyramidal approach is adopted, images need to be convoluted with a Gaussian and sub-sampled (see pyramidal approach in Section 4.3.2). Because of the convolution, the effect of the background on the image gradients becomes very strong (Figure 4.4c-d). Figure 4.5c-d show that the gradients of the convoluted images are dominated by the background, rendering the detection of the particles motion extremely challenging.

This problem can be mitigated by filtering the images before processing them. A high pass filter can be adopted, prior convolution, to remove any low intensity gradient from the image. Alternatively, a background removal algorithm [60] can also be implied to alleviate this problem. Figure 4.6 shows an example of high pass filter applied to the vortex images. Arrows in red show the result of the first guess of displacements (highest pyramid level) evaluated with LKT and amplified for displaying purpose. The initial guess for the filtered images looks more in agreement with the physics of the flow: displacements for the non-filtered images are particularly wrong near the top and bottom edges of the field, because of the aforementioned artificial gradients.

#### 4.4.3 Image disparity

Another problem that needs special attention when optical flow algorithms are implemented, is the effect of intensity disparity between steady particle images. As already mentioned in the previous section, the intensity of particle images can be different between two frames (i.e. laser cavity inequalities, out of plane motion, etc.). Since LKT is driven by image gradients,

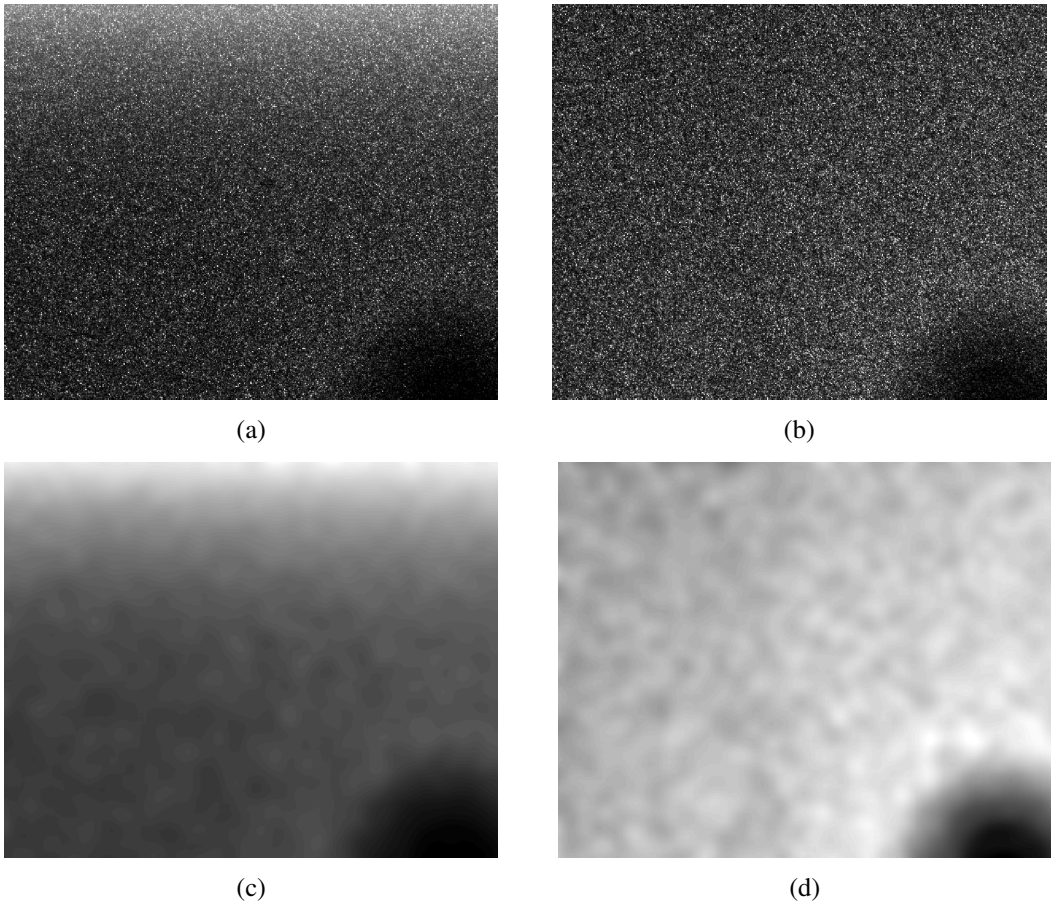


Figure 4.4: Two sequential PIV images of a vortex (a-b). Images convoluted with a Gaussian before being sub-sampled for the pyramidal approach (c-d)

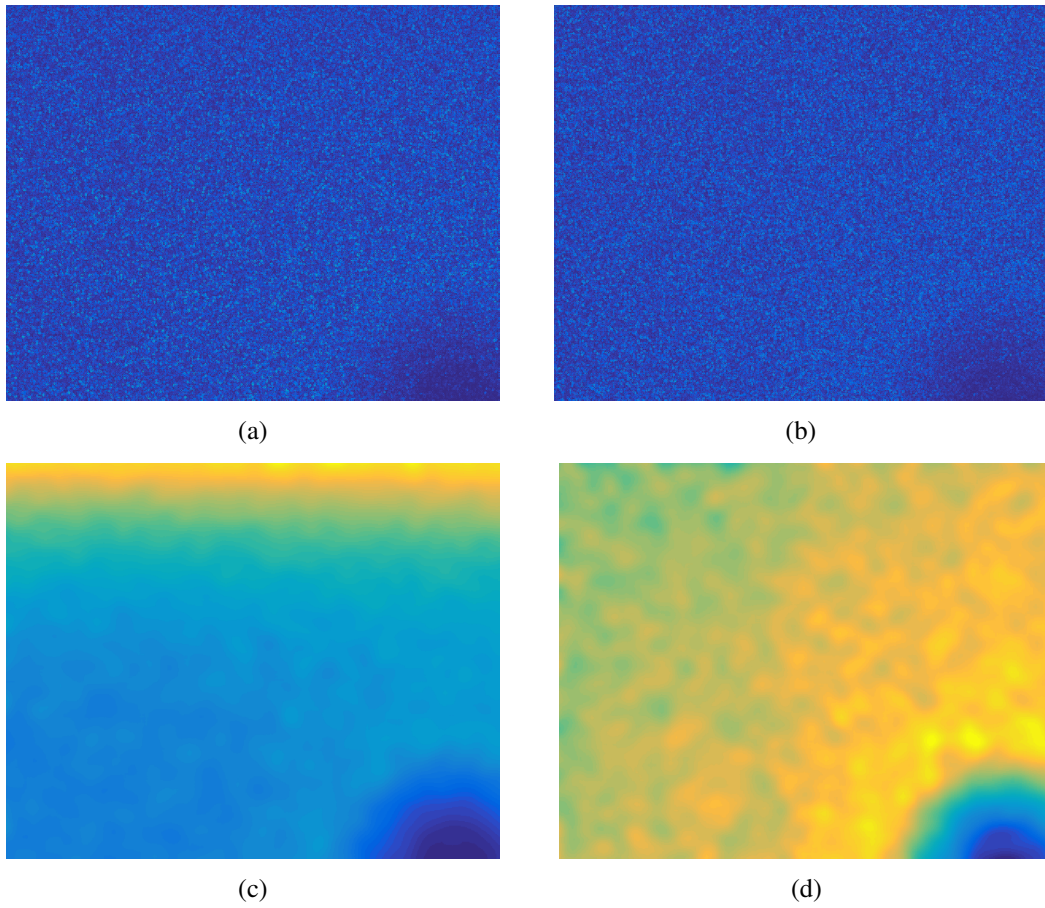


Figure 4.5: Magnitude of gradients pertaining the images in Figure 4.4.

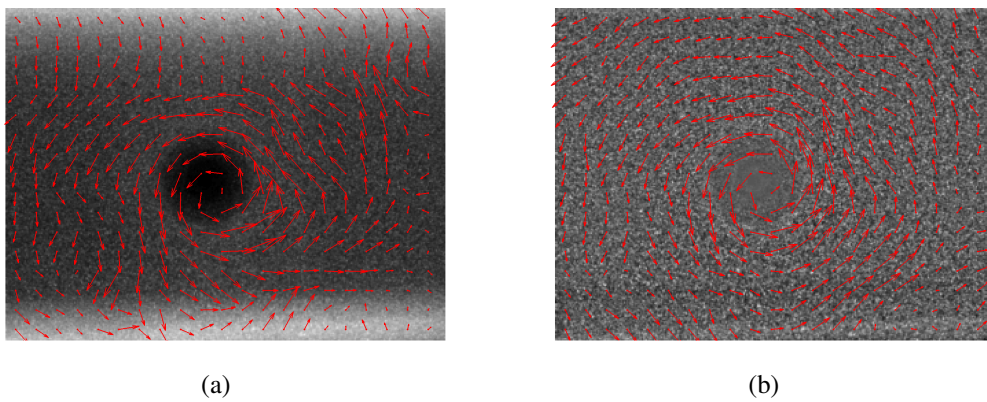


Figure 4.6: Displacement field for the highest level of the pyramidal LKT in case of (a) original non-filtered images and (b) high-pass filtered images.

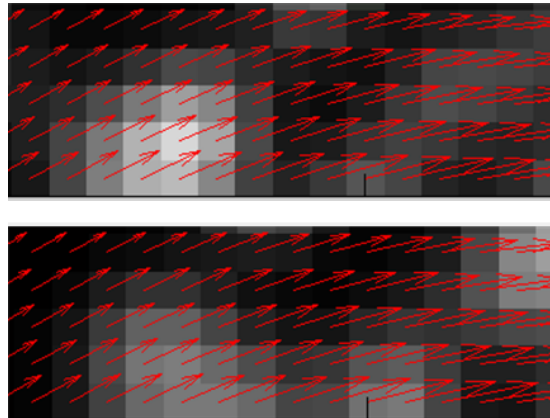


Figure 4.7: Detail of interrogation windows containing steady particles with varying image intensity. Red arrows show the wrong optical flow estimated by LKT, scaled for displaying purpose.

this difference in image intensity can give rise to artificial erroneous displacements. Figure 4.7 shows an example of this problem, where two consecutive images are perfectly overlapping. In spite of the perfect match between the two images, the optical flow estimated (red arrows) is wrong. In fact, the particle image on the left of the first image has a similar light intensity to the particle on the right of the second image, therefore LKT tries to minimise this disparity by warping the first image to the right.

Also in this case, the problem of image disparities can be mitigated by pre-processing the images. A local histogram equalization, for example, can equalize the intensity of particle images reducing its effect on the displacements. However, this kind of image pre-processing can affect the quality of the sub-pixel resolution, besides contributing to the additional computational effort of algorithm.

#### 4.4.4 User defined parameters

The configuration parameters necessary to set up a standard PIV algorithms are typically the windows size (initial  $WS_{init}$  and final  $WS_{final}$ ), the number of predictor-correct iterations and some threshold related to the quality of images (SNR threshold, vector validation residual, etc.). Those parameters are very common in every available PIV software and are well known to the experienced PIV user. Although additional settings like the use of weighting functions [69], adaptive sampling [105] or sub-pixel algorithm [120] may have strong effect on the quality of the measurement, they do not affect the overall behaviour of the algorithm, which is almost always based on cross-correlation. When optical flow techniques are implemented, the user defined parameters are very different and their effect on the behaviour of the PIV algorithm can be unexpected.

The most important parameters to set up in an LKT algorithm are: the windows size  $WS$ , the maximum number of iterations  $N_{it}$  (not to be confused with predictor-corrector iterations, see Section 4.3), the norm  $dp$  of the minimum correction allowed for the displacement  $p$  (see Section 4.3), the warping function  $W$  (constant, linear, parabolic or combinations of them) and the number of pyramid levels  $N_p$ . As already described in this chapter, all of these parameters can have a strong influence on the outcome of the analysis and need to be fine-tuned according to specific test cases. For example, a velocity field with strong gradients but small displacements, like a high frequency sinusoid of one pixel amplitude, could easily be analysed with  $N_p = 1$  and a parabolic warping function, although values of  $dp$  and  $N_{it}$  should be adjusted by trial and error according to the level of image noise. Instead, the same sinusoidal field with an amplitude of 8 pixels would necessitate much more attention on  $N_p$ , that should be adjusted again by trial and error, together with the windows size  $WS$ .

In addition to the choice of the LKT parameters, further decisions must be taken to render optical flow suitable for PIV image analysis: the choice of the warping function (or a combination of them), the multi-grid parameters (if implemented), the pre-processing filters, and so forth. The choice of these settings can be very complicated, it must be adapted to specific images and no general solution was found in the current investigations. This complexity of the algorithm, together with the additional computational cost (to be discussed hereafter), render the choice of optical flow techniques less attractive compared to standard cross-correlation.

## 4.5 Computational cost

The computational effort of LKT applied to PIV analysis is very hard to estimate and strongly depends on the type of implementation adopted (i.e. warping function, pyramidal, multi-grid...) and the parameters chosen. Based on experience, on average, the computational effort of the LKT is comparable to direct cross-correlation<sup>1</sup>. Figure 4.8 shows the computational time necessary to estimate a constant displacement field of  $u = 1$  pixel in an interrogation window of variable size from 16 to 128 pixels. LKT was tested with two sets of parameters:  $N_{it} = 10$ ,  $dp_{min} = 0.01$ ,  $N_p = 1$  (blue curve) and  $N_{it} = 100$ ,  $dp_{min} = 10^{-8}$ ,  $N_p = 1$  (red curve).

Results in Figure 4.8 show that for small window sizes (less than 32 pixels) direct cross-correlation and cross-correlation with FFT perform equally, with LKT (blue) being 3 to 4 times slower. For bigger window sizes, correlation evaluated with FFT can be up to 10 times faster than direct cross-correlation, and 7-8 times faster than LKT (blue). When the threshold for LKT is adjusted from  $dp = 0.01$  to  $dp = 10^{-8}$ , the computational time increases by 3 to 4

<sup>1</sup>The reader should note that while the computational time of LKT is comparable to direct cross-correlation, modern computers can perform cross-correlation through FFT, which is about one order of magnitude faster. This speed improvement is not not achievable with LKT.

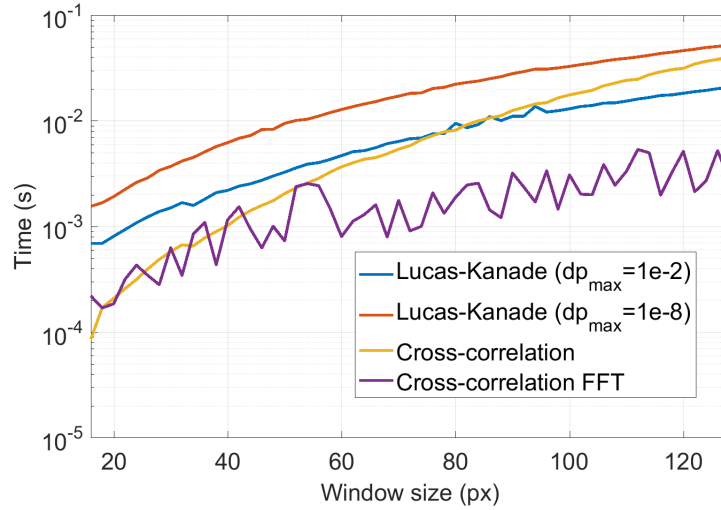


Figure 4.8: Comparison of computational time for Lucas-Kanade and cross-correlation (direct and FFT), for an interrogation window of variable size and a synthetic image describing a displacement of 1 pixel.

times. In spite of the higher precision for the solution  $\underline{p}$ , the final accuracy of the displacement field remains in the order of 0.01 pixels. This result introduces an additional complication when implementing LKT for PIV. In fact, the parameter  $dp$  should be optimised in order to get the best accuracy possible, yet maintaining the minimum computational time.

The reader should note that these results must be considered with caution, as they only apply for a single correlation window and a constant displacement field. Higher intensity amplitudes require additional pyramid levels  $N_p$  for LKT and potentially a higher number of iterations to resolve the displacement. Moreover, the implementation of certain pre-processing techniques, which might be essential for LKT to work, will exponentially increase the computational time, rendering the application of optical flow non feasible for practical applications.

## 4.6 Conclusions

The use of cross-correlation for the analysis of PIV images poses severe limitations to the detection of displacement fields in case of strong in-plane gradients. Optical flow based techniques offer a tempting alternative thanks to their peculiar ability to describe the flow between two interrogation areas with higher order functions. This chapter investigated the implementation of a specific optical flow technique, the Lucas-Kanade Tracker, for its application to the analysis of PIV images.

The choice of the warping function to model the flow displacement was shown to have a strong impact on the stability of the algorithm: while quadratic functions should yield a higher

spatial resolution, the presence of quadratic terms makes the LKT very unstable and unpredictable. The adoption of a constant function as initial guess for the linear or quadratic cases was considered too, but the outcome of the solution was observed to be very erratic and dependant on the image conditions. Different implementations of LKT were proposed, including a pyramidal approach to deal with high intensity displacements, the use of cross-correlation to estimate the first guess of the displacement and a multi-grid implementation of LKT. All the solutions tested showed comparable results with standard cross-correlation but with different computational costs and the introduction of additional user-defined parameters. The latter is of particular importance since no general methodology exists to select optimal parameters, and the wrong choice of settings can produce completely wrong results or exceptionally high computational times.

One of the main problems observed in the implementation of LKT was reliability. In fact, in spite of the good results shown in controlled conditions (synthetic images), its application to experimental images was observed to strongly depend on the quality of images, background, noise, image disparity, loss of pairs, etc.. Moreover, the use of LKT prevents the quality of the measurement from being reliably quantified. While the SNR provides a good indicator for cross-correlation based techniques, none of the parameters tested for LKT (such as norm of  $dp$ , image disparity...) provided a reliable indicator of quality.

The general application of LKT to experimental PIV images was thus observed to be very challenging. The additional complexity of LKT, and the unpredictability of the results, especially when contrasted with the speed and simplicity of a cross-correlation based PIV algorithm, renders the practical application of LKT for PIV image analysis very complicated and non-advised for its general use.

# Chapter 5

## Multiple-peak PIV

The content of this chapter was submitted to the journal *Experiments in Fluids* with the title “On dealing with multiple correlation peaks in PIV”. The paper was accepted and, at the time of writing, it is currently being revised with minor corrections.

### 5.1 Abstract

A novel algorithm to analyse PIV images in the presence of strong in-plane displacement gradients and reduce sub-grid filtering is proposed in this chapter. Interrogation windows subjected to strong in-plane displacement gradients often produce correlation maps presenting multiple peaks. Standard multi-grid procedures discard such ambiguous correlation windows using a signal to noise (*SNR*) filter. The proposed algorithm improves the standard multi-grid algorithm allowing the detection of splintered peaks in a correlation map through an automatic threshold, producing multiple displacement vectors for each correlation area. Vector locations are chosen by translating images according to the peak displacements and by selecting the areas with the strongest match. The method is assessed on synthetic images of a boundary layer of varying intensity and a sinusoidal displacement field of changing wavelength. An experimental case of a flow exhibiting strong velocity gradients is also provided to show the improvements brought by this technique.

### 5.2 Introduction

Standard analysis of PIV images generally involves the division of sequential recordings into smaller interrogation areas and estimating the displacement of recorded particle images captured within those areas by means of cross-correlation. Particle images moving together in the same direction will produce a single strong peak in the cross-correlation map, allowing

the retrieval of a representative displacement vector. For this analysis to be conducive, local in-plane displacement gradients must be negligible and an upper limit of 0.05 pixels/pixel is often suggested in literature [51]. When strong in-plane displacement gradients are present, interrogation areas are populated by particle clusters moving in different directions. As a consequence, the correlation peak will broaden and deform as the gradients increase, until the peak splinters into multiple peaks (Figure 5.1) [87]. The unique displacement vector obtained from the correlation map is then no longer representative of the underlying flow field. Non-uniform displacement fields and deformations in the particle image pattern therefore constitute a strong source of error for PIV [43] and must be treated carefully. While smaller interrogation window sizes are preferential to reduce the local velocity gradients, such reduced windows contain fewer particle images thereby increasing the measurement uncertainty and limiting the maximum displacement measurable [4]. Both contradicting requirements on the sizing of the correlation windows contribute to a limitation in the achievable dynamic velocity range of PIV [1].

One of the prevailing solutions adopted to increase attainable spatial resolution and dynamic velocity range is the iterative multi-grid approach proposed by Scarano and Riethmüller [89]. The technique suggested involves the analysis of images with wide interrogation areas first, used as “predictor” of the displacement field. Velocity predictors are adopted to deform consecutive image snapshots with the aim of reducing the relative particle image displacement. This step is typically combined with a reduction of the window size and a displacement correction using the velocity predictors. The initial window size should be large enough to capture the widest displacement in the flow field, while the final size should be small enough to contain a sufficient amount of particle images. The benefit of the multi-grid algorithm is an increase in spatial resolution and an improved velocity dynamic range, which is the reason of its widespread use and success. However, in the presence of splintered peaks in the first iteration of the analysis, a reliable estimation of the flow field is impossible. This gives rise to an unrepresentative displacement predictor, which influences the remainder of the iterative process.

Besides the use of advanced image processing algorithms, a straightforward lowering of the time-separation between sequential images can be applied to reduce the displacement peak discrepancy. This yields however a reduction in dynamic velocity range while augmenting the relative error [15]. In case of time-resolved PIV datasets, Hain and Kähler presented a strategy to selectively interrogate image snapshots temporally separated by locally optimised values to increase accuracy and dynamic range [37]. Persoons *et al.* on the other hand devised an intricate multi-pulse separation technique, where pulse separations across several exposures are adjusted to increase dynamic range [73]. The majority of PIV applications continue to rely on standard double-pulsed systems however, imposing a unique separation time between recordings. As such, a solution to the problematic of multiple correlation peaks appearing must

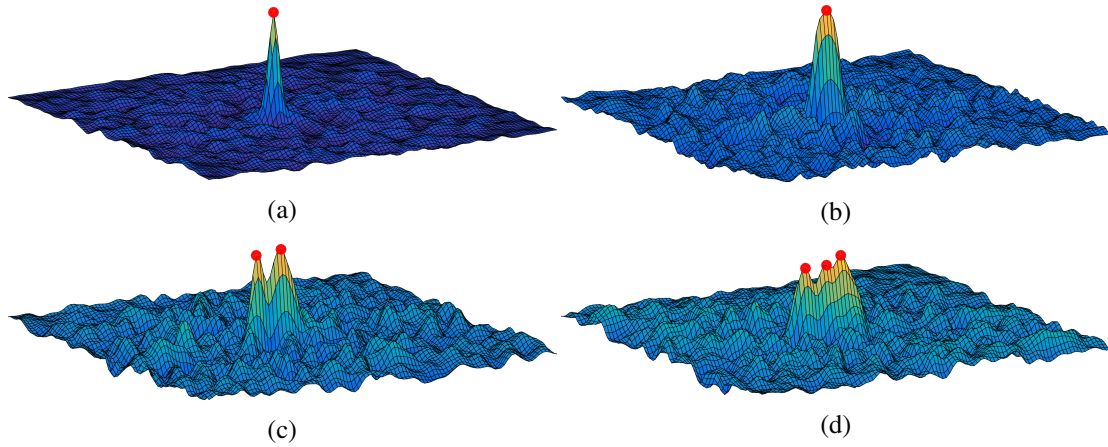


Figure 5.1: Effect of displacement gradients on the correlation map. The figure illustrates the correlation map between interrogation windows subjected to a shear flow of varying intensity. In-plane gradients are respectively: (a) 0.01, (b) 0.05, (c) 0.1 and (d) 0.5 pixels/pixel. As the gradient increases, the correlation map contains multiple detectable peaks, marked with red dots.

be sought from an algorithmic perspective.

The standard approach adopted in many PIV algorithms to circumvent the problem of numerous peaks in the correlation map is to simply discard peaks below a certain Signal-to-Noise (*SNR*) threshold (typically 1.2 to 1.5) [50]. *SNR* is defined as the ratio between the highest and the second highest peak and can be indicative of measurement quality [123]. However, a *SNR* below the threshold does not necessarily imply unreliable peaks. Multiple correlation peaks can be of equal height and well above the noise level. This *SNR*-based solution thus helps to increase the robustness of the measurement by dealing with the ambiguity of multiple peaks, but does not offer a solution to the problem of displacement vector representativeness. It will be shown in this chapter that complex displacement fields with high amplitude oscillations indeed remain impossible to be measured even with the adoption of a *SNR* threshold. A particular solution utilising correlation peak amplitudes was proposed in [84]; peak-height weighted averaging of the displacements related to all the peaks in the correlation map. While this suggestion mitigates the problem when multiple peaks relate to similar displacements, it remains insufficient in case of very dissimilar displacements. When dealing with high intensity opposite velocities such as in case of shear layers, shock waves, vortices, etc., the average of the peaks will produce a nearly zero displacement, augmenting the possibility of iterative multi-grid schemes to fail. To deal with velocity gradients in a recursive local-correlation algorithm, Hart [39] proposed to start with a large initial window and use the identified peak in the correlation map as an estimate to limit the range of possible particle displacements in sub-regions. Although this process can, in theory, be carried out down to correlation windows containing a single particle image, the dependency on the initial displacement estimate remains. Exactly

this value can be compromised by the appearance of multiple peaks in case of strong displacement gradients. A “Reverse Hierarchical process” was proposed in [82]. Rather than initiating the analysis from the largest scale, the solution proposed was to build a correlation map by starting from the smallest scale and adding interrogation areas based on inter-level correlation correction and validation. Also in this case, dynamic range and spatial resolution are shown to be improved, although no mention is made in case of splintered peaks. Corresponding correlation windows can also be sized differently [54]. Such an approach could potentially help mitigate the problem of multiple peaks by taking the advantages of using small and large correlation window together. However, correlation maps produced were shown to be noisier and less reliable due to the smaller regions correlated. More importantly, improvements in accuracy and measurement range were shown to rely on displacement vectors obtained in the previous iteration. Alternatively, the interrogation process follows the standard implementation and image intensities captured within correlation windows are altered. Spatial resolution in case of non-uniform velocity fields was shown to be drastically improved in [68] by multiplying interrogation windows with a weighting function prior to correlation, thereby increasing the importance of central pixels within a correlation window compared to those on the periphery. Several shapes and sizes of weighting functions were tested in [9], proving that the adoption of weighting functions can improve the spatial results more than simply reducing the interrogation window size. Notwithstanding the great improvements shown, the use of weighting functions was circumscribed to velocity fields of small-scale amplitudes. Weighting functions reduce the luminosity of particles on the edges of the interrogation area, thus inherently discarding the information regarding the displacement of those particle images. Weighting functions therefore lower the probability of multiple correlation peaks appearing, but simultaneously produce velocity vectors which are not necessarily representative of the underlying displacement field captured within the interrogation areas. Irrespective of the correlation response, also the vector location must be appropriate. In [124], the problem of velocity gradients has also been tackled in terms of vector location. Displacement vectors are usually anchored in the geometric centre of the interrogation area. This is not necessarily representative of the fluid motion in case of non-uniform velocity fields. The solution proposed by Young *et al.* was to anchor the vectors to a location more representative of the underlying flow motion. This involved shifting the particle image intensities according to the identified displacement, multiplying the shifted intensity fields and anchoring the vector to the location of the maximum element in their multiplication plane. In spite of the improvements produced by this method, a single vector per correlation window was produced, limiting its application in case of multiple peaks.

The algorithms mentioned afore all highlight the problematic surrounding the appearance of multiple peaks in a correlation map when high velocity gradients are present, yet, none offer a satisfactory solution. In this chapter a novel Multiple Peak PIV algorithm (MP-PIV) is proposed, capable of dealing with splintered peaks in the correlation-map. Details of the

methodology are provided in Section 5.3. In short, every prominent peak is considered to be a potential displacement. The suggested methodology enables the measurement of these displacements by detecting and analysing all the peaks of the correlation map, producing multiple vectors per correlation window. This approach thus improves the measurement of displacements in case of strong in-plane gradients. The procedure is articulated in two sub-processes. First, strong significant peaks are selected and discerned from random noise. This process is carried out through an automatic thresholding method exploiting the correlation map histogram. Each selected peak then produces one or more vectors anchored to a sub-correlation grid. Vector locations are chosen by shifting the images according to each displacement and by checking the quality of the overlapping images through cross-correlation. Not only is all the valid information contained in the correlation map used to the fullest, also vector locations become more accurate allowing a better estimation of the velocity predictor. Numerical analyses through Monte-Carlo simulations are presented for a boundary layer of varying amplitude and a sinusoidal velocity field of variable frequency in Section 5.4. Together with an experimental test case (Section 5.5 all assessments indicate the proposed solution to yield a drastic improvement in PIV measurements' accuracy and attainable resolution.

### 5.3 Methodology

The Multiple Peak PIV (MP-PIV) methodology proposed in this work utilises aspects of the iterative predictor-corrector algorithm presented in [89] and is outlined in Figure 5.2. Interrogation areas are still distributed on a Cartesian grid and cross-correlated. Contrary to the standard approaches however, vectors are not located in the geometrical centres of these areas. Instead, once each pair of correlation windows is evaluated, multiple peaks are detected and discerned from the correlation noise as described in Section 5.3.1. A second layer of sub-correlation windows (or sub-interrogation areas) is then used to select the displacement vectors and anchor them to the sub-windows' geometrical centres (Section 5.3.2). As per common multi-grid approaches where interrogation windows are iteratively halved, sub-correlation window sizes are half the size of the parent window with a minimum of 17 pixels. In order to find the most adequate sub-interrogation area for each vector, the initial interrogation areas are shifted (not deformed) according to each of the peaks' displacement. A secondary cross-correlation between the shifted images is performed once more in the sub-interrogation areas and high signal-to-noise ratios indicate the sub-window's centre to be appropriate to allocate the vector. Otherwise the node is left available for the analysis of a different peak. Peaks for which no good match was found are automatically discarded.

Once correlation windows have been analysed, the displacement field is validated using a normalised median threshold [119] and corrupted vectors are replaced using the median of

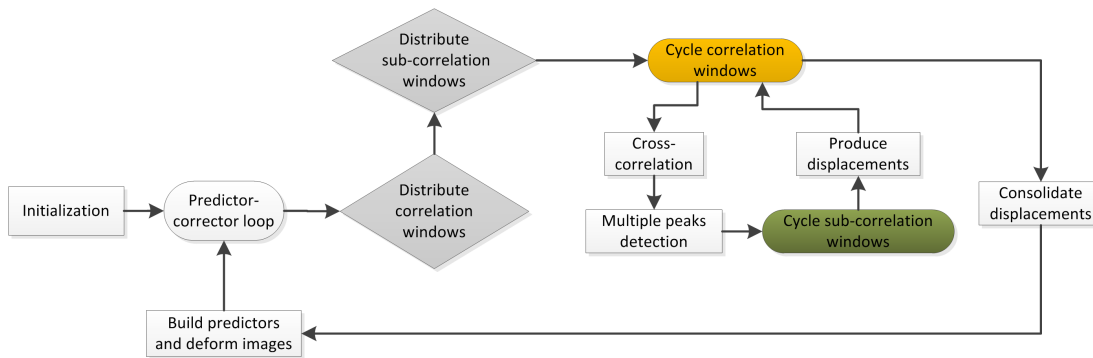


Figure 5.2: Flow chart of the MP-PIV algorithm. Notice the collocation of two different sets of correlation points: correlation windows to detect displacements and sub-correlation windows to anchor vectors.

their neighbours. The final displacement field is then interpolated to produce a displacement predictor for the successive iterations.

### 5.3.1 Multiple peak detection

The cause of multiple peaks in a correlation map can be due to several reasons. If particle images move uniformly, one single peak will appear in the correlation map. If clusters of particles move in different directions within the same interrogation area, the correlation map will show distinct peaks for each cluster. Also when individual particle images move in random directions, particles disappear from the first to the second image or images are poorly seeded and contaminated with noise, cross-correlation will equally produce a map presenting multiple peaks. These peaks are not necessarily related to actual displacements though (Figure 5.3 left). It is therefore essential to discern proper peaks associated to displacements from random noisy peaks (see Figure 5.3). In MP-PIV, this task is automatically carried out in three successive steps. Peaks are first detected as local extrema in the correlation map through a simple local maxima detection in an 8-by-8 neighbourhood. These local correlation maxima include both displacement peaks and correlation noise and require further filtering. In the second step candidate displacement peaks are selected using the automatic triangle threshold method [127]. Details about the method are provided in the next paragraph. Finally, valid peaks are retained through a user-defined *SNR*.

#### Triangle thresholding

The automatic thresholding method adopted in this work to distinguish displacement peaks from correlation noise was proposed for the first time in [127] to discern bright objects from a dark background. The method is used here to exploit the histogram of the correlation map and,

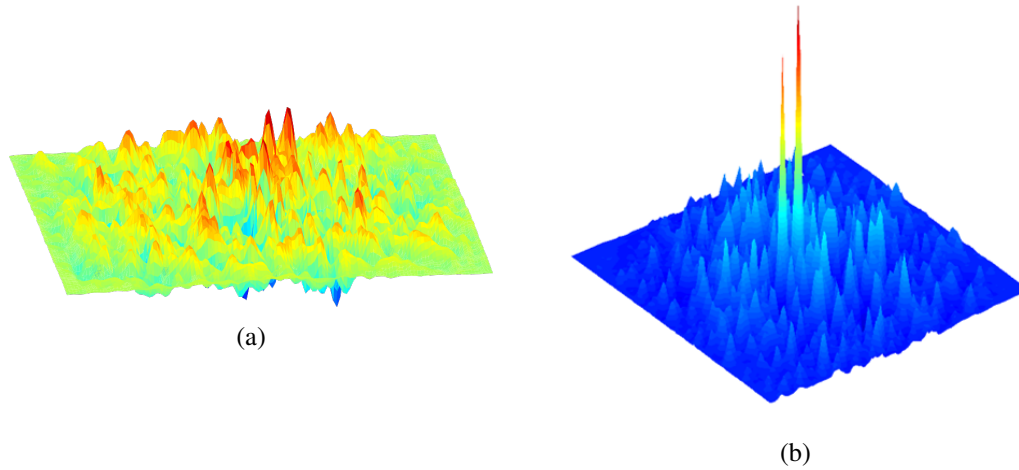


Figure 5.3: Examples of correlation maps with multiple peaks due to (a) bad correlation and (b) multiple displacements.

in particular, its peculiar shape in case of PIV images. Since correlation peaks only constitute a small portion of the histogram, they can be easily distinguished from background noise with a geometrical process of maximization. Given the histogram of the correlation map, as depicted in Figure 5.4, the line between the maximum number of elements (*Max pdf*) and the maximum intensity of the correlation (*Max corr*) is considered. For each bin of the histogram, the distance between its value and the *max-max* line is evaluated. This distance is plotted in red in Figure 5.4 above the triangle. The bin location corresponding to the maximum distance, incremented by a normalized offset (typically 0.1), is considered as a threshold to discern good peaks from correlation noise, i.e. the first peak-selection is done on the basis of correlation peak amplitude.

### Peak refinement by Signal-to-Noise Ratio

An accustomed measure of the correlation peak's reliability and validation heuristic of the obtained particle image displacement estimate is the common ratio between the highest and second highest peak amplitude. In MP-PIV this definition is revisited, since a *SNR* close to one actually implies both correlation peaks to be of equal magnitude and to potentially contain particle image displacement information provided they are both above the correlation noise. The afore triangle threshold presents an automatic means of discerning strong peaks from the correlation noise based on the peak heights. However, in case of noisy correlation maps (Figure 5.3 left), displacement peaks might be hard to detect or not even exist, potentially compromising the triangle threshold. For this reason, a secondary peak refinement is implemented.

Given  $N$  candidate peaks selected by the triangle threshold (e.g. the five highest peaks in Figure 5.5), and denoting the set of sorted correlation peak values in descending order as  $P = \{P_1, P_2, \dots, P_N\}$ , the *SNR* of the  $i^{th}$  peak is defined as

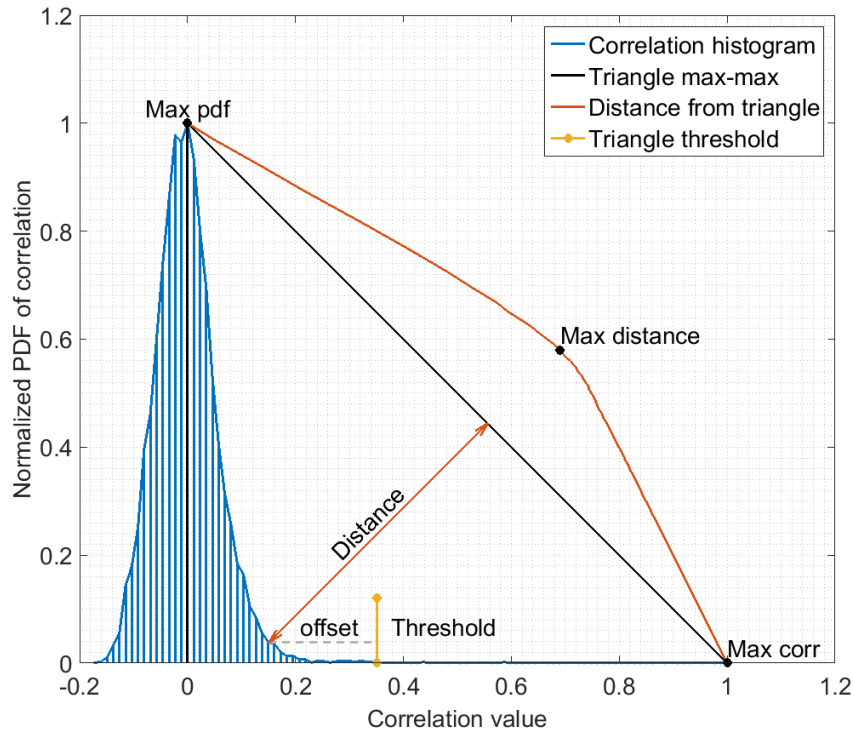


Figure 5.4: The principle of triangle thresholding as an automated method to discern strong peaks from correlation noise. The blue plots represents the histogram (PDF) of the correlation map, with the black line connecting the maximum of the correlation (on the x-axis) with the maximum value of the PDF (on the y-axis). The red plots represents the distance between the max-max line and the values of the histogram. The maximum value of this distance, shifted by an offset of typically 0.1, yields the automatic threshold.

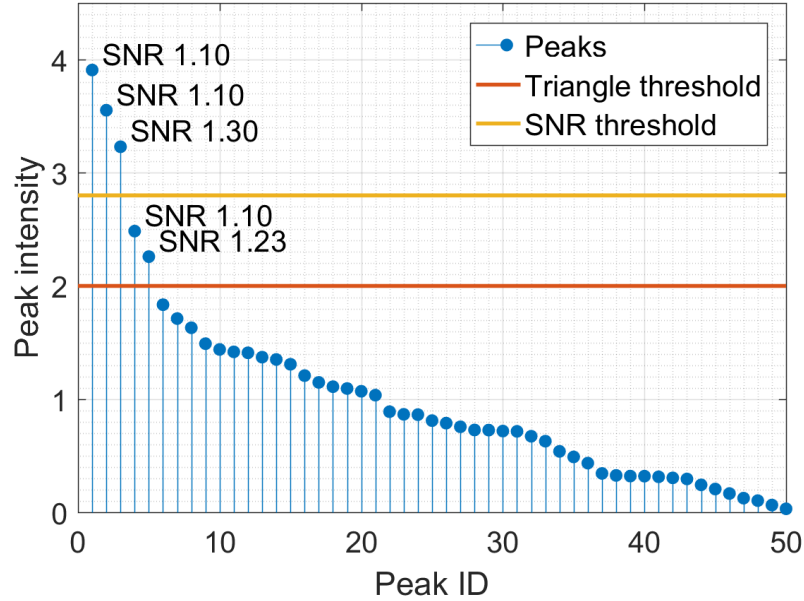


Figure 5.5: Illustration of the correlation peak refining process using Signal-to-Noise Ratio ( $SNR$ ). The example shows an application containing 50 randomly generated peaks, extracted from a normal distribution, sorted from the highest to the smallest. The first peak selection is based on peak amplitude through the triangle-threshold method. The secondary selection is based on the consecutive  $SNR$  with a user-defined lower limit.

$$SNR_i = \frac{P_i}{P_{i+1}} \quad (5.1)$$

The subset of peaks considered for further investigation are then all peaks preceding the first peak within the set  $P$  (hence of higher amplitude) for which the  $SNR_i$  is higher than a user-defined threshold  $\sigma_{thr}$ . Figure 5.5 shows an example of this filter for 50 peaks. The first five peaks are considered on the basis of the triangle threshold. With a typical  $SNR$  threshold of 1.3, the third peak is the first for which the  $SNR_i$  is above the threshold. Accordingly, only the first three peaks are retained for further consideration as these peaks are supposed to be sufficiently distinguishable from correlation noise. Once the selection of correlation peaks is refined, displacement vectors are collocated on a sub-correlation grid, as described in the next section.

### 5.3.2 Vector allocation

The detection of multiple peaks in the correlation map provides the necessary information regarding the captured particle image displacements. The missing information is still the spatial distribution of these displacements i.e. where displacement vectors should be positioned in

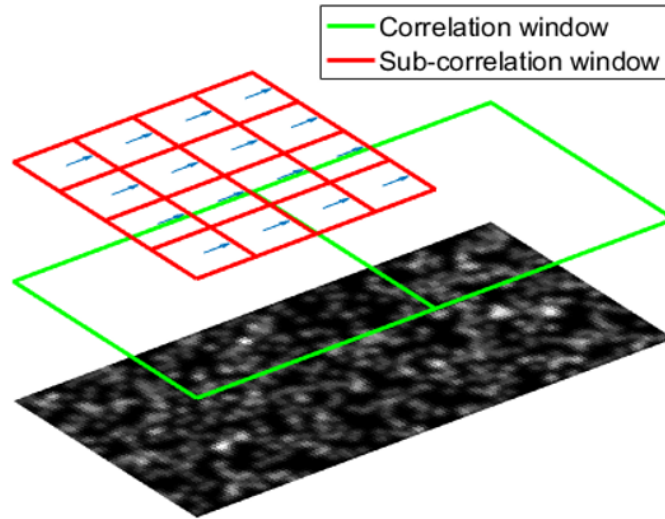


Figure 5.6: Layout of correlation and sub-correlation windows adopted in the MP-PIV algorithm. Correlation windows (green) are used to detect multiple displacements peaks. No vector is allocated in these areas. Instead, sub-correlation windows (red) are used to assess each of the selected potential particle displacements. Displacements yielding the highest correlation peak within a sub-window are anchored to the geometrical centre of the sub-correlation window.

the interrogation area. The solution proposed in this work is to anchor the displacement vectors to a grid of sub-correlation windows, as shown in Figure 5.6, thus retaining a structured vector distribution. Peaks selected from the previous step are processed from the highest to the lowest. For each peak, interrogation areas are shifted in line with standard image deformation routines ([10]). The grid of sub-interrogation areas (shown in green in Figure 5.6) is subsequently cross-correlated to measure the quality of mutual particle image overlap. Sub-correlation maps presenting one single peak (high  $SNR$ ) indicate good locations to anchor the considered displacement vector in its centre. If multiple peaks appear (low  $SNR$ ), the grid node will be left for the analysis of the next peak. In order to increase the displacement accuracy and speed up the predictor-corrector convergence, sub-correlation maps are also used to provide an additional sub-pixel correction to the displacement corresponding to the scrutinized correlation peak [120].

This vector positioning procedure ensures that higher peaks will always have a priority on smaller peaks, increasing the robustness of the algorithm. Moreover, velocity vectors will only be generated if good particle image matching locations are available. A detailed description of the algorithm can be found in Algorithm 1. The method is implemented in a predictor-corrector fashion, as already shown in Figure 5.2. Once all the correlation windows are processed, displacement vectors are validated using the normalized median threshold [119] and interpolated on a pixel-grid using quintic spline [10].

**Algorithm 1** Description of MP-PIV algorithm

---

```

1: Distribute correlation windows ( $W_{1,\dots,N}$ )
2: for Each interrogation window  $W_i$  do
3:   Select corresponding image portions  $A_i$  and  $B_i$ 
4:   Perform cross-correlation:  $\Phi_i = A_i \otimes B_i$ 
5:   Identify and select multiple peaks in  $\Phi_i$ : ( $P_{1,\dots,k}$ )
6:   for Each peak  $P_j$  do
7:     Determine sub-pixel displacement:  $\mathbf{ds}_j = (dx_j, dy_j)$ 
8:     Divide  $W_i$  into sub-correlation windows:  $SW_{1,\dots,M}$ 
9:     for Each sub-window  $SW_m$  do
10:      Select corresponding image portions  $A_{i,m}$  and  $B_{i,m}$ 
11:      Shift  $B_{i,m}$  by  $-\mathbf{ds}_j$ :  $B_{i,m,j}^*$ 
12:      Perform cross-correlation:  $\Phi_{i,m,j} = A_{i,m} \otimes B_{i,m,j}^*$ 
13:      Measure signal-to-noise ratio SNR for  $\Phi_{i,m,j}$ 
14:      Measure displacement correction  $\mathbf{ds}_{m,j}$ 
15:      if SNR >  $\sigma_{thr}$  then
16:        Anchor displacement  $\mathbf{ds}_j + \mathbf{ds}_{m,j}$  to centroid of  $SW_{i,m}$ 
17:      end if
18:    end for
19:  end for
20: end for

```

---

## 5.4 Numerical assessment

Improvements achieved with MP-PIV by resolving splintered peaks have been quantified through Monte-Carlo analyses. Assessments have been performed on synthetic images involving two different velocity fields: a boundary layer of increasing freestream velocity, tested for different seeding densities, and a sinusoidal field of varying frequency, tested for different amplitudes. Synthetic images were generated using Gaussian shaped tracer images, with diameters drawn from a normal probability  $\mathcal{N}(\mu, \sigma^2) = \mathcal{N}(3 \text{ pixel}, 1 \text{ pixel}^2)$ . The mean intensity of particles was 50% of the maximum gray scale and the standard deviation was 18%, with images discretised in 16 bits.

MP-PIV was tested and compared to four different PIV techniques. The first technique, referenced hereafter as MGRID, is similar to the multi-grid algorithm of [89] but without any vector validation. In a slightly modified version of MGRID, MGRIDF, a SNR filter is introduced to automatically exclude vectors with a SNR below 1.3. MGRIDF is thus identical to standard multi-grid methods. In order to investigate the improvements in terms of spatial resolution, intensity weighting as suggested by [68] has been included and is referred to as LFC (Local Field Correction). Finally, a PIV algorithm adopting cross-correlation between windows of different sizes (DSIW: Different Sized Interrogation Windows) was also considered as described by [54]. An overview of the considered algorithms in terms of their difference in settings is given in Table 5.1.

Symbol	Peaks	Weighting	SNR filter	Cross-correlation
MGRID	Single	No	No	Same size
MGRIDF	Single	No	Yes	Same size
LFC	Single	Yes	No	Same size
DSIW	Single	No	Yes	Different size
MP-PIV	Multiple	No	Yes	Same size

Table 5.1: Summary of the algorithms used in the numerical assessment.

### 5.4.1 Boundary layer

The displacement field  $(u, v)$  related to a laminar boundary layer on flat plate was simulated by resolving Prandtl's equations [75] in the vicinity of a wall, i.e. Blasius' solution;

$$2\frac{d^3f}{d\eta^3} + f\frac{d^2f}{d\eta^2} = 0 \quad \text{with} \quad f(0) = \frac{df}{d\eta}(0) = 0 \quad \text{and} \quad \lim_{\eta \rightarrow \infty} \frac{df}{d\eta}(\eta) = \infty \quad (5.2)$$

$$u = U_\infty \frac{df}{d\eta}, \quad v = \frac{1}{2} \sqrt{\frac{\nu U_\infty}{x}} \left\{ \eta \frac{df}{d\eta} - f \right\}, \quad \eta = \mathcal{N} \sqrt{\frac{U_\infty}{\nu x}} \quad \text{and} \quad \delta = \frac{5.0}{\sqrt{U_\infty/\nu x}}$$

The freestream displacement  $U_\infty$  was adjusted from 0.5 to 33 pixels with increments of 0.5 pixels. A total of 5000 independent simulations were performed for each displacement. The simulations were repeated for three seeding densities: 0.03, 0.1 and 0.3 particles per pixel (ppp). The boundary layer thickness  $\delta$  was set to a constant 64 pixels and the error analysis was focused on an image portion of 65-by-65 *pixels*<sup>2</sup> in size adjacent to the wall. Window sizes  $WS$  were reduced from 65 to 17 pixels in three refinement steps. Imposing a 75% window overlap, a final displacement field with a constant vector spacing of 4 pixels was obtained giving a total of 225 vectors. A plot of the velocity profiles is presented in Figure 5.7.

Results are shown in terms of normalised error ( $\varepsilon$ ). Given the obtained displacement values  $(\hat{u}, \hat{v})$  and the corresponding ideal values  $(u_{id}, v_{id})$ , the error was evaluated as:

$$\varepsilon = \frac{1}{U_{ref}} \sqrt{\frac{1}{N} \sum_{i=1}^N (u_{id} - \hat{u}_i)^2 + (v_{id} - \hat{v}_i)^2} \quad (5.3)$$

where  $U_{ref}$  is the spatially averaged velocity  $U_{ref} = \frac{1}{N} \sqrt{\sum_i u_{id}^2 + v_{id}^2}$ . Plots of the measurement error are presented against the freestream velocity  $U_\infty$  and the maximum rate of strain  $S$ ;

$$S_{max} \equiv \left. \frac{\partial u}{\partial y} \right|_{y=0} = \frac{5.0 U_\infty}{\delta} \left. \frac{d^2 f}{d\eta^2} \right|_{\eta=0} \equiv \frac{1.6605 U_\infty}{\delta} \quad (5.4)$$

Equation 5.4 expresses the velocity gradient in terms of pixels/pixel, which, given the

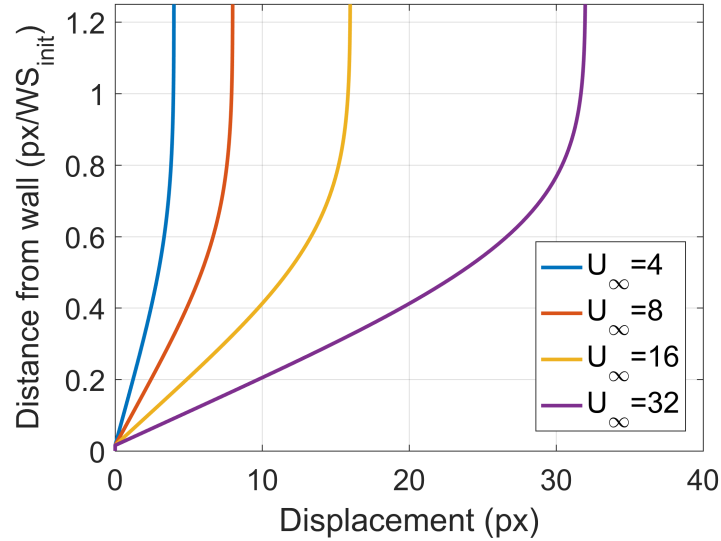


Figure 5.7: Boundary layer profiles across the initial interrogation window ( $WS_{init} = 65 \text{ pixels}$ ), for different freestream pixel displacements ( $U_{\infty}$ ), imposed in the numerical assessments.

imposed values, ranged from 0.013 pixels/pixel ( $U_{\infty} = 0.5 \text{ pixels}$ ) to 0.85 pixels/pixel ( $U_{\infty} = 33 \text{ pixels}$ ).

Figure 5.8a presents the results of the error analysis for a seeding density of 0.03 ppp. For such a small seeding density, DSIW is unable to produce a reliable correlation map and produces noisy results even for the smallest gradients tested. By increasing the freestream velocity,  $\epsilon$  for DSIW appears to initially decrease. However, the reader should note that the absolute error ( $\epsilon U_{ref}$ ) is actually increasing. The observable tendency is only due to the adopted normalization in equation 5.3. The other image processing approaches present a constant normalised error  $\epsilon$  of approximately 0.03 up to a gradient of 0.2 pixels/pixel. After this point, MGRID, MGRIDF and LFC present a sharp increase in error while MP-PIV remains constant. When gradients are increased up to 0.5 pixels/pixel, the normalised error for MP-PIV increases to 0.10 compared to 0.20 (MGRIDF), 0.25 (LFC), 0.32 (MGRID) and 0.36 (DSIW). Increasing the velocity gradients even further from 0.5 to 0.6 pixels/pixel, standard PIV algorithms produce error levels which are more than 20% the  $U_{ref}$  whereas the error with MP-PIV remains below 20% up to a gradient of 0.7 pixels/pixel.

In Figure 5.8b, the curves for a seeding density of 0.1 ppp show a similar behaviour to the case of lower seeding density (Figure 5.8a), with the biggest difference being the change in error with DSIW. For this seeding density, the reliability of DSIW has improved, yielding error levels on par with the other methodologies tested. It is worth noting the difference between MGRID and MGRIDF. The mere implementation of a  $SNR$  threshold in MGRIDF allows a reduction of the error when dealing with less severe gradients, confirming the detrimental effect

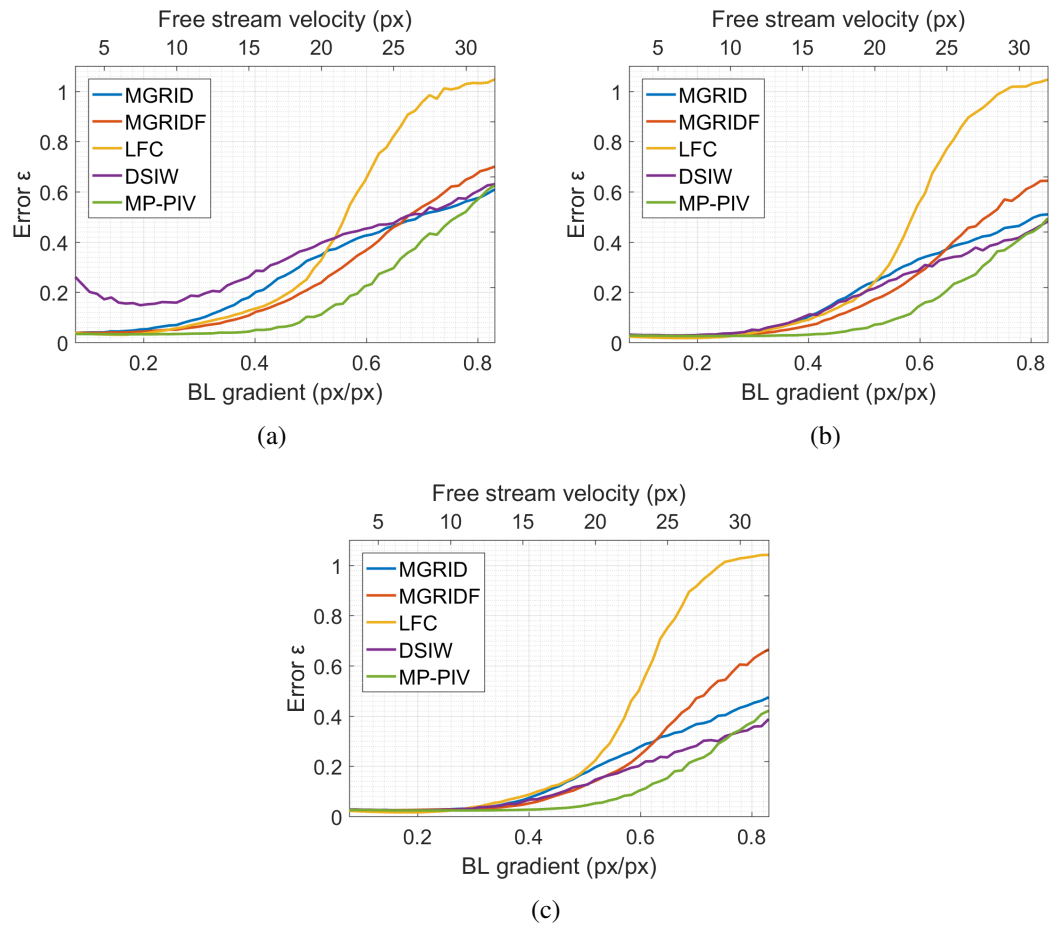


Figure 5.8: Results for the boundary layer simulation. Normalised error plots are presented for three different levels of seeding density: (a) 0.03, (b) 0.1 and (c) 0.3 ppp.

of multiple correlation peaks if left untreated. However, at higher gradients imposing a *SNR* threshold inhibits the detection of a valid correlation peak among multiple peaks of (near-)equal magnitude, increasing the overall error. Best results are obtained by MP-PIV with lowest error levels throughout the entire range of gradients tested. LFC, which aims to enhance spatial resolution, produces error levels which are slightly lower than the other techniques tested, but only in the lower range of gradients (between 0 and 0.25 pixels/pixel). The adoption of a weighting window is well-documented to increase the spatial resolution of the measurement ([9], [69]). Current results show though that weighting can be harmful. Particles belonging to the periphery of the window will contribute less to the correlation peak, producing worse results in case of high amplitude displacements. This observation is confirmed by the error levels produced by LFC in case of high gradients. Figure 5.8a-c show that the error generated by LFC for gradients higher than 0.5 pixels/pixel can be more than twice the error produced by the other techniques.

With increasing seeding density error levels generally reduce. At a seeding density of 0.3 ppp (Figure 5.8c) DSIW produces results which are slightly better than MGRID, MGRIDF and LFC, especially in case gradients are higher than 0.5 pixels/pixel. However, also in this case, MP-PIV obtains the lowest error levels across almost the entire range of gradients tested, confirming it being the most suitable methodology for complex velocity fields.

### 5.4.2 Sinusoid test

To characterise the behaviour and improvements of MP-PIV even further, the algorithms' response to a one-dimensional sinusoidal displacement field was considered:

$$u_{id}(x, y) = A \sin\left(y \frac{2\pi}{\lambda} + \phi\right) \quad (5.5)$$

Sinusoidal displacements were imposed by adjusting the normalised wavelength from 0.25 to 1.5 and randomly selecting the phase  $\phi$  in a Monte-Carlo fashion. The normalised wavelength was defined as the ratio between the smallest correlation window size  $WS_{\min} = 17 \text{ pixels}$  and imposed sinusoidal wavelength  $\lambda$ ;  $\lambda^* = WS_{\min} / \lambda$ . Amplitudes  $A$  of 3, 5 and 7 pixels were imposed. Measured displacement fields were fitted with a sinusoid and the reconstructed amplitude  $\hat{A}$  was normalised with the imposed  $A$  producing an evolution in *normalised amplitude*  $\hat{A}/A$  with normalised wavelength  $\lambda^*$ . For all sinusoids tested, the seeding density was kept at a constant value of 0.1 ppp. Images were analysed once again with initial window sizes of 65 pixels and iteratively halved to 17 pixels. A mutual window overlap of 75% was set to obtain a final vector spacing of 4 pixels.

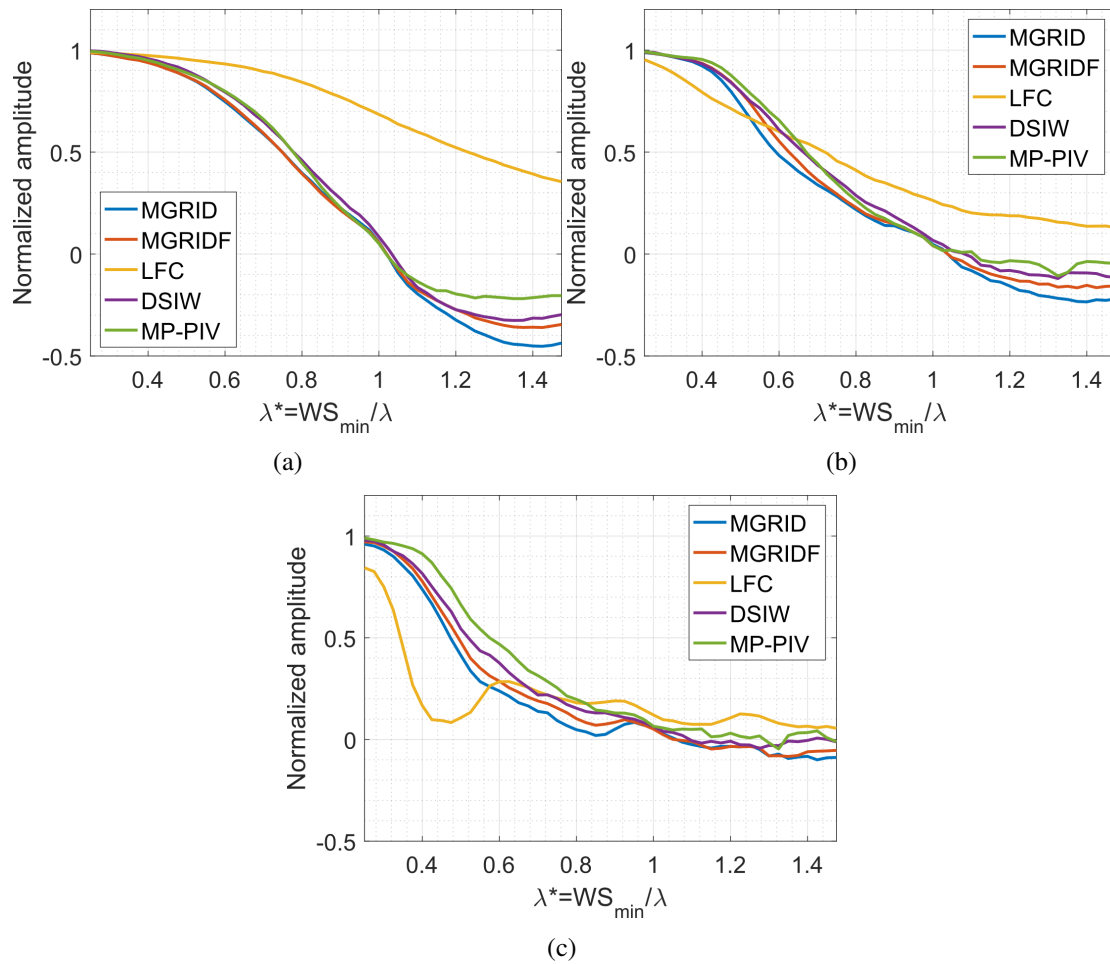


Figure 5.9: Plots of the normalised amplitude  $\hat{A}/A$  for the numerical assessment involving a sinusoidal displacement field considering three different amplitudes: (a)  $A=3$ , (b)  $A=5$  and (c)  $A=7$  pixels.

For a sinusoid of 3 pixels of amplitude, results are presented in Figure 5.9a. The plots show that for small amplitudes the frequency response of cross-correlation resembles the expected behaviour of a moving average ([88],[102]). MP-PIV performs slightly better compared to the other approaches, except for LFC. For this specific velocity field, the spatial resolution obtained using LFC is superior to the other techniques tested, with values of normalized amplitude higher than 0.5 up to  $\lambda^* \approx 1.1$ . This increased spatial resolution is to be expected as the advantages of using a weighting functions have already been shown in the literature [9]. From a practical perspective however, smaller amplitudes demand reduced temporal separation between snapshots, which as advocated is not always optimal. When the sinusoid amplitude is increased from 3 to 5 pixels (Figure 5.9b), LFC begins to show the same deficiencies as presented in Section 5.4.1 with an increased amplitude modulation for  $\lambda^* < 0.6$  compared to the other analysis approaches. At  $A = 5 \text{ pixels}$ , MP-PIV behaves slightly better than the other methods tested, offering a marginally higher spatial resolution in the range  $\lambda^* = 0.3$  to 0.7. Increasing the sinusoid amplitude even further (Figure 5.9c) to  $A = 7 \text{ pixels}$ , the frequency response of all the algorithms becomes completely different from the standard moving average assumption, confirming the strong non-linearity of the PIV algorithm [102]. When a sinusoid of 7 pixels amplitude is analysed, MP-PIV presents the best spatial resolution among all the algorithms tested, with LFC showing the worst spatial resolution for the same reason as described in Section 5.4.1.

### 5.4.3 Computational effort

An absolute measurement of the computational effort for MP-PIV is impossible to provide since it is entirely dependent on the complexity of the flow. In case of simple velocity fields (i.e. flow gradients are such that correlation maps contain a single peak), the computational overload is only constituted by the vector positioning process. All the parameters being equal to a standard PIV algorithm (i.e. correlation window size, vector spacing, number of iterations, interpolation technique, etc.), the additional overload for MP-PIV slows down the analysis by a factor of 1.5. However, such a comparison is unfair. In fact, MP-PIV produces a denser displacement field from the first iteration and could potentially reduce the number of iterations required for the predictor-corrector to converge, saving computational time compared to a standard PIV algorithm.

When multiple peaks are present, the computational overload depends on several factors, including but not limited to: the quality of the images, the seeding density, the complexity of the flow, the sensitivity ( $\sigma_{thr}$ ) chosen by the user, etc.. For very complex interrogation windows (more than five peaks detected), a computational time up to six times higher was experienced. However, the reader should note that the additional computational time for a single correlation window does not necessarily imply a slower analysis for the entire image, since a slower but

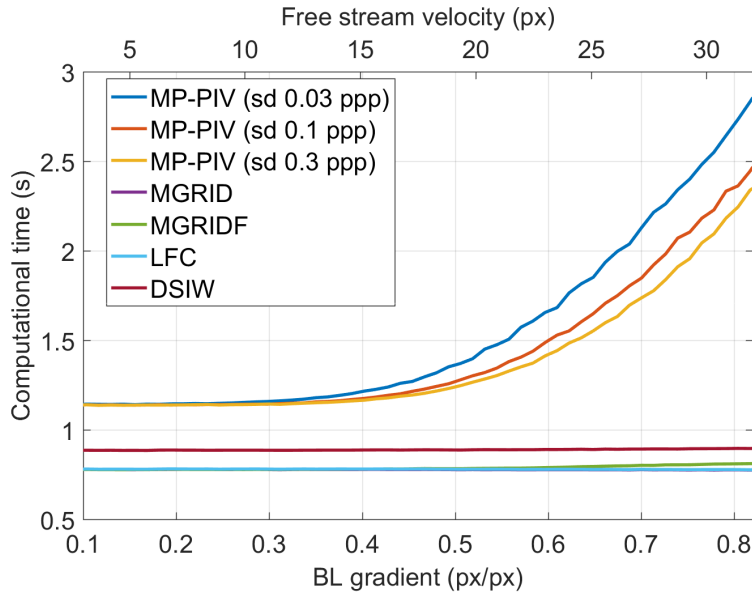


Figure 5.10: Computational time for different techniques analysed in Table 5.1. The computational time for MP-PIV is strongly dependent on the complexity of the flow field.

more accurate displacement field in the first iteration allows a potential reduction in the required number of successive iterations.

Figure 5.10 presents the computational time for MP-PIV and other techniques described in Table 5.1 for a pair of synthetic images of a boundary layer as described in Section 5.4.1. As the amplitude of the boundary layer increases, the flow becomes more complex and the computational time of MP-PIV rises as advocated. MP-PIV has been tested for three different seeding densities, 0.03, 0.1 and 0.3 ppp (particles per pixel) to show the dependency of the computational time on the amount of particle images. As the seeding becomes denser, the underlying flow is better sampled and correlation maps will contain more information, enabling an increased number of correlation windows to be elaborated by MP-PIV and rendering a more accurate flow field (cf. Figure 5.8).

## 5.5 Experimental application

To assess the proposed MP-PIV algorithm in more realistic conditions, an application to experimental PIV images of the wake flow behind a porous disc is proposed. Measurements were conducted behind a circular disc placed in the low turbulence wind tunnel of the University of Bristol. This tunnel attains turbulence levels below 0.05% and has an octagonal test section of 0.8 m×0.6 m. Four 3 mm diameter piano-wires held the disc in place, which was subjected to

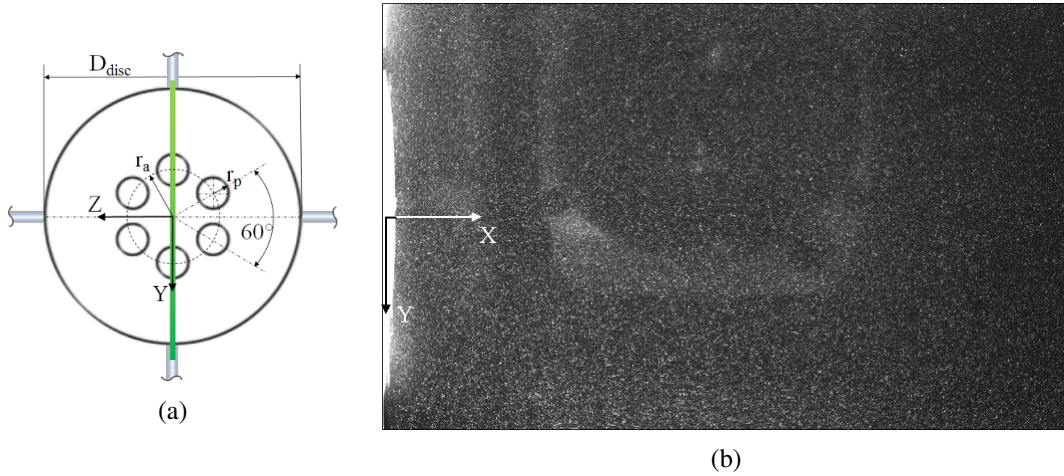


Figure 5.11: (a) Sketch of the porous disc tested. The green line indicates the location of the PIV measurement plane. (b) Exemplary PIV image recording illustrating the reflections off the disc surface (left) and mirror images/reflections (middle). Flow is from left to right.

a freestream velocity of 30 m/s impinging perpendicular to the frontal surface. The disc had a thickness of 6 mm and a diameter  $D_{disc}$  of 6 cm resulting in a negligible blockage of 0.16% at a diameter-based Reynolds number  $Re_D$  of  $11.6 \cdot 10^4$ . Six perforations, each with a radius  $r_p$  of 3.87 mm ( $r_p \approx 0.065 \cdot D_{disc}$ ), were located at a radius  $r_a$  of 1.08 cm to establish a porosity  $\beta$  (open/closed area) of 0.10 (Figure 5.11a).

Seeding was generated by atomizing a mixture of PEG-80 and water producing  $1 \mu\text{m}$  tracer particles. Illumination was provided by a Litron 200 mJ laser with a repetition rate of 15 Hz. An optical arrangement of cylindrical and spherical lenses transformed the laser beam into a 1 mm thick laser sheet positioned along the centre of two pores. Images were recorded with a Speedsense M340 camera. A 75 mm focal length lens with f-stop set at 16 was utilized, producing particle image diameters of approximately 2-3 pixels. The CMOS sensor consisted of  $10 \mu\text{m}$  pixels arranged in a  $2560 \times 1600$  array. With a calibration factor of 15.5 pixels/mm the corresponding field of view covered approximately 2.75 disc diameters downstream and  $1.72 \cdot D_{disc}$  in vertical direction. The separation between laser pulses was set at  $40 \mu\text{s}$ , producing a maximum particle image displacement of approximately 25 pixels at the pores. An exemplary image snapshot is depicted in Figure 5.11b.

Images were analysed using the same algorithms adopted in the previous section. The window size was reduced from 256 to 16 pixels in five predictor-corrector iterations and a mutual overlap of 75% between correlation windows was imposed. Images were interpolated using quintic spline [10] and velocity fields were validated using the normalized median threshold [119].

The average velocity field is shown, together with the displacement magnitude, in Figure 5.12. With a jet-like flow issuing from the pores, velocity gradients in the order of  $\frac{\partial u}{\partial y} \equiv$

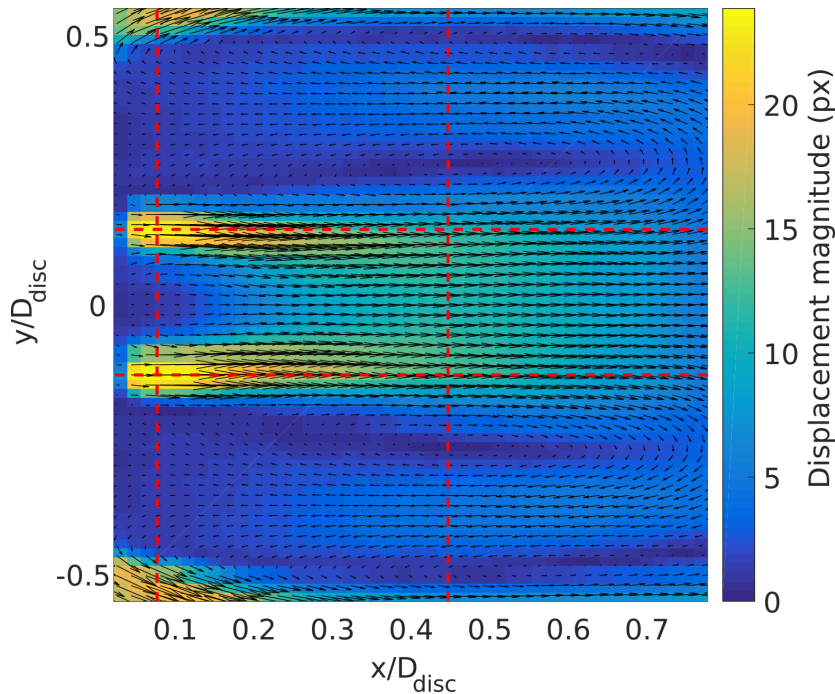


Figure 5.12: Average displacement field (sub-sampled for displaying purpose) and average displacement magnitude for the disc images. Red dashed lines are the locations where profiles are extracted (Figures 5.13 and 5.14).

0.6 pixels/pixel are encountered near the geometrical pore boundaries. Horizontal gradients  $\frac{\partial u}{\partial x}$  can be as high as 1.1 pixels/pixel. Velocity profiles for the horizontal displacement are extracted along the red dashed lines and are presented in Figure 5.13 and 5.14. The first remarkable result is the behaviour observed with DSIW. Due to the low seeding density of the images, estimated to be approximately 0.05 ppp, DSIW produces correlation maps which are far too noisy to produce a reliable displacement field. As a result, velocity profiles for DSIW, presented in Figure 5.13 and 5.14 differ completely from the other techniques tested. This behaviour was already shown in the numerical assessment (Figure 5.8a) and is confirmed by this experiment. The use of DSIW is therefore strongly discouraged in case of images presenting low seeding density.

Results of Figure 5.13-5.14 are in agreement with the observation of the numerical assessment in that LFC is unable to measure gradients in case of high intensity displacements. This is the case near the pores of the disc. From the horizontal profile, the maximum displacements measured on the jet centerlines with LFC are 22.1 (upper jet) and 23.0 pixels (lower jet), whereas MP-PIV is able to measure displacements, in identical locations, of 23.6 and 24.0 pixels. Measured displacements with MGRID and MGRIDF are between those obtained with LFC and MP-PIV, in accordance with the synthetic results for the boundary layer (Figure 5.8).

The discrepancies in vertical velocity profiles depicted in Figure 5.14 are consistent with

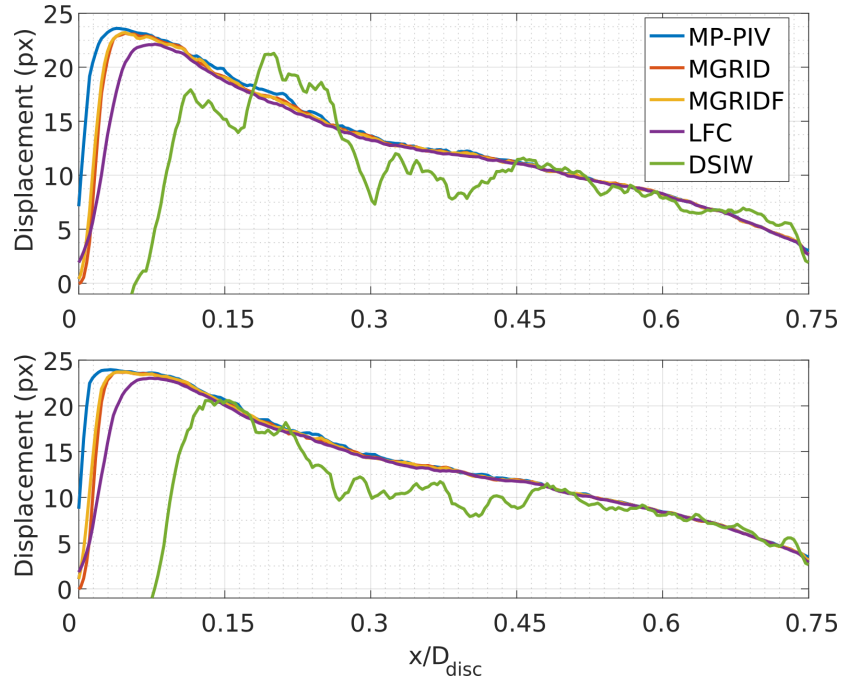


Figure 5.13: Profiles of mean horizontal velocity component extracted along respectively  $y/D_{disc} \approx \pm \frac{1}{6}$  in Figure 5.12. See Table 5.1 for a description of the considered methods.

the previous observations. The velocity profiles in Figure 5.14a, taken in vicinity of the jets show strong modulations in peak jet velocity depending on the image processing methodology; LFC attains a maximum displacement of 17.0, MGRID and MGRIDF of 23.2 and MP-PIV of 24.0 pixels. DSIW returns entirely erroneous results. For the velocity profiles in Figure 5.14b, extracted further downstream, gradients are less intense and the velocity profiles agree more closely, which supports the results of the numerical assessments.

### Residual displacements

The higher displacements measured by MP-PIV are not necessarily an indication of better measurements. In order to investigate the error for experimental images, a post-processing analysis which will be referred to as *Residual displacements* is proposed. For each pair of analysed snapshots the final displacement field is used to deform the initial images, as per standard predictor-corrector iterations. Deformed images are then re-analysed, independently, with three different window sizes: 16, 32 and 64 pixels. The vector spacing is kept constant to 32 pixels and the norm of the displacement, for each window size, is stored. The maximum displacement among the three windows tested is then selected and referred to as the residual displacement (*RD*). This analysis of *RD* provides a robust indicator of quality of the measurement for experimental images; a displacement vector is correct when the PIV images, deformed with that vector, are perfectly overlapping in the vector's neighbourhood. The reader

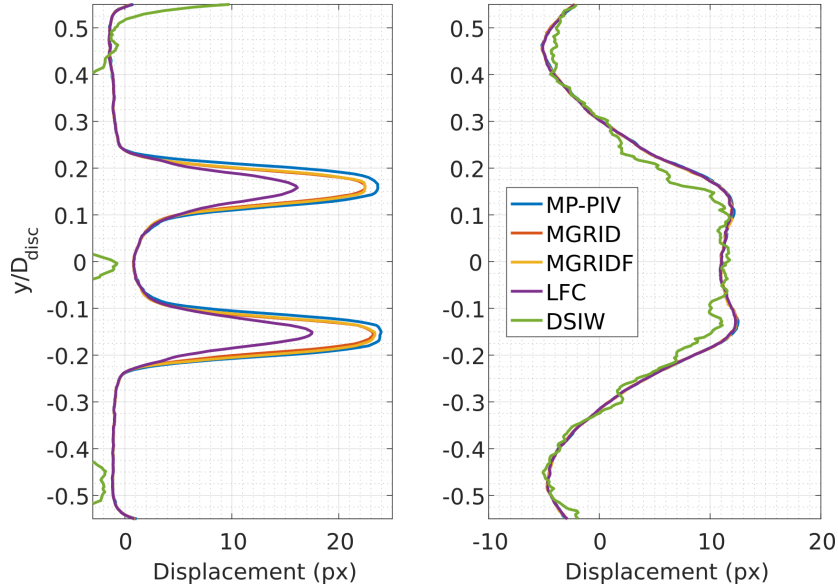


Figure 5.14: Vertical profiles of the  $u$  component of the mean velocity extracted along the vertical red dashed lines of Figure 5.12 at respectively  $x/D_{disc} \approx 0.1$  and  $x/D_{disc} \approx 0.45$ . Description of the methods in the legend can be found in Table 5.1.

should note that  $RD$  cannot be used as a correction for local vectors (as per standard multi-grid algorithms) since vectors from the  $RD$  result from a process involving multi-sized interrogation areas and do not follow from an iterative window size halving.

A comparison for all the methodologies tested in terms of ensemble averaged  $RD$  is presented in Figure 5.15. In the vicinity of the jets high particle displacement approximating 25 pixels can be encountered as the pores act as *vena contracta*, accelerating the flow. The velocity gradients in this area are too high for a standard PIV algorithm as corroborated by the  $RD$ -values shown in Figure 5.15b-e. The residual displacement for DSIW is extremely high and not even comparable with the other techniques tested. This behaviour is in agreement with the velocity profiles shown in the previous section and provides another confirmation of the unsuitability of DSIW for lower seeding densities. Figure 5.15a-d show very similar  $RD$  fields with the main difference being near the pore exits and disc rim ( $y/D_{disc} \approx \pm 0.5$ ) whereas the bulk of the flow presents resolvable velocity gradient magnitudes. Here, the residual displacements for MP-PIV are shown to be the lowest among all the techniques tested, with LFC being the highest and MGRID/MGRIDF being in between.

Horizontal profiles for the average  $RD$  are presented in Figure 5.16 for the red dashed lines of Figure 5.12. The profiles show MP-PIV attaining  $RD$  levels below 3 pixels, confirming its better suitability to describe the flow displacement in case of strong gradients and high intensity displacements. Values of  $RD$  near the jets for MGRID/MGRIDF are around 4 to 5 pixels, and 8 to 9 pixels for LFC, with more than 18 pixels for DSIW. Far away from the jets, similar values

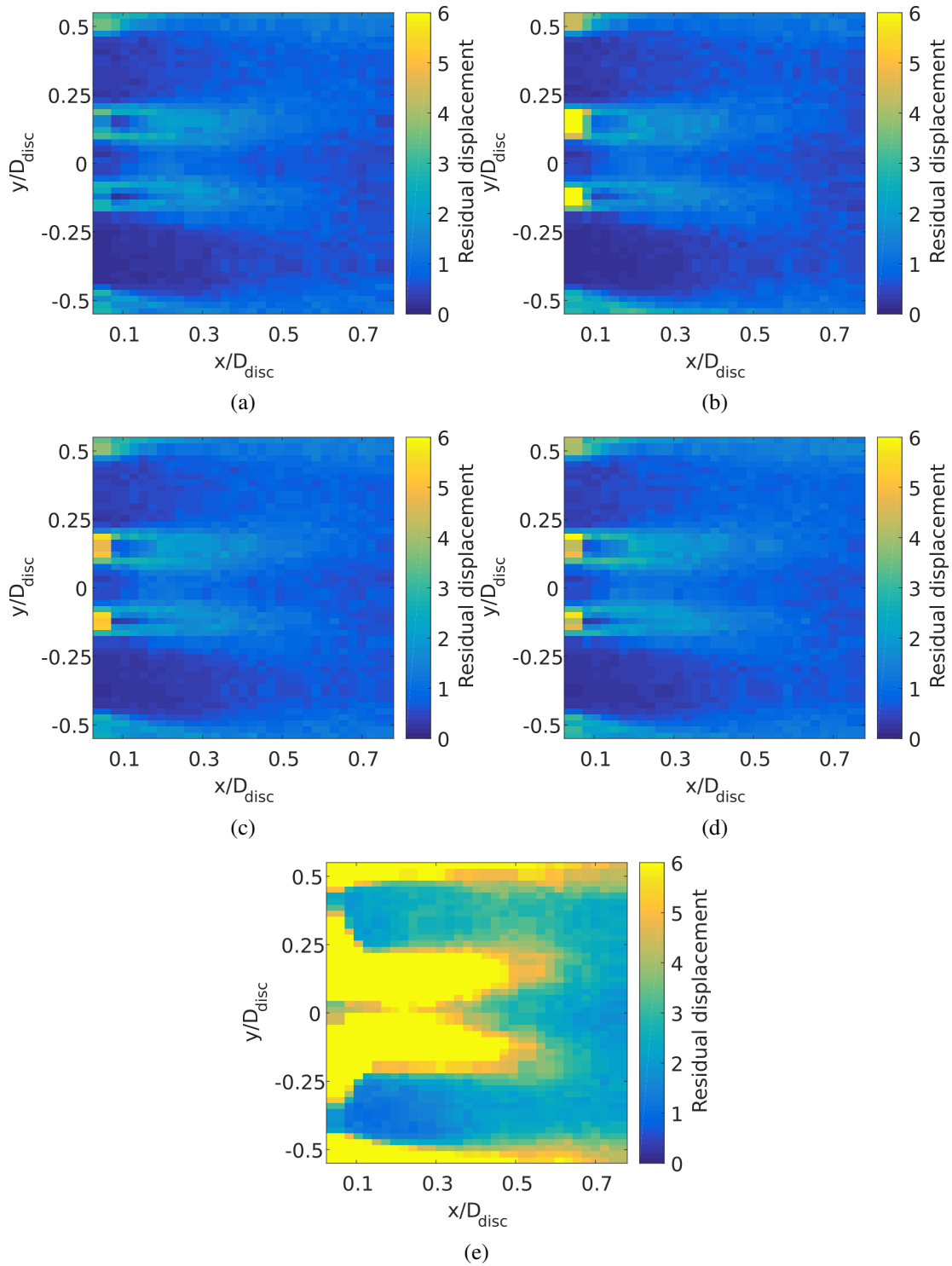


Figure 5.15: Average residual displacements for (a) MP-PIV, (b) LFC, (c) MGRID, (d) MGRIDF, (e) DSIW. Values of the residual for (e) DSIW were cut because the same scale as other methods was used for consistency. MP-PIV attains the lowest levels of residual near the jets area, where gradients are the strongest.

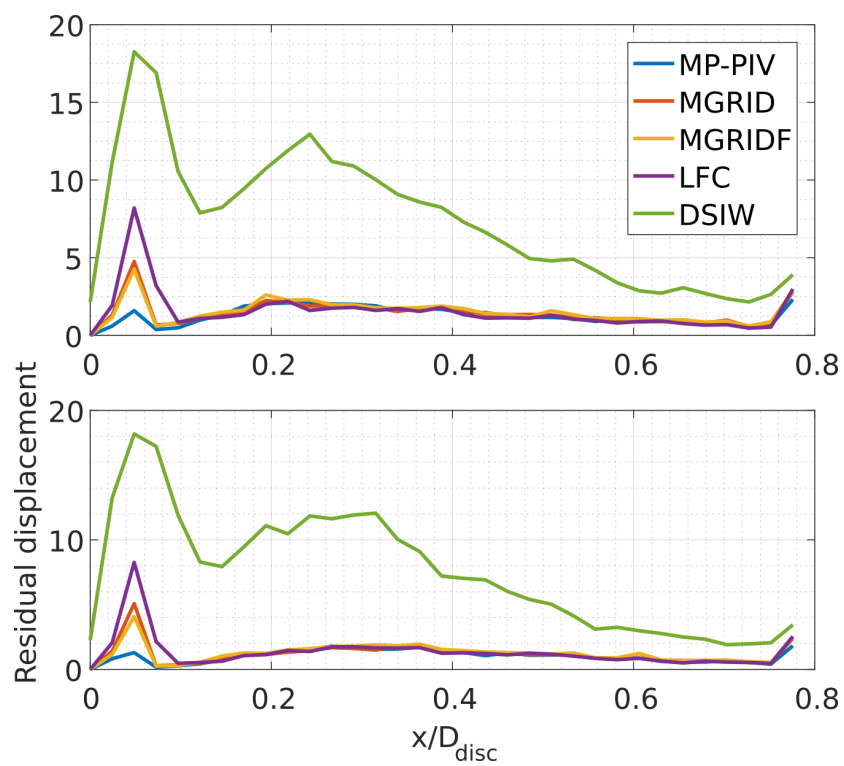


Figure 5.16: Horizontal profiles of the residual displacement extracted along the red dashed lines ( $y/D_{disc} \approx \pm \frac{1}{6}$  respectively) of Figure 5.12.

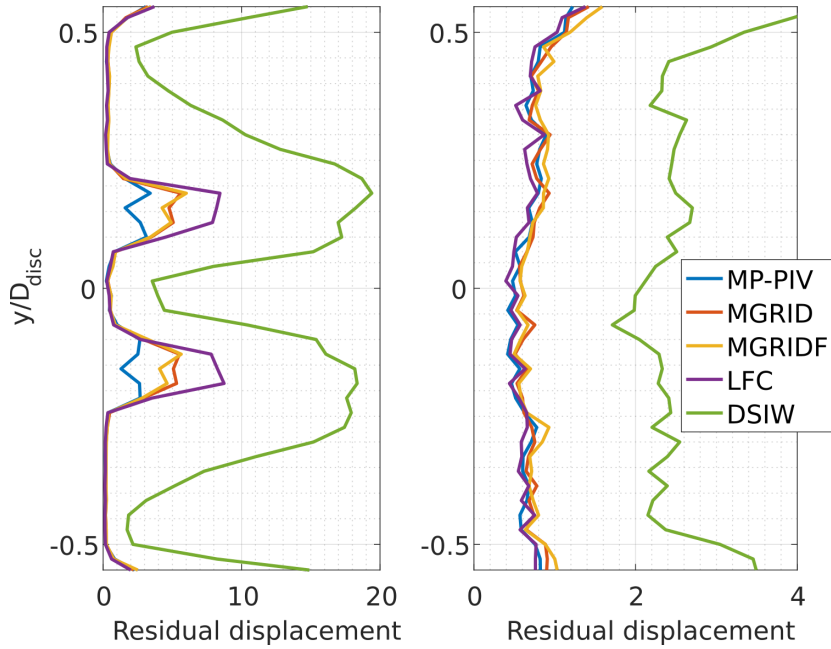


Figure 5.17: Vertical profiles of the residual extracted at respectively  $x/D_{disc} \approx 0.1$  and  $x/D_{disc} \approx 0.45$  (red dashed lines of Figure 5.12).

of  $RD$  are experienced for all the methodologies tested, with DSIW still producing the highest  $RD$ .

The vertical profiles for  $RD$  are finally shown in Figure 5.17. The plots present once again a generally higher value of  $RD$  in the vicinity of the jets ( $x/D_{disc} \approx 0.05$ ) where gradients are the highest and standard PIV algorithms fail to measure the displacements. MGRID and MGRIDF produce a  $RD$  of about 4 pixels, LFC values are around 8 pixels and DSIW is completely out of line with  $RD$  in excess of 18 pixels. Results are the best for MP-PIV, with levels of  $RD$  below 2 pixels across the entire profile.

## 5.6 Conclusions

Correlation maps in PIV image analyses can present multiple peaks when strong gradients in particle image displacement are encountered within interrogation windows. A method to detect relevant correlation peaks and generate multiple vectors per interrogation region was proposed. Strong peaks are automatically discerned from the correlation noise using a threshold based on the histogram of the correlation map. Selected peaks are analysed in sequence to understand which areas of the interrogation window contribute to which identified correlation peak. This task is fulfilled through a secondary grid of sub-interrogation areas, each half the size of the parent correlation window. The geometrical centres of these sub-windows serve as an-

chor locations for subsequent displacement vectors. For each identified correlation peak, sub-interrogation windows are translated according to the corresponding displacement. The most suitable displacement for each sub window is then found through a secondary cross-correlation based on, among all the tried displacements pertaining the identified peaks, the strongest *SNR*.

The algorithm has been assessed with Monte-Carlo simulations performed with two synthetic flow fields: a boundary layer of varying intensity and a one dimensional sinusoidal field of varying frequency and amplitude. Results indicated the proposed algorithm, MP-PIV, was able to outperform existing PIV methodologies by allowing a lower measurement error in the presence of strong velocity gradients, attaining errors which are as low as half the alternatives tested. Moreover, results for the sinusoid test showed an improved spatial resolution in case of high amplitudes.

Finally, an experimental test case offered a further opportunity to explore the advantages of MP-PIV in case of real images. Images for a porous disc were analysed with different image processing methodologies and residual displacements were presented and compared. Velocity profiles and residual displacements confirmed the results obtained for the synthetic test cases with MP-PIV allowing a better measurement of image displacements in the flow area most affected by velocity gradients.

Future works on this method include the investigation of higher order functions (i.e. vorticity, Q-criterion, etc.) and the effect of multiple peaks on these. The reduction of the error (and residual displacement) demonstrated by MP-PIV can potentially allow a better measurement of higher order functions thanks to a better estimation of the velocity gradients.

# Chapter 6

## Vector validation

The content of this chapter was published in the journal *Experiments in Fluids* with the title “Adaptive vector validation in image velocimetry to minimise the influence of outlier clusters” [57].

### 6.1 Abstract

The universal outlier detection scheme [119] and the distance-weighted universal outlier detection scheme for unstructured data [24] are the most common PIV data validation routines. However, such techniques rely on a spatial comparison of each vector with those in a fixed-size neighbourhood and their performance subsequently suffers in the presence of clusters of outliers. This chapter proposes an advancement to render outlier detection more robust while reducing the probability of mistakenly invalidating correct vectors. Velocity fields undergo a preliminary evaluation in terms of local coherency, which parametrizes the extent of the neighbourhood with which each vector will be compared subsequently. Such adaptivity is shown to reduce the number of undetected outliers, even when implemented in the afore validation schemes. In addition, an alternative residual definition is proposed, considering vector magnitude and angle adopting a modified Gaussian-weighted distance-based averaging median. This procedure is able to adapt the degree of acceptable background fluctuations in velocity to the local displacement magnitude. The traditional, extended and recommended validation methods are numerically assessed on the basis of flow fields from an isolated vortex, a turbulent channel flow and a DNS simulation of forced isotropic turbulence. The resulting validation method is adaptive, requires no user-defined parameters and is demonstrated to yield the best performances in terms of outlier under- and over-detection. Finally, the novel validation routine is applied to the PIV analysis of experimental studies focused on the near-wake behind a porous disc and on a supersonic jet, illustrating the potential gains in spatial resolution and accuracy.

## 6.2 Introduction

As already mentioned several times in this thesis, cross-correlation is the most common operator to analyse PIV images [51]. Although versatile, the robustness and accuracy of correlation are strongly influenced by image quality, notably image noise and particle image density, and underlying flow features such as velocity gradients [115] and flow curvature [90]. An insufficient number of particle images to constitute a traceable pattern or too strong a distortion of the particle image pattern between snapshots can lead to erroneous velocity estimates. Incorrect vectors in turn severely penalise the iterative image analysis process and the computation of derivative quantities [27], while further deteriorating measurement uncertainty. Vector outlier detection has consequently received considerable attention within the PIV community resulting in a variety of detection schemes.

The work in [97], for example, identifies spurious vectors on the basis of continuity in the afore-mentioned pattern deformation adopting Delaunay tessellation. However, a simpler and more commonly applied approach to discern an erroneous displacement vector in the post-processing stage is through its comparison with respect to neighbouring vectors. This can be either along the temporal and/or spatial dimension. In the former, even for non-time resolved PIV data, Proper Orthogonal Decomposition (POD) has been implemented as a filter ([113], [80]). Intermediate outlier detection in iterative image processing sequences can however only rely on spatial information. Artificial neural networks have been proposed to evaluate the interconnection between individual vectors in the instantaneous velocity field [55]. A more straightforward prediction of the model vector is based on the local median of a  $3 \times 3$  neighbourhood, followed by imposing a fixed, uniform threshold on the residual between the scrutinised vector and estimator [118]. To relax the limitation of a spatially invariant threshold, the implementation of an adaptive threshold utilising a local velocity variability based on the moving average of the vectors was proposed [78]. In [119], Westerweel proposed a reliable and robust threshold adopting a normalised median threshold (hereafter referred to as NMT); the difference between a correct vector and its estimator, which is based on the neighbourhood median, must fall within two times the median of the discrepancy between the neighbouring vectors and the prediction. Though widely applied, [24] highlights this approach to be unsuitable for unstructured data such as in Particle Tracking Velocimetry (PTV) or adaptive PIV routines [105] and should include a weighting inversely proportional to the distance between vectors. This technique will be referred to as DW-NMT.

Both NMT and DW-NMT approaches have been categorically demonstrated to identify isolated outliers even if local median tests may suffer from under- and over-detection [52]. The former refers to failing to detect an outlier. Especially in the presence of clusters of erroneous vectors, the augmented fluctuation level causes the normalised threshold to be on a par with correct vectors. These faulty vectors are subsequently wrongly considered correct. Clustering

of outliers is a quite common problem in PIV due to low seeding areas or strong light reflections on surfaces, and the inherent problem for validation is worth the attention. Over-detection refers to the case of classifying correct vectors as erroneous, which is prone in the presence of strong velocity gradients. To minimise this sensitivity, [67] iteratively discriminated outliers on the basis of a validation criterion utilising predictions from interpolations considering the eight nearest vectors assessed to be coherent. Coherency was quantified as the ratio between the mean residual and the mean magnitude. This solution was shown to minimise the overall influence of outliers in data validation, but at the cost of complexity. Moreover, as already stated, the method would fail in the presence of outlier clusters and continued the need of defining an appropriate validation threshold. The latter has been addressed by [96] through the implementation of a spatially varying threshold. Prior to evaluating the residual between the measured vector and the prediction, potential outliers are identified using a median filter and replaced with a distance-based Gaussian-weighted average. After adding a user-defined constant, the filtered discrepancy serves as a heuristic for the local median test. This approach yielded promising results in terms of reducing over- and under-detection despite the continuing need of refinement of the introduced constant. To further mitigate over-detection, [125] distinguishes between spurious vectors and variations due to local velocity gradients by incorporating a local thin-plate spline model to which vectors are compared. By adjusting the degree of smoothness in the spline model and the vector removal criterion over-detection could be diminished in the presence of significant velocity gradients.

This chapter presents a novel adaptive vector validation algorithm capable of (1) detecting clusters of outliers, (2) reducing the degree of over-detection, (3) overcoming the restrictions of existing methodologies by negating user-input and (4) safeguarding computational simplicity. Although the process still applies the concept of median-normalized thresholds, three ideas are introduced which elaborate on the findings of the studies mentioned afore. First, the number of neighbours for comparison is adjusted based on local flow coherency. The latter is quantified by means of second-order regression. The assumption is that clusters of outliers are characterized by a higher variance (randomness) and the size of the vector basis for comparison must be extended accordingly. This step renders the validation algorithm fully adaptive. Second, an averaged-weighted-median is introduced to reduce over-detections by relaxing the importance of distant data sites. Third, erroneous vectors are defined as local anomalies in vector direction and magnitude whereas traditionally validation is based on the Cartesian velocity components. The reader should note that this work does not investigate the appropriate method of outlier replacement. The interested reader can find further information in relevant references such as [67], [31], [77], [92], etc.

After illustrating the problematic surrounding outlier identification, the suggested methodology is explained in section 6.4. Section 6.5 concerns the assessment on the basis of benchmark velocity fields contaminated with synthetic spurious vectors. Appreciable amelioration

in under- and over-detection is demonstrated. Incorporation of the adaptive neighbourhood is also shown to be a very efficient concept to decrease the number of under-detections when applied to the traditional techniques. The improved validation process is finally incorporated in a recursive multi-grid image analysis routine and applied to the experimental wake of a porous disc and supersonic jet in section 6.6.

### 6.3 Problem Statement: coherency

Human vision is considered the best tool in the identification of outliers and its strength lies in the cognitive ability to distinguish coherent structures [81]. Each vector is unconsciously juxtaposed with its closest neighbours and this basis for comparison is extended until a recognisable pattern emerges providing sufficient reliability to discriminate outliers. This process is illustrated in Figure 6.1. The small collection of vectors in Figure 6.1a could be deemed invalid if only the local neighbourhood were to be considered. However, extending the neighbourhood it becomes clear the vectors form part of either a coherent structure (Figure 6.1b) or outlier cluster (Figure 6.1c). While classic spatial outlier detection methodologies consult a restricted vicinity of typically 8 ( $3 \times 3 - 1$ ) to 24 ( $5 \times 5 - 1$ ) vectors, the example highlights the need to adaptively expand the locality as to emulate human vision. Simultaneously, a group of actual outliers should not influence the validation process in such a manner as to invalidate correct vectors (over-detection).

Prior to validating a vector, an appropriate neighbourhood extent must therefore be selected. The methods of [67] and [96] both incorporate an initial consistency heuristic to specify the basis for vector comparison in the following process stage. However, neither method accounts for the adverse effect of velocity gradients in coherent structures. As depicted in Figure 6.1c both methods conjecture several correct elements of the vector collection as incoherent. A majority of vectors may consequently be invalidated already in the preparatory stage and excluded or replaced successively. Either approach inherently neglects underlying flow physics and essentially filters measured data thereby influencing the overall accuracy of the results. Instead, in the current work it is argued that each vector should be considered valid from the outset and coherency should only dictate the extent of the proximity to take into account. Considering the typical decay in spatial velocity correlations, a weighting inversely proportional with spacing must be applied to reflect the influence of each comparative vector. Differentiation between vectors must thus take place at a later stage, with care to minimise the effect of outliers. Such an approach will greatly reduce the percentage of over-detection, irrespective of the degree of vector accumulation.

Concerning the validation criteria, these are most commonly based on velocity component magnitudes. These magnitudes are attributed an acceptable fluctuation level during validation

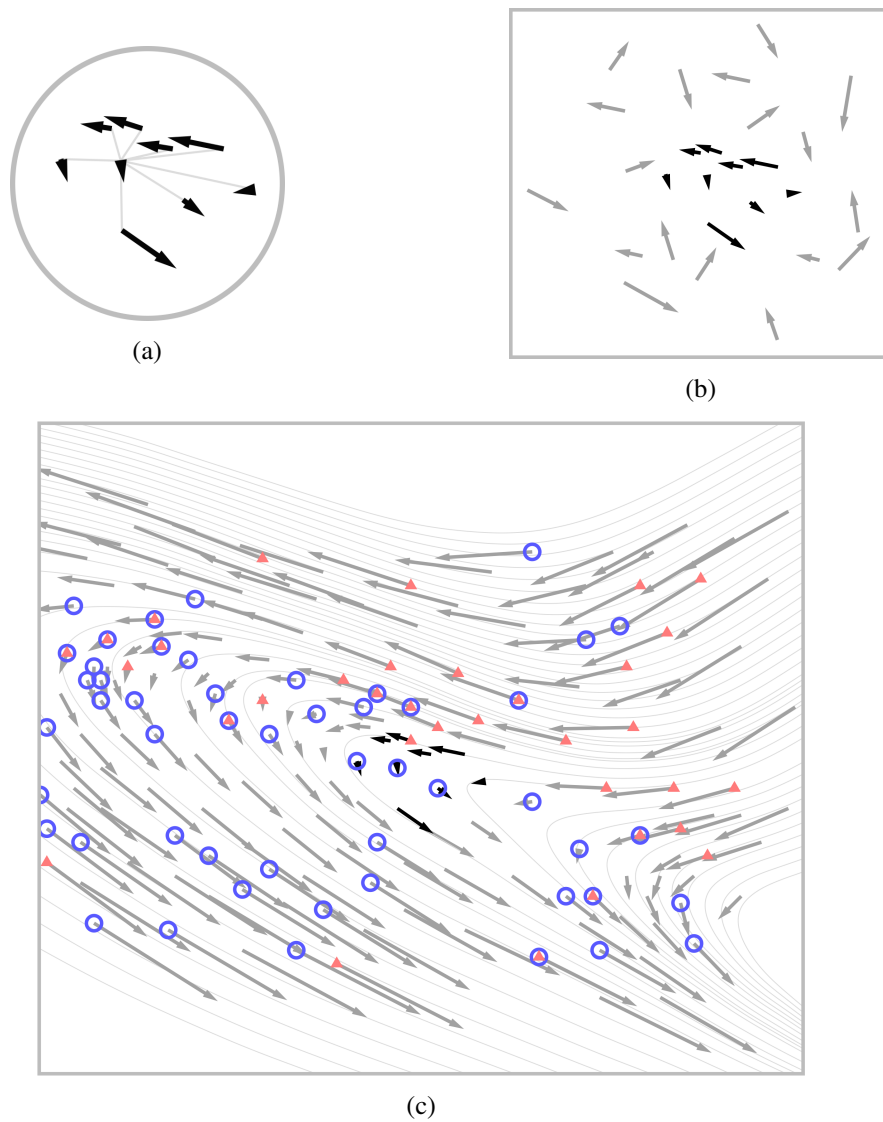


Figure 6.1: Illustration of the need for adaptive neighbourhood selection in vector validation. (a) Detail of a scrutinised vector and its closest neighbours. Only by expanding the local neighbourhood does it become clear these vectors belong to (b) outlier cluster or (c) a valid flow structure or. Symbols in (c) indicate which vectors are considered incoherent based on [67] (*blue circle*) and the median test of [96] (*orange triangle*).

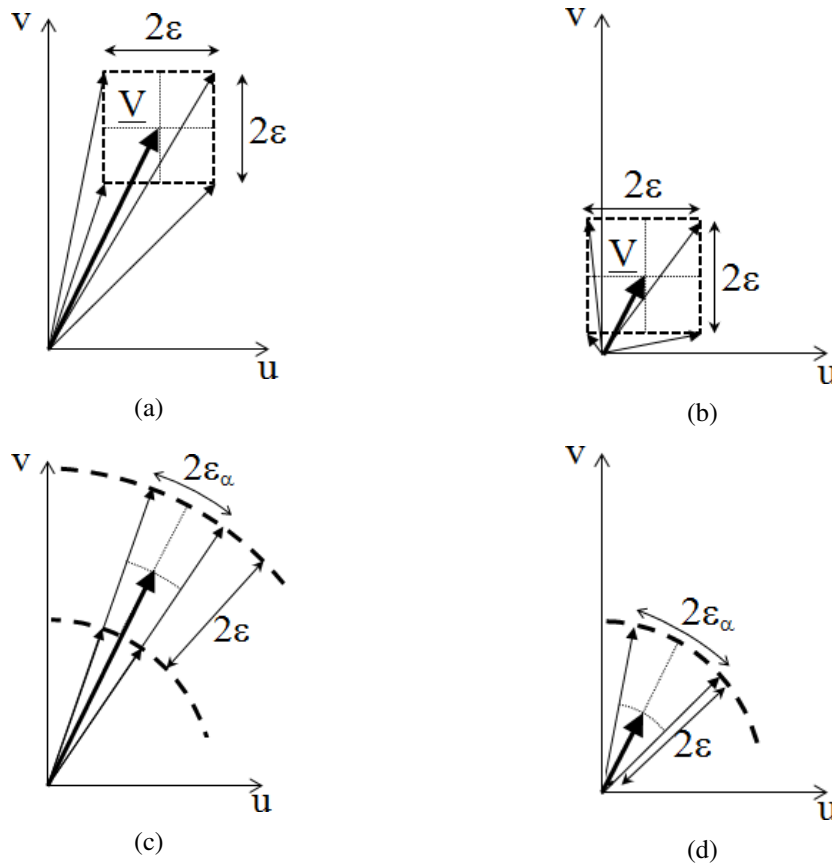


Figure 6.2: Acceptable vector variations for a fluctuation level  $\varepsilon$  in (a) both horizontal and vertical velocity components  $u$  and  $v$  respectively for larger and (b) small vector magnitudes. Limits in variations with adaptive angle variations  $\varepsilon_\alpha$  for (c) large and (d) small vector magnitudes.

[119], which is assimilated with the typical RMS level  $\varepsilon$  of 0.1 pixels in displacement data. A simple graphical representation in Figure 6.2a indicates that this fluctuation can lead to validation of vectors which are sufficiently different. More importantly, this disparity increases as the vector magnitude decreases (Figure 6.2b) necessitating a variable background fluctuation level proportional to the vector magnitude. On the other hand, imposing such adaptive fluctuation levels  $\varepsilon_\alpha$  in the angular direction while allowing tangential fluctuations of  $\varepsilon$  shows a promising reduction in potential vector disparity (Figure 6.2c-d). Such validation criteria are in line with the observation of [81] that human vision mainly identifies anomalies in patterns based on deviations in angle and magnitude.



Figure 6.3: Three steps in adaptive vector validation; based on a metric for vector coherency the number of vectors in the local vicinity is increased to provide a reliable basis for subsequent outlier detection.

## 6.4 Methodology

This chapter addresses the problematic of over- and under-detection when validating PIV and PTV data. To account for spatially varying vector densities and flow properties, an adaptive validation process with a three-tiered structure is proposed (Figure 6.3). The problem of under-detected outliers due to their aggregation in clusters is settled through a comparison of vectors with a variable number of neighbours based on flow coherence. Over-detection is dealt with by different improvements; an average Gaussian-weighted distance-based median estimation and a revised calculation of vector discrepancy. The starting point of the latter is the local median concept [119] because of its demonstrated robustness. In the current work, the residual calculation is altered on the basis of vector orientation and magnitude and implement an adaptive estimation of the acceptable level of noise-induced velocity fluctuations. The proposed methodology thus consolidates an adaptive weighted angle and magnitude threshold and will be referred to with the abbreviation AWAMT.

### 6.4.1 Coherence adaptive neighbourhood level

To define the required number of neighbouring vectors, this work introduces a heuristic for coherency. It is argued that the condition for a vector to be considered coherent is its agreement with a second-order surface fitted to its eight closest neighbours. It is important to underline that this coherence function is not used to discern correct vectors from outliers. Coherency is only used to predict the number of neighbours to be taken into account when estimating the local true flow velocity. The choice of the surface for the velocity components is of the form  $\Phi = a_0 + a_1y + a_2x + a_3xy + a_4y^2 + a_5x^2$ . To minimise the influence of outliers on the parabolic regression, a diagonal matrix  $W$  is implemented containing Gaussian weights utilising the deviation  $\sigma_j$  of each vector from the local median (including all nine vectors) as argument:

$$W_{j+1,j+1} = e^{-\frac{1}{2} \cdot \frac{\sigma_j^2}{\kappa_j^2}} \quad (6.1)$$

where the index  $j = 0 \dots 8$  is for each vector in the neighbourhood. The parameter  $\sigma_j$  is the difference between each vector and the median of the neighbours:

$$\sigma_j^2 = (u_j - u_m)^2 + (v_j - v_m)^2 \quad (6.2)$$

with  $u_m = \text{median}(u_j)$ ,  $v_m = \text{median}(v_j)$ . Finally, the coefficient  $\kappa_j$  is evaluated as:

$$\kappa_j = \varepsilon + 1/9 \cdot \sum \sigma_j \quad (6.3)$$

where  $\varepsilon$  is the background error. The coefficients of the parabolic surface fitted to the components of the nine vectors are then estimated in a least-squares manner:

$$a = (X^T W X)^{-1} (X^T W f) \quad (6.4)$$

where  $a = [a_0 \ a_1 \ \dots \ a_5]^T$  are the coefficient of the surface  $\Phi$ ,  $f$  are the velocities to be fitted  $f = [(u, v)_j]$ , and  $X$  are the positions of the points  $X = [1 \ y_j \ x_j \ x_j y_j \ y_j^2 \ x_j^2]$ .

The coherence  $C$  is subsequently quantified as the average residual between the scrutinised vector's components  $u_0$  and  $v_0$  and  $\Phi_{u,v}$  evaluated at the vector's location  $(x_0, y_0)$ , normalized with the median of the vector magnitudes  $|V|_m$  and background error  $\varepsilon$  [119];

$$C = \frac{C_u + C_v}{2} \quad (6.5)$$

with:

$$C_{(u,v)} = \frac{1}{(|V|_m + \varepsilon)^2} (\Phi_{(u,v)}(X_0, y_0) - (u_0, v_0))^2 \quad (6.6)$$

and

$$|V|_m = \text{median} \left( \sqrt{u_j^2 + v_j^2} \right). \quad (6.7)$$

The differentiation between coherent and non-coherent vectors is thereon done by thresholding; values of  $C$  inferior to the threshold  $T$  are classified as coherent. Although the threshold  $T$  can be adjusted to reflect the sensitivity of the number of neighbours to the size of clusters, performances were found to be relatively unaffected by the choice of  $T$  and a threshold of 10% was empirically found to yield a reliable and generally robust selection criterion.

Once the coherence function has been evaluated for all the data points in the vector field, the level of neighbourhood  $L$  for each data point is progressively increased considering the neighbours of the neighbours until at least half of the basis for comparison comprises coherent vectors. Note that  $L$  is a spatially varying parameter. To account for vector dependency due to correlation window overlap WOR, a minimum value for  $L$  is imposed which depends on WOR;

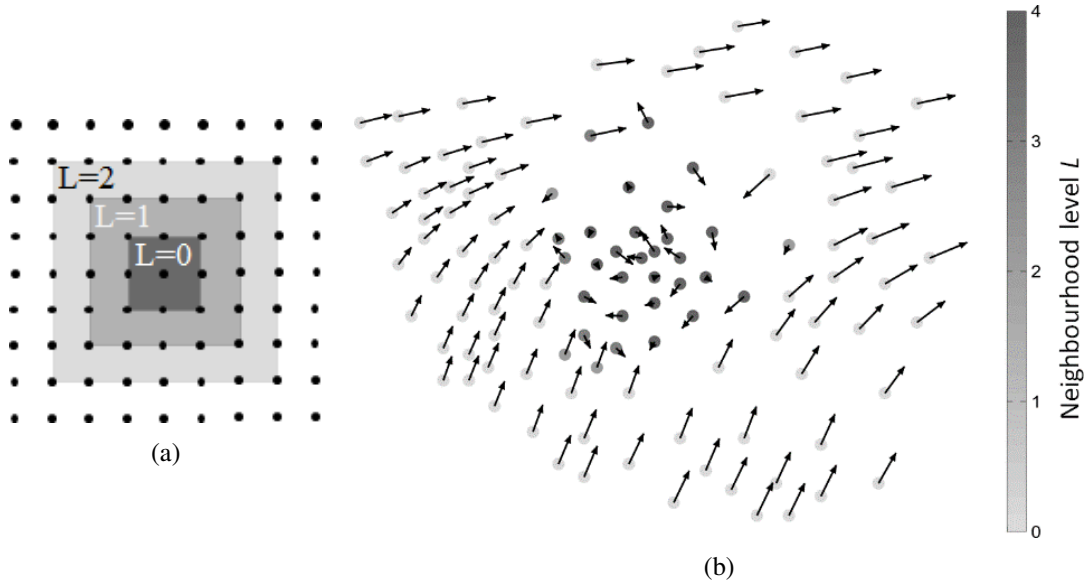


Figure 6.4: (a) Incremental neighbourhood level with  $L_{\min} = 0$  in case of a vector placement on the nodes of a structured grid (b) Illustration of the automatic evaluation of the required neighbourhood level  $L$  indicated by the greyscale. The central area of the flow field has been artificially contaminated with outliers. Towards the centre of the cluster the level increases, indicative of strongly in-coherent vectors necessitating an enlarged number of vectors for validation.

$$L_{\min} = \text{round}(4 \cdot \text{WOR}) \quad (6.8)$$

In the case of a structured grid, for example, the total number of neighbours  $N_o$  is readily given as  $N_o = (2L + 3)^2 - 1$  (Figure 6.4a). This stopping criterion ensures the median of an examined neighbourhood will return a reliable and coherent prediction for ensuing validation purposes since at least half the considered adjoining vectors are deemed coherent. The coherency check accordingly addresses the effects of under- and over-detection in the presence of outlier clusters and is straightforward to implement in existing validation routines.

Figure 6.4b illustrates the outcome of the coherency test when a cluster of outliers is surrounded by coherent vectors. The local neighbourhood level gradually increases towards the centre of the cluster, as indicated by the greyscale, such that each outlier can be compared with a reliable prediction even when surrounded by outliers.

#### 6.4.2 Adaptive angle and magnitude median normalised residual

While the methodology presented above will be shown to already improve standard validation processes, two additional modifications were implemented to the traditional normalised residual calculation to further lessen the number of over-detections; (1) average Gaussian weighted

median estimation and (2) comparison of direction and magnitude instead of Cartesian vector components. The underlying principle still remains consistent with common detection routines; a normalised residual is evaluated for each vector of the field based on the fluctuation of its neighbours and is used to discern correct vectors from outliers.

### Average-weighted median estimation

To identify the scrutinised vector as being erroneous, a comparison is required with an adequate estimation of the true, underlying flow vector. Such a prediction is ideally based on interpolation of neighbouring vectors. Because of the fundamental sensitivity of interpolation to the presence of spurious vectors, the median offers a more robust alternative. Following the selection of an adequate neighbourhood level based on coherency, a distance-based weighting is introduced when calculating a vector prediction from the  $N_o$  vectors to reflect their relative importance. While still inversely proportional with spacing  $d_i$  between the central vector located at  $(x_o, y_o)$  and those in the constrained vicinity, in this work the weights  $w_i$  are drawn from a Gaussian functional in line with adaptive Gaussian windowing (AGW) with optimal filter width  $\sigma$  [6];

$$w_i = \exp\left(\frac{-d_i^2}{\sigma^2}\right), \text{ with } \sigma = \frac{1.24}{N_o} \sum_{i=1}^{N_o} d_i \quad (6.9)$$

While these weights could already be used to obtain a vector prediction through the weighted median, a better estimation can be achieved by recalling the average in this estimation. The resulting average-weighted median operation will be symbolised in the following by  $\text{awmed}(\cdot)$ . The concept of this novel process is illustrated considering the velocity magnitude, i.e.  $\text{awmed}(|V|)$ , for the situation in Figure 6.5a where the central vector is adjoined by  $N_o$  neighbours (here  $N_o = 8$ ). The  $N_o$  velocity magnitudes (indicated by the vertical abscissa location of the  $\bullet$  symbols) are sorted in ascending order  $|V|^S$  with the corresponding weights  $w^S$ , attributed according equation 6.9, represented by the bar widths in Figure 6.5b. The weighted median (solid vertical line) is located at half the cumulative sum  $S_{w, N_o}$  of the weights  $w^S$  per its definition. To classify as an outlier, vectors will need a magnitude sufficiently different from this value. Such vectors will consequently have weights lying at the extremes of the set  $w^S$ . Vectors with weights lying in the immediate vicinity of the weighted median on the other hand cannot constitute outliers and can thus be used for reliable interpolation. An averaging interval  $\Delta w$  varying between 0 and 1 and centred on the weighted median is therefore introduced. The new, average-weighted median value is finally evaluated as the weighted average of those velocity magnitude values of which the bar widths overlap with the  $\Delta w$  interval. A description of  $\text{awmed}$  can be found in Algorithm 2 for pseudo code.

---

**Algorithm 2** Description of the average-weighted median in pseudo-matlab code. Refer to Figure 6.5 for a graphic display

---

```

1: procedure AWMED( $V, w, dw$ )           ▷ The awmed of  $V$  with weights  $w$  and interval  $dw$ 
2:   [ $sV, si$ ] = sort( $V$ );                 ▷ Sort Velocities
3:    $sw = w(si)$ ;                         ▷ Sort weights as velocities
4:    $Scum = cumsum(sw)$ ;                  ▷ Cumulative sum of weights
5:    $mid = 0.5 \cdot Scum(end)$ ;           ▷ Centre of the weights interval
6:    $dwh = dw \cdot mid$ ;                  ▷ Half averaging interval
7:    $iA = \text{find}(Scum \leq mid - dwh, 1, 'last') + 1$ ;   ▷ First averaging interval point
8:    $iB = \text{find}(Scum \leq mid + dwh, 1, 'last') + 1$ ;   ▷ Last averaging interval point
9:    $iA(\text{isempty}(iA)) = 1$ ;             ▷ Check first point
10:   $ind = (iA + 1) : (iB - 1)$ ;          ▷ Vector of interval points
11:  if ( $iB - iA \leq 1$ ) then
12:     $ind = []$ ;                          ▷ Check interval size
13:  end if
14:   $sV = [sV(iA); sV(ind); sV(iB)]$ ;     ▷ Build velocity and weight vectors
15:   $sw = [(Scum(iA) - mid + dwh); sw(ind); (mid + dwh - Scum(iB - 1))]$ ;
16:   $V_{awmed} = \text{sum}(sV \cdot sw) / \text{sum}(sw)$ ;   ▷ Weighted average of values in interval
17: end procedure

```

---

Note that this average-weighted median constitutes a form of weighted AGW interpolation but with improved reliability against outliers since the considered neighbours are less likely to be outliers. A unity value of  $\Delta w$  degenerates the operation into a weighted average of all neighbouring values whereas a value of 0 yields again the weighted median. As will be demonstrated in section 6.5, a value of  $\Delta w = 0.3 \sim 0.5$  is found to offer a generically conducive compromise between over- and under-detection (Figure 6.7).

### Angle and magnitude validation

The single validation parameter will be the normalised residual  $r^*$  combining the individual residuals  $r_\alpha$  and  $r_{|V|}$  related to respectively a vector's angle  $\alpha$  and magnitude  $|V|$ ;

$$r^* = \sqrt{r_\alpha^2 + r_{|V|}^2} \quad (6.10)$$

where

$$r_{|V|} = \frac{||V_o| - |V|_{awmed}|}{\text{median}(|V|_j - |V|_{awmed}) + \varepsilon} \quad (6.11)$$

$$|V|_{awmed} = \sqrt{\text{awmed}(u_j)^2 + \text{awmed}(v_j)^2} \quad (6.12)$$

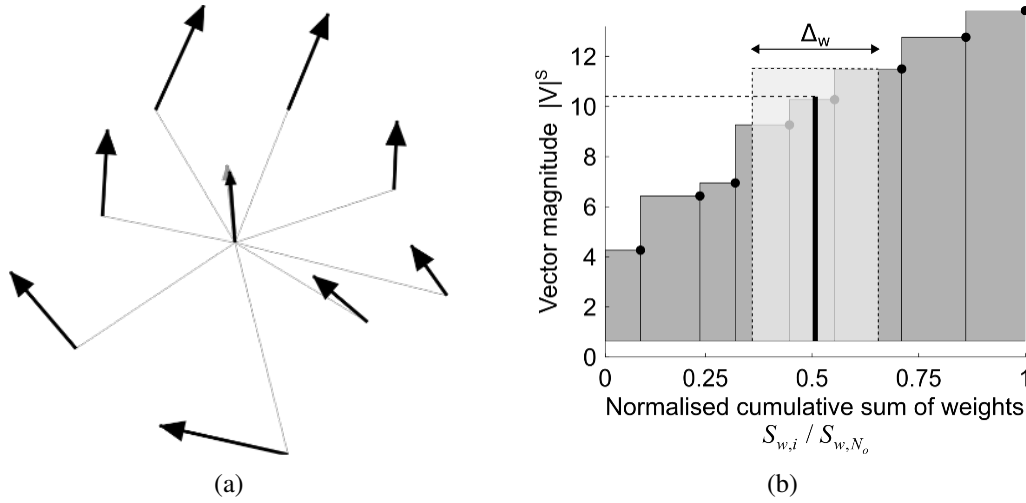


Figure 6.5: (a) Vector validation involves the comparison of the central (black) vector with the predicted vector (grey) on the basis of the neighbouring vectors. The prediction follows from an average-weighted median. (b) Weights in the  $\text{awmed}(\cdot)$  operator depend on the distance between the investigated vector and its neighbours following equation 6.9 and are reflected in the bar widths. An interval  $\Delta w$  is centred on the weighted median (solid black line) and the weighted average is taken of the data overlapping the defined interval.

$$|V|_j^2 = u_j^2 + v_j^2 \quad (6.13)$$

with the index  $j = 1 \dots N_o$  ranging in the variable number of neighbours  $N_o$ .

The denominator of  $r_{|V|}$  invokes the standard median operator since the median norm  $|V|_{awm}$  already applies a distance weighting. Parameter  $\varepsilon$  relates again to the measurement error and is indicative of the background error for the vector magnitude ( $\varepsilon \approx 0.1$  pixels). The normalised residual in angle is calculated in a similar manner;

$$r_\alpha = \frac{\alpha_o^*}{\text{median}(\alpha_j^*) + \varepsilon_\alpha} \quad (6.14)$$

with

$$\alpha_j^* = \min(|\alpha_j - \alpha_{awm}|, 2\pi - |\alpha_j - \alpha_{awm}|) \quad (6.15)$$

The choice of  $\alpha_j^*$  ensures angle differences to be smaller than  $\pi$  radians. Value  $\alpha_j$  is the simple arc-tangent of the displacement components. Angle  $\alpha_{awm}$  considers the average-weighted median of the individual phases to negate any bias originating from vector magnitudes;

$$\alpha_j = \tan^{-1} \left( \frac{v_j}{u_j} \right) \quad \text{and} \quad \alpha_{awm} = \tan^{-1} \left( \frac{\text{awmed}(\sin(\alpha_j))}{\text{awmed}(\cos(\alpha_j))} \right) \quad (6.16)$$

Misdetection of outliers is addressed by automatic adaptation of the acceptable RMS level in  $\alpha_j$  to predicted vector magnitude; the minimum measurable angle is defined by the angle of the triangle formed by  $|V|_{\text{awm}}$  and  $\varepsilon$ ;

$$\varepsilon_\alpha = \tan^{-1} \left( \frac{\varepsilon}{|V|_{\text{awm}}} \right) \quad (6.17)$$

Once the normalized residual has been evaluated throughout the vector field,  $r^*$  values below a threshold of 2 are considered non-valid. This value is in agreement with the findings of [119] and [24].

### Computational effort

The selection of the adequate neighbourhood level and the evaluation of the average-weighted median can be expected to come with some computational overhead. To estimate the increase in processing time as a result of the elaborated vector validation, the evaluation of the experimental images discussed in further detail in section 6.6 are considered. The total processing time for the porous disc recordings with AWAMT increased by a factor of 1.01 relative to the traditional NMT. Similarly, the ratio in computation time between NMT and AWAMT for the analysis of the 280 image recordings related to the supersonic jet equalled 1.05. Stand-alone, the proposed validation based on magnitude and angle, although strongly dependent on flow type, number of outliers and clustering factor, was approximately 4 times more computationally intense compared to the standard routine based on Cartesian components. The above heuristics are only exemplary and pertinent to the current test cases. Nevertheless, results imply the computational expense of the more elaborate AWAMT method to be marginal relative to the overall process and will be shown to be outweighed by the achievable improvement in measurement accuracy in the remainder of this chapter.

## 6.5 Numerical assessment

### 6.5.1 Evaluated test cases

In order to assess the proposed adaptive vector validation in terms of ameliorated under- and over-detection ratios, deterministic velocity fields were contaminated with spurious vectors.

Three flow cases were considered; a turbulent channel flow, a cellular vortex and isotropic turbulence (Figure 6.6). The first two flow fields were obtained from the PIV Challenge website ([99], [100]). The PIV images were analysed with an adaptive PIV algorithm [105]. This

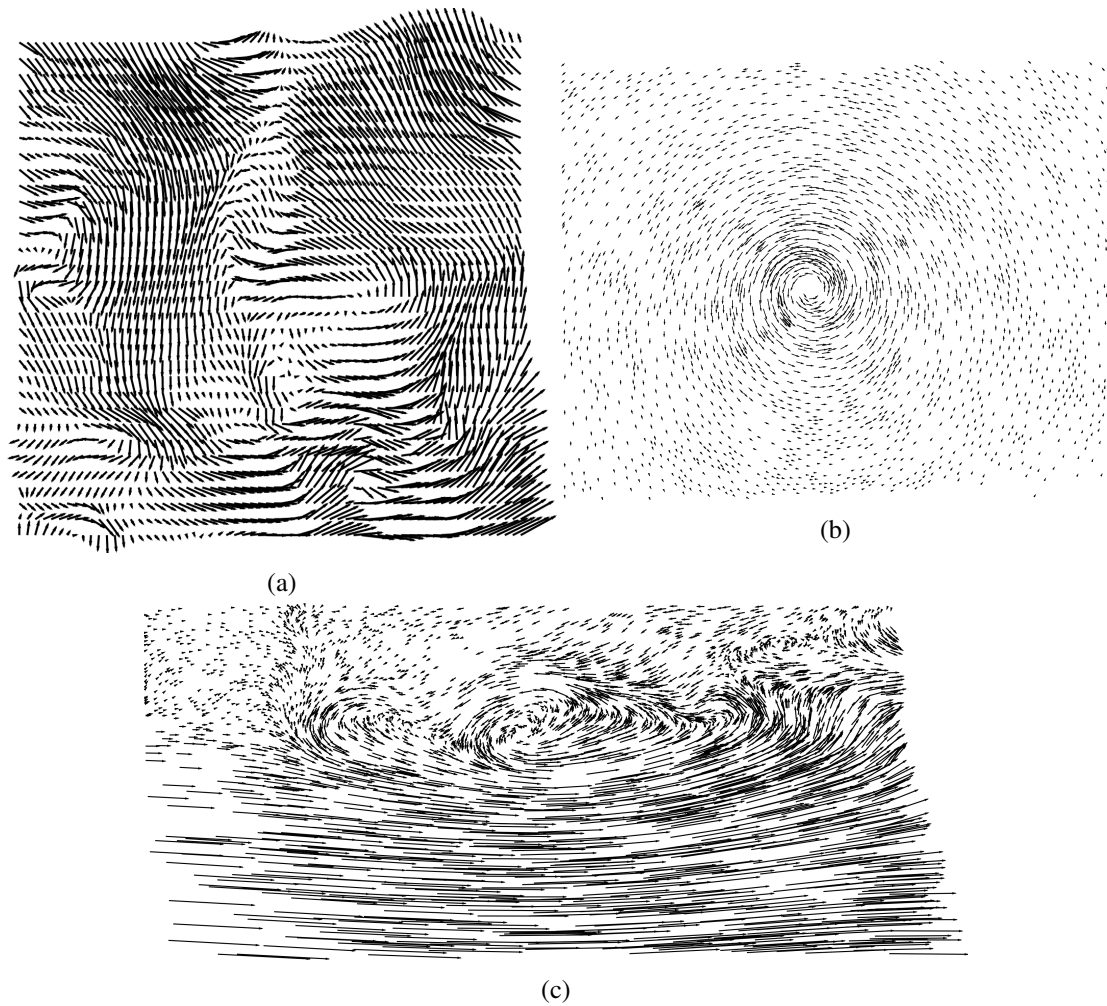


Figure 6.6: Flow test cases used to assess vector validation algorithms (a) turbulent channel flow [99] (b) isolated vortex [100] (c) DNS simulation of isotropic turbulence [53].

algorithm locates and sizes correlation windows on the basis of local seeding density and velocity gradients, thus returning velocity data on an unstructured grid. Images were initially sampled with square correlation window sizes of 128 pixels and recursively refined. To enforce a very gradual reduction in interrogation window size, 20 refinement iterations were imposed to yield a minimum final window size of 15 pixels. Bias of the results towards any of the assessed outlier detection routines was avoided by manually inspecting at each intermediate iteration vector areas producing high levels of local variation. Potential outliers were accordingly replaced by the local median. The third test case consisted of readily available Direct Navier-Stokes velocity data provided on a structured grid from the Johns Hopkins Turbulence Databases [53].

The vector fields were selected as to cover a wide variety of vector field characteristics (Figure 6.6). Both the channel flow and vortex are characterised by spatially non-isotropic flow features. The vortex represents an isolated region of strong velocity gradients, while the turbulent channel flow portrays besides a region of circular motion a strong spatial variation in flow properties. In the outer area the flow is quasi-uniform, whereas approaching the wall the vector field becomes more turbulent with accompanying variations in both vector magnitude and direction. The isotropic turbulence case, on the other hand, features a spatially more uniform distribution of vector magnitudes and directions.

To simulate realistic velocity fields containing outliers, each of the three final velocity fields was corrupted with spurious vectors of prescribed characteristics. In particular two pertinent parameters were varied in line with [96]; outlier magnitude and clustering. When replacing a vector  $V_o = (u_o, v_o)$  with a spurious element  $V_s = (u_s, v_s)$ , the outlier norm is defined to be a percentage  $M$  of the local vector magnitude. The erroneous velocity components are then calculated by multiplying the norm with a random number distributed uniformly between -1 and 1,  $U([-1, 1])$ , resulting in an outlier with random direction and deviating a certain percentage in magnitude from the correct local velocity;

$$u_s = \frac{|V_s|}{\sqrt{2}} \cdot U([-1, 1]), v_s = \frac{|V_s|}{\sqrt{2}} \cdot U([-1, 1]) \quad (6.18)$$

with

$$|V_s| = M|V_o| = M\sqrt{u_o^2 + v_o^2} \quad (6.19)$$

The clustering factor  $C_f$  is defined as the number of randomly imposed neighbouring vectors, each with magnitude ratio  $M$  (Figure 6.7). Clusters were distributed randomly across the vector fields. In the simulations  $C_f$  is varied between 1 and 40, where a value of one equals randomly located isolated outliers. While it can be argued that cluster sizes of 40 vectors are rare, cluster sizes in the order of 10 are commonly encountered when dealing with image regions of poor quality, low seeding or insufficient spatial resolution in regions of strong velocity

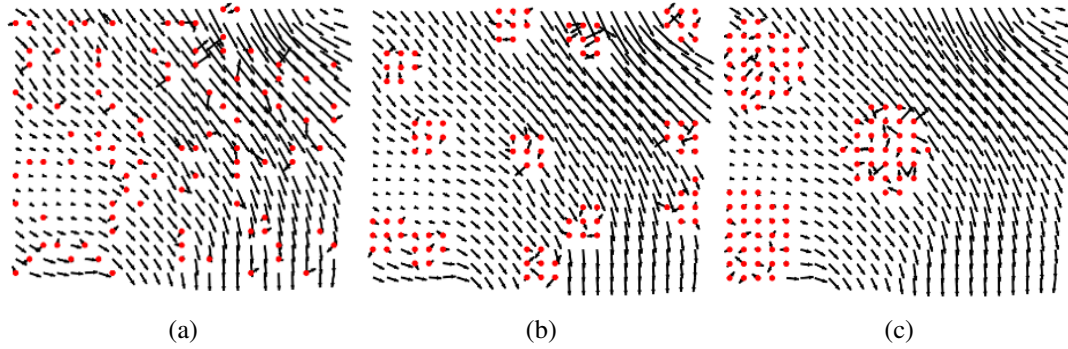


Figure 6.7: Sample vector field with imposed outliers located at red circles, with  $M = 1$  (a)  $C_f = 1$ , (b)  $C_f = 8$  and (c)  $C_f = 32$ .

gradients. Nevertheless, the extent of  $C_f$  allows the detection of any asymptotic tendency. The number of imposed erroneous vectors was kept constant irrespective of  $C_f$  at at least 15% the total number of vectors in accordance with good PIV practice. Above this critical value, experimental settings would generally have to be re-evaluated to possibly mitigate the amount of outliers and enhance measurement reliability.

For each outlier parameter setting, 3000 Monte-Carlo simulations were performed to ensure convergence in statistical findings. Results are presented in terms of over- and under-detection ratios  $R_o$  and  $R_u$  respectively. Parameter  $R_o$  is defined as the ratio between the number of correct vectors wrongly detected as outliers ( $N_w$ ) and the total number of vectors (valid and invalid) in the field  $N_t$ , while  $R_u$  expresses the ratio between the number of missed outliers ( $N_m$ ) and the imposed number of spurious vectors ( $N_i$ ).

$$R_o = \frac{N_w}{N_t} \text{ and } R_u = \frac{N_m}{N_i} \approx \frac{N_m}{0.15 \cdot N_t} \quad (6.20)$$

In addition, the ratio between  $N_m$  and  $N_t$ , denoted by  $R_u^*$ , allows the calculation of the percentage of erroneously invalidated correct vectors ( $N_w$ ) with respect to either the number of correct vectors ( $N_c$ ) or the number of imposed outliers ( $N_i$ );

$$\frac{N_w}{N_c} = \frac{R_o N_t}{N_t - N_i} = R_o \cdot \left(1 - \frac{R_u^*}{R_u}\right)^{-1} \quad (6.21)$$

with

$$\frac{N_w}{N_i} = \frac{R_o R_u}{R_u^*} \quad (6.22)$$

and

$$R_u^* = \frac{N_m}{N_t}. \quad (6.23)$$

Table 6.1 presents an overview of the definition of the different parameters for clarity.

Symbol	Description	Definition
$N_c$	number of correct vectors	
$N_i$	number of imposed outliers	
$N_t$	total number of vectors	$= N_i + N_c$
$N_w$	number of correct vectors classed as outliers	
$N_m$	number of missed outliers	
$R_o$	over-detection ratio	$= N_w/N_t$
$R_u$	under-detection ratio	$= N_m/N_i$
$R_u^*$	re-scaled under-detection ratio	$= N_m/N_t$

Table 6.1: Parameters used in validation method assessment.

### 6.5.2 Validation algorithm performance

Figure 6.8 presents the results of Monte-Carlo simulations to illustrate the effect of  $\Delta w$  in the average-weighted median on the validation performance in terms of over- and under detection. The relevant flow fields were degraded with outliers of randomness  $M = 5$  and clustering factor of 1. Though not presented, observable tendencies remained consistent when altering either  $M$  or  $C_f$ .

For small  $\Delta w$  the average-weighted median serves as a standard distance-weighted median providing a robust outlier detection criterion in terms of under-detection. Nevertheless, this approach is less efficient than interpolation. Increasing  $\Delta w$  will assimilate the  $awmed(\cdot)$  with an adaptive Gaussian weighted interpolation, utilising only vectors which are less likely to be outliers and warrant a reliable interpolation. When increasing  $\Delta w$  more vectors, including potential outliers, are again taken into account thereby reducing the reliability of the interpolation. This renders the validation less stringent, under-detecting more vectors (Figure 6.8a) yet simultaneously classifying fewer correct data values as erroneous (Figure 6.8b). Detection ratios  $R_u$  and  $R_o$  will consequently obey opposite behaviours with varying  $\Delta w$ . Figure 6.8 corroborates  $R_u$  to increase in an exponential fashion whereas the over-detection ratio shows a quasi-linear decline. Given that the depicted tendencies are quasi flow-case independent, a value of  $\Delta w = 0.3 \sim 0.5$  is proposed as a generally conducive compromise to minimise both the under- and over-detection.

Figures 6.10-6.12 present the under- and over-detection ratios defined in equation 6.20 with varying sizes of outlier clusters for the three flow cases when fixing the magnitude ratios  $M$  respectively to 0.1, 1 and 10. Results of the new algorithm (AWAMT) are juxtaposed with the NMT [119] and DW-NMT method [24]. To stress the importance of the adaptivity introduced in the current work, both methodologies have been extended to include the coherency test and automatically select the adequate number of neighbours in the validation process. These extended routines are annotated as ANMT and ADW-NMT respectively. Although cluster sizes

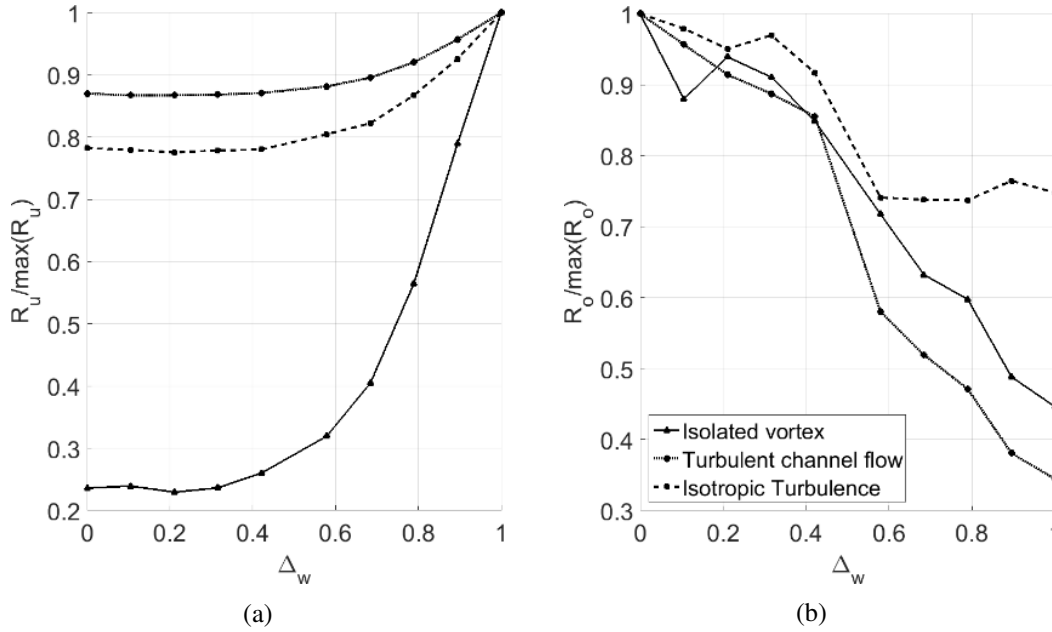


Figure 6.8: Evolution in normalised (a) under-detection and (b) over-detection ratios (normalisation by maximum value) with varying  $\Delta_w$  for flow fields representing an isolated vortex [99], turbulent channel flow [100] and DNS simulation of isotropic turbulence [53].

$C_f$  were incremented in steps of one, data symbols are depicted sporadically to retain figure clarity.

Independent of the considered flow case, all figures substantiate the detrimental influence of outlier clusters. With growing cluster size,  $R_u$  initially rises steeply up to  $C_f = 10$ . Depending on the  $M$ -value, for larger clusters either a quasi-constant level is reached or  $R_u$  continues to grow more gradually. For the turbulent channel flow case with  $M = 0.1$  (at  $C_f = 10$ ) this results in the inability to detect up to 90% of imposed outliers with NMT or DW-NMT (Figure 6.10). By increasing  $M$ , the outliers' disparity grows, facilitating their detection. Figures 11-13 imply the overall levels of  $R_u$  to decrease by roughly a factor  $0.66 \sim 0.75$  for every increase in order of magnitude of  $M$ . At  $M = 1$  this still leaves 10-40% of the individual ( $C_f = 1$ ) spurious vectors undetected by the NMT method, deteriorating to 40-60% and above for clusters containing more than 10 vectors.

An asymptotic behaviour with  $C_f$  is also observed in the over-detection ratio  $R_o$ , though strongly dependent on the flow type and randomness level. For  $M = 0.1$  application of NMT to the isolated vortex for example returns a ratio  $N_w/N_i$  growing from 15% at  $C_f = 1$  to 23% at  $C_f = 10$ , reaching a quasi-constant level of 20% for larger  $C_f$ . When augmenting  $M$  to 10 these ratios alter to 11%, 15% and 16% respectively. Data related to the DNS vector field for  $M = 0.1$  on the other hand results in  $N_w/N_i = 0.026$  ( $C_f = 1$ ), 0.033 ( $C_f = 10$ ) and 0.013 ( $C_f = 40$ ) while ratios become negligible (less than 0.05%) for  $M = 10$ . The observable flow dependency can

be explained as follows. With exception of the central area, neighbouring vectors in the vortical flow field show a high degree of similarity. As a result any small discrepancy can render a vector invalid leading to an elevated over-detection. Because of their inherent nature, the turbulent flows on the other hand allow slightly more variation in each vector before it is identified as spurious. Over-detection is also prominent at the edge of outlier clusters because a correct velocity estimate may seem incoherent with its nearest (spurious) neighbours as illustrated in Figure 6.9.

Adopting a distance-based weighting (DW-NMT) offers an improvement in over-detection only in case of unstructured data in accordance with the findings of [24]. The current figures suggest such achievements to be again strongly reliant on flow-case and randomness magnitude  $M$ . The cellular vortex case for example indicates DW-NMT to lower the over-detection  $R_o$  from approximately 2.5% with NMT to 1% across the range of  $M$  values (Figures 11-13). Such gains are however less prominent in the channel flow and of course nihil for structured DNS data. Moreover, distance-weighting is observed to adversely address under-detection as related  $R_u$  values are consistently higher or at least on a par with NMT, even in case of isolated spurious vectors ( $C_f = 1$ ).

The presented results advocate the beneficial impact when implementing an adaptive neighbourhood extent (exemplified in Figure 6.9) in NMT and DW-NMT. At low  $M$  under-detection can be reduced by roughly a factor 1.5; when applied to the wall turbulent flow field for example, for a cluster of 10 vectors  $R_u$  drops from 90% to 65% and from 80% to 65% in case of the DNS flow (Figure 6.10). Improvements become most remarkable at higher levels of randomness where  $R_u$  is lowered by at least a factor 4; from 30% to 7% at  $C_f = 10$  and  $M = 10$  for the channel flow and from 20% to 4% for the DNS case (Figure 6.12). Improvement is also achieved in  $R_o$  as a result of the added adaptivity, though the relative improvement drops with higher  $M$ -values. Irrespective of cluster size, coherency adaptivity lowers the NMT-related  $R_o$  level. At  $M = 1$  for example by 0.1% for the vortex field and 0.01% for the channel flow, whereas for  $M = 0.1$  the differences in the vortex flow amount to 1% at  $C_f = 5$  and 0.3% at  $C_f = 40$ .

Maintaining a constant cluster size of 8 vectors and varying the outlier randomness further corroborates the neighbourhood adaptivity to attain under- and over-detection levels sufficiently below those of the standard approaches (Figure 6.12). Under-detection ratios of traditional validation routines asymptotically reach values of 20% with increasing  $M$  compared to levels approaching 0% when implementing adaptivity. For the case of the isolated vortex, NMT retains 2% over-detection whereas the original and extended DW-NMT and AWAMT reach levels below 0.8%. This is an important finding as it implies traditional validation routines are, contrary to those enhanced with adaptivity, unable to identify all spurious vectors within the cluster, independent of their magnitude. While appreciable gains can be achieved in

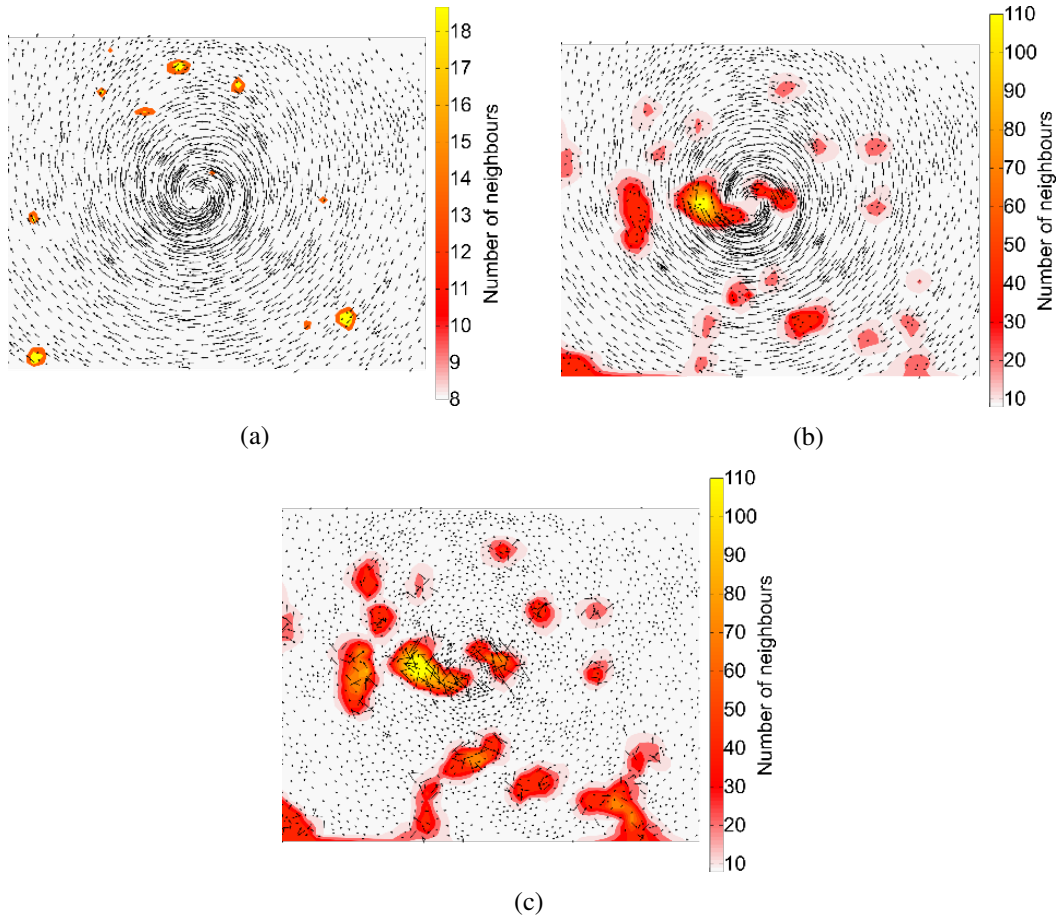


Figure 6.9: Influence of cluster-size and outlier magnitude on neighbourhood level  $L$  in the case of the vortex flow (a)  $C_f = 1$  (isolated outliers),  $M = 0.1$  (b)  $C_f = 10$ ,  $M = 0.1$  (c)  $C_f = 10$ ,  $M = 10$ . With increasing size of outlier clusters and outlier magnitude, the number of neighbours  $N_o$  considered in the average-weighted median operation increases adaptively. Increased neighbourhood levels emanate from the outliers to surrounding vectors, indicative of their non-localised detrimental influence towards over-detection.

$R_u$ , all validation methods reach comparable asymptotic values in over-detection when applied to more turbulent flows.

Validation on the basis of residuals in magnitude and orientation allows the AWAMT approach proposed within this work to further reduce over- and under-detections. The potential advantages will be particularly noticeable at lower  $M$  and displacement magnitudes in the order of one pixel or below. Figure 6.10 advocates the adaptation of the background fluctuation level in vector phase to its magnitude to offer noticeable improvements particularly at  $M = 0.1$ . Across the various flow fields AWAMT consistently yields the lowest  $R_u$  and  $R_o$  levels compared to the standard and enhanced median threshold techniques. Under-detection levels are overall lessened by roughly 10% compared to the improved ANMT and ADW-NMT. Changes in  $R_o$  are flow dependent but vary between 0.15% and 0.3%. With increasing  $M$  relative improvements obtained by adding the magnitude and angle validation diminish compared to the benefit of purely a varying neighbourhood.

To summarise, the performed assessment has shown the traditional NMT and DW-NMT to be highly sensitive to the presence of outlier clusters especially in terms of under-detection. Although over-detection is prominent in the vicinity of such clusters, it is strongly dependent on the local level of velocity fluctuation and lowers as randomness increases. By adapting the considered neighbourhood level to local flow coherency, under-detection can be improved considerably in the case of large outlier clusters and strong spatial velocity variations while gains in over-detection are most noticeable with smaller displacements. Further improvements in under- and over-detection are achieved by adapting the validation process to consider vector magnitude and orientation, whereby ameliorations are particularly noticeable in case of smaller displacements. Incorporation of an adaptive weighted angle and magnitude threshold in the vector validation process is subsequently expected to be most beneficial to reduce under- and over-detection in turbulent flows, flows containing strong velocity gradients, image sequences with small particle image displacements and image recordings of lower quality which would give rise to outlier clusters. This will be confirmed by the experimental assessment in the following section.

## 6.6 Experimental application

Vector validation can have a strong influence on the outcome of a PIV analysis. Because of its iterative nature, the influence of non-detected spurious vectors or incorrectly replaced velocities is propagated into the image deformation stage with associated consequences. To assess the new vector validation algorithm in a real application, the adaptive routine has been applied to experimental PIV images of the near-wake flow behind a porous disc and over-expanded supersonic jet and compared with the conventional NMT technique.

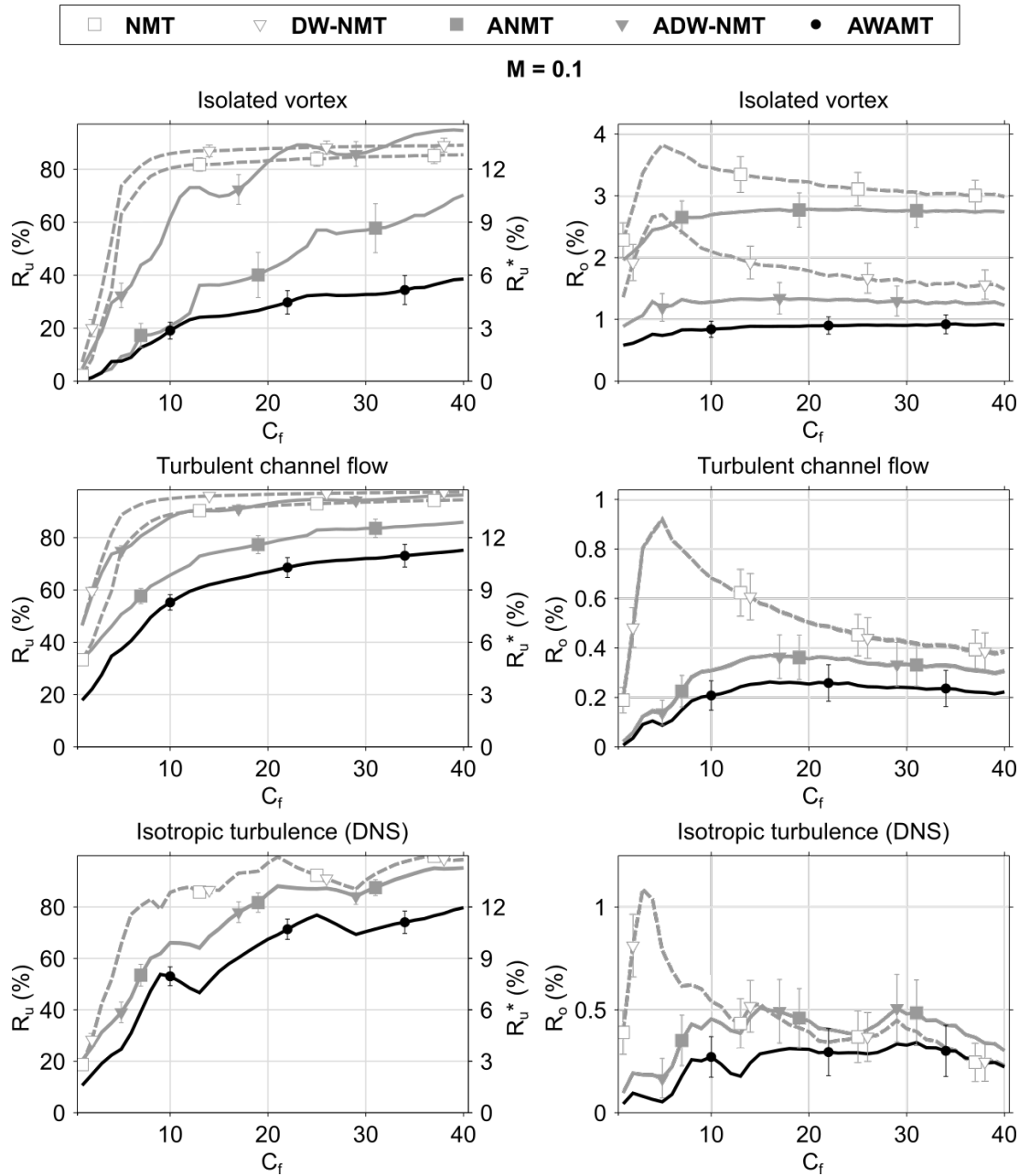


Figure 6.10: Comparison between universal outlier detection (NMT), distance-weighted outlier detection (DW-NMT), NMT and DW-NMT extended with a variable neighbourhood (ANMT and ADW-NMT) and the proposed adaptive weighted angle and magnitude thresholding (AWAMT) in terms of the evolution in under-detection  $R_u$  and  $R_u^*$  (left column) and over-detection  $R_o$  (right column) with increasing cluster size of outliers for the case of unstructured velocity data of a cellular vortex (top row), turbulent channel flow (middle row) and structured DNS simulation data of isotropic turbulence (bottom row). The maximum magnitude of the outlier was set at 10% of the local velocity ( $M = 0.1$ ).

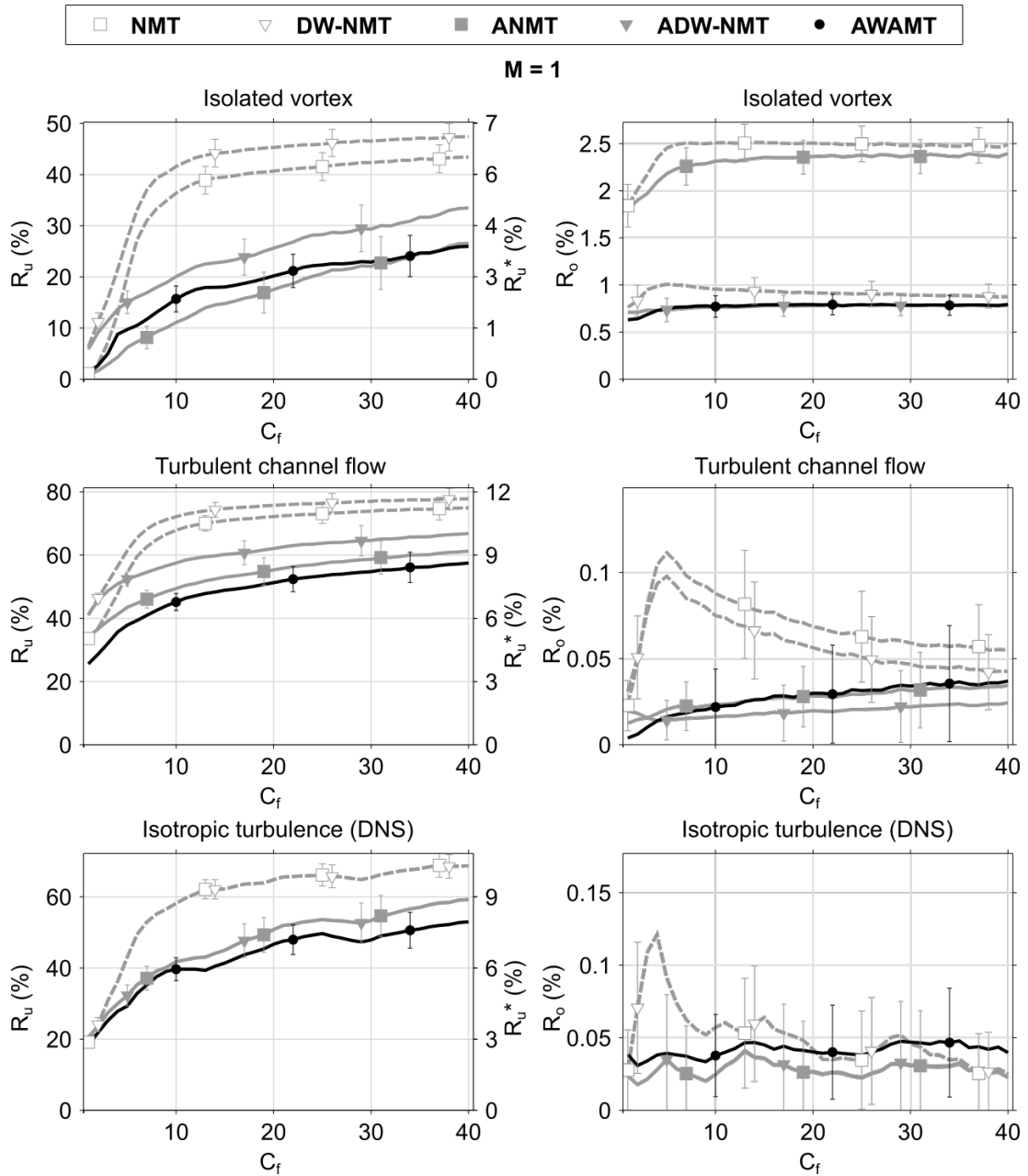


Figure 6.11: Comparison between vector validation methodologies applied to velocity fields contaminated with imposed outlier clusters of varying size and fixed magnitude. The maximum magnitude of the outlier was set at 100% of the local velocity ( $M = 1$ ). See Figure 6.10 for further details and legend entries.

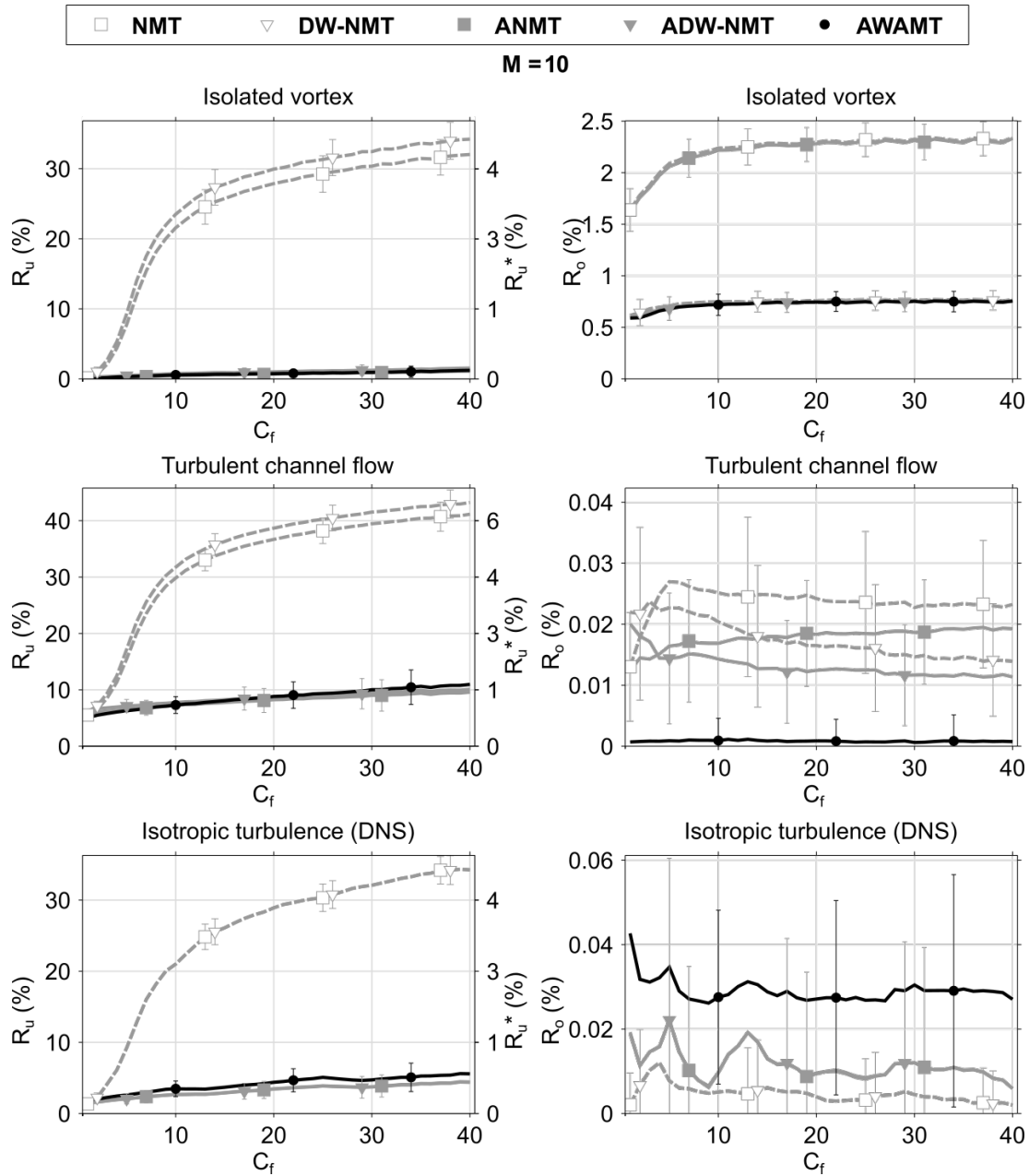


Figure 6.12: Comparison between vector validation methodologies applied to velocity fields contaminated with imposed outlier clusters of varying size and fixed magnitude. The maximum magnitude of the outlier was set at 10 times the local velocity ( $M = 10$ ). See Figure 6.10 for further details and legend entries.

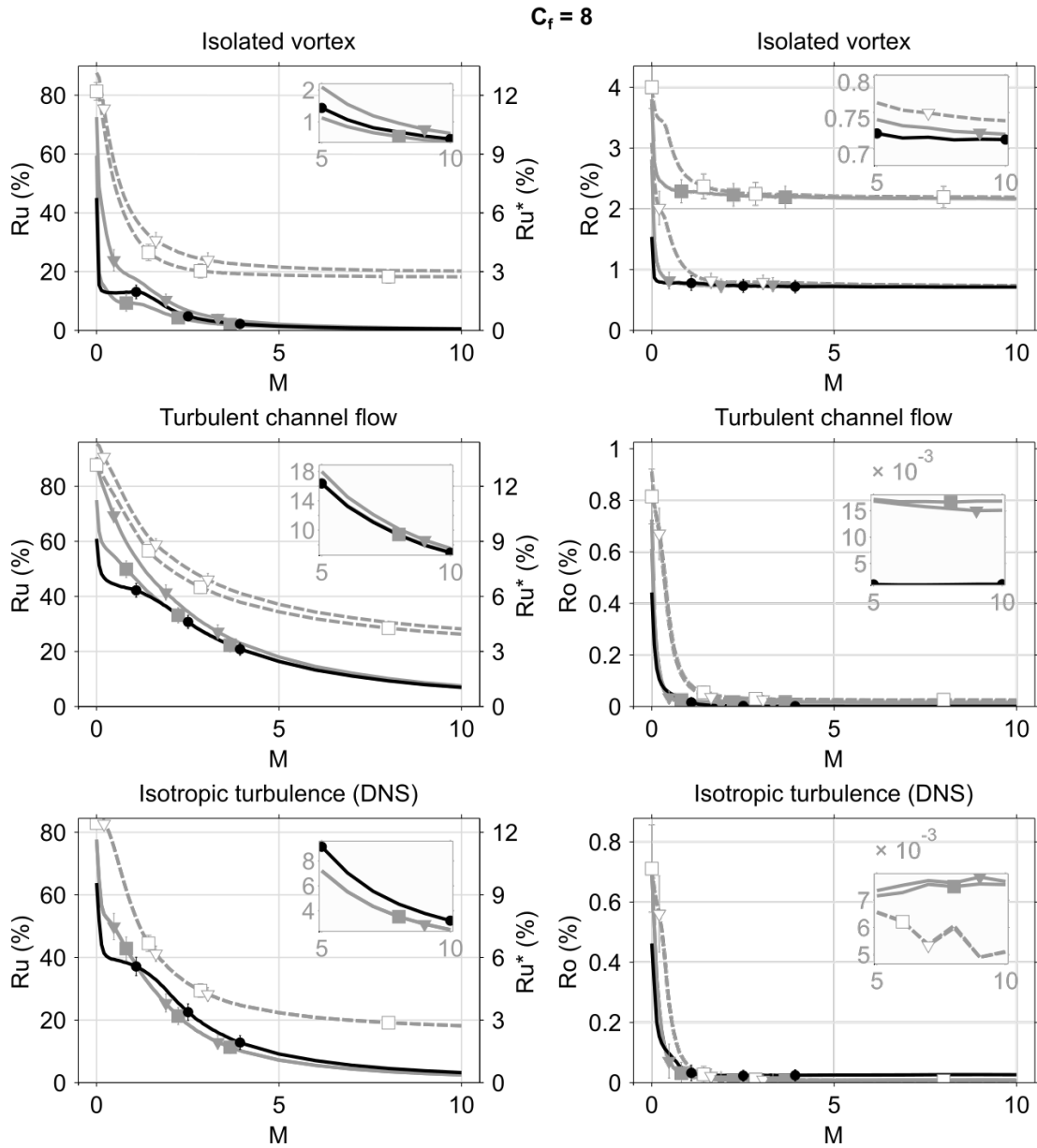


Figure 6.13: Comparison between vector validation methodologies applied to velocity fields contaminated with imposed outlier clusters of fixed size ( $C_f = 8$ ) and varying magnitude. See Figure 6.10 for further details and legend entries.

### 6.6.1 Porous disc

PIV measurements were performed with a 2D2C Dantec Dynamics PIV system on the image dataset described in Section 5.5 of Chapter 3. In total 500 image recordings were analysed with a standard PIV processing routine incorporating iterative correlation window size reduction [89] and image deformation using quintic B-spline interpolation [10]. Correlation windows were reduced in four iterations to final sizes of  $37 \times 37$  pixels<sup>2</sup> ( $\sim 2.4 \text{ mm} \times 2.4 \text{ mm}$ ) with an overlap of 50% resulting in a structured vector field with approximately 1.2 mm grid spacing. For every iteration, the obtained vector field was subjected to validation utilizing either the universal outlier method (NMT) or the newly proposed adaptive weighted angle and magnitude threshold technique (AWAMT). Invalidated vectors were subsequently replaced with the median of the eight closest neighbours.

The undersampled ensemble-averaged flow field behind the porous disc is detailed in Figure 6.14 and shows complex flow features. Flow with momentum higher than the free-stream is ejected from the pores and interacts with the outer shear layers to create zones of recirculating flow on the upper and lower part of the disc. Between approximately  $1.2 \cdot D_{\text{disc}}$  and  $2 \cdot D_{\text{disc}}$  a large zone of reverse flow appears. This region is formed by the merging of the outer shear layers, forging two stagnation points along the centreline at the zone edges. In addition, two outward vortices are present within the reverse flow zone. The near wake pushes the free-stream outwards similar to the bluff body wake behind solid discs [48], which merges again at approximately  $2.5 \cdot D_{\text{disc}}$  downstream initiating wake recovery. It should be noted that such features are only present in the time-average. From an instantaneous perspective the jets display a flapping behaviour, giving rise to the appearance of the multiple stagnation points in the ensemble average. This flapping is in reaction to the vortex shedding from the disc which takes place at random locations along the circumference [61]. The flapping in addition gives rise to mobile zones of turbulence and accompanying velocity gradients, making the flow a challenging test case for vector validation.

Figure 6.15 juxtaposes contour maps quantifying the percentage of replaced vectors in the final iteration,  $R = R_o + R_u^*$ , by the NMT and AWAMT method across the image ensemble. Since outliers are replaced, this quantity  $R$  is indicative of the vector validation performance in detecting outliers. The detrimental effect of laser reflections can be observed in the vicinity of the disc for both validation methods. It was argued that existing vector validation routines are susceptible to over-detection in regions of higher turbulence intensity. Figure 6.15 attests especially the bounding shear-layers of the disc and jets, and jet interaction region to be attributed a higher percentage of outliers compared to the bulk. However, Figure 6.15 also demonstrates the AWAMT approach to consistently detect fewer outliers in these regions compared to NMT. This supports the Monte-Carlo simulations which indicated AWAMT to abate the number of undetected outliers and lower the number of over-detections. In the shear-layers of the jets

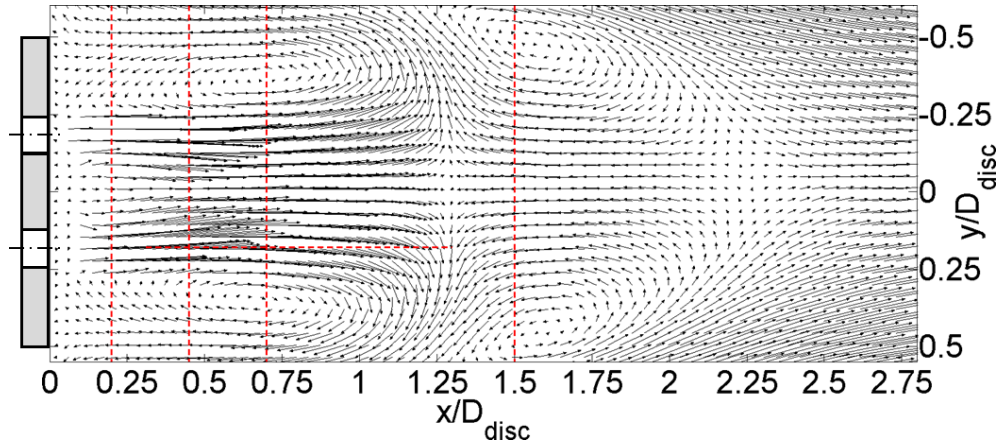


Figure 6.14: Ensemble-averaged flow field (under-sampled by a factor 3 in both directions for clarity) of 500 snapshots of the near-wake behind the porous disc. Dashed red lines indicate the locations of the extracted velocity profiles.

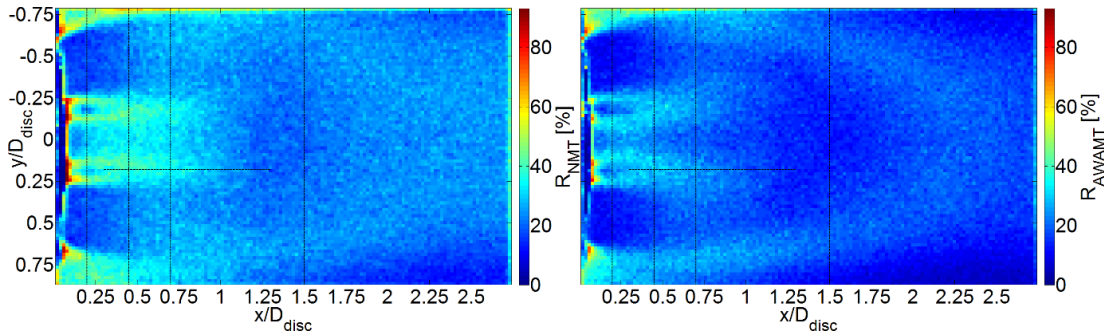


Figure 6.15: Comparison of the number of replaced vectors across the PIV data series (500 images) as per the outcome using (left) NMT vector validation (right) AWAMT vector validation. Dashed lines indicate the locations of profile extraction.

exiting from the perforations for example, NMT invalidates 60% of the vectors compared to 30% by AWAMT. In the outer shear-layers AWAMT lowers the number of replaced outliers on average from 30% to 15%.

The advantage of coherence adaptivity in terms of measurement accuracy is highlighted in Figures 6.16 and 6.16 where ensemble averaged profiles in horizontal velocity and longitudinal turbulence obtained with NMT, ANMT and AWAMT are juxtaposed. Despite the higher uncertainty in second-order statistics as a result of the limited number of velocity fields, tendencies in differences between the validation methods will prevail and can be used to qualitatively assess performances. While velocity profiles at  $x/D_{\text{disc}} = 0.2$  are on a par in the regions  $|y/D_{\text{disc}}| < 0.1$  and  $|y/D_{\text{disc}}| > 0.25$ , a larger disparity between the validation methodologies can be observed in jet centreline velocities. Whereas ANMT and AWAMT yield a peak velocity ratio of approximately 1.05 and 1.1 respectively, NMT predicts a ratio of approximately 0.8. The observed modulation in jet velocity thus shows a strong correlation with  $R$  as the

inherent vector re-interpolation will introduce a smoothening effect. The coherence adaptivity in ANMT and AWAMT reduces over-detection and limits the assimilated modulation, corroborating the importance of the proposed adaptivity process. Travelling downstream, the two pore jets increase in width and the centrelines arc inwards to merge at  $x/D_{\text{disc}} = 0.7$  similar to well-documented parallel jet theory [7]. Velocity gradients gradually reduce in strength and validation based on vector magnitude and direction becomes less stringent, causing ANMT and AWAMT to attain similar results. An under-estimation of the jet centreline velocity obtained with NMT remains noticeable; 0.64 for AWAMT and ANMT compared to 0.61 with NMT at  $x/D_{\text{disc}} \approx 0.7$ .

To provide an estimate of the underlying true flow field, PIV data extracted along  $y/D_{\text{disc}} = 0.18$  is superimposed with results obtained from a two-component Dantec Dynamics Laser Doppler Anemometry (LDA) system operating in crossed beam mode (Figure 6.16b). The LDA measurement volume extended approximately  $0.17 \text{ mm}$  ( $\approx 0.0028 \cdot D_{\text{disc}}$ ) in streamwise normal direction providing spatially highly resolved measurement data. Because of the inherent beam alignment, measurements closest to the disc were restricted to 0.3 disc diameters. Velocity samples were spaced approximately  $0.017 \cdot D_{\text{disc}}$  up to 1.3 diameters downstream. At each measurement location, velocity statistics were evaluated on the basis of typically 6000 instantaneous samples sampled at 4 kHz from which the depicted error bars at 95% confidence level were inferred.

The observable tendency in LDA data confirms velocity exiting from the pores can surpass the free-stream condition, suggesting the holes to act as contractions. Towards the disc, the magnitude of the average LDA horizontal velocity component is seen to exceed the PIV data which is caused by the bias of the PIV data towards lower velocities. Given its small interrogation volume and by weighting velocity data by the corresponding transit times, LDA velocity data will suffer to a much lesser extent from such a bias [34]. As shown in Figure 6.16, in the region  $0.3 \leq x/D_{\text{disc}} \leq 0.9$  where  $R_{\text{NMT}} > R_{\text{AWAMT}}$ , NMT yields the lowest velocity values in comparison with AWAMT, advocating the improved accuracy of the latter. Incorporating coherence adaptivity clearly enhances the accuracy of the ensemble average velocity data (cf. ANMT vs. NMT), which can be further improved by means of validation based on velocity magnitude and direction (cf. AWAMT vs. ANMT). Beyond 0.9 disc diameters, differences in the percentage of replaced vectors by the two methods become smaller and all validation methods return velocity data coinciding with LDA data.

The smoothening inherent to vector replacement can also be used to explain the smaller amplitudes in longitudinal fluctuations obtained with NMT as opposed to ANMT and AWAMT (Figure 6.17a). Differences in root mean square value of the streamwise velocity tend to persist further downstream as opposed to the velocity magnitude and are still visible at  $x/D_{\text{disc}} = 1.5$ . Nearer to the disc, at  $x/D_{\text{disc}} = 0.2$ , the turbulence levels predicted with NMT surmount those of AWAMT and ANMT. However, LDA data corroborates these lower levels of AWAMT

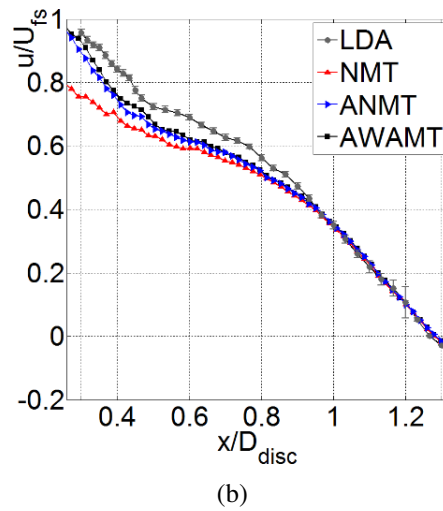
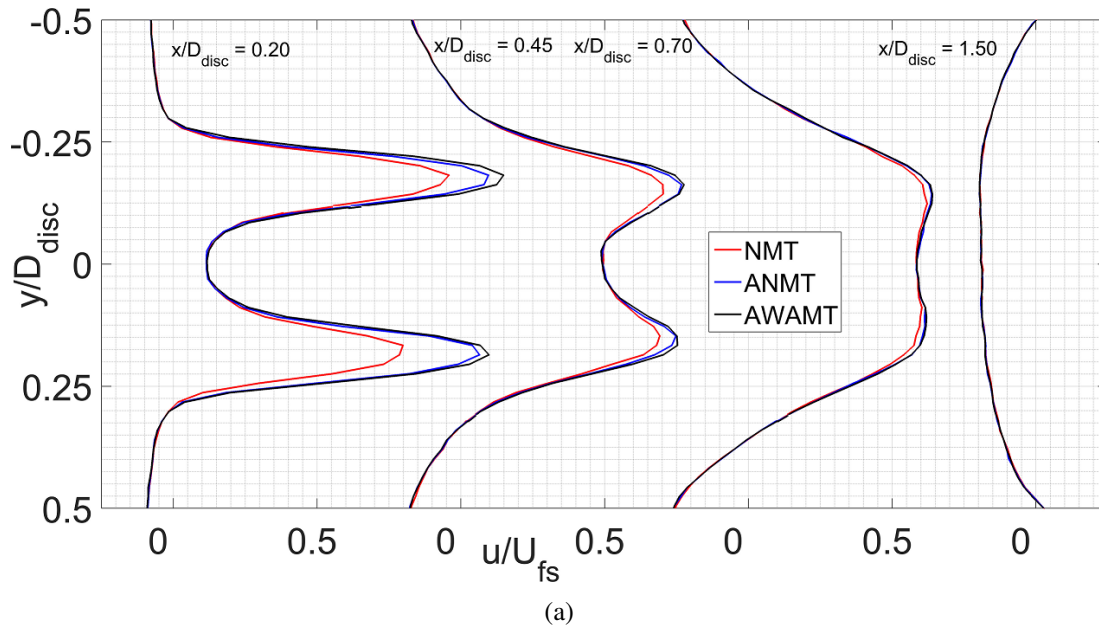


Figure 6.16: (a) Profiles in horizontal velocity component extracted along the vertical directions indicated in Figure 6.14. (b) Comparison of streamwise velocity along the lower jet centreline obtained from LDA and PIV data incorporating NMT, ANMT and AWAMT validation.

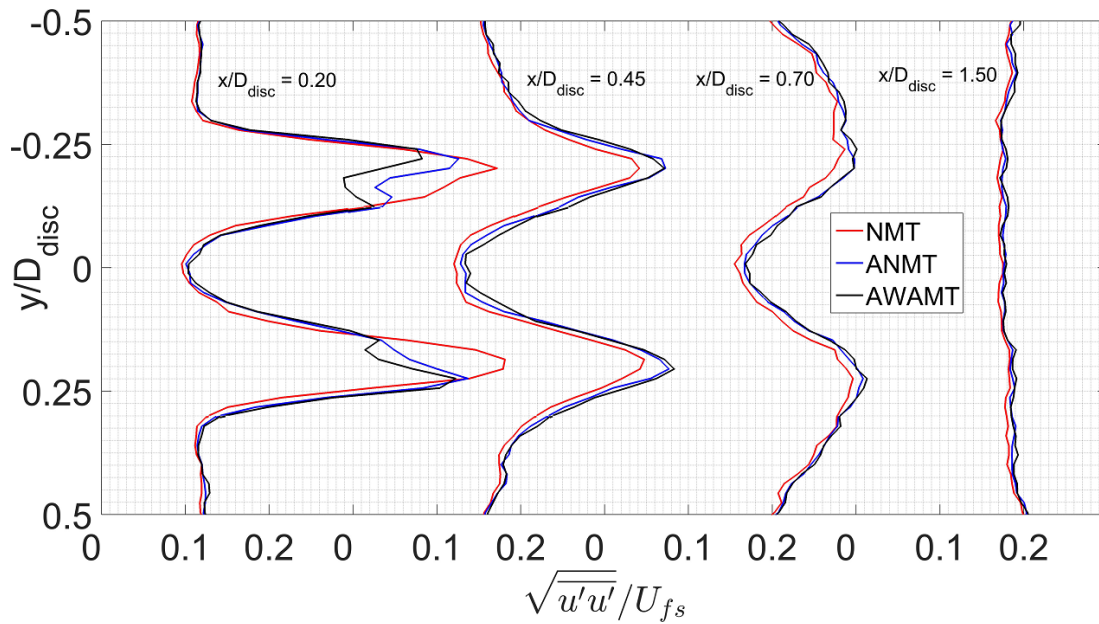
in Figure 6.17b, further substantiating the conduciveness of the proposed validation criteria in AWAMT. Despite heightened uncertainty, AWAMT and ANMT also show to capture the higher levels in longitudinal turbulence measured with LDA between  $0.5 \cdot D_{\text{disc}}$  and  $1.1 \cdot D_{\text{disc}}$  (Figure 6.17b). On the basis of the improved accordance with LDA data, this example has demonstrated the potential gain in accuracy of PIV data and therefore implies the importance of the vector validation process within iterative image analyses in case of turbulent flows.

## 6.6.2 Over-expanded supersonic jet

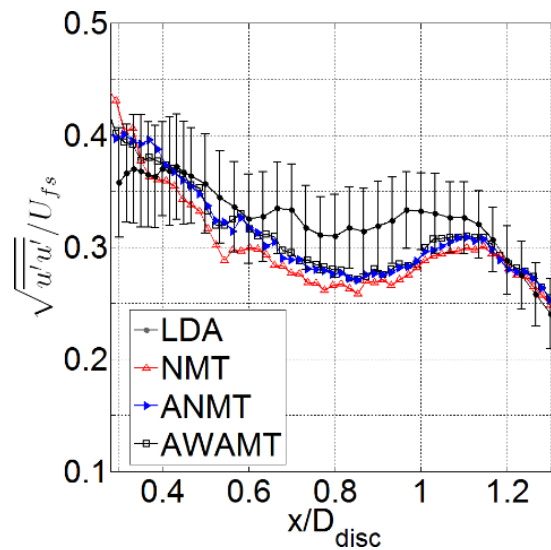
Experiments were conducted at the von Karman Institute for Fluid Dynamics, Brussels. The supersonic over-expanded jet flow was issued from a conical nozzle with exit diameter  $D_{\text{noz}}$  of 17.3 mm and throat diameter of 5.85 mm. A pressure ratio between stagnation chamber and ambient of 25 was imposed, producing an exit velocity  $U_{\text{jet}}$  of approximately 633 m/s equivalent to a maximum displacement of about 9.5 pixels. At a Mach number of 3.33, normal shock relations predict a velocity of 153.4 m/s ( $\approx 2.3$  pixels) downstream of the first normal shock at the nozzle exit ( $u/U_{\text{jet}} \approx 0.24$ ). Submicron oil tracer particles issued from a Laskin nozzle were injected upstream of the nozzle. The flow was illuminated in a light sheet of 0.5 mm thickness by a Nd:Yag laser pulsed at  $0.5 \mu\text{s}$ . A 12 bits PCO digital camera captured a field of view of approximately  $4 \times 2 \text{ cm}^2$  covered by a sensor area of  $1280 \times 544 \text{ pixels}^2$ , equating to a conversion factor of  $34 \mu\text{m}/\text{pixel}$ . Details regarding the experimental campaign can be found in [46]. A total of 280 PIV image pairs were analysed with the same interrogation algorithm as described in the porous disc case adopting final square correlation windows of size  $WS/D_{\text{noz}} \approx 0.037$  and 50% mutual overlap.

The characteristic shock cell patterns of the over-expanded jet, which are visible in the average velocity field (Figure 6.18b), are emphasised by strong gradients in seeding density as illustrated in Figure 6.18a, enabling the first normal shock to be easily discerned. The image recording further reveals the absence of seeding in the outer jet areas near the nozzle exit and the presence of turbulent mixing layers. Moreover, sliplines emanating from the intersection points of oblique shocks with the Mach disc [126] are visible as regions of lower density. These shear layers grow and merge at the jet's centreline to develop a turbulent wake [56]. The presence of both inhomogeneous seeding concentrations and rapid changes in flow scales makes this flow field susceptible to over-detection and constitutes a challenging test case for vector validation.

Comparison of the percentage of replaced vectors  $R$  in Figure 6.19 reveals the traditional NMT approach to replace a higher number of vectors ( $\approx 30\%$ ) in the vicinity of the normal shock ( $x/D_{\text{noz}} \approx 0.25$ ) compared to AWAMT ( $R_{\text{AWAMT}} \approx 10\%$ ). This tendency can be observed to continue along the central sliplines. The outer turbulent shear layers are also susceptible to a slightly higher probability of vector replacement with NMT due to the velocity gradients.

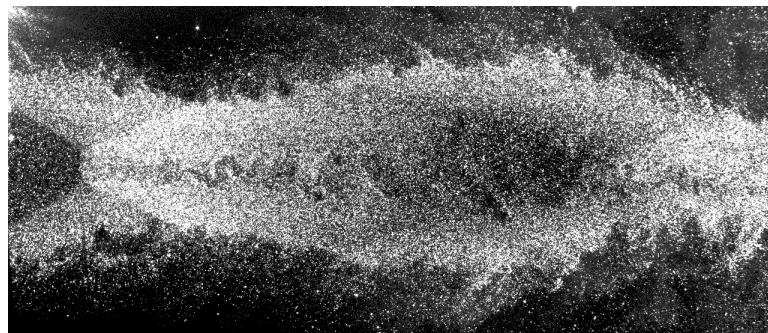


(a)

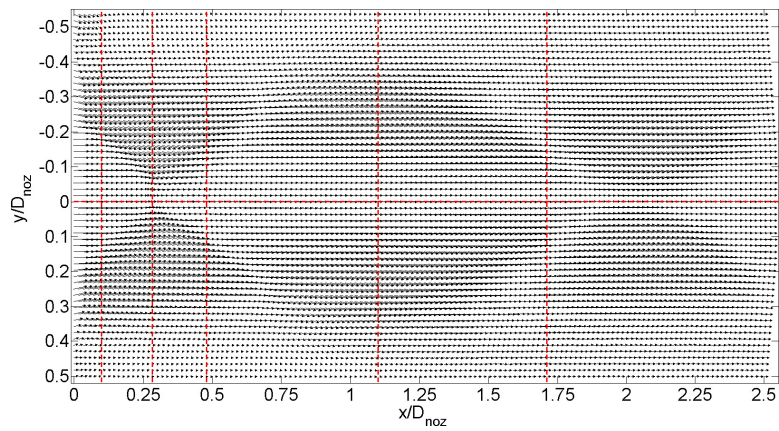


(b)

Figure 6.17: (a) Profiles in longitudinal turbulence intensity extracted along the vertical directions indicated in Figure 6.14. (b) Comparison in longitudinal turbulence intensity along the lower jet centreline obtained from LDA and PIV data incorporating AWAMT and NMT validation.



(a)



(b)

Figure 6.18: (a) Experimental PIV recording of an over-expanded jet at Mach 3.33 (contrast enhanced for clarity) and (b) Ensemble averaged velocity field (undersampled by a factor 2 for readability). Red lines indicate the locations of the extracted profiles.

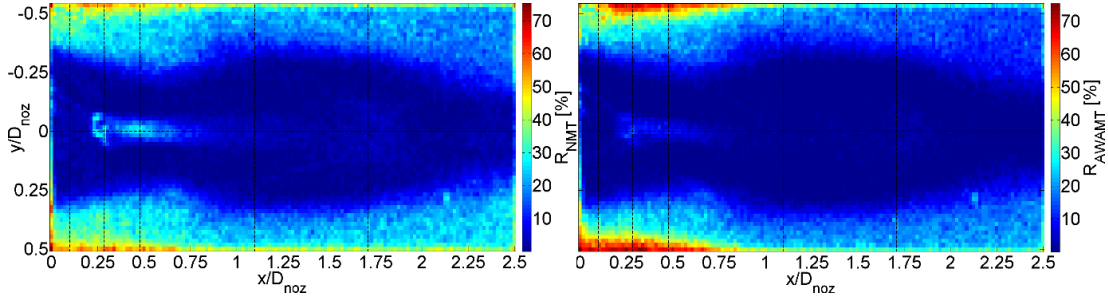


Figure 6.19: Comparison of the number of replaced vectors across the PIV data series (280 images) for the case of the over-expanded supersonic jet as per the outcome using (left) NMT vector validation (right) AWAMT vector validation.

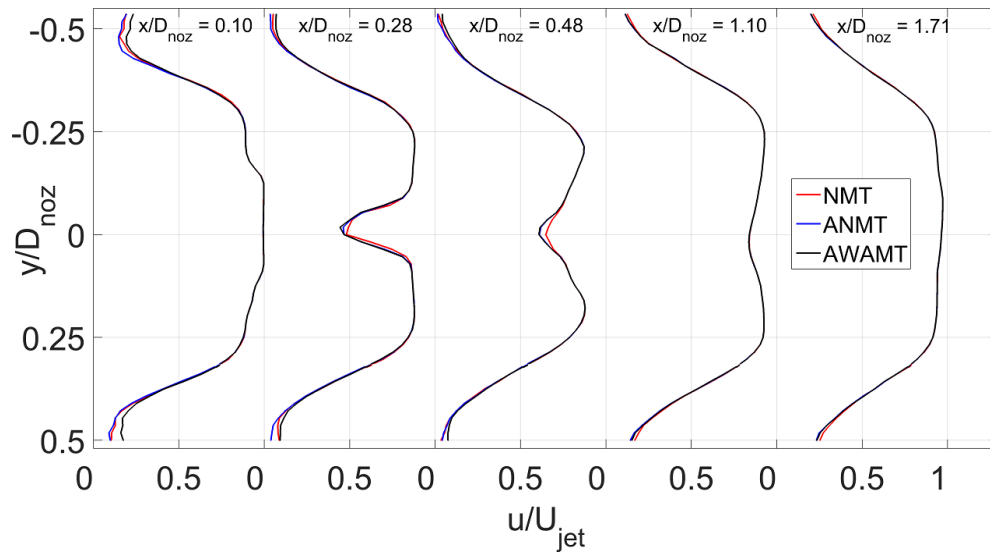
On the other hand, NMT arguably invalidates less vectors in the regions of very low seeding density ( $x/D_{\text{noz}} \leq 0.75$ ,  $|y/D_{\text{noz}}| \approx 0.5$ ) where unreliable correlation can be expected whereas AWAMT correctly invalidates a higher percentage of vectors.

The detrimental effects of over-detection are again noticeable when juxtaposing profiles of ensemble statistics in horizontal velocity magnitude (Figure 6.20) and turbulence intensity (Figure 6.21). Near the nozzle ( $x/D_{\text{noz}} = 0.1$ ) differences between NMT, ANMT and AWAMT in terms of streamwise velocity are negligible within the potential core of the jet but become apparent in the outer, poorly seeded regions. The outer regions are nevertheless attributed heightened RMS levels as vectors, even when reinterpolated, remain unreliable in this region (Figure 6.21). It should be noted that presented quantitative data in terms of higher order statistics are associated with larger uncertainty due to the small number of flowfields. This does not however endanger their potential to evaluate comparative performances of the assessed validation methods. The profile positioned at  $x/D_{\text{noz}} = 0.28$  is slightly behind the normal shock. The work in [46] estimated the amplitude of the normal shock's average longitudinal oscillation  $\Delta x$  caused by the interaction between the turbulent boundary layer and oblique shocks to be in the order of 1 mm ( $\Delta x/D_{\text{noz}} \sim 0.06$ ). In this area NMT replaces about 30% of the vectors. Given the nominal stepwise variation in velocity across the shock, replaced velocities will thus tend towards either higher or lower values. This is evidenced by the corresponding probability density functions (Figure 6.21b). The bi-modal probability density function (pdf) relevant to NMT shows elevated probabilities at  $u/U_{\text{jet}} \approx 0.3$  and  $u/U_{\text{jet}} \approx 0.6$  whereas AWAMT allows more variety in the retrieved velocity data. Although not depicted, the distribution in horizontal velocity obtained with ANMT is nearly identical to AWAMT, explaining the agreement between the two approaches in terms of mean and turbulence statistics. The inherent velocity bias with NMT artificially introduces a higher longitudinal turbulence level which is visible in the turbulence profile at the corresponding spatial location (Figure 6.21a). At  $x/D_{\text{noz}} = 0.48$  the extraction line crosses the turbulent sliplines. Because of the validation utilising coherency heuristics in AWAMT and ANMT, less vectors are incorrectly identified as

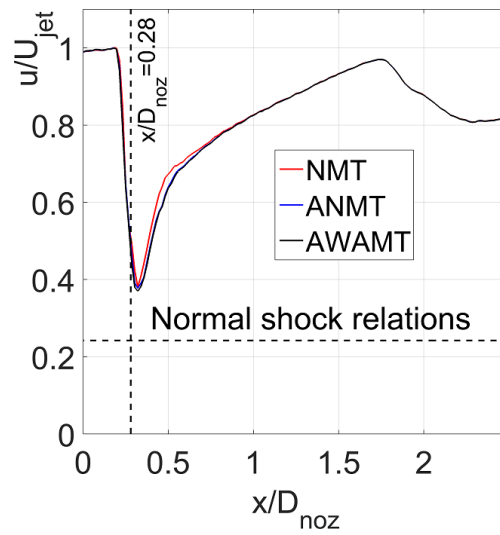
outliers, minimising any induced smoothening contrary to the lower turbulence levels obtained with NMT (Figure 6.20a). This is in line with the findings for the porous disc. The advantage of the alternative validation process is further evidenced in Figure 6.21a by the elevated fluctuation levels in the outer shear layers, which at this downstream position start to become properly seeded. More importantly, NMT hinders accurate retrieval of the evolution in centreline velocity across the shock. Figure 6.20b reveals choosing a more conducive vector validation process is capable of reducing the associated modulation in velocity jump;  $u/U_{\text{jet}} = 0.38$  with NMT and  $u/U_{\text{jet}} = 0.37$  with AWAMT versus the theoretical value of  $u/U_{\text{jet}} = 0.24$ . A difference between AWAMT and ANMT is also noticeable with the latter yielding a  $u/U_{\text{jet}} = 0.375$ . The figure also shows that by incorrectly replacing more vectors along the turbulent slipline (cf. Figure 6.19), NMT predicts a faster velocity recovery. Further downstream differences between the validation methods become negligible in terms of vector replacement equating their performances relevant to velocity statistics.

## 6.7 Conclusions

Velocity fields obtained from PIV image analysis techniques are always contaminated with erroneous vectors and such outliers often appear in clusters as a result of underlying degraded image quality or strong gradients in flow velocity. Existing validation methodologies for instantaneous PIV velocity fields are commonly based on comparison of the scrutinised vector with its immediate neighbourhood. As a result, such methods are unable to detect false vectors when clustered and are moreover prone to mistakenly invalidate correct vectors. For this reason a novel adaptive method for outlier detection has been proposed in this chapter with the aim to render validation processes more robust in the presence of outlier clusters. The detection of false vectors will thereby be improved and over-detection can be reduced without the need to fine-tune inherent parameters. The proposed method emulates the process of outlier detection in human vision whereby the considered neighbourhood for comparison is a-priori extended until the database is sufficiently reliable for posterior validation tasks. Selection of the appropriate vicinity is dictated by a measure of coherency. The latter is quantified as the discrepancy between local velocity values and a parabolic regression. For each vector, the neighbourhood is automatically enlarged until at least half the enclosed vectors are coherent. To further improve the validation algorithm, vector comparison is performed on the basis of magnitude and direction instead of the traditional horizontal and vertical vector components. To limit the potential diversity in vector direction, the acceptable background fluctuation level is automatically adjusted to the vector magnitude and constitutes a second feature of adaptivity. Moreover, applicability to both structured and unstructured data grids is ensured by the implementation of a distance-based Gaussian weighting system.



(a)



(b)

Figure 6.20: (a) Profiles in average horizontal velocity extracted along the vertical directions indicated in Figure 6.18b. (b) Mean streamwise velocity along the jet centreline.

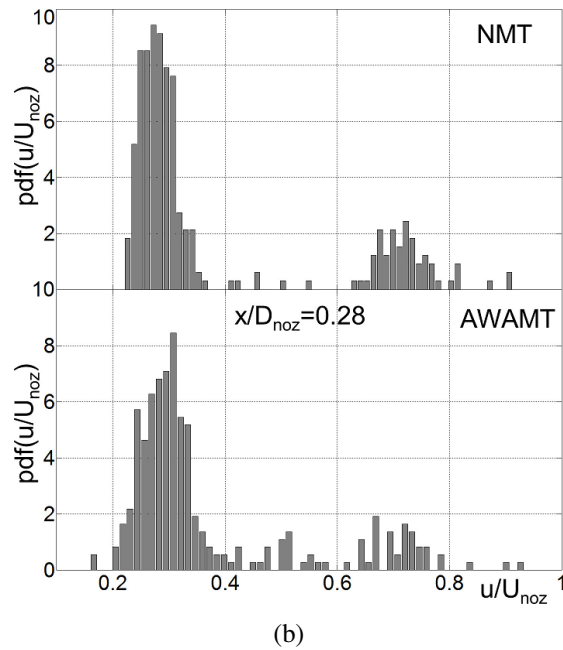
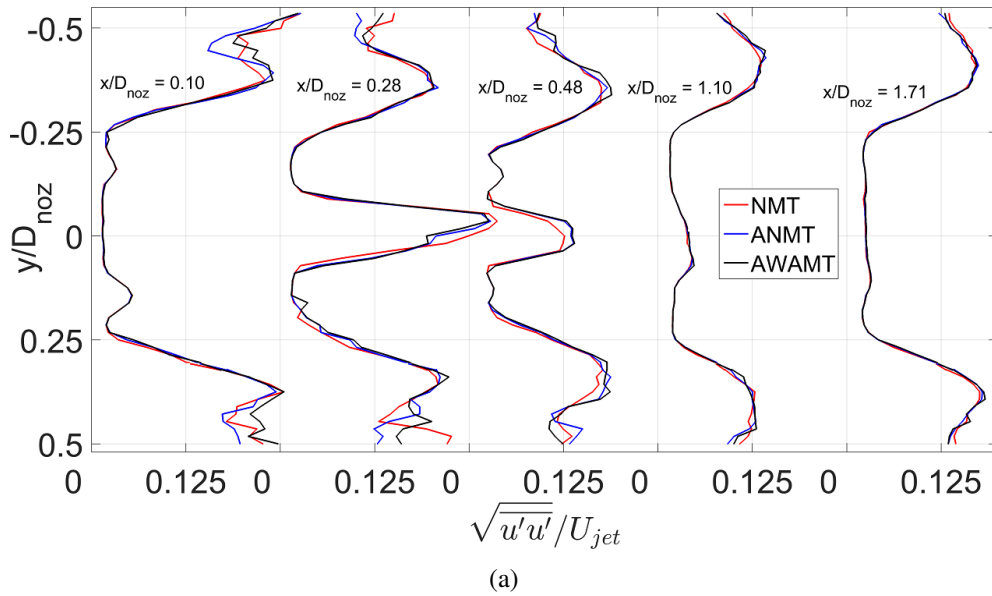


Figure 6.21: (a) Profiles in longitudinal turbulence intensity extracted along the vertical directions indicated in Figure 6.18b. (b) Comparison in probability distribution of horizontal velocity at  $x/D_{noz} = 0.28$  incorporating NMT and AWAMT vector validation in PIV.

The algorithm has been assessed with Monte-Carlo simulations using three flow fields; an isolated vortex, a turbulent channel flow and a DNS simulation of isotropic turbulence. Flow fields were contaminated with outliers of varying magnitude and degree of clustering. The common outlier detection schemes resulted in high numbers of undetected outliers and number of wrongly invalidated correct vectors. Depending on the amount of clustering and outlier magnitude as much as 80% of the spurious vectors could remain undetected, while 3% of the total vectors could be over-detected. Implementation of the coherency adaptivity dramatically improved the outlier detection, potentially reducing the under-detection by as much as one-fourth for small outlier magnitudes or even one-tenth for larger magnitudes. These findings advocate coherency adaptivity to be a powerful tool to improve the performance of existing validation routines even in the presence of outlier clusters. The concept is computationally simple and implementation is straightforward, even in established validation routines. Validation on the basis of angle and magnitude enabled a further lowering of the missed outliers and mistaken outliers especially in case of lower displacement magnitudes. Overall, the proposed validation method proved to be the most robust and general without any reliance on user-defined parameters. Related validation performances consistently surpassed the traditional routines and were better or at least on a par with the adaptivity enhanced conventional methodologies. When implemented in a standard PIV image analysis process and applied to experimental PIV images of a porous disc's near-wake and over-expanded supersonic jet, the proposed outlier detection routine was shown to be capable of identifying more erroneous vectors (improved under-detection). As a consequence of the adaptive validation in terms of velocity magnitude and direction, over-detection was simultaneously reduced in turbulent flow regions. When incorporating the presented validation method PIV data was in better agreement with LDA measurements and theoretical analyses, proving its ability to ameliorate the measurement accuracy and resolution.



# Chapter 7

## Conclusions

### 7.1 Summary of results

In this thesis, two of the most critical limitations of PIV were investigated: the measurement of velocities close to objects and the study of flow subjected to strong in-plane velocity gradients. Several techniques and algorithms were developed throughout this work and this chapter will serve as a summary of the most important discoveries.

The measurement of velocities near walls and interfaces was conducted in Chapter 2 and Chapter 3. The contribution of Chapter 2 was a novel algorithm to automatically generate logical masks for the application to PIV. The suggested algorithm was able to discern particle images from interfaces in a completely automatic way, based on the statistical information contained in several PIV images. Successful synthetic and experimental results proved the feasibility of this method. Due to its simplicity and low computational effort, it can be easily implemented as an additional step in any existing PIV algorithm. Its implementation will enable the automation of measurements near objects and interfaces by removing the need of manually generating a logical mask for every experiment performed, and by drastically reducing the overall time to analyse images and obtain results.

The approach to improve measurements near interfaces in Chapter 3 followed a different strategy. In this case, the suggested methodology was a transformation of the PIV images in vicinity of the interface to minimise the overlap between the correlation windows and the object itself. The information of the boundary was provided through a logical mask (generated automatically or manually), that was used to produce a numerical transformation, adopted to deform particle images. Pixel intensities were mapped onto a logical plane where the interface became a straight line: rectangular correlation windows were located on this plane and aligned with the straightened interface to minimise the boundary overlap. This technique, known as image mapping, already existed in the literature and showed some promising results when

applied to cylindrical objects, but it had never been fully investigated before. The contribution of Chapter 3 is a deep analysis of image mapping, starting from the generation of the mesh from a logical mask, to the problem of window sizes and the implications of pixel re-sampling on the logical plane. The results of Chapter 3 indicated that the advantages of using image mapping only exist in a very limited set of conditions, depending on the interface geometry (radius of curvature), the amount of image noise, the type of implementation of PIV algorithm and more importantly, the underlying flow topology. Due to the added computational cost and the strong dependence of the results on the geometry tested, the application of image mapping was not generally advised. Instead, the use of more consolidated adaptive image processing techniques was found to be more conducive.

The problem of strong velocity gradients limiting the application of PIV was investigated in Chapter 4 and Chapter 5. Once again, two different lines of inquiry were followed. Chapter 4 investigated the use of an optical flow technique, the Lucas-Kanade Tracker (LKT), in replacement of cross-correlation to analyse particle image displacements. The LKT allowed the estimation of motion between two frames by assuming a warping function that was tested for constant, linear and quadratic configurations. In theory, the implementation of LKT with quadratic warping function should have allowed a better estimation of the flow field in case of flow curvature (and strong gradients). Unfortunately, the algorithm proved to be very unstable and susceptible to light variations within the interrogation window, which are common in non-ideal experimental PIV images. The contribution of Chapter 4 was therefore a study on the implementation of LKT for the analysis of PIV images. Different combinations of LKT, cross-correlation and multi-grid algorithm were studied, and several possible implications were observed. The outcome of Chapter 4 was that, in spite of the tempting characteristics of LKT, its application to the analysis of PIV image was very challenging, as it required fine tuning of several parameters, which are not common for the standard PIV user. Moreover, the unpredictable behaviour of LKT and the additional computation effort due to the method, do not make it very suitable and robust for the general use on experimental PIV images.

Due to the unpromising results obtained with LKT, Chapter 5 focussed on the use of cross-correlation to overcome the problem of strong gradients. The attention was concentrated on a peculiar characteristic of the correlation map when it presents broadened and splintered peaks, appearing when the interrogation areas are subjected to strong velocity gradients. Standard PIV algorithms are unable to cope with multiple peaks in correlation maps and the typical approach is to discard the whole correlation, including any possible information on displacements included in it. This behaviour can be very harmful for iterative PIV algorithms, especially when strong gradients are combined with high intensity displacements. Missing information on a high intensity displacement can produce a wrong velocity predictor that will lead the algorithm to failure. The contribution of Chapter 5 was a novel PIV algorithm that is able to deal with multiple peaks in correlation maps by producing multiple vectors per interrogation win-

dow. The proposed method, named MP-PIV (Multiple Peak PIV), automatically detects strong peaks in the correlation map and analyses them in sequence to find which areas of the interrogation region contribute to each peak. The task was fulfilled by adopting a sub-interrogation grid used to anchor displacement vectors: for each peak displacement, sub-regions were translated and cross-correlated to find the best matching regions. The algorithm was assessed on synthetic and experimental images and results showed very promising improvements. The proposed algorithm was able to detect displacements with lower error at higher displacement gradients, and obtained a better spatial resolution in case of high amplitude oscillation displacement field. The application on experimental images confirmed the synthetic results, providing further proofs of the improvements.

Finally, Chapter 6 investigated a very important aspect of every PIV algorithm, which is vector validation. Standard validation techniques are based on the comparison of each vector to its eight closest neighbours, but this approach can be misleading when the flow is subjected to strong gradients or the velocity measurements are scattered (i.e. when interface-adaptive PIV algorithms are involved). The number of neighbours should, in fact, be adjusted according to the flow conditions to avoid the over-detection of outliers in case of strong gradients, or the under-detection in case of outlier clusters. The contribution of Chapter 6 was a novel algorithm for the validation of velocity vectors in PIV, reducing the ratio of over- and under-detected vector fields corrupted by outliers. This task was carried out using an adaptive neighbourhood size that is automatically adjusted based on the coherence of the flow. If gradients are weak, fewer vectors are considered for the validation, but in case of strong gradients or outlier clusters, more neighbours are included for comparison. The method also introduced additional novelties, like a weighting system to take into account scattered displacement vectors, a more accurate way to evaluate the median and a distance/magnitude comparison. Results showed that the proposed methodology was able to drastically reduce the ratio of over- and under-detection, especially in case of clustered outliers. The application of this new validation method to the analysis of experimental PIV images also showed measurement improvements, advocating the importance of vector validation in PIV algorithms.

## 7.2 Future work

The work of this thesis was aimed to improve the quality of PIV measurements and enable the application of this technique to experimental conditions that constitute a limitation in current algorithms. In spite of the positive results obtained, the problems of measurement in vicinity of interfaces and in case of strong gradients are still far to be solved, and require further research. While this thesis provides tailored solutions to specific problems, future work should be focussed on the construction of a more general framework that combines all these solutions together. Such a framework should be able to identify the experimental conditions and

automatically select the most suited methodology to obtain optimal measurements. However, for this architecture to exist, all its basic components should be first studied and understood thoroughly, in order to predict exactly their behaviour in any foreseeable condition.

An additional aspect that requires more attention is the validation and assessment of novel PIV algorithms. In fact, while specific test cases can be designed with synthetic images, the behaviour of advanced PIV algorithms can be so complex that their response can be very different when applied to experimental PIV images. In fact, real images often present image characteristics which are very unique for a certain experiment and they are therefore hard to simulate in a synthetic environment, like camera noise, sensor defects, lens distortion, vibrations, turbulence, light source imperfections, etc.. Moreover, the lack of a ground truth for experimental images constitutes a strong limitation to the validation of these algorithms in real conditions, leaving too much space for subjective interpretation. For this reason, future research should also be focussed on the validation side of the PIV measurements, both algorithmically, with error quantification techniques, and experimentally, with specially controlled studies that allow redundant measurements of the flow characteristics.

## List of references

- [1] R J Adrian. “Dynamic ranges of velocity and spatial resolution of particle image velocimetry”. In: *Measurement Science and Technology* 8 (1999), pp. 1393–1398. ISSN: 0957-0233. DOI: 10.1088/0957-0233/8/12/003.
- [2] RJ Adrian. “Laser velocimetry”. In: *Goldstein R (ed) Fluid mechanics measurements*. 1983, pp. 155–244.
- [3] Ronald J. Adrian. “Double exposure, multiple-field particle image velocimetry for turbulent probability density”. In: *Optics and Lasers in Engineering* 9.3-4 (1988), pp. 211–228. ISSN: 01438166. DOI: 10.1016/S0143-8166(98)90004-5.
- [4] Ronald J Adrian. “Particle-Imaging Techniques for Experimental Fluid Mechanics”. In: *Annual Review of Fluid Mechanics* 23.1 (1991), pp. 261–304. ISSN: 0066-4189. DOI: 10.1146/annurev.fl.23.010191.001401.
- [5] Ronald J Adrian. “Twenty years of particle image velocimetry”. In: *Experiments in Fluids* 39.2 (2005), pp. 159–169. ISSN: 0723-4864. DOI: 10.1007/s00348-005-0991-7.
- [6] Juan C. Agüí and J. Jiménez. “On the performance of particle tracking”. In: *Journal of Fluid Mechanics* 185.-1 (1987), p. 447. ISSN: 0022-1120. DOI: 10.1017/S0022112087003252.
- [7] Elgin a. Anderson and Robert E. Spall. “Experimental and Numerical Investigation of Two-Dimensional Parallel Jets”. In: *Journal of Fluids Engineering* 123.2 (2001), p. 401. ISSN: 00982202. DOI: 10.1115/1.1363701.
- [8] T. Astarita. “Adaptive space resolution for PIV”. In: *Experiments in Fluids* 46.6 (2009), pp. 1115–1123. ISSN: 0723-4864. DOI: 10.1007/s00348-009-0618-5.
- [9] T. Astarita. “Analysis of weighting windows for image deformation methods in PIV”. In: *Experiments in Fluids* 43.6 (2007), pp. 859–872. ISSN: 0723-4864. DOI: 10.1007/s00348-007-0314-2.
- [10] Tommaso Astarita and G. Cardone. “Analysis of interpolation schemes for image deformation methods in PIV”. In: *Experiments in Fluids* 38.2 (2005), pp. 233–243. ISSN: 0723-4864. DOI: 10.1007/s00348-004-0902-3.

- [11] Simon Baker and Iain Matthews. “Lucas-Kanade 20 Years On: A Unifying Framework”. In: *International Journal of Computer Vision* 56.3 (2004), pp. 221–255. ISSN: 0920-5691. DOI: 10.1023/B:VISI.0000011205.11775.fd.
- [12] J. L. Barron, D. J. Fleet, and S. S. Beauchemin. “Performance of optical flow techniques”. In: *International Journal of Computer Vision* 12.1 (1994), pp. 43–77. ISSN: 0920-5691. DOI: 10.1007/BF01420984.
- [13] J. M. Barry. “SPLINS & SMOOTH, two Fortran smoothing routines”. In: *Australian Atomic Energy Commission* (1973).
- [14] Tom Bobach et al. “Natural neighbor extrapolation using ghost points”. In: *Computer-Aided Design* 41.5 (2009), pp. 350–365. ISSN: 00104485. DOI: 10.1016/j.cad.2008.08.007.
- [15] a. Boillot and A. K. Prasad. “Optimization procedure for pulse separation in cross-correlation PIV”. In: *Experiments in Fluids* 21.2 (1996), pp. 87–93. DOI: 10.1007/BF00193911.
- [16] William M. Chan and Joseph L. Steger. “Enhancements of a three-dimensional hyperbolic grid generation scheme”. In: *Applied Mathematics and Computation* 51.2-3 (1992), pp. 181–205. ISSN: 00963003. DOI: 10.1016/0096-3003(92)90073-A.
- [17] Dmitry Chetverikov, M. Nagy, and J. Verestoy. “Comparison of tracking techniques applied to digital PIV”. In: *Proceedings 15th International Conference on Pattern Recognition. ICPR-2000*. Vol. 4. IEEE Comput. Soc, 2000, pp. 619–622. ISBN: 0-7695-0750-6. DOI: 10.1109/ICPR.2000.902995.
- [18] K. T. Christensen. “The influence of peak-locking errors on turbulence statistics computed from PIV ensembles”. In: *Experiments in Fluids* 36.3 (2004), pp. 484–497. ISSN: 0723-4864. DOI: 10.1007/s00348-003-0754-2.
- [19] T.F. Cootes, G.J. Edwards, and C.J. Taylor. “Active appearance models”. In: *IEEE Transactions on Pattern Analysis and Machine Intelligence* 23.6 (2001), pp. 681–685. ISSN: 01628828. DOI: 10.1109/34.927467. arXiv: 10.1.1.128.4967.
- [20] R. B. D’agostino, A. Belanger, and R. B. D’Agostino Jr. “A Suggestion for Using Powerful and Informative Tests of Normality”. In: *The American Statistician* 44.4 (1990), pp. 316–321.
- [21] Niels G. Deen et al. “On image pre-processing for PIV of single- and two-phase flows over reflecting objects”. In: *Experiments in Fluids* 49.2 (2010), pp. 525–530. ISSN: 0723-4864. DOI: 10.1007/s00348-010-0827-y.

- [22] E. Delnoij et al. “Ensemble correlation PIV applied to bubble plumes rising in a bubble column”. In: *Chemical Engineering Science* 54.21 (1999), pp. 5159–5171. ISSN: 00092509. DOI: 10.1016/S0009-2509(99)00233-X.
- [23] David Douglas and Thomas Peucker. “Algorithms for the reduction of the number of points required to represent a digitized line or its caricature”. In: *The Canadian Cartographer* 10.2 (1973), pp. 112–122.
- [24] J Duncan et al. “Universal outlier detection for particle image velocimetry (PIV) and particle tracking velocimetry (PTV) data”. In: *Measurement Science and Technology* 21.5 (2010), p. 057002. ISSN: 0957-0233. DOI: 10.1088/0957-0233/21/5/057002.
- [25] David Dussol et al. “Automatic dynamic mask extraction for PIV images containing an unsteady interface, bubbles, and a moving structure”. In: *Comptes Rendus Mécanique* 344.7 (2016), pp. 464–478. ISSN: 16310721. DOI: 10.1016/j.crme.2016.03.005.
- [26] F. G. Ergin, B. B. Watz, and N. Wadhwa. “Pixel-accurate dynamic masking and flow measurements around small breaststroke-swimmers using long-distance MicroPIV”. In: *11th International Symposium on Particle Image Velocimetry* (2015).
- [27] Ali Etebari and Pavlos P. Vlachos. “Improvements on the accuracy of derivative estimation from DPIV velocity measurements”. In: *Experiments in Fluids* 39.6 (2005), pp. 1040–1050. ISSN: 0723-4864. DOI: 10.1007/s00348-005-0037-1.
- [28] G. Fasano and A. Franceschini. “A multidimensional version of the Kolmogorov-Smirnov test”. In: *Mon. Not. R. astr. Soc.* 225 (1987), pp. 155–170.
- [29] Cyrille K. Feudjio et al. “Extracting and smoothing contours in mammograms using Fourier descriptors”. In: *Journal of Biomedical Science and Engineering* 07.03 (2014), pp. 119–129. ISSN: 1937-6871. DOI: 10.4236/jbise.2014.73017.
- [30] Ichiro Fujita, Marian Muste, and Anton Kruger. “Large-scale particle image velocimetry for flow analysis in hydraulic engineering applications”. In: *Journal of Hydraulic Research* 36.3 (1998), pp. 397–414. ISSN: 0022-1686. DOI: 10/c8qr7q.
- [31] Damien Garcia. “A fast all-in-one method for automated post-processing of PIV data”. In: *Experiments in Fluids* 50.5 (2011), pp. 1247–1259. ISSN: 0723-4864. DOI: 10.1007/s00348-010-0985-y.
- [32] Damien Garcia. “Robust smoothing of gridded data in one and higher dimensions with missing values”. In: *Computational Statistics & Data Analysis* 54.4 (2010), pp. 1167–1178. ISSN: 01679473. DOI: 10.1016/j.csda.2009.09.020.
- [33] R C Gonzalez, R E Woods, and S L Eddins. *Digital Image Processing Using MATLAB*. McGraw Hill Education, 2013. ISBN: 9780070702622.

- [34] RD Gould and WK Loseke. “A comparison of four velocity bias correction techniques in Laser Doppler Velocimetry”. In: *J Fluids Eng* 115.3 (1993), pp. 508–514.
- [35] L Gui, S T Wereley, and Y H Kim. “Advances and applications of the digital mask technique in particle image velocimetry experiments”. In: *Measurement Science and Technology* 14.10 (2003), pp. 1820–1828. ISSN: 0957-0233. DOI: 10.1088/0957-0233/14/10/312.
- [36] Lichuan Gui and Wolfgang Merzkirch. “Phase-separation of PIV measurements in two-phase flow by applying a digital mask technique”. In: *ERCOFTAC Bull* 30 (1996), pp. 45–48.
- [37] R. Hain and C. J. Kähler. “Fundamentals of multiframe particle image velocimetry (PIV)”. In: *Experiments in Fluids* 42.4 (2007), pp. 575–587. ISSN: 0723-4864. DOI: 10.1007/s00348-007-0266-6.
- [38] Robert M. Haralick, Stanley R. Sternberg, and Xinhua Zhuang. “Image Analysis Using Mathematical Morphology”. In: *IEEE Transactions on Pattern Analysis and Machine Intelligence* PAMI-9.4 (1987), pp. 532–550. ISSN: 0162-8828. DOI: 10.1109/TPAMI.1987.4767941.
- [39] D. P. Hart. “Super-resolution PIV by recursive local-correlation”. In: *Journal of Visualization* 3.2 (2000), pp. 187–194. ISSN: 1343-8875. DOI: 10.1007/BF03182411.
- [40] Y.a. Hassan et al. “Simultaneous velocity measurements of both components of a two-phase flow using particle image velocimetry”. In: *International Journal of Multiphase Flow* 18.3 (1992), pp. 371–395. ISSN: 03019322. DOI: 10.1016/0301-9322(92)90023-A.
- [41] Markus Honkanen and Holger Nobach. “Background extraction from double-frame PIV images”. In: *Experiments in Fluids* 38.3 (2005), pp. 348–362. ISSN: 0723-4864. DOI: 10.1007/s00348-004-0916-x.
- [42] H Huang, D Dabiri, and M Gharib. “On errors of digital particle image velocimetry”. In: *Measurement Science and Technology* 8.12 (1997), pp. 1427–1440. ISSN: 0957-0233. DOI: 10.1088/0957-0233/8/12/007.
- [43] H. T. Huang, H. E. Fiedler, and J. J. Wang. “Limitation and improvement of PIV, Part I”. In: *Experiments in Fluids* 15.3 (1993), pp. 168–174. ISSN: 0723-4864. DOI: 10.1007/BF00189883.
- [44] Carlos M Jarque and Anil K Bera. “A Test for Normality of Observations and Regression Residuals”. In: *International Statistical Review / Revue Internationale de Statistique* 55.2 (1987), p. 163. ISSN: 03067734. DOI: 10.2307/1403192. arXiv: arXiv:1011.1669v3.

- [45] Young Jin Jeon and Hyung Jin Sung. “PIV measurement of flow around an arbitrarily moving body”. In: *Experiments in Fluids* 50.4 (2011), pp. 787–798. ISSN: 0723-4864. DOI: 10.1007/s00348-010-0855-7.
- [46] A Jerónimo, ML Riethmuller, and O Chazot. “PIV application to Mach 3.75 over-expanded jet”. In: *Proceedings 11th international symposium on application of laser techniques to fluid mechanics, Lisbon, Portugal*. Lisbon, Portugal, 2002.
- [47] Christian J. Kähler et al. “Main results of the 4th International PIV Challenge”. In: *Experiments in Fluids* 57.6 (2016), p. 97. ISSN: 0723-4864. DOI: 10.1007/s00348-016-2173-1.
- [48] TR Kalra and PHT Uhlherr. “Properties of bluff body wakes”. In: *4th Australasian conference on hydraulics and fluid mechanics*. Melbourne, Australia, 1971.
- [49] Takeo Kanade and Bruce D. Lucas. “An Iterative Image Registration Technique with an Application to Stereo Vision”. In: *Proceedings of the 7th International Joint Conference on Artificial Intelligence - Volume 2* (1981).
- [50] Richard D Keane and Ronald J Adrian. “Optimization of particle image velocimeters. Part I : Double pulsed systems”. In: *Measurement Science and Technology* 1 (1990), pp. 1202–1215.
- [51] Richard D. Keane and Ronald J. Adrian. “Theory of cross-correlation analysis of PIV images”. In: *Applied Scientific Research* 49.3 (1992), pp. 191–215. ISSN: 0003-6994. DOI: 10.1007/BF00384623.
- [52] A Lecuona, J Nogueira, and Rodríguez PA. “Data validation, interpolation and signal to noise increase in iterative PIV methods”. In: *Proceedings of the 11th international symposium on applications of laser techniques to fluid mechanics*. July. Lisbon, Portugal, 2002.
- [53] Yi Li et al. “A public turbulence database cluster and applications to study Lagrangian evolution of velocity increments in turbulence”. In: *Journal of Turbulence* 9.31 (2008), pp. 1–29. ISSN: 1468-5248. DOI: 10.1080/14685240802376389. arXiv: 0804.1703.
- [54] D. Liang, C. Jiang, and Y. Li. “A combination correlation-based interrogation and tracking algorithm for digital PIV evaluation”. In: *Experiments in Fluids* 33.5 (2002), pp. 684–695. ISSN: 0723-4864. DOI: 10.1007/s00348-002-0527-3.
- [55] D. Liang, C. Jiang, and Y. Li. “Cellular neural network to detect spurious vectors in PIV data”. In: *Experiments in Fluids* 34.1 (2003), pp. 52–62. ISSN: 0723-4864. DOI: 10.1007/s00348-002-0530-8.
- [56] E S Love et al. “Experimental and theoretical studies of axisymmetric free jets”. In: *NASA Technical report R-6* (1959), p. 298.

- [57] Alessandro Masullo and Raf Theunissen. “Adaptive vector validation in image velocimetry to minimise the influence of outlier clusters”. In: *Experiments in Fluids* 57.3 (2016), p. 33. ISSN: 0723-4864. DOI: 10.1007/s00348-015-2110-8.
- [58] Alessandro Masullo and Raf Theunissen. “Automated mask generation for PIV image analysis based on pixel intensity statistics”. In: *Experiments in Fluids* 58.6 (2017), p. 70. ISSN: 0723-4864. DOI: 10.1007/s00348-017-2357-3.
- [59] Alessandro Masullo and Raf Theunissen. “On the applicability of numerical image mapping for PIV image analysis near curved interfaces”. In: *Measurement Science and Technology* 28.7 (2017). ISSN: 0957-0233. DOI: 10.1088/1361-6501/aa6c8f.
- [60] M.A. Mendez et al. “POD-based background removal for particle image velocimetry”. In: *Experimental Thermal and Fluid Science* 80 (2017), pp. 181–192. ISSN: 08941777. DOI: 10.1016/j.expthermflusci.2016.08.021.
- [61] J. J. Miao et al. “On vortex shedding behind a circular disk”. In: *Experiments in Fluids* 23.3 (1997), pp. 225–233. ISSN: 0723-4864. DOI: 10.1007/s003480050106.
- [62] M. Miozzi. “Particle Image Velocimetry using Feature Tracking and Delaunay tessellation”. In: *12th International Symposium on Applications of Laser Techniques to Fluid Mechanics*. Lisbon, 2004, pp. 1–12.
- [63] Monica Moroni and Antonio Cenedese. “Comparison among feature tracking and more consolidated velocimetry image analysis techniques in a fully developed turbulent channel flow”. In: *Measurement Science and Technology* 16.11 (2005), pp. 2307–2322. ISSN: 0957-0233. DOI: 10.1088/0957-0233/16/11/025.
- [64] Chuong V. Nguyen et al. “Interfacial PIV to resolve flows in the vicinity of curved surfaces”. In: *Experiments in Fluids* 48.4 (2010), pp. 577–587. ISSN: 0723-4864. DOI: 10.1007/s00348-010-0824-1.
- [65] Thien Duy Nguyen, John Craig Wells, and Chuong Vinh Nguyen. “Velocity measurement of near-wall flow over inclined and curved boundaries by extended interfacial particle image velocimetry”. In: *Flow Measurement and Instrumentation* 23.1 (2012), pp. 33–39. ISSN: 09555986. DOI: 10.1016/j.flowmeasinst.2011.12.006.
- [66] H. Nobach and M. Honkanen. “Two-dimensional Gaussian regression for sub-pixel displacement estimation in particle image velocimetry or particle position estimation in particle tracking velocimetry”. In: *Experiments in Fluids* 38.4 (2005), pp. 511–515. ISSN: 0723-4864. DOI: 10.1007/s00348-005-0942-3.
- [67] J Nogueira, A Lecuona, and P a Rodríguez. “Data validation, false vectors correction and derived magnitudes calculation on PIV data”. In: *Measurement Science and Technology* 8.12 (1997), pp. 1493–1501. ISSN: 0957-0233. DOI: 10.1088/0957-0233/8/12/012.

- [68] J Nogueira, A Lecuona, and P a Rodríguez. “Local field correction PIV, implemented by means of simple algorithms, and multigrid versions”. In: *Measurement Science and Technology* 12.11 (2001), pp. 1911–1921. ISSN: 0957-0233. DOI: 10.1088/0957-0233/12/11/321.
- [69] J. Nogueira, A. Lecuona, and P. A. Rodríguez. “Local field correction PIV: on the increase of accuracy of digital PIV systems”. In: *Experiments in Fluids* 27.2 (1999), pp. 107–116. ISSN: 0723-4864. DOI: 10.1007/s003480050335.
- [70] Nobuyuki Otsu. “A Threshold Selection Method from Gray-Level Histograms”. In: *IEEE Transactions on Systems, Man, and Cybernetics* 9.1 (1979), pp. 62–66. ISSN: 0018-9472. DOI: 10.1109/TSMC.1979.4310076.
- [71] Jinsoo Park et al. “PIV measurements of flow around an arbitrarily moving free surface”. In: *Experiments in Fluids* 56.3 (2015), p. 56. ISSN: 0723-4864. DOI: 10.1007/s00348-015-1920-z.
- [72] E Paterna et al. “Mitigation of surface reflection in PIV measurements”. In: *Measurement Science and Technology* 24.5 (2013), p. 057003. ISSN: 0957-0233. DOI: 10.1088/0957-0233/24/5/057003.
- [73] Tim Persoons and Tadhg S. O’Donovan. “High Dynamic Velocity Range Particle Image Velocimetry Using Multiple Pulse Separation Imaging”. In: *Sensors* 11.1 (2010), pp. 1–18. ISSN: 1424-8220. DOI: 10.3390/s110100001.
- [74] R. L. Plackett. “Karl Pearson and the Chi-Squared Test”. In: *International Statistical Review / Revue Internationale de Statistique* 51.1 (1983), p. 59. ISSN: 03067734. DOI: 10.2307/1402731.
- [75] L Prandtl. “Zur berechnung der grenzschichten”. In: *ZAMM-Journal of Applied Mathematics and Mechanics/Zeitschrift für Angewandte Mathematik und Mechanik* 18.1 (1938), pp. 77–82.
- [76] G. M. Quénot, J. Pakleza, and T. A. Kowalewski. “Particle image velocimetry with optical flow”. In: *Experiments in Fluids* 25.3 (1998), pp. 177–189. ISSN: 0723-4864. DOI: 10.1007/s003480050222.
- [77] Samuel G Raben, John J Charonko, and Pavlos P Vlachos. “Adaptive gappy proper orthogonal decomposition for particle image velocimetry data reconstruction”. In: *Measurement Science and Technology* 23.2 (2012), p. 025303. ISSN: 0957-0233. DOI: 10.1088/0957-0233/23/2/025303.
- [78] M Raffel, B Leitl, and J Kompenhans. “Data Validation for Particle Image Velocimetry”. In: *Laser Techniques and Applications in Fluid Mechanics*. Ed. by R. J. Adrian et al. January. Berlin, Heidelberg: Springer Berlin Heidelberg, 1993. ISBN: 978-3-662-02887-2. DOI: 10.1007/978-3-662-02885-8.

- [79] Markus Raffel, Christan E Willert, and Jürgen Kompenhans. *Particle Image Velocimetry*. Berlin, Heidelberg: Springer Berlin Heidelberg, 1998. ISBN: 978-3-662-03639-6. DOI: 10.1007/978-3-662-03637-2.
- [80] Marco Raiola, Stefano Discetti, and Andrea Ianiro. “On PIV random error minimization with optimal POD-based low-order reconstruction”. In: *Experiments in Fluids* 56.4 (2015), p. 75. ISSN: 0723-4864. DOI: 10.1007/s00348-015-1940-8.
- [81] Beta Reiz and Sndor Pongor. “Psychologically Inspired, Rule-Based Outlier Detection in Noisy Data”. In: *2011 13th International Symposium on Symbolic and Numeric Algorithms for Scientific Computing*. IEEE, 2011, pp. 131–136. ISBN: 978-1-4673-0207-4. DOI: 10.1109/SYNASC.2011.57.
- [82] Janos Rohály, F. Frigerio, and D. P. Hart. “Reverse hierarchical PIV processing”. In: *Measurement Science and Technology* 13.7 (2002), p. 304. ISSN: 09570233. DOI: 10.1088/0957-0233/13/7/304.
- [83] O Ronneberger, Markus Raffel, and Jürgen Kompenhans. “Advanced evaluation algorithms for standard and dual plane particle image velocimetry”. In: *Proceedings of the 9th International Symposium on Applied laser techniques to fluid mechanics*. 1998, pp. 13–16.
- [84] G I Roth and J Katz. “Five techniques for increasing the speed and accuracy of PIV interrogation”. In: *Measurement Science and Technology* 12.3 (2001), pp. 238–245. ISSN: 0957-0233. DOI: 10.1088/0957-0233/12/3/302.
- [85] X. Ruan, X. Song, and F. Yamamoto. “Direct measurement of the vorticity field in digital particle images”. In: *Experiments in Fluids* 30.6 (2001), pp. 696–704. ISSN: 0723-4864. DOI: 10.1007/s003480000249.
- [86] Arnaud Sanchis and Atle Jensen. “Dynamic masking of PIV images using the Radon transform in free surface flows”. In: *Experiments in Fluids* 51.4 (2011), pp. 871–880. ISSN: 0723-4864. DOI: 10.1007/s00348-011-1101-7.
- [87] F Scarano. “Iterative image deformation methods in PIV”. In: *Measurement Science and Technology* 13.1 (2002), R1–R19. ISSN: 0957-0233. DOI: 10.1088/0957-0233/13/1/201.
- [88] F. Scarano. “Theory of non-isotropic spatial resolution in PIV”. In: *Experiments in Fluids* 35.3 (2003), pp. 268–277. ISSN: 0723-4864. DOI: 10.1007/s00348-003-0655-4.
- [89] F Scarano and M L Riethmuller. “Advances in iterative multigrid PIV image processing”. In: *Experiments in Fluids* 29.7 (2000), S051–S060. ISSN: 0723-4864. DOI: 10.1007/s003480070007.

- [90] Fulvio Scarano. “A super-resolution particle image velocimetry interrogation approach by means of velocity second derivatives correlation”. In: *Measurement Science and Technology* 15.2 (2004), pp. 475–486. ISSN: 0957-0233. DOI: 10.1088/0957-0233/15/2/023.
- [91] U Scholz and C J Kähler. “Automated Image Processing and Segmentation for mask generation in PIV”. In: *Proceedings of the 12th international symposium on applications of laser techniques to fluid mechanics*. Lisbon, 2004.
- [92] Andrea Sciacchitano, Richard P. Dwight, and Fulvio Scarano. “Navier–Stokes simulations in gappy PIV data”. In: *Experiments in Fluids* 53.5 (2012), pp. 1421–1435. ISSN: 0723-4864. DOI: 10.1007/s00348-012-1366-5.
- [93] Andrea Sciacchitano and Fulvio Scarano. “Elimination of PIV light reflections via a temporal high pass filter”. In: *Measurement Science and Technology* 25.8 (2014), p. 084009. ISSN: 0957-0233. DOI: 10.1088/0957-0233/25/8/084009.
- [94] Stan Sclaroff and John Isidoro. “Active Blobs”. In: *Proc. International Conference on Computer Vision*. Mumbai, India, 1998.
- [95] Jianbo Shi and Carlo Tomasi. “Good features to track”. In: *Proceedings of IEEE Conference on Computer Vision and Pattern Recognition CVPR-94*. December. IEEE Comput. Soc. Press, 1994, pp. 593–600. ISBN: 0-8186-5825-8. DOI: 10.1109/CVPR.1994.323794.
- [96] A-M Shinnee, J D Bugg, and R Balachandar. “Variable threshold outlier identification in PIV data”. In: *Measurement Science and Technology* 15.9 (2004), pp. 1722–1732. ISSN: 0957-0233. DOI: 10.1088/0957-0233/15/9/008.
- [97] X Song et al. “A new tracking algorithm of PIV and removal of spurious vectors using Delaunay tessellation”. In: *Experiments in Fluids* 26.4 (1999), pp. 371–380. ISSN: 0723-4864. DOI: 10.1007/s003480050300.
- [98] G. Sridhar and J. Katz. “Drag and lift forces on microscopic bubbles entrained by a vortex”. In: *Physics of Fluids* 7.2 (1995), pp. 389–399. ISSN: 1070-6631. DOI: 10.1063/1.868637.
- [99] M Stanislas, K Okamoto, and C Kähler. “Main results of the First International PIV Challenge”. In: *Measurement Science and Technology* 14.10 (2003), R63–R89. ISSN: 0957-0233. DOI: 10.1088/0957-0233/14/10/201.
- [100] M. Stanislas et al. “Main results of the Second International PIV Challenge”. In: *Experiments in Fluids* 39.2 (2005), pp. 170–191. ISSN: 0723-4864. DOI: 10.1007/s00348-005-0951-2.
- [101] J L Steger. “The Chimera method of flow simulation”. In: *Workshop on applied CFD, Univ of Tennessee Space Institute*. Vol. 188. 1991.

- [102] R Theunissen. “Theoretical analysis of direct and phase-filtered cross-correlation response to a sinusoidal displacement for PIV image processing”. In: *Measurement Science and Technology* 23.6 (2012), p. 065302. ISSN: 0957-0233. DOI: 10.1088/0957-0233/23/6/065302.
- [103] R. Theunissen et al. “Confidence estimation using dependent circular block bootstrapping: application to the statistical analysis of PIV measurements”. In: *Experiments in Fluids* 44.4 (2008), pp. 591–596. ISSN: 0723-4864. DOI: 10.1007/s00348-007-0418-8.
- [104] Raf Theunissen and Michel L Riethmuller. “Particle Image Velocimetry in Lung Bifurcation Models”. In: *Particle Image Velocimetry*. Berlin, Heidelberg: Springer Berlin Heidelberg, 2008, pp. 73–101. ISBN: 978-3-540-73528-1. DOI: 10.1007/978-3-540-73528-1\_5.
- [105] Raf Theunissen, Fulvio Scarano, and M L Riethmuller. “An adaptive sampling and windowing interrogation method in PIV”. In: *Measurement Science and Technology* 18.1 (2007), pp. 275–287. ISSN: 0957-0233. DOI: 10.1088/0957-0233/18/1/034.
- [106] Raf Theunissen, Fulvio Scarano, and M. L. Riethmuller. “On improvement of PIV image interrogation near stationary interfaces”. In: *Experiments in Fluids* 45.4 (2008), pp. 557–572. ISSN: 0723-4864. DOI: 10.1007/s00348-008-0481-9.
- [107] Joe F. Thompson. “A general three-dimensional elliptic grid generation system on a composite block structure”. In: *Computer Methods in Applied Mechanics and Engineering* 64.1-3 (1987), pp. 377–411.
- [108] Joe F. Thompson, Bharat K. Soni, and Nigel P. Weatherill. *Handbook of grid generation*. Ed. by B. Stern and Sylvia Wood. 1999. ISBN: 978-1-4200-5034-9. DOI: 10.1201/9781420050349.
- [109] Denis Tisserant and Frans A E Breugelmans. “Rotor blade-to-blade measurements using particle image velocimetry”. In: *The american society of mechanical engineers* 95-GT-99 (1995).
- [110] L. Tsuei and Ömer Savaş. “Treatment of interfaces in particle image velocimetry”. In: *Experiments in Fluids* 29.3 (2000), pp. 203–214. ISSN: 0723-4864. DOI: 10.1007/s003489900068.
- [111] G Usera, a Vernet, and J a Ferré. “Considerations and improvements of the analysing algorithms used for time resolved PIV of wall bounded flows”. In: *Proceedings of the 12 th International Symposium on Applications of Laser Techniques to fluid mechanics, Lisbon, Portugal, July* (2004), pp. 11–15.

- [112] Peter Vennemann et al. “In vivo micro particle image velocimetry measurements of blood-plasma in the embryonic avian heart”. In: *Journal of Biomechanics* 39.7 (2006), pp. 1191–1200. ISSN: 00219290. DOI: 10.1016/j.jbiomech.2005.03.015.
- [113] HongPing Wang et al. “Proper orthogonal decomposition based outlier correction for PIV data”. In: *Experiments in Fluids* 56.2 (2015), p. 43. ISSN: 0723-4864. DOI: 10.1007/s00348-015-1894-x.
- [114] J Westerweel. “Fundamentals of digital particle image velocimetry”. In: *Measurement Science and Technology* 8.12 (1997), pp. 1379–1392. ISSN: 0957-0233. DOI: 10.1088/0957-0233/8/12/002.
- [115] J. Westerweel. “On velocity gradients in PIV interrogation”. In: *Experiments in Fluids* 44 (2008), pp. 831–842. ISSN: 07234864. DOI: 10.1007/s00348-007-0439-3.
- [116] J Westerweel. “Theoretical analysis of the measurement precision in particle image velocimetry”. In: *Experiments in Fluids* Suppl. (2000), S3–S12.
- [117] Jerry Westerweel. “Digital Particle Image Velocimetry - Theory and Application -”. PhD thesis. 1993.
- [118] Jerry Westerweel. “Efficient detection of spurious vectors in particle image velocimetry data”. In: *Experiments in Fluids* 16 (1994), pp. 263–247.
- [119] Jerry Westerweel and Fulvio Scarano. “Universal outlier detection for PIV data”. In: *Experiments in Fluids* 39.6 (2005), pp. 1096–1100. ISSN: 0723-4864. DOI: 10.1007/s00348-005-0016-6.
- [120] C E Willert and M Gharib. “Digital particle image velocimetry”. In: *Experiments in Fluids* 10.4 (1991), pp. 181–193. DOI: 10.1007/BF00190388.
- [121] Christian Willert. “Stereoscopic digital particle image velocimetry for application in wind tunnel flows”. In: *Measurement Science and Technology* 8.12 (1997), pp. 1465–1479. ISSN: 0957-0233. DOI: 10.1088/0957-0233/8/12/010.
- [122] G Wolberg. “Digital image warping”. In: *IEEE Computer Society Press*. Los Alamitos, 1990.
- [123] Zhenyu Xue, John J Charonko, and Pavlos P Vlachos. “Particle image velocimetry correlation signal-to-noise ratio metrics and measurement uncertainty quantification”. In: *Measurement Science and Technology* 25.11 (2014), p. 115301. ISSN: 0957-0233. DOI: 10.1088/0957-0233/25/11/115301.
- [124] C N Young, D a Johnson, and E J Weckman. “A method to anchor displacement vectors to reduce uncertainty and improve particle image velocimetry results”. In: *Measurement Science and Technology* 15.1 (2004), pp. 9–20. ISSN: 0957-0233. DOI: 10.1088/0957-0233/15/1/002.

- 
- [125] C. N. Young, D. a. Johnson, and E. J. Weckman. “A model-based validation framework for PIV and PTV”. In: *Experiments in Fluids* 36.1 (2004), pp. 23–35. ISSN: 0723-4864. DOI: 10.1007/s00348-003-0602-4.
- [126] K Bülent Yüceil, M Volkan Ötügen, and Engin Arik. “Underexpanded sonic jets: a PIV study”. In: *10th international symposium on application of laser techniques to fluid mechanics*. Lisbon, Portugal, 2000.
- [127] G. W. Zack, W. E. Rogers, and S. A. Latt. “Automatic measurement of sister chromatid exchange frequency”. In: *The Journal of Histochemistry and Cytochemistry* 25.7 (1977), pp. 741–753.